Title

Mechanistic insights into the regulation of microtubule assembly and dynamic instability by tau and MMAE

Permalink

https://escholarship.org/uc/item/1r982032

Author

Best, Rebecca Leah

Publication Date

2020

Peer reviewed|Thesis/dissertation

University of California
Santa Barbara

Mechanistic insights into the regulation of microtubule assembly and dynamic instability by tau and MMAE

A dissertation submitted in partial satisfaction
of the requirements for the degree

Doctor of Philosophy
in
Molecular, Cellular, and Developmental Biology

by

Rebecca Leah Best

Committee in charge:

> Professor Stuart C. Feinstein, Chair
> Professor Kathleen Foltz
> Professor Leslie Wilson
> Professor Herbert Waite

December 2020

The Dissertation of Rebecca Leah Best is approved.

_____

Professor Kathleen Foltz

_____

Professor Leslie Wilson

_____

Professor Herbert Waite

_____

Professor Stuart C. Feinstein, Committee Chair

November 2020

Mechanistic insights into the regulation of microtubule assembly and dynamic
instability by tau and MMAE

To Nikki LaPointe, for letting me follow you around for three years. Not only did you teach me pretty much everything I know about tau and microtubules, you showed me what it means to do good science and to be a good lab member. Your kindness, dedication, intelligence, humor, and curiosity continue to inspire me in and outside of lab. This would not exist without you.

And to Stu Feinstein, for teaching me to see the forest for the trees.

Acknowledgements

First and foremost, I would like to thank my advisor, Professor Stu Feinstein, for giving me an incredible education that stretched far beyond benchwork into grant writing, project administration, mentorship, lab management, and navigation through the seemingly endless levels of bureaucracy. His encouragement, support, and advice provided the ideal training environment for both my personal growth and the growth of my scientific perspective. I would also like to thank Nikki LaPointe, who patiently taught me how to polymerize MTs, purify tau, and helped me wade into the depths of statistical analysis. Nikki and Stu's enthusiastic persistence in the face of inevitable scientific obstacles taught me how much fun science can be, and has made it an absolute pleasure to be in the Feinstein lab.

I would also like to thank Professor Kathy Foltz for being a non-stop source of support, encouragement, and inspiration for the past ten years, ever since I took her introduction to research honors seminar my first year of undergraduate study. Kathy's commitment to her students, research, teaching, and community is truly remarkable.

I would also like to thank the other members of my dissertation committee, Professors Les Wilson and Herb Waite, for the genuine curiosity, enthusiasm for science, and helpful advice they brought to each of our meetings and discussions.

I would especially like to thank Kevin Ruan, who I have been privileged enough to mentor, first as an undergraduate and then as a master's student, since we both joined the lab in 2015. Kevin was the best undergraduate I could have possibly asked for, and working with him side-by-side as he grew into the conscientious, curiosity-driven, and talented scientist he is today has been one of the most rewarding experiences of my PhD. I would also like to thank all the members of the Feinstein, Wilson-Jordan, and Safinya lab groups, especially Bretton Fletcher and Christine Tchounwou, for their

Curriculum Vitæ
Rebecca Leah Best

Education

2020	Ph.D. in Molecular, Cellular, and Developmental Biology (Expected), University of California, Santa Barbara.
2019	M.A. in Molecular, Cellular, and Developmental Biology, University of California, Santa Barbara.
2014	B.S. in Cellular and Developmental Biology, University of California, Santa Barbara.

Professional Employment

2019-2020	Associate Biological Scientist, Apeel Sciences.
2017-2020	Teaching Assistant, Developmental Neurobiology, Department of Molecular, Cellular, and Developmental Biology, University of California, Santa Barbara.
2012 – 2015	Private tutor, CollegeboundSB, Santa Barbara, CA
2012 – 2014	Chemistry tutor, Campus Learning Assistance Services, University of California, Santa Barbara.
2011 - 2012	Tutor/mentor, Santa Barbara Pathways Program, University of California, Santa Barbara.

Publications

In preparation	Best R.L.*, LaPointe N.E.*, Azarenko O.*, Miller, H. Genualdi C., Chih S., Shen B-Q., Jordan M.A., Wilson L., Feinstein S.C., Stagg N.J. (*contributed equally) Microtubule and Tubulin Binding and Regulation of Microtubule Dynamics by the Antibody Drug Conjugate (ADC) Payload, Monomethyl Auristatin E (MMAE): Mechanistic Insights into MMAE ADC Peripheral Neuropathy.
2019	Best, R.L., LaPointe, N.E., Liang, J., Ruan, K., Shade, M.F., Wilson, L., Feinstein, S.C. Tau isoform -specific stabilization of intermediate states during microtubule assembly and disassembly. J Biol Chem, 294, 12265-12280.
2017	Best, R. L., Chung, P. J., Benbow, S. J., Savage, A., LaPointe, N. E., Safinya, C. R., Feinstein, S. C. Expression and isolation of recombinant tau. Methods Cell Biol, 141, 3-26.

Awards

2017 – 2020	NSF Graduate Research Fellowship (GRFP) (1650114), "Unraveling an unexpected effect of tau on the structure of microtubule ends"
2019	Best annual presentation by a fourth-year graduate student, awarded by peers for best talk by a fourth-year student in graduate student-run seminar series, Department of Molecular, Cellular, and Developmental Biology, University of California, Santa Barbara.
2018	Excellence in Neuroscience Research Award, awarded for best talk by a graduate student at the twenty-first annual Neuroscience Research Symposium, University of California, Santa Barbara.
2017	Semi-finalist, UCSB Grad Slam, award-winning campus-wide competition for the best three-minute talk by a graduate student, University of California, Santa Barbara.
2016	Storke Academic Excellence Award, awarded for the highest GPA in the core courses among first-year MCDB graduate students, University of California, Santa Barbara.
2015 – 2016	UC Regents' Graduate Fellowship, provided one year of funding to a promising first-year graduate student, University of California, Santa Barbara.
2014	Distinction in the Major, awarded to students who demonstrated an outstanding commitment to undergraduate research, University of California, Santa Barbara.
2014	Highest Honors, awarded to the top 2.5% of the graduating class, University of California, Santa Barbara.
2014	Academic Excellence Award, University of California, Santa Barbara.
2010 – 2014	UC Regents' Undergraduate Scholar, four-year scholarship awarded to incoming undergraduates with outstanding academic achievement, University of California, Santa Barbara.
2013	Undergraduate Research and Creative Activities (URCA) grant recipient, "Natural variation in aging-related effects on memory in D. mel.," Department of Molecular, Cellular, and Developmental Biology, University of California, Santa Barbara.
2013	Perlegos Summer Research Fellow, "Natural variation in aging-related effects on memory in D. mel.," Department of Molecular, Cellular, and Developmental Biology, University of California, Santa Barbara.

Fields of Study

Major Field: Biochemistry underlying neural development and Alzheimer's disease

Abstract

Mechanistic insights into the regulation of microtubule assembly and dynamic
instability by tau and MMAE

by

Rebecca Leah Best

Microtubules (MTs) are dynamic cytoskeletal polymers that are essential for many cel-
lular processes, including cell division, maintenance of cellular shape, intracellular trans-
port, and cell signaling. Their dynamic, switch-like behavior, known as MT dynamic
instability, arises from the conformational changes associated with GTP hydrolysis by
β-tubulin, but exactly how the tubulin conformational cycle contributes to the overall
MT dynamic state remains unclear. Proper regulation of MT dynamicity is critical across
almost all cell types, but their necessity for proper chromosome alignment and division
during mitosis make them an especially effective target for anti-cancer drugs targeting
rapidly dividing tumor cells. Despite the broad use of these MT-targeting agents (MTAs)
as chemotherapeutics, we often lack understanding of the mechanisms of action under-
lying the global changes they enact on MT dynamics. We investigated the binding of
MTA Monomethyl auristatin E (MMAE), as a free drug or as an antibody-drug conju-
gate (ADC), to MTs and free tubulin subunits, and characterized its effects upon MT
dynamics and MT morphology as well as cell proliferation, cell cycle regulation, and
the generation of mitotic spindle abnormalities in cultured human cells. In combination
with comparisons made to other MTAs, our data provide further insights into the molec-
ular mechanisms underlying normal MMAE action as well as those governing MMAE
ADC-induced peripheral neuropathy.

In cells, MT-associated proteins (MAPs) help to regulate MT dynamics. Tau is a

neuronal MAP that regulates the critical growing and shortening behaviors of neuronal MTs, and its normal activity is essential for neuronal development and maintenance. Accordingly, aberrant tau action is tightly associated with Alzheimer's disease and is genetically linked to several additional neurodegenerative diseases known as tauopathies. Indeed, one often suggested model for pathological tau action in Alzheimer's and related, dementia-causing tauopathies is the destabilization of axonal MTs, leading to aberrant axonal transport and neuronal cell death. Although tau's most well-characterized activity is its promotion of net MT growth and stability, the precise mechanistic details governing its regulation of MT dynamics remain unclear.

We used the slowly-hydrolyzable GTP analog, guanylyl-(α,β)-methylene-diphosphonate (GMPCPP), to examine the structural effects of tau at MT ends that may otherwise be too transient to observe. We found that co-incubation of GMPCPP tubulin and tau resulted in the formation of extended, multiprotofilament-wide tubulin spirals emanating i) from the ends of pre-assembled MTs at 25 °C, ii) from free tubulin heterodimers at 4 °C, and iii) from free tubulin heterodimers at 34 °C. While 3R and 4R tau isoforms promoted MT assembly intermediates similarly, 4R tau stabilized disassembly spiral intermediates much more effectively than 3R tau, consistent with 4R tau's more effective suppression of MT shortening events. Importantly, all of these spiral structures were also observed, albeit at much lower frequencies, in the absence of tau, and have also been observed in previous studies of both GTP and GMPCPP tubulin, consistent with the notion that that they are *bona fide* intermediates in the MT assembly/disassembly processes.

Finally, three tau proteins harboring mutations that cause neurodegeneration and dementia were differentially compromised in their abilities to stabilize intermediate structures. Taken together, we propose that tau promotes the formation/stabilization of intermediate states in MT assembly and disassembly by promoting both longitudinal

and lateral tubulin–tubulin contacts. We hypothesize that these activities represent fundamental aspects of tau action that normally occur at the GTP-rich ends of GTP/GDP MTs and that may be compromised in neurodegeneration-causing tau variants.

Contents

List of Figures

List of Tables

Abbreviations

3R	3-repeat tau
4R	4-repeat tau
A_{350}	Light scattering at 350 nm
AD	Alzheimer's disease
ADC	Antibody-drug conjugate
ANOVA	Analysis of variance
CIPN	Chemotherapy-induced peripheral neuropathy
CTT	C-terminal tail
D	Aspartic acid
E	Glutamtic acid
EB	End binding protein
E. coli	*Escherichia coli*
EDTA	Ethylene diamine tetraacetic acid
EGTA	Ethylene glycol tetraacetic acid
FTDP-17	Fronto-temporal dementia with parkinsonism linked to chromosome 17
GDP	Guanosine diphosphate
GLM	Generalized linear model
GMPCPP	Guanylyl-α-β-methylenediphosphonate
GTP	Guanosine triphosphate
GTPγS	Guanosine 5-O-γ-thiotriphosphate
IC_{50}	half maximal inhibitory concentration
K_d	Dissociation constant
kDa	kiloDalton
LLPS	Liquid-liquid phase separation

MAP	Microtubule-associated protein
MMAE	Monomethyl auristatin E
MT	microtubule
MTA	Microtubule targeting agent
MTBR	Microtubule-binding region
MW	Molecular weight
NFT	Neurofibrillary tangle
NTR	N-terminal region
OH	Ordered heterogeneity
OTS	Orthogonal translation system
PBS	Phosphate buffered saline
PRR	Proline-rich region
pSer	Phospho-Serine
pThr	Phospho-Threonine
SDS-PAGE	Sodium dodecyl sulfate gel electrophoresis
SRB	Sulforhodamine B
$t_{1/2}$	half time for maximal assembly
$t_{1/10}$	one-tenth time for maximal assembly
T-DM1	ado-trastuzumab emtansine
TEM	Transmission electron microscopy

Chapter 1

Introduction

1.1 Microtubules

Microtubules (MTs) are dynamic cytoskeletal polymers that are assembled from heterodimers of α- and β-tubulin. Heterodimers must be GTP-bound to assemble into MTs, a process that is primarily governed by the formation of longitudinal, or head-to-tail, tubulin-tubulin bonds, which are estimated to be $\sim$5x stronger than tubulin-tubulin lateral bonds (Fig. 1.1; [Mandelkow et al., 1991, Vanburen et al., 2002]). Although the precise mechanistic details governing MT nucleation remain elusive, it is generally believed that heterodimers first associate longitudinally to form protofilaments, 13-15 of which laterally associate to form a MT (Fig. (1.1). At some point post-incorporation into the lattice, the GTP bound to β-tubulin is hydrolyzed, resulting in conformational changes that introduce additional strain into the MT lattice and MTs that are more prone to "catastrophe," a rapidly shortening state in which the weaker lateral contacts between protofilaments are lost and protofilaments peel outward from the body of the MT [Mandelkow et al., 1991, Bähler et al., 2008, Vanburen et al., 2002, Sept et al., 2003, Margolin et al., 2011, Brouhard and Rice, 2014, Alushin et al., 2014]. MTs experiencing catastrophe also occasionally exhibit rescue, a phenomenon in which the rapidly shrinking MT switches back to a period of growth or attenuation.

1

MTs are critically important to the maintenance of cellular structure and function in many different cell types, but they are especially essential to mitosis, where they are responsible for the establishment of the mitotic spindle and the alignment and subsequent separation of sister chromosomes [Inoue and Salmon, 1995]. This critical importance during cell division makes MTs make an especially attractive target for chemotherapeutic drugs that target rapidly dividing cancer cells. Indeed, microtubule targeting agents (MTAs) are a diverse group of chemotherapeutic drugs that have been and continue to be used with great success to combat many types of cancer [Argyriou et al., 2012, 2011, Carlson and Ocean, 2011, Windebank and Grisold, 2008]. Mechanistically, MTA action derives from their ability to alter the delicate balance of MT dynamics and/or regulatory mechanisms controlling MT dynamics and MT-based transport, which, in turn, leads to improper mitotic spindle formation, mitotic arrest, and tumor cell death (for more on MTA action and cellular consequences, see chapter 4; [Steinmetz and Prota, 2018, Argyriou et al., 2012, Field et al., 2014, Jordan and Wilson, 2004]).

1.1.1   Dynamic instability

This dynamic, switch-like behavior, known as MT dynamic instability, arises from the conformational changes associated with GTP hydrolysis by β-tubulin, but exactly how the tubulin conformational cycle contributes to the overall MT dynamic state remains unclear. MTs have long been proposed to possess a stabilizing "GTP" or "GDP-Pi" cap at their ends composed of tubulin heterodimers that have not yet undergone conversion to GDP. The size of this cap has been somewhat controversial, with original estimates predicting small cap sizes (see [Caplow, 1992, Carlier, 1992, Desai and Mitchison, 1997, Erickson and O'Brien, 1992] for review), some just a single layer of tubulin dimers thick [Caplow and Shanks, 1996, Panda et al., 2002], while more recent estimates predict cap

A

β-GTP   β-GDP

α   P_i   α

Tubulin heterodimer

B

Intra-dimer interface → ← Inter-dimer interface

Longitudinal contacts

Lateral contacts

C

25 nm

MT end-on view

D

GTP

GDP

Disassembly products

Protofilament

Catastrophe

Rescue

(+) end

Sheet

Shortening microtubule

(-) end

Growing microtubule

Attenuated microtubule
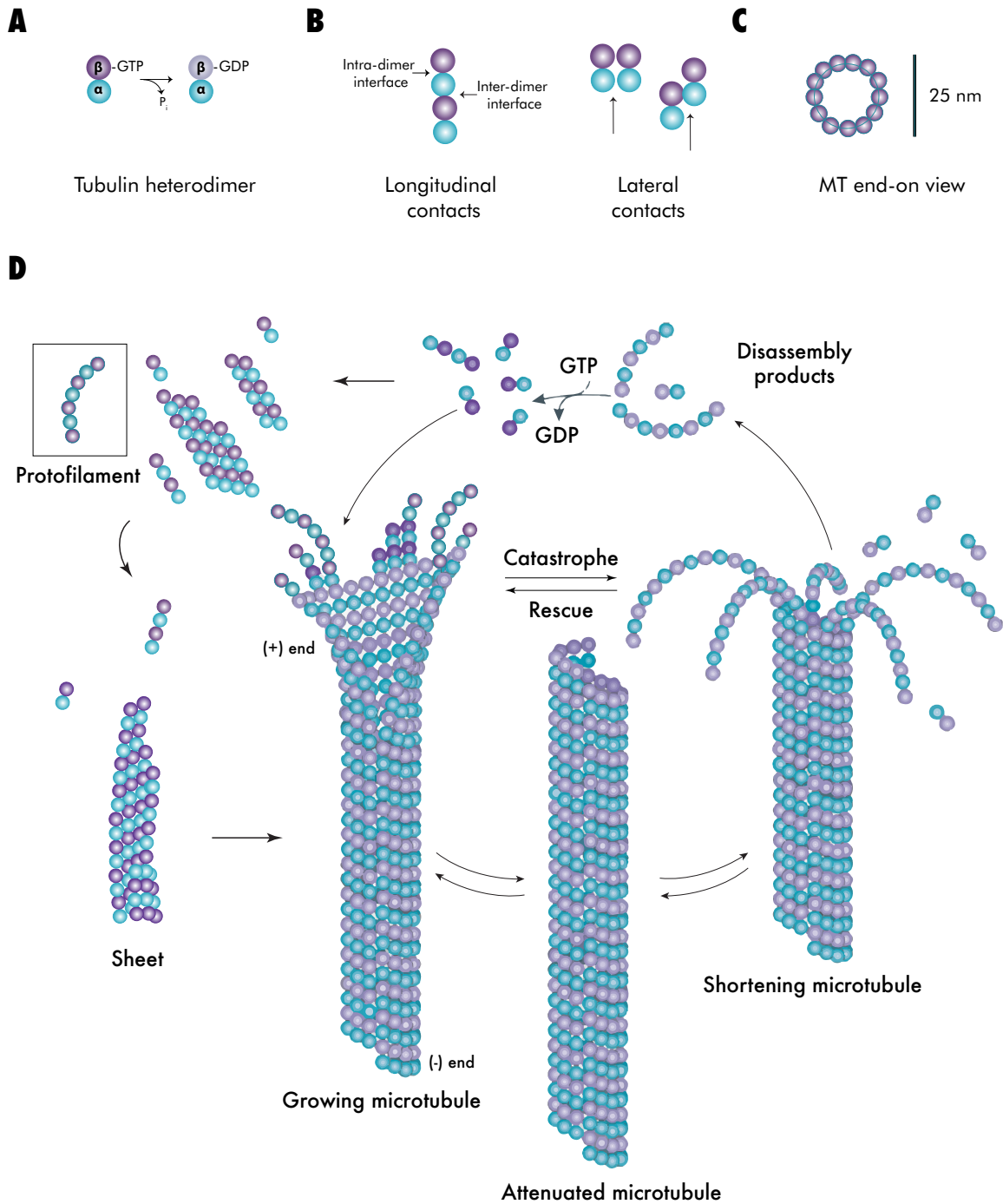
Figure 1.1: **MT life cycle** Schematic of the various stages of dynamic instability. (A) Individual heterodimers hydrolyze GTP on β-tubulin following assembly into the MT lattice. (B, left) Illustration of longitudinal tubulin-tubulin contacts at the inter-dimer interface (arrow), with intra-dimer interface also shown. (B, right) Lateral tubulin-tubulin contacts (arrows), including both homotypic (left, α-α and β-β) and heterotypic (right, α-β) types. (C) End-on view of a MT. (D) Various proposed stages in dynamic instability. Adapted from [Conde and Caceres, 2009].

lengths of several hundred tubulin dimers [Bieling et al., 2007, Seetapun et al., 2012].
Ultimately, the GTP cap serves to promote further MT elongation and prevent catastrophe. Early models attributed the stabilizing effect of the GTP cap and assembly competency of GTP tubulin to an inherent difference in tubulin's intrinsic curvature between the GTP and GDP state (with GTP possessing a straight conformation and GDP possessing a curved conformation). This model was supported by the observed tapered, gently curving GTP tubulin sheets that formed at fast-growing MT ends [Chretien et al., 1995, Muller-Reichert et al., 1998, Simon and Salmon, 1990], which were much straighter than the highly curved protofilament "rams horns" observed at depolymerizing MT ends [Mandelkow et al., 1991, Muller-Reichert et al., 1998, Simon and Salmon, 1990]. However, more recent work indicates that, while GTP tubulin is straighter than GDP tubulin, it is also curved, arguing that straightening occurs as MT-specific lateral contacts are established [Alushin et al., 2014, Brouhard and Rice, 2014, Rice et al., 2008]. Thus, rather than protofilament curvature, the most recent picture of the conformational changes that accompany GTP hydrolysis includes a $\sim$2-Angstrom compaction of the interface between longitudinally-associated heterodimers and rotation of α-tubulin into a more bent structure [Alushin et al., 2014, Zhang et al., 2015, 2018]. This is believed to strengthen inter-dimer longitudinal contacts (Fig. 1.1B), but it is also proposed to cause a two-step perturbation in lateral contacts, ultimately resulting in MT catastrophe as the lateral contacts become too weak to overcome the intrinsic strain of the lattice-confined dimers [Manka and Moores, 2018, Zhang et al., 2018]. This model of enhanced longitudinal inter-dimer bonds due to GTP hydrolysis is consistent with the observation that whole protofilaments (maintaining longitudinal contacts) peel away from MTs during cation-induced MT catastrophe [Mandelkow et al., 1991, Muller-Reichert et al., 1998]. However, there is still some disagreement over whether it is the breakage of the heterotypic lateral contacts (α-tubulin interacts with β-tubulin) found only at the MT

"seam," [Zhang et al., 2018] or the breakage of the homotypic lateral contacts (α-α or β–β contacts) found throughout the rest of the MT lattice [Manka and Moores, 2018] that is ultimately driving the loss of overall MT stability.

1.1.2   Microtubule ends

Due to the intrinsic polarity of the tubulin heterodimer, MTs possess distinct ends, the plus and minus ends, which are defined by their terminal subunits (β- or α-tubulin, respectively) (Fig. 1.1D). This polar nature results in uniquely dynamic MT ends, with plus ends being faster-growing and overall more dynamic than minus ends [Atherton et al., 2017], perhaps due to their differential protofilament curvatures and therefore lateral inter-protofilament interactions. This suggests that the increased stability of minus ends may derive from their ability to more easily accommodate the intrinsic curvature of tubulin [Atherton et al., 2017] and/or resulting differences in the off-rate of incoming GTP-bound heterodimers [Strothman et al., 2019]. This model is further supported by experiments showing that, while both plus and minus exhibit the same GTP-dependent assembly and disassembly behavior, minus ends do so at comparatively slower rates and can exhibit pausing, a phenomenon which is not observed for MT plus ends in vitro [Doodhi et al., 2016, Erickson and O'Brien, 1992, Walker et al., 1988]. Furthermore, while the removal of the GTP cap by severing resulted in rapid disassembly at MT plus ends, minus ends were more stable and could easily re-grow following severing [Walker et al., 1989].

The structure of the MT end has been elusive, in part due to its intrinsically dynamic nature. Initial *in vitro* studies suggested that growing MT plus ends were mostly blunt, i.e. containing laterally bonded protofilaments of similar lengths, and a small fraction of ends possessed gently curved, sheet-like extensions that ranged from 50-2000 nm

(corresponding to $\sim$6-250 tubulin dimers) long and lengthened with increasing growth rates [Mandelkow et al., 1991, Chretien et al., 1995, Erickson, 1974]. Subsequent studies suggested that $\sim$30-40% of growing MT plus ends are actually tapered, i.e. containing protofilaments with both heterogeneous lengths[Janosi et al., 1998, Guesdon et al., 2016, Wang et al., 2005, Maurer et al., 2014, Gardner et al., 2011, Zakharov et al., 2015, Van-Buren et al., 2005] and exhibiting heterogeneous curvatures [Janosi et al., 1998]. When considered in the context of the recent cryo-electron microscopy (cryo-EM) structures showing that GTP tubulin is also highly curved in solution [Alushin et al., 2014, Zhang et al., 2018], this implies that the progressive increase in the number of lateral bonds tubulin dimers maintain at MT ends drives their progressive straightening and closing up of the nascent MT lattice. This is consistent with reports that end-bound dimers possessing 2 lateral bonds were approximately half-straightened [Wang et al., 2005]), those with 3-5 lateral bonds were straighter still [Janosi et al., 1998], and those with 6 lateral bonds were straightened into a MT-like conformation [Guesdon et al., 2016, Zhang et al., 2015, Brouhard and Rice, 2018]. However, a recent electron tomography study, which did not require the high pressure and potentially MT depolymerization-promoting conditions necessary in the earlier studies, suggested that protofilaments at the growing MT end actually grow independently of one another and maintain their individual curvatures [McIntosh et al., 2018]. In fact, the gently curving sheets seen by Chretien et al. [1995] and others were rarely observed in McIntosh et al. [2018]'s experiments (across 6 different species of cell lines as well as in vitro) [McIntosh et al., 2018]. Strikingly, McIntosh et al. [2018] observed no structural differences between protofilaments at growing and shortening MT ends, challenging a long-standing belief in the field that growing and shrinking MT ends maintain distinct structures. This idea, however, is consistent with the similarities in curvature reported for the GTP and GDP tubulin states [Alushin et al., 2014, Brouhard and Rice, 2014, Zhang et al., 2018], cellular studies showing a

similar "flared" morphology resulting from outward protofilament curvature during both growth and shortening events [McIntosh et al., 2008, 2013, Hoog et al., 2011], as well as with our own work showing that the MT-associated protein (MAP) tau stabilizes similar intermediate structures at MT ends during both MT assembly and MT disassembly ([Best et al., 2019]; discussed more in chapter 3).

The observed correlation between the MT end structure/state and the overall MT dynamic state has led some to propose an "end-driven" model of MT dynamics, which hypothesizes that the formation of a meta-stable intermediate state at MT ends dictates whether or not rescue from catastrophe will occur [Fees and Moore, 2019]. Another, non-mutually exclusive model relating the mechanics of GTP hydrolysis to the biochemistry of MT dynamics is the "lattice-driven" model in which it is the state of the MT lattice, propagated over the distance of the MT to the MT ends, that dictates MT dynamicity. Ultimately, it seems a "unified model" incorporating both lattice-driven and end-driven models is most likely, particularly when considering that long-range mechanical coupling between tubulin subunits in the lattice will not only affect lattice state, but will also affect MT end state [Brouhard and Rice, 2018, de Forges et al., 2016, Akhmanova, 2018]. Small shifts in hydrogen bond arrangement at the site of nucleotide exchange on β-tubulin, for example, can propagate over long lattice distances and result in the protofilaments running at a slightly different skew angle, which, in turn, would alter the inter-protofilament lateral interactions and result in altered properties of MT dynamicity [Zhang et al., 2018]. In this way, the MT lattice state would serve as an incredibly powerful common integration point for the many factors that affect MT dynamics in vivo, including tubulin nucleotide state, tubulin isoforms, tubulin post-translational modification (PTM), and different MAP binding partners [Zhang et al., 2018]. This allows for exquisite potential points of control over the MT system via the regulation of a multitude of tubulin properties, such as protofilament curvature/skew, lattice spacing, and dimer twist, but

also allows for combinatorial binding and a common "code" all MAPs can "read" [Zhang et al., 2018].

1.2   Tau

Tau is an intrinsically disordered (IDP), microtubule-associated protein (MAP) found primarily in neuronal axons and cell bodies. Alternative splicing of tau RNA results in the expression of six different tau isoforms in the adult human CNS ([Goedert et al., 1989, Himmler, 1989]; Fig. 1.2), where, under normal circumstances, it is necessary for the establishment and maintenance of neuronal cell polarity and cell morphology, in addition to various MT-dependent functions such as axonal transport [Bunker et al., 2004, Drubin et al., 1986, 1985, Caceres and Kosik, 1990, Esmaeli-Azad et al., 1994, Liu et al., 1999, Stamer et al., 2002].

Aberrant tau biochemistry has long been correlated with Alzheimer's disease (AD) and related dementias, and genetic analyses have demonstrated unequivocally that both structural and regulatory errors in tau action and expression can cause neurodegeneration and dementia in FTDP-17, PSP, and a number of other tauopathies closely related to AD [Brunden et al., 2009, Garcia and Cleveland, 2001, Hernandez and Avila, 2007, Lee, 2001, Morris et al., 2011, Wolfe, 2009]. Among the proposed mechanisms of pathological tau action is altered tau-MT interactions, ultimately leading to MT destabilization and tau self-aggregation into neurofibrillary tangles (NFTs), which are considered a hallmark of AD. While good evidence has been presented supporting both loss-of-function [Brunden et al., 2009, 2010, Levy et al., 2005] and gain-of-toxic-function mechanisms [Vossel et al., 2015, 2010], the molecular mechanism(s) by which aberrant tau action or regulation results in disease remains unknown.

Tau's best understood function is to regulate MT dynamics, which are critical in order

for MTs to perform their essential functions. In the adult brain, alternative splicing of exon 10 results in equal expression of tau proteins possessing either 3 or 4, highly conserved, imperfect MT binding repeats, denoted as 3R or 4R, respectively (Fig. 1.2). Mechanistically, 3R and 4R tau regulate MT dynamics by:

1. lowering the critical concentration of tubulin dimers required for MT assembly [Panda et al., 2003, Gustke et al., 1994, Cleveland et al., 1977],

2. moderately increasing MT growth rates [Panda et al., 2003, Drechsel et al., 1992], and

3. increasing the amount of time MTs spend in an attenuated or static state [Panda et al., 1995, 2003, Bunker et al., 2004, Drechsel et al., 1992, Breuzard et al., 2013].

Interestingly, while both 4R and 3R tau promote net MT growth and overall stability, 4R tau stabilizes MTs against disassembly far more effectively than 3R tau by suppressing both the average rate and length of shortening events [Bunker et al., 2004, Panda et al., 2003, Trinczek et al., 1995], leading to reduced catastrophe frequency [Trinczek et al., 1995, Drechsel et al., 1992, Panda et al., 1995, 2003, Breuzard et al., 2013]. Mutations that disturb the normal isoform ratio between 3R and 4R tau (causing 75:25 4R tau:3R) result in early-onset neurodegeneration and dementia [Hutton et al., 1998, Spillantini et al., 1998], underscoring the different activities of the wild-type tau isoforms and the delicate balance of MT dynamics. However, the molecular mechanisms by which tau binding to tubulin heterodimers and MTs enables its global regulation of MT dynamics, as well as by which aberrant tau action/regulation results in disease, remain poorly understood.

Normal and pathological tau action is regulated by post-translational modification (PTM), a form of regulation that is likely to be especially important given tau's IDP

nature. It is widely appreciated that pathological tau is hyper-phosphorylated relative to normal tau (containing an estimated 8 phosphates per molecule compared to $\sim$2 normally) [Wang et al., 2016], and tau phosphorylation precedes its pathological aggregation in tauopathy patients [Braak et al., 1994, Mondragón-Rodríguez et al., 2008]. Despite the critical role tau phosphorylation clearly plays in pathological tau action, it has been extremely challenging to study it in a rigorous and site-specific manner. More specifically, due to tau's large number of phosphorylatable residues (87 in the longest isoform) and its IDP nature, preparation of phosphorylated tau via purified kinases for experimental work suffers from both uncertain efficiency and specificity. These issues can be avoided by a pseudo-phosphorylation approach (e.g. replacing serine or threonine with a negatively charged amino acid such as glutamic or aspartic acid via site-directed mutagenesis), but the biological relevance of this imperfect mimic is very debatable. Ultimately, rigorous insight into the fundamentally important question of how tau's hyperphosphorylation relates to its pathological dysfunction, aggregation, and downstream neurodegeneration in AD remains elusive.

Due to its intrinsic disorder, tau is typically subdivided based on its amino acid composition into the following regions (see Fig. 1.2):

1. the N-terminal region (NTR),

2. the proline-rich region (PRR),

3. the microtubule-binding region (MTBR), and the

4. C-terminal tail (CTT).
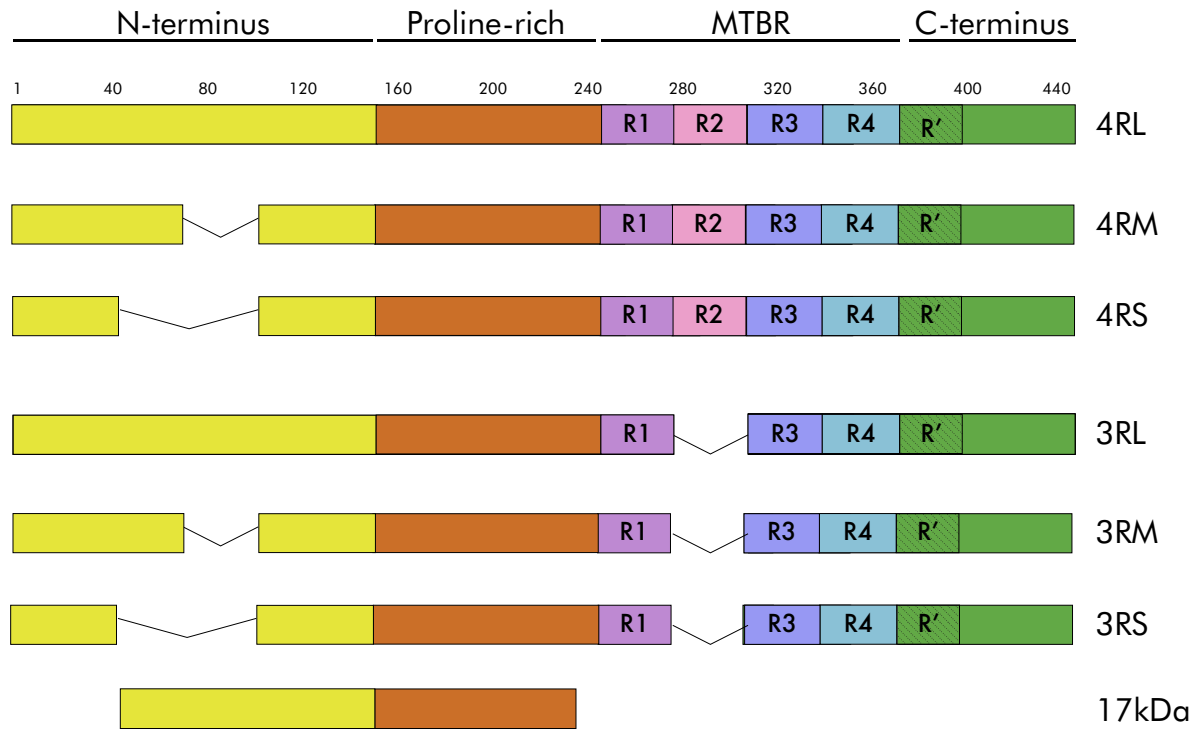
Figure 1.2: **Tau schematic** Six tau isoforms with major features labeled, including its N-terminal region (NTR), proline-rich region, microtubule-binding region (MTBR) containing 3 or 4 imperfect repeat regions (R1 - R4), and C-terminal tail (CTT), including the pseudo-repeat R'. The 17 kDa fragment (amino acids 45-230), a neurotoxic tau fragment which accumulates in the CNS of patients with Alzheimer's disease but not healthy controls, is shown on the bottom.

1.3   Tau structure and function

1.3.1   Microtubule binding region (MTBR)

Traditionally, tau's MT-binding repeats (Fig. 1.2) were considered the primary drivers of the tau-MT interaction [Goode and Feinstein, 1994, Gustke et al., 1994, Butner and Kirschner, 1991, Lee et al., 1988], and the MTBR forms the core of pathological tau aggregates [Fitzpatrick et al., 2017]. Perhaps unsurprisingly, many of the disease-causing

tau mutations and pathologically phosphorylated residues are found within tau's MTBR, where they may disrupt the electrostatically-mediated interaction between tau and tubulin and increase tau self-aggregation into NFTs [Wang et al., 2016, Kellogg et al., 2018]. Within the MTBR, the presence of multiple tubulin-binding motifs per tau enables a single tau molecule to bind multiple tubulin heterodimers simultaneously, which likely contributes to its ability to promote MT nucleation, assembly, and net MT stability [Li and Rhoades, 2017, Kellogg et al., 2018]. However, the nature and location of these tubulin-binding sites has remained somewhat elusive, in part due to tau's IDP nature, which, until recently, precluded the obtainment of high-resolution cryo-EM structures of tau bound to a MT. Indeed, tau has been proposed to bind at multiple sites on a MT, both along the outer MT surface [Kellogg et al., 2018, Al-Bassam et al., 2002] and within the MT lumen [Kar et al., 2003, Martinho et al., 2018]. Further, tau has been proposed to promote both lateral [Duan et al., 2017, Kar et al., 2003, Best et al., 2019] and longitudinal [Al-Bassam et al., 2002, Devred et al., 2004, Kadavath et al., 2015, Kellogg et al., 2018, Best et al., 2019] contacts between tubulin dimers.

Recent technological advances enabled Kellogg et al. [2018] to obtain the long-sought after tau-MT structure at the highest resolution to date, showing tau as a "narrow, discontinuous density" along the outer ridge of each protofilament, suggesting that each tau repeat in the MTBR binds to one tubulin heterodimer, resulting in one 4R tau molecule longitudinally linking 4 tubulin dimers along the outer MT/protofilament surface [Kellogg et al., 2018] and enhancing longitudinal tubulin-tubulin bonds [Kellogg et al., 2018, Al-Bassam et al., 2002]. While this structure represents a huge advance in our understanding of tau-MT interactions, it does not account for tau's observed promotion of lateral tubulin-tubulin contacts such as are observed during tau-mediated stabilization of intermediate states in MT assembly and disassembly (see chapter 3 for more detail) or during tau-mediated MT-bundling [Scott et al., 1992].

1.3.2 C-terminal tail and R' (CTT and R')

It is becoming increasingly evident that tau's other regions also play key roles in the regulation of its binding to tubulin and MTs and its promotion of MT assembly. For example, the MTBR is followed by an approximately 25-residue, highly conserved "pseudo-repeat" region, denoted R', found in tau's CTT (Fig. 1.2) that has been implicated as a significant contributor to the tau-tubulin interaction and tau's promotion of MT assembly [Li and Rhoades, 2017]. Specifically, the presence of R' promoted the formation of large, heterogenous tau:tubulin "fuzzy complexes," a collection of dynamic structures containing different tau:tubulin molar ratios [Li and Rhoades, 2017]. The larger and more heterogeneous fuzzy complexes (>1:2 tau:tubulin heterodimer stoichiometry) positively correlated with increased MT nucleation, while the loss of R', even in constructs containing the entire MTBR, resulted in the loss of that heterogeneity, a drastic shift towards lower tau:tubulin binding stoichiometry (approaching 1:1), and decreased polymerization rates [Li and Rhoades, 2017]. Altogether, these results support the presence of an additional tubulin binding site or site(s) located in R' and are consistent with the notion that fuzzy complexes generally form when one or more of the proteins, in this case tau, binds the other via the interaction of multiple short binding sites connected by disordered linkers [Li and Rhoades, 2017]. Interestingly, Fung et al. [2020] found that tubulin's disordered, C-terminal tails, which are implicated in the tau-tubulin interaction [Devred et al., 2004] but were not resolved in Kellogg et al. [2018]'s cryo-EM study, also hugely impacted fuzzy complex formation, with their loss resulting in decreased size and heterogeneity of these complexes [Fung et al., 2020]. Altogether, R' appears to also bind to tubulin, possibly via interaction(s) with tubulin's C-terminal tails, and enhances tau's assembly-promoting activity.

1.3.3   Proline-rich region (PRR)

Tau's PRR was found early-on to strongly contribute to tau binding to and promotion of MT assembly and stability [Goode et al., 1997, Gustke et al., 1994, Brandt and Lee, 1993, Lewis et al., 1989]. More recent results suggest that the PRR can also independently mediate tau's binding to and promotion of tubulin assembly [McKibben and Rhoades, 2019]. In fact, constructs composed of the PRR alone (amino acids 148-244, lacking any MT-binding repeats) possessed strong tubulin binding affinity and assembly-promoting activity, outperforming constructs containing either the entire MTBR alone (amino acids 244-372) or the MTBR+R' (amino acids 244-395) [McKibben and Rhoades, 2019]. The PRR exhibited saturable binding to tubulin at a maximum stoichiometry of 1 tau: 2 tubulin dimers, suggesting the presence of two tubulin binding sites [McKibben and Rhoades, 2019]. This was in marked contrast to the PRR+MTBR+R' construct, which exhibited non-saturable binding and, unlike the PRR alone, promoted the formation of large tau:tubulin fuzzy complexes that positively correlated with polymerization rate [Li and Rhoades, 2017, McKibben and Rhoades, 2019]. Taken together, these data suggest that cooperativity between tubulin binding sites contained within the PRR, MTBR, and R' is required for tau's interactions with soluble tubulin and its promotion of MT assembly [McKibben and Rhoades, 2019]. Furthermore, Kellogg et al. [2018]'s lack of observed tubulin-PRR interactions in their cryo-EM structure may have been due to the majority of the PRR being absent from the constructs used to obtain the highest resolution structure [Kellogg et al., 2018]).

Altogether, the presence of two tubulin binding sites within the PRR, three or four in the MTBR, and one or more in R' is consistent with tau binding to MTs reaching saturation at a molar ratio on the order of 1 tau per 5–10 tubulin dimers [Drechsel et al., 1992, Hirokawa et al., 1988, Kim et al., 1986], as well as 4R tau's effectiveness

in powerfully suppressing MT dynamics and reducing both the rate and extent of MT shortening at sub-stoichiometric concentrations of as low as 1 tau:473 tubulin dimers [Panda et al., 1995, 2003]. Despite recent progress, there is much to be discovered about the nature(s) of the tau-tubulin and tau-MT interactions, as well as how these interactions result in tau's global effects on MT dynamics. For example, tau sequences that interact with soluble tubulin dimers may be distinct from those that interact with MTs [Elbaum-Garfinkle et al., 2014, Kadavath et al., 2015, Li et al., 2015]. On the other hand, the lack of an inter-dimer interface on soluble tubulin or a protofilament may lead to "preferential" interactions between tau's different MT-binding repeats and soluble vs lattice-bound tubulin [Fung et al., 2020].

1.3.4   N-terminal region (NTR)

Tau's NTR, also called the "projection domain" due to its projection away from the MT surface during tau-mediated MT bundling, remains enigmatic. The presence or absence of exons 2 and/or 3 in tau's NTR dictates the number of negatively charged N-terminal inserts (0, 1, or 2, denoted "short" (S), "medium" (M), and "long" (L), respectively) in the protein (Fig. 1.2; [Himmler, 1989]). While early studies of tau binding to MTs showed the NTR possessed little MT-binding activity on its own [Goode et al., 1997, Gustke et al., 1994], its removal from the full-length protein resulted in an increase in tau's MT-binding affinity [Gustke et al., 1994]. This was recently confirmed by McKibben and Rhoades [2019], who showed that the addition of the NTR to both the PRR as well as to the MTBR+R' inhibited their binding to and promotion of MT assembly [McKibben and Rhoades, 2019]. Collectively, this suggests that tau's NTR may play an inhibitory role in its ability to bind to tubulin, possibly by shielding some or all of the weak binding sites distributed in the rest of the tau molecule. Intriguingly,

the presence of exons 2 and/or 3 had no effect on the NTR's inhibition of tau-promoted assembly, in contrast to its impact on the inter-MT spacing within MT bundles, with longer projection domains resulting in increased inter-MT distance [Chen et al., 1992, Gustke et al., 1994], suggesting a distinct regulatory mechanism for soluble tubulin vs MTs [McKibben and Rhoades, 2019]).

Tau's NTR has also been suggested to mediate normal tau dimer- or higher-order oligomerization, which Feinstein et al. [2016] proposed may be necessary for physiological tau action [Makrides et al., 2003, Rosenberg et al., 2008, Feinstein et al., 2016]. Tau's N-terminus was necessary for its dimer/oligomerization (hereafter referred to as "oligomerization" for the sake of simplicity), and an N-terminally derived tau fragment, the 17 kDa fragment (amino acids 45-230; Fig. 1.2), which lacks the MTBR and accumulates in the central nervous systems of patients suffering from AD and related tauopathies but not healthy controls [Park and Ferreira, 2005, Amadoro et al., 2006, Sinjoanu et al., 2008, Reinecke et al., 2011, Ferreira and Bigio, 2011, Nicholson and Ferreira, 2009] was sufficient for tau oligomerization [Feinstein et al., 2016]. This led Feinstein et al. [2016] to hypothesize that tau oligomerization, mediated by via an electrostatic "zippering" along two antiparallel N-termini, results in multivalent tau:tubulin complexes that may, for example, facilitate binding of multiple tubulin subunits to a growing MT end [Feinstein et al., 2016]. Consistent with this model of normal tau oligomerization, Wegmann et al. [2016] used a split luciferase approach to show that full-length tau normally formed at least dimers (and possibly higher order oligomers) in HEK293 cells and their media [Wegmann et al., 2016]. In addition, Li and Rhoades [2017] observed infrequent, tau-mediated crosslinking of samples containing the most highly heterogenous fuzzy complexes, suggesting that tau-tau interactions may facilitate cross-linking of tau:tubulin complexes and thereby promote MT nucleation [Li and Rhoades, 2017]. Despite these recent advances in understanding of tau biochemistry, there are still many unanswered questions

16

regarding tau's mysterious NTR and its roles in normal and pathological tau action.

1.4 Tau's recognition of different tubulin conformational states

1.4.1 Curved vs straight

Due to the need for tight regulation of dynamic instability, many MAPs have been proposed to preferentially bind to different tubulin nucleotide and/or conformational states (e.g. straight vs curved, GTP vs GDP) to result in their unique effects on MT dynamic instability. For example, MAPs EB1 and EB3 bind specifically to growing MT ends and promote MT growth as well as both rescue and catastrophe [Akhmanova and Steinmetz, 2015, Yang et al., 2017]. While some have proposed that EBs bind to the GTP cap region on growing MT ends, they exhibit poor binding to MTs assembled with the non-hydrolyzable GTP analog, guanylyl-(α,β)-methylene-diphosphonate (GM-PCPP), which is thought to best model the GTP cap [Maurer et al., 2011, 2012, Zhang et al., 2018]. Instead, the EBs preferentially bind to MTs assembled with GTPγS, a GTP analog proposed to correspond to the post-hydrolysis but pre-phosphate release, GDP-Pi, tubulin state found in the region immediately behind the GTP cap [Zhang et al., 2018]. Other MAPs, including XMAP215, exhibit preferential binding to curved tubulin dimers (independently of nucleotide state) and promote their straightening, effectively "handing off" up to 25 dimers to the MT lattice [Brouhard and Rice, 2018, Akhmanova and Steinmetz, 2015]. While tau preferentially accumulates on curved tubulin structures, including tubulin rings as well as curved sections of the MT lattice [Duan et al., 2017, Balabanian et al., 2017, Samsonov et al., 2004, Tan et al., 2019, Ettinger et al., 2016], it is unclear if or how this preference underlies tau's mechanistic effects on MT dynamics. MT ends

are proposed to share features with early nucleation intermediates [Zhang et al., 2018], so tau's preference for curved tubulin may result in its enrichment on both soluble GDP and GTP states and at MT ends, where its promotion of both lateral and longitudinal tubulin-tubulin bonds would lead to an accumulation of normally transient intermediates during MT nucleation, elongation, and disassembly [Best et al., 2019]. Ultimately, gaining a clear understanding of how the tubulin conformational cycle is differentially influencing and being influenced by tau and other MAPs to regulate MT dynamics will be key to understanding tau's normal, physiological functions as well as its pathology in neurodegenerative disease.

1.4.2 Tau's preferential binding of tubulin nucleotide states

1.4.2.1 Tau binding to MTs and MT ends

Early studies showed that tau decoration of MTs appeared to be uniform [Murphy and Borisy, 1975, Sloboda and Rosenbaum, 1979], supporting its binding to both GDP and GTP tubulin states. This was consistent with Kellogg et al. [2018]'s cryo-EM structure of MT-bound tau, which showed tau binding at an "anchor point" on tubulin that was proposed to be unchanged by GTP hydrolysis [Kellogg et al., 2018], accounting for tau's ability to promote tubulin ring formation (made up of longitudinally bound tubulin dimers) from disassembling MTs [Devred et al., 2004], as well as its ability to copolymerize with tubulin through multiple cycles of assembly and disassembly [Weingarten et al., 1975]. Despite tau's uniform decoration of MTs by fluorescent protein co-localization, Breuzard et al. [2013] observed two distinct tau-tubulin FRET populations on cellular MTs, with "hotspots" of relatively stronger tau-tubulin interactions emerging at MT plus ends during MT rescue and pause events [Breuzard et al., 2013]. These hotspots, which appeared about every 60 tubulin dimers, suggested that tau was having structural effects

at MT plus ends that facilitated MT rescue and pause events, alluding to its binding of GDP tubulin within the MT lattice and/or GTP subunits at MT ends [Breuzard et al., 2013]. In addition, the stoichiometry of tau binding also demonstrates that tau binds along the length of GDP regions in MTs. The tau-stabilized projections that we observed at the ends of pre-assembled, highly stable MTs containing the non-hydrolyzable GTP analog, GMPCPP, indicate that tau is either able to bind directly to GTP tubulin at MT ends and/or that it is having effects on the MT lattice that are then resulting in changes at MT ends ([Best et al., 2019], see also chapter 3). Interestingly, while tau has been traditionally viewed as a MT stabilizer, Qiang et al. [2018] reported that its depletion in rat cortical neurons resulted in the loss of GTP-rich MT labile regions at MT plus ends without affecting the stable, GDP-rich lattice regions [Qiang et al., 2018], suggesting that tau was necessary for the conservation of and/or polymerization of these dynamic, GTP-rich regions [Qiang et al., 2018, Barbier et al., 2019]. Taken together, these data suggest that tau binds to both the GTP-rich MT end as well as the GDP-rich MT lattice, although the nature of these two interactions may differ.

In contrast, Castle et al. [2020] and Duan et al. [2017] reported that tau avoided GTP-rich MT ends and preferentially bound to the GDP tubulin lattice [Castle et al., 2020, Duan et al., 2017]. They described tau's offset from MT ends by several hundred nanometers during periods of growth, whereas it shifted to true MT ends during periods of shortening [Castle et al., 2020]. Tan et al. [2019] also proposed nucleotide-dependent differences in tau binding after they observed discrete tau condensates form along the lattice of GDP but not GMPCPP MTs [Tan et al., 2019]. However, it is critical to note that Duan et al. [2017]'s and Tan et al. [2019]'s experiments were done in the presence of taxol, a MT-stabilizing drug which altered MT lattice structure [Diaz et al., 1998], caused rapid tau dissociation from MTs [Samsonov et al., 2004, Breuzard et al., 2013], promoted the loss of many tau-tubulin hotspots [Breuzard et al., 2013], and which may

even compete with tau for binding [Makrides et al., 2004, Kar et al., 2003]. Notably, whereas taxol's stabilizing effects arise from its straightening of GDP-bound tubulin into a GTP-like conformation, it has little effect on the GTP-bound state [Kellogg et al., 2017]. Thus, tau's observed dissociation from the MT lattice in taxol's presence may reflect the loss of GDP tubulin's intrinsic lattice strain and/or the altered MT lattice configuration due to decreased protofilament number [Diaz et al., 1998]. Further complicating the matter, tau itself alters protofilament number (even within the same MT) [Choi et al., 2009], which may cause lattice defects that later become sites of rescue such as Castle et al. [2020] observed. In addition, MTs can undergo self-repair in response to mechanical or other stress, resulting in GTP tubulin incorporation within the otherwise GDP MT [Aumeier et al., 2016], which makes it difficult to draw conclusions of nucleotide-dependent binding differences in a normal GDP/GTP context.

Ultimately, Castle et al. [2020]'s results can be reconciled with those suggesting that tau does bind to MT ends if they are considered in the context of the electron tomography study from McIntosh et al. [2018], which showed that growing MT ends possessed similarly curved protofilaments to depolymerizing ends [McIntosh et al., 2018]. Thus, it is possible that tau, which preferentially binds to curved tubulin states [Samsonov et al., 2004, Breuzard et al., 2013, Castle et al., 2020], is binding to these curved GTP tubulin protofilaments at growing MT ends that have not yet formed the lateral interactions that will lead to their straightening into the lattice proper [McIntosh et al., 2018]. If so, the short lengths and/or lifetimes of these protofilament extensions in the GTP context would likely preclude their resolution in studies using fluorescence microscopy [Castle et al., 2020]. Consistent with this interpretation, we were unable to resolve the tau-stabilized projections we observed at GMPCPP MT ends [Best et al., 2019] from the MT body by fluorescence microscopy (unpublished observation). It is worth noting that the presence of a high-affinity tau binding site at MT ends would be very difficult, if not

impossible, to detect amongst the more abundant GDP tubulin binding sites along the length of the MT lattice (∼13 sites at MT ends vs 100s-1000s along the MT lattice), especially using traditional experimental approaches, which calculate the bulk average binding affinity across all sites on a MT.

Taken together, these data suggest that tau is binding at the terminus of MT ends, presumably to curved GTP tubulin, where it may be enacting structural changes (such as straightening) that promote MT growth and overall MT stability. Tau's preference for curved tubulin states and likely promotion of partial straightening would both enable increased rates of GTP tubulin incorporation as well as result in tau dissociation upon protofilament straightening. Moreover, 4R tau's binding to and stabilization of an intermediate structure(s) at MT ends during MT disassembly may delay shortening events and reduce catastrophes. Finally, within the context of the MT lattice, tau preferentially binds to GDP tubulin over GTP tubulin, likely due to GDP tubulin's higher intrinsic strain and increased propensity to return to a highly curved state within the confines of the straight MT lattice.

1.4.2.2   Tau binding to soluble tubulin

While tau has been proposed to preferentially bind to GDP tubulin within the context of the MT lattice [Castle et al., 2020, Duan et al., 2017, Tan et al., 2019], less is known about its preferential binding to different soluble tubulin nucleotide states. Duan et al. [2017] proposed that tau's high affinity binding to and stabilization of dolostatin-10 ring stacks are evidence of its GDP preference [Duan et al., 2017], but these rings are inside-out relative to the MT lattice and expose a completely different binding interface than is generally exposed on soluble tubulin or an intact MT. Rather, tau's high binding affinity is most likely due to its preference for binding to curved tubulin states and/or to the unique intradimer interface that these rings possess [Samsonov et al., 2004, Tan et al.,

2019, Ettinger et al., 2016]. Furthermore, despite tau's stabilization of GDP tubulin rings under MT depolymerizing conditions [Scheele and Borisy, 1978, Kirschner et al., 1974, Nogales et al., 2003, Weingarten et al., 1975], it is unable to promote soluble GDP tubulin assembly into protofilaments or MTs. This is in marked contrast to tau's promotion of GTP tubulin rings, ring stacks, and spiral oligomers (reminiscent of its stabilization of GMPCPP tubulin spirals from dimers at 4 °C [Best et al., 2019]), even under conditions unfavorable to tubulin assembly [Kutter et al., 2016, Devred et al., 2004]. These intermediate structures may be related to the tau-tubulin "fuzzy complexes" that formed between tau and soluble GTP tubulin and positively correlated with MT assembly [Li and Rhoades, 2017, Fung et al., 2020]. Taken together, tau appears either not to bind to soluble GDP tubulin or not to affect GDP tubulin in the same way it affects GTP tubulin. The latter possibility seems most likely, as Castle et al. [2020] observed no differences in tau's affinity for soluble GDP vs GMPCPP tubulin [Castle et al., 2020]. Taken together, tau appears to bind to soluble tubulin independently of its nucleotide state, although its effects on MT nucleation appear to be primarily exerted via its action on GTP and not GDP tubulin.

1.4.3   Concluding remarks

We are just beginning to appreciate the complex relationship between hydrolysis-driven tubulin conformational transitions, the effects of long-range mechanical coupling of tubulin subunits, and the consequences for MT dynamic instability. While non-hydrolyzable GTP analogues, such as GMPCPP and GTPγS, have proven to be powerful tools in the study of MT dynamic instability, their imperfect recapitulation of the GTP or GDP states requires careful interpretation of results [Roostalu et al., 2015, 2020]. Recent technological advances that have enabled the recombinant production of tubulin have

led to the identification of several tubulin point mutants which completely or partially inhibit GTP hydrolysis and/or the conformational changes associated with it, providing increasing insights into the complex biochemical and mechanical cycle of a MT [Geyer et al., 2015, Roostalu et al., 2015, 2020]. Comparison of tau's and other MAPs' effects on MT dynamics to the effects of tubulin mutations that confer tubulin and MTs with similar dynamic properties may therefore provide some insight into their mechanistic regulation of MT dynamic instability. For example, 4R tau acts to:

1. lower the critical concentration of tubulin dimers required for MT assembly [Panda et al., 2003, Gustke et al., 1994, Cleveland et al., 1977],

2. moderately increase MT growth/elongation rates [Panda et al., 1995, 2003, Drechsel et al., 1992, Cleveland et al., 1977],

3. increase the amount of time MTs spend in an attenuated or static state [Panda et al., 2003, 1995, Bunker et al., 2004, Drechsel et al., 1992, Breuzard et al., 2013],

4. suppress the frequency of MT catastrophes [Trinczek et al., 1995, Drechsel et al., 1992, Panda et al., 1995, 2003, Breuzard et al., 2013] by decreasing both average rate and length of shortening events [Bunker et al., 2004, Panda et al., 2003, Trinczek et al., 1995], and

5. decrease the dissociation rate of GTP tubulin from MT ends [Trinczek et al., 1995].

These effects on MT dynamics are similar to those reported for a β-tubulin mutant, T238A, identified in yeast by Geyer et al. [2015], which, like GMPCPP, promoted increased spontaneous nucleation, $\sim$100-fold suppression of the shortening rate, and decreased catastrophe frequency, all without affecting the rates of GTP hydrolysis or MT elongation/growth rate [Geyer et al., 2015, Roostalu et al., 2015]. Whereas it was the uncoupling of the tubulin conformational cycle from its nucleotide state that resulted

MT hyperstability in T238A MTs, the E254A mutation in α-tubulin completely inhibited GTP hydrolysis in β-tubulin, which also resulted in increased MT nucleation as well as MT hyper-stability [Roostalu et al., 2020, Hyman et al., 1992]. Assessment of tau and other MAP action in these and other mutant tubulin contexts will likely improve our understanding the complex relationship between tubulin nucleotide state, conformation, and biochemical activity and provide powerful insights into physiological and pathological tau action.

Chapter 2

Expression and isolation of recombinant tau

In this chapter, we describe methods for the purification of both untagged and polyhistidine tagged tau protein. These protocols utilize a bacterial expression system to produce the tau isoform of interest, followed by heat treatment and column chromatography to separate tau from impurities. These techniques yield a biochemically pure protein with which to pursue any number of questions regarding the mechanisms of tau action.

2.1 Permissions and Attributions

The content of chapter 2 is the result of a collaboration with Peter J. Chung, Sarah J. Benbow, April Savage, Nichole E. LaPointe, Cyrus R. Safinya, and Stuart C. Feinstein. My contribution to this work was in the development and compilation of various tau isolation protocols as well as in writing and editing the manuscript. This work has previously appeared in the book Methods in Tau Cell Biology [Best et al., 2017]. It is reproduced here with the permission of UCSB `https://doi.org/10.1016/bs.mcb.2017.06.001`.

2.2   Background

Preparation of purified tau protein free from contaminants or breakdown products is essential to any investigation of tau action. Tau was originally isolated from bovine and porcine brains after it was observed to co-purify with tubulin [Weingarten et al., 1975]. Further separation of tau and tubulin was achieved using phosphocellulose (PC) ion-exchange column chromatography, which takes advantage of tubulin's acidity and resultant inability to adsorb to the column resin to separate it from positively charged, resin-binding microtubule-associated proteins (MAPs) [Weingarten et al., 1975]. As a result, a PC column can be employed to deplete MAPs, such as tau, from a tubulin prep to yield biochemically pure tubulin [Sloboda and Rosenbaum, 1982, Williams and Lee, 1982]. Subsequent protocols exploited tau's intrinsic heat stability and acid solubility to separate it from other MAPs [Cleveland et al., 1977, Lindwall and Cole, 1984]. It is worth noting that although heat treatment may affect structure and function of other proteins, no evidence of functional alterations to tau's microtubule stabilizing and assembly-promoting activities has been reported to date [Drubin et al., 1986, Fellous et al., 1977, Lindwall and Cole, 1984, Weingarten et al., 1975], likely due to tau's intrinsically disordered nature.

Current purification methods generally employ a bacterial expression system to generate the tau isoform of interest. This system can be adapted to the purification of both untagged tau as well as tau that has been fused to a poly-histidine (His) tag or other tags such as glutathione S-transferase (GST). In our lab, both techniques exploit tau's intrinsic hardiness to heat to separate it from heat-labile elements. Finally, column chromatography is used to isolate tau from contaminants and breakdown products. There are many variations on this basic strategy, several of which are presented elsewhere in this volume. In this chapter, we present in detail our standard protocols for isolation of

untagged and His-tagged tau.

In brief, BL21(DE3) E. coli cells are transformed with a cDNA plasmid containing the desired tau isoform adjacent to a lac operator and T7 promotor. Protein expression is initiated by addition of IPTG in standard culture medium or by lactose in auto-induction medium [Studier, 2005]. Cells are subsequently collected by centrifugation, re-suspended, and lysed using a French press. The cell lysate is then heated to 90 °C to denature and precipitate heat-labile proteins, which are then removed by centrifugation. Further purification of the cleared lysate is achieved using column chromatography. The type of column utilized is dependent upon the nature of the tau construct. Untagged tau is purified using a phosphocellulose (PC) column followed by a hydrophobic interaction chromatography (HIC) column to remove breakdown products. Poly-His tagged tau is affinity purified using a nickel (Ni) column, which binds to the His tag and allows for separation from contaminants. Inclusion of a cleavable sequence between the tag and the protein enables subsequent cleavage and removal of the tag and eliminates the possibility of effects arising from the presence of the positively charged tag. After all chromatography steps, tau-containing fractions are identified using SDS- PAGE/Coomassie Blue staining and then pooled, concentrated, and exchanged into storage buffer (Fig. 2.1).

2.3   Isolation of Untagged Tau Proteins

2.3.1   Preparation of tau-expressing E. coli via transformation

1. Prepare LB agar plates containing the appropriate antibiotic and concentration for plasmid selection (For LB/Ampicillin (Amp) plates, a final concentration of $50 - 100 \, \text{ug/mL}$ Amp is recommended).

2. Transform BL21(DE3) competent cells with the desired tau plasmid, and perform

27
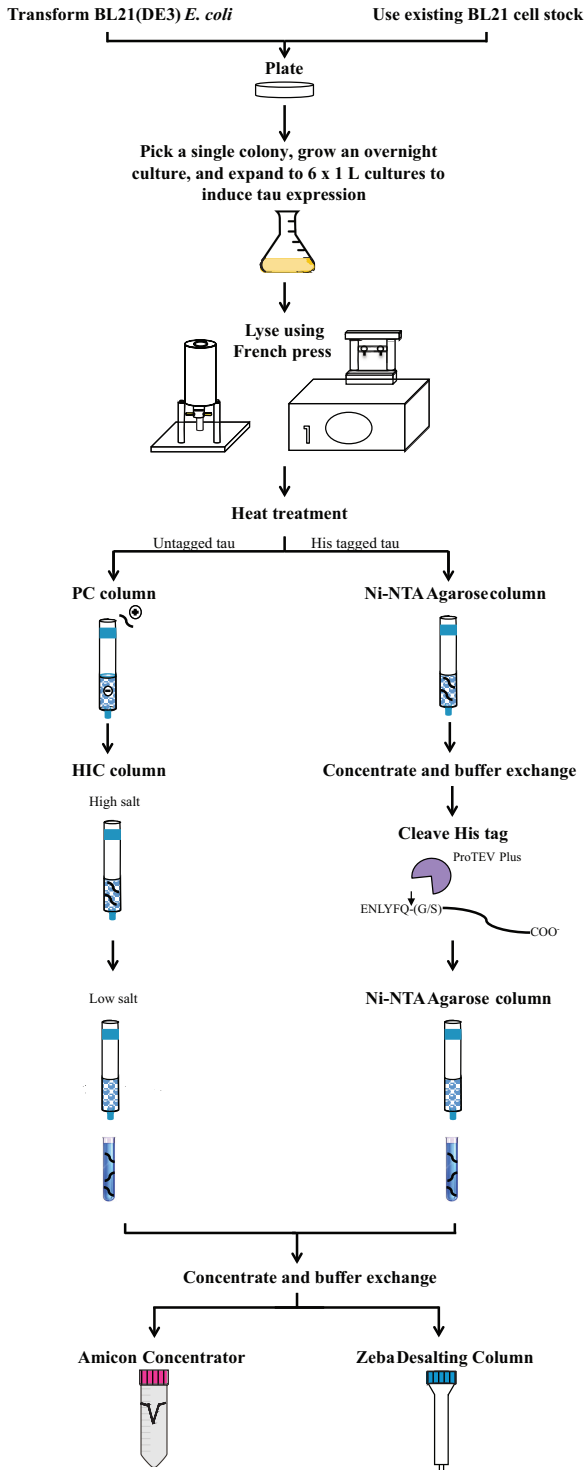
Figure 2.1: **Isolation of untagged tau and His tagged tau.** Schematic of the protocol for the isolation of untagged and His tagged tau using a bacterial (BL21(DE3)) expression system. Tau expression is induced in bacteria using lactose or IPTG. Cells are collected, lysed, and treated with heat to denature heat-labile elements. Column chromatography is used to separate tau from contaminants, and the purified protein is concentrated and exchanged into storage buffer.

a parallel transformation with pUC19 plasmid, a negative control. See Invitrogen protocol for specific instructions.

3. Pipet $25-$ and $50\,\mathrm{uL}$ of transformed cells onto individual plates for each condition, streaking with sterile inoculation loop to evenly spread bacterial cells.

4. Incubate at $37\,°\mathrm{C}$ for $\sim$18 hours. Do not allow plates to overgrow.

5. Remove plates from incubator, wrap with parafilm, and store at $4\,°\mathrm{C}$ until ready to proceed to next step. Plates are best used within 1-2 days.

Notes

- Other *E.coli* cell strains are available, any number of which may be suitable for tau expression. The primary considerations are that cells are specifically engineered for recombinant protein expression and that they are compatible with the planned transformation strategy (i.e. are either chemically competent or electrocompetent).

- Place competent cells on ice immediately upon removal from the $-80\,°\mathrm{C}$, and start the transformation right away.

- Competent cells are susceptible to mechanically-induced lysis, so pipetting should NOT be used to mix competent cells. Instead, mix by gently tapping or swirling the tube.

- Ampicillin is light sensitive, so LB/Amp plates should be stored in the dark. To confirm that the ampicillin is functional, non-transformed cells or cells transformed with a cDNA plasmid that lacks ampicillin resistance (Amp^{R}) may be plated in parallel as a control.

- Plates should always be stored and incubated lid-side down in order to prevent condensation from dripping onto media surface.

2.3.2   (Alternative) Plate cells from previously prepared glycerol stock of transformed E. coli

1. Prepare LB/Amp plates.

2. On ice, thaw a glycerol stock of BL21(DE3) cells that contain the tau plasmid of interest, as well as a control stock of cells lacking any AmpR. Glycerol stocks are prepared by mixing 1 mL of an overnight culture with 400 uL of 100% glycerol and are stored at $-80\,°C$ in a screw-top vial.

3. Draw a line along the bottom of each plate to divide it in half. One half will be used for the control cells, and the other will be for the tau-expressing cells.

4. Holding each cell stock tube at an angle to prevent contamination, dip a sterile inoculation loop into one of the cell stocks and streak the appropriate half of the plate. Turn the loop over and streak a second plate with the remaining liquid on the loop.u

5. Repeat step 4 with the control cell stock.

6. Place the plates at $37\,°C$ for $\sim$18 hours.

7. Remove the plates from the incubator, parafilm, and store at $4\,°C$ until ready to proceed to the next step. Plates are best used within 1-2 days.

Notes

- In steps 2-3, cell stocks do not need to be completely thawed for plate streaking,

just thawed enough that some liquid can be removed from vial with the inoculation
loop.

- The control cell stock may additionally be plated on either: a) a plate with the
  appropriate antibiotic for plasmid selection or b) an antibiotic-free LB plate. Either
  option confirms that the control cells are alive and verifies that functional ampicillin
  is preventing growth on the LB/Amp plates.

Materials and equipment

- Invitrogen One Shot BL21(DE3) Transformation Kit (C6000-03) or similar

- Tau plasmid cDNA stock (concentration should be between $1\,\text{ng/uL}$ and $10\,\text{ng/uL}$),
  or glycerol stock of tau-transformed cells

- Ampicillin sodium salt (Fisher Sci BP1760-5): stock solution is prepared at $50\,\text{mg/mL}$-
  $100\,\text{mg/mL}$ (1000x) in nanopure water and then sterile filtered and stored in single-
  use aliquots at $-20\,°\text{C}$.

- Luria Broth (LB): $10\,\text{g/L}$ Bacto-tryptone, $5\,\text{g/L}$ yeast extract, $10\,\text{g/L}$ NaCl in
  nanopure water

- LB/Ampicilin agar plates: recipe as above, plus $15\,\text{g/L}$ agar. Autoclave with a
  stir bar inside the flask, and transfer to a stir plate after autoclaving. Add the
  antibiotic once the mixture has sufficiently cooled, and then pour into sterile petri
  dishes. Leave lids cracked open until steam no longer builds up when closed, and
  then leave at room temperature overnight to set. Seal each plate with parafilm,
  return to petri dish sleeve, and store at $4\,°\text{C}$. Plates are best used within 1-2
  months.

- 37 °C shaking and non-shaking incubators

- 42 °C water bath for heat shock during transformation (or as indicated in manufacturer's protocol)

- Flame-sterilized inoculation loop

2.3.3   Overnight starter cultures

1. Autoclave 240 mL of LB in each of 2 x 500 mL Erlenmeyer flasks.

2. Add Amp to cooled LB ($50-100\,\mathrm{ug/mL}$ final concentration), mixing thoroughly.

3. Use a sterile method to pick a single colony from a plate prepared in 2.3.1 or 2.3.2 to inoculate each of the two flasks.

4. Repeat step 3 to transfer a single colony to the second flask. This second colony and flask are a backup in case the first does not grow.

5. Place both flasks in a 37 °C shaking incubator for 18 hours (we use 220 rpm in our Eppendorf model I2500).

6. In the meantime, prepare 6 L of auto-induction media (AIM), leaving room for the 50X "5052" sugars ($20\,\mathrm{mL/L}$) that will be added after autoclaving to prevent caramelization. Divide into 6 x 2L flasks at 980 mL per flask and autoclave.

7. Autoclave 7 screw-top 500 mL centrifuge-compatible bottles for bacterial pelleting (1 for 18 h culture and 6 for 24 h cultures).

Notes

- Molecular biology best practices suggest starting with a smaller overnight culture and then scaling up to 250 mL, but we find this works well.

Materials and equipment

- 500 mL LB/Amp

- Plates containing bacterial colonies

- 2 x 500 mL Erlenmeyer flasks

- 37 °C shaking incubator

- 6 x 2L Erlenmeyer flasks, baffled for increased aeration (Sigma CLS44232XL)

- 50X "M" salts: 1.25 M Na_2HPO_4, 1.25 M KH_2PO_4, 2.5 M NH_4Cl, 250 mM Na_2SO_4. Add salts slowly when preparing to ensure complete mixing. Gentle heat may be necessary to encourage dissolution. Filter sterilize.

- 50X "5052" sugars: 25% glycerol (v/v), 138.8 mM glucose, 292.1 mM α-D-lactose. Filter sterilize.

- Auto-induction media (AIM), 6L, divided into 6 x 2 L flasks: 10 g/L bacto-tryptone, 5 g/L yeast extract, 1X "M" salts. After autoclaving and just before use, add 1X "5052" sugar solution and appropriate antibiotic.

- 7 x 500 mL screw-top centrifuge bottles (ThermoFisher #312110-0016)

2.3.4   Auto-induction of tau expression

1. Remove 18 h cultures from the shaking incubator. Cultures should be cloudy to indicate bacterial growth. Remove 1 mL of culture for later analysis by SDS-PAGE ("pre-induction" sample).

2. Make a glycerol cell stock from one or both overnight cultures: 1 mL culture + 400 uL 100% sterile glycerol in a screw-top vial. Store at −80 °C.

33

3. Pellet bacteria from one 18 h culture (the same culture used to make cell stock) at 5000 rpm (4200 x g) for 15 min at 4 °C in an RC-5 centrifuge with a GS-3 rotor. Discard the other 18 h culture.

4. During the spin, add Amp (final concentration $50-100$ ug/mL) and 20 mL of 50X 5052 sugars to each flask of AIM.

5. When spin is complete, re-suspend bacterial pellet in AIM as follows:

    (a) Remove supernatant and discard.

    (b) Take 10 mL of AIM from each 2 L flask (60 mL total), and use it to re-suspend the bacterial pellet. Vortex bottle to help start the process and then use a 10 mL serological pipet to create a homogenous, clump-free suspension.

    (c) Add 10 mL of re-suspended bacteria to each flask. Divide any extra volume evenly between the flasks.

    (d) Incubate for 24 h at 37 °C, shaking at $\sim$220 rpm.

6. Chill GS-3 and SS-34 rotors for the next day, as well as the French press cell.

Notes

- During re-suspension in step 5, pipetting directly at the bottle walls helps to break up clumps of bacteria and achieve homogeneity. Keep the cells cold during this process by performing it on ice.

- Cells preferentially use the glucose in the AIM as their energy source. The glucose is depleted once the culture reaches sufficient density, and the cells switch to using lactose, which induces expression of the recombinant protein [Studier, 2005].

- An alternative to AIM is to induce expression directly with isopropyl-β-D- thio-galactoside (IPTG). In that case, grow cultures in LB, and monitor until $OD_{600}=$ 0.8 – 1.0. Add IPTG to 1 mM, incubate 2 h, and then harvest. Note that in our hands this method of induction generally results in decreased protein yield compared to AIM.

Materials and equipment

- 2 x 18 h cultures

- 100% glycerol, sterile

- Amp stock (1000X), $100\,\mathrm{mg/mL}$

- 2 x 500 mL screw-top bottles (one sterile for bacteria, one for balance)

- Pipetman and sterile serological pipets

- Shaking incubator

- RC-5 centrifuge and GS-3 rotor or similar (also chill for next day of prep)

2.3.5   Harvest bacteria

1. Save 1 mL of induced culture to verify induction using SDS-PAGE (compare to pre- induction sample taken in section 2.3.4).

2. Pellet bacteria from 24 h auto-induced cultures in 6 x 500 mL sterile screw-top bottles at 5000 rpm (4200 x g) for 15 min at $4\,°C$, GS-3 rotor, RC-5 centrifuge. Discard supernatant, refill bottles, and repeat until all bacteria are pelleted.

3. Re-suspend bacteria in BRB80 + 0.1% βME ($1\,\mathrm{uL/mL}$) + AEBSF ($5\,\mathrm{uL/mL}$ of 100 mM stock). Use 10 mL of buffer per pair of screw-top bottles.

(a) Pour off supernatant and add 10 mL of BRB80/βME/AEBSF to first bottle. To re-suspend bacteria, use a metal spatula (cleaned with 70% ethanol) to gently scrape at pellet, layer by layer, while swirling spatula in buffer. Note: It is also possible to skip this step and re-suspend with only a serological pipet as described in step 3b.

(b) Once the pellet is re-suspended, pipet mixture with a 10 mL serological pipet until it is a homogenous, clump-free suspension.

(c) Transfer suspension to the paired bottle and repeat steps 3a and 3b.

(d) Transfer re-suspended bacteria to a 50 mL conical tube.

(e) Repeat steps 3a-3d with the other two sets of paired bottles.

(f) Rinse bottles with 5 mL BRB80/βME/AEBSF and add to 50 mL conical tube(s) (use same 5 mL for all 6 bottles).

Notes

- Keep everything on ice throughout these steps and subsequent steps to minimize protease activity.

- During step 2, multiple spins will be needed to get all 6 L of bacterial culture pelleted. Keep cultures in 37 °C incubator until ready to pellet. If part of a culture is used, keep it at 4 °C until the remainder is used.

- Re-suspension may be started during the final spin if some bottles are done earlier.

- There should be 35-40 mL of re-suspended bacteria per 50 mL conical tube, as the French press holds 40 mL max.

- BRB80 and all other buffers should be filter sterilized (using 0.2 um filters)

- Do not add βME to buffers until just before use, as dilute βME will rapidly lose activity (See product information for more details).

Materials and equipment

- 6 x 500 mL screw-top bottles sterilized in an autoclave

- 6 x 1L, 24 h auto-induced cultures

- Sorvall RC-5 centrifuge and GS-3 rotor or equivalent, chilled

- Pipetman and serological pipets

- 50 mL Falcon conical tubes

- 50 mL BRBB80: 80 mM Pipes, 1 mM MgSO$_4$, 1 mM EGTA, pH 6.8, filter sterilized

- β-mercaptoethanol (βME; Sigma M3148)

- 4-(2-Aminoethyl)benzenesulfonyl fluoride hydrochloride (AEBSF; Sigma A8456): prepare 100 mM stock in nanopure water and store in single-use ($\sim$250 uL) aliquots at $-20\,°\mathrm{C}$.

2.3.6   Lyse by French press

1. Assemble the chilled French press cell and set the volume to 40 mL.

2. Run 40 mL of nanopure water for the first press. (See manufacturer's guidelines for specific instructions).

3. Reset piston to 40 mL and load bacteria. For optimal results, maintain a steady flow while pressing, around 1200 psi (or as per manufacturer's guidelines). Collect any bacteria that were not pressed from the sample chamber using a transfer pipet.

4. Repeat step 3 until all bacteria have been pressed three times. Samples should become more viscous as they are French pressed. Note the volume of your cell lysate.

5. Run 40 mL of nanopure water for the final press to start the cleaning process.

6. Disassemble the French press cell and clean all parts with soap and water (no scrub brushes). Do a final rinse with deionized water and dry thoroughly before storing at room temperature.

Notes

- If leaking occurs, check: a) that the nylon ball in the flow valve is present and functional and b) that the flow valve handle is finger tight.

- During dismantling and refilling, hold the French press cell at an angle to avoid resting weight on the piston.

- Alternative lysis methods include sonication and rapid freeze-thaw cycles. Whichever process is chosen, care should be taken to keep the lysate cold.

Materials and equipment

- Bacterial cell suspension (approximately 80 mL)

- 40 mL nanopure water

- Plastic transfer pipets

- French press with Glen Mills Manual-Fill 40K Cell (FA-032) or similar

2.3.7   Heat denaturation and high-speed centrifugation

1. Denature heat-labile proteins by transferring 50 mL conical tubes containing pressed lysate to $90-95\,°C$ water bath and incubating for 10 min.

2. Transfer lysate to 50 mL polypropylene tubes and seal with parafilm. It may be necessary to push parafilm up to the lip of the polypropylene tube to prevent tubes from getting stuck in the centrifuge rotor.

3. Pellet cell debris at 13,000 rpm (20,200 x g) in an RC-5 centrifuge with an SS-34 rotor, 40 min at $4\,°C$.

4. Transfer supernatant to 50 mL conical tubes.

5. Reserve a sample of the supernatant to include in a diagnostic SDS-PAGE gel.

Notes

- Make sure conical tubes are tightly capped during heating.

Materials and equipment

- $90-95\,°C$ water bath

- RC-5 centrifuge with SS-34 rotor or equivalent, chilled

- Several 50 mL polypropylene tubes compatible with centrifuge

- Several 50 mL conical tubes

2.3.8   Phosphocellulose (PC) chromatography

2.3.8.1   Column pre-cycling

Do this the same day you plan to use the column.

1. Weigh 10 g phosphocellulose into a 1L glass beaker (final column volume will be approximately 50 mL).

2. Add 500 mL of 0.5 M NaOH and stir gently with a serological pipet tip.

3. Allow resin to settle 5 min.

4. Carefully pour off fines (pulverized resin that will not have settled to the bottom).

5. Add ∼400 mL of 0.5 M sodium phosphate buffer (pH 7) and stir. Repeat steps 3 and 4.

6. Repeat step 5 until pH is ∼7, measured by pH strips (usually one more time).

7. Pour off final sodium phosphate buffer and add 500 mL of 0.5 M HCl. Repeat steps 3 and 4.

8. Repeat step 5 to exchange into sodium phosphate buffer as above until pH is ∼7. It is usually sufficient to exchange 2x with ∼400 mL each, and then once more with the remaining phosphate buffer.

9. Exchange into BRB80 as in previous steps, 2x with ∼400 mL each time. Store the equilibrated resin in a minimal amount of BRB80 buffer at 4 °C until use.

2.3.8.2   Batch bind and run column

1. Add equal volumes of equilibrated PC resin to 50 mL conicals containing equal amounts of post-heat treatment, post-spin lysate.

2. Add βME (1 uL/mL, 0.1% final) and 0.1 mM AEBSF (1 uL/mL of 100 mM stock) to resin/lysate mixture.

3. Put conical tubes on a rotator at 4 °C for at least 30 min (up to 2 h) to allow tau to bind to resin. Set up column during this time.

4. Invert 50 mL conicals containing resin/lysate mixture to ensure mixture is homogenous. Remove a sample for a diagnostic gel, and then pour the mixture of resin and lysate into an empty column. Use a peristaltic pump (Rainin Rabbit or equivalent) set to ~3 mL/min, and let it run as you pour the mixture into the column. Collect the flow- through in an appropriately labeled beaker and store at 4 °C.

5. It is important to minimize resin loss as this will result in protein loss and decreased yield. To collect the last of the resin, rinse the 50 mL conicals with 5 mL of BRB80 + 0.1% βME and gently pipet it into the column to avoid disturbing the resin bed.

6. Wash column with 100 mL (2 column volumes, CV) of BRB80 + 0.1% βME. Collect the wash in an appropriately labeled beaker and store at 4 °C. Collect the last 1 mL of the wash separately as a sample for a diagnostic gel.

7. Elute tau with a step gradient of ammonium sulfate in BRB80 + 0.1% βME, collecting $\frac{1}{2}$ CV fractions. Place fractions on ice immediately as they come off the column. Remove a sample of each fraction to run on a gel and store remainder at -20 °C.

   (a) 50 mL of 50 mM $(NH_4)_2SO_4$ (collect 2 x 25 mL fractions).

   (b) 100 mL of 150 mM $(NH_4)_2SO_4$ (collect 4 x 25 mL).

   (c) 50 mL of 250 mM $NH_4)_2SO_4$ (collect 2 x 25 mL).

   (d) Run a gel to identify tau-containing fractions (Fig. 2.2).
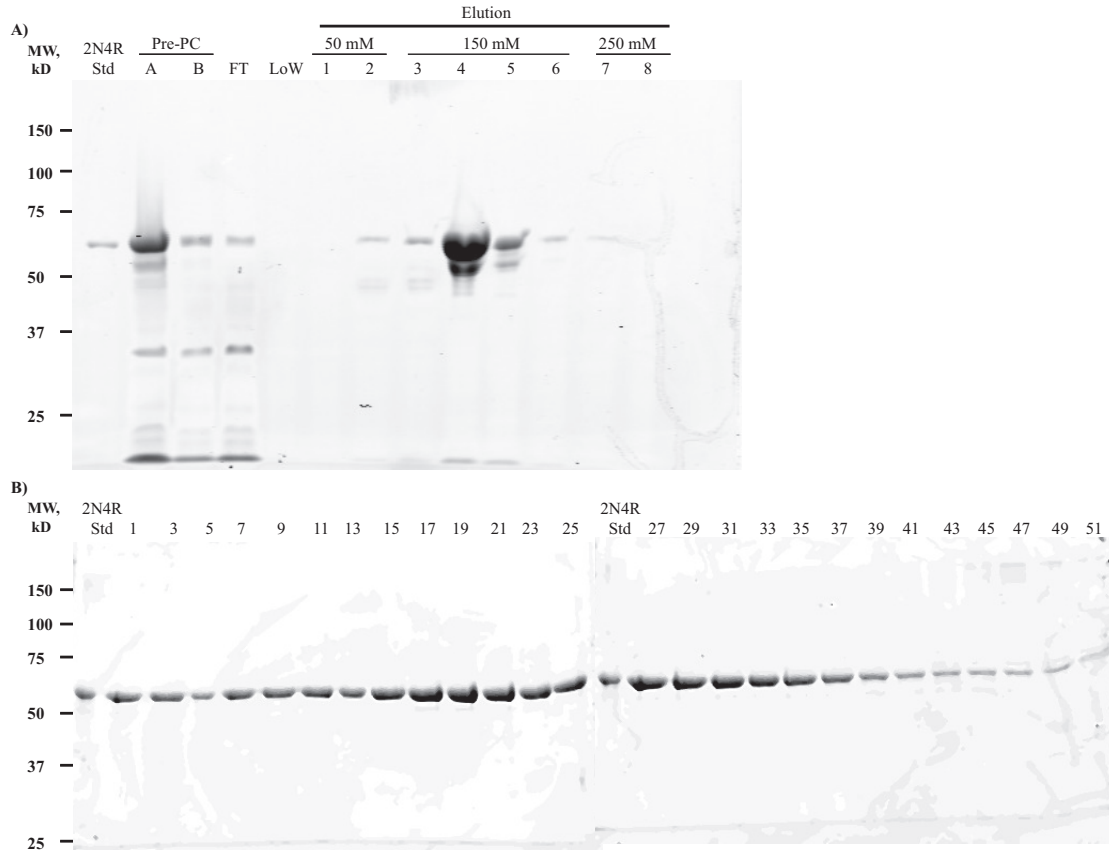
Figure 2.2: **Phosphocellulose (PC) column and hydrophobic interaction chromatography (HIC) column diagnostic SDS-PAGE gels.** (A) Tau ("2N4R" isoform, 441 amino acids) is bound to PC resin and eluted with increasing concentrations of ammonium sulfate. Fractions are run on an SDS-PAGE gel against a regular molecular weight standard and a tau molecular weight standard ("2N4R" isoform) to identify those that contain tau. "Pre-PC" refers to post-heat treatment cell lysate collected immediately prior to the column. Lane A is a tau-enriched sample that was incubated with PC resin. Lane B is the same lysate prior to resin addition. "FT" is the flow-through collected during column loading. "LoW" is the last 1 mL of column wash. Elution fractions 1-8 are shown with the indicated concentration of ammonium sulfate (see section 2.3.8). (B) Tau- containing PC fractions were pooled and run on a HIC column to separate tau from the lower molecular weight bands (likely contaminants and/or breakdown products) visible in PC elution fractions. Every other fraction collected from the HIC column was run on an SDS-PAGE gel against a regular molecular weight standard and a tau molecular weight standard ("2N4R" isoform, 441 amino acids) to identify fractions containing pure tau protein (see section 2.3.9).

Notes

- When making sodium phosphate buffer, the components should be added gradually to a 2 L graduated cylinder with a large stir bar in order to create a fully dissolved and homogenous solution.

- The pH of BRB80 must be adjusted after the addition of ammonium sulfate. We therefore find it convenient to prepare and pH a stock solution of BRB80 + 2 M NH$_4$)$_2$SO$_4$ and then combine this with BRB80 to make the PC column elution buffers described above.

- It is important to collect and save the flow-through from all columns throughout the prep in order to detect issues with resin binding (depending on the isoform being purified, the tau will bind with lower or higher affinity according to its amino acid composition and resultant electrostatic profile).

- Do not let the column resin run dry. Air bubbles can be removed from the top of the solution with a serological pipet tip.

- Whenever you add additional volume to the column, add slowly so as not to disturb the resin. This can be done by setting the pipet to "slow" and pipetting around the top ridge of the column using a slow circular motion, letting the solution run down the sides.

- Adjust the speed of the peristaltic pump as necessary. There is a trade-off between amount of time it takes to run the column and the amount of interaction time samples will have with the PC resin. If a peristaltic pump is not available, the column can be run under gravity flow.

- Following the procedure, running water through the column collection lines will prevent the buildup of salt precipitates.

- The diagnostic PC column gel does not need to be rigorously quantitative, and so the staining process can be sped up in a microwave. Heat the gel in stain for 30s on full power, and then immediately cover the container with aluminum foil and place on a shaker for 20 min before switching to destain.

Materials and equipment

All buffers must be passed through a $0.2\,\mathrm{um}$ *filter to sterilize them and to remove any particulates; for some chromatography systems degassing is also recommended. See manufacturer's instructions for your specific column/system.*

- 500 mL 0.5 M NaOH

- 500 mL 0.5 M HCl

- 2 L of 0.5 M sodium phosphate buffer, pH 7.0. Prepare as 305 mM Na_2HPO_4 and 195 mM $(NH_4)_2SO_4$. There is no need to adjust the pH.

- 10 g phosphocellulose resin; we use P11 (Whatman 4071200), but cellulose phosphate (Sigma C2258) is a substitute that is currently more readily available.

- pH strips

- Serological pipet tips

- β-mercaptoethanol (βME)

- AEBSF stock

- 100-200 mL column, empty

44

- Peristaltic pump (optional)

- 1 L BRB80

- BRB80 + 2M $(NH_4)_2SO_4$ (pH 6.80), stock solution for preparing elution buffers. Add βME immediately prior to use:

  - 50 mL of BRB80 + 50 mM $(NH_4)_2SO_4$ with 0.1% βME

  - 100 mL of BRB80 + 150 mM $(NH_4)_2SO_4$ with 0.1% βME

  - 50 mL of BRB80 + 250 mM $(NH_4)_2SO_4$ with 0.1% βME

2.3.9   Hydrophobic interaction chromatography (HIC column)

2.3.9.1   Equilibration

1. Equilibrate column one day in advance. If this is a new column, follow the manufacturer's instructions for new columns. Then, equilibrate the column for the tau prep using BRB80 and BRB80 + 1.25M $(NH_4)_2SO_4$ (both filtered, pH 6.80):

   (a) Rinse column with 10 CV "Buffer B" (BRB80)

   (b) Rinse column with 15 CV "Buffer A" (BRB80 + 1.25 M $(NH_4)_2SO_4$

2.3.9.2   HIC column

1. Thaw protein-containing fractions in a beaker of room temperature water and then immediately transfer to ice. Minimize time at room temperature.

2. Add $(NH_4)_2SO_4$ to tau-containing fractions to bring the $(NH_4)_2SO_4$ concentration to 1.25 M. Add a little bit at a time to avoid protein precipitation, and mix by gently inverting the tube. We do not adjust the pH at this step.

3. Just before loading onto the HIC column, filter protein through a 0.22 um filter.

4. Load sample onto the column at 1 mL/min. Monitor the conductivity (we use an in-line conductance meter), and spike the solution with BRB80 + 2M ammonium sulfate if it drops below 150 mS. Take care not to introduce air into the column during this process.

5. Collect the flow-through in an appropriately labeled beaker.

6. Wash column with 10 CV Buffer A (50 min at 1 mL/min). Collect the wash in a labeled beaker or conical tube, keeping the last 1 mL separate. Take samples of the "total wash" and "last of wash" for a diagnostic gel.

7. Elute tau from the column using the following program, collecting 1.4 mL fractions throughout:

   (a) 0-60% Buffer B for 100 min

   (b) 60-100% Buffer B for 10 min

8. Prepare a sample from every second fraction for a diagnostic gel. Cover fractions with parafilm and store at 4 °C.

9. Rinse the column with 100% Buffer B for 10 min. Collect in a 15 mL Falcon tube as "last of elution."

10. Run SDS-PAGE gels of the samples prepared in step 8, stain with Coomassie, and then destain overnight (Fig. 2.2).

11. Clean column and fraction collector line. We monitor this process with an in-line conductance meter

   (a) Rinse with nanopure water 10-20 CV (conductance <1.00 mS)

(b) Clean with 0.5M NaOH (conductance = ∼115 mS)

(c) Rinse with nanopure water 10-20 CV (conductance <1.00 mS)

(d) If storing long term, rinse with 5 CV 30% EtOH/nanopure water

Notes

- These conditions work well for wild-type tau isoforms. Truncated or mutant tau constructs may require a higher concentration of ammonium sulfate for efficient binding.

- If spiking with additional ammonium sulfate, note that it may take several minutes to reflect a change in conductance (depending on the placement of the conductance meter). Allow sufficient time before any additional spiking.

- An in-line UV detector can identify fractions carrying the peak of the eluted protein, greatly reducing the number of fractions that need to be examined by SDS-PAGE gels. However, gels are indispensable for detecting the presence of breakdown products and other contaminants.

- For different tau isoforms and constructs the ideal binding and elution conditions may vary. It is therefore prudent to save all washes and flow-throughs, and to take samples throughout the process for diagnostic SDS-PAGE gels.

- A common alternative for this final chromatography step is a sizing column.

Materials and equipment

All buffers must be passed through a 0.22 um filter to sterilize them and to remove any particulates; for some chromatography systems degassing is also recommended. See manufacturer's instructions for your specific column/system.

- HiTrap Phenyl HP hydrophobic interaction column (HIC), 5 mL (GE Healthcare 17-1351-01)

- Chromatography system, LP BioLogic or similar with an in-line conductance meter

- "Buffer A:" BRB80 + 1.25M $(NH_4)_2SO_4$, pH 6.8, with 0.1% βME (added immediately prior to use)

- "Buffer B:" BRB80, pH 6.8 with 0.1% βME (added immediately prior to use)

- BRB80 + 2M $(NH_4)_2SO_4$, pH 6.8

- Nanopure water, filtered

- 0.5 M NaOH, filtered

- 30 - 50 mL sterile syringe and 0.22 um filter

- βME

- Test tubes for fraction collection

2.3.10   Protein concentration and buffer exchange

1. Pool HIC column fractions that contain clean protein.

   (a) Use a 5 mL serological pipet to remove fractions from test tubes, and combine them into a 50 mL conical. Use a p200 to collect any remaining liquid from test tubes.

2.3.10.1 Option A: Concentration and buffer exchange in Amicon concentrators

2. Concentrate and buffer exchange into BRB80 + 0.1% βME using Amicon Ultra concentrators (10,000 MWCO), spinning at 4,000 rpm (3300 x g) at 4 °C in an RC-5 centrifuge, SH-3000 swinging bucket rotor.

   (a) Rinse concentrators first by doing a 10 min spin with BRB80+0.1% βME.

   (b) Discard BRB80 + 0.1% βME and load pooled fractions.

   (c) Spin for 40 min.

   (d) Save the flow-through in case of a concentrator malfunction, and then top off concentrators with any additional volume of pooled fractions. Spin for 40 min.

   (e) Repeat step 2d until all fractions have been added to the concentrator.

   (f) If more than one concentrator was used, pool samples into one concentrator by gently pipetting the solution in the filter to resuspend protein and transferring volume to second concentrator. Try to avoid touching the filter with the pipet tip.

   (g) Spin for $\sim$30 min., or until total volume is less than 500 uL. Record volume.

   (h) Bring the volume up to $\sim$11-12 mL in BRB80 + 0.1% βME, gently pipetting to distribute the protein. Record the new volume and calculate the dilution factor (dilution factor = new volume/original volume). Spin for 60 min, or until the volume is less than 500 uL. Record this volume.

   (i) Repeat step 2h until the total dilution factor is >10,000 (obtained by multiplying the dilution factors at each step). This will probably take 3-4 rounds. The final volume should be 500 uL or less.

(j) Gently pipet remaining liquid in the concentrator to resuspend the protein. Transfer the solution to a sterile Eppendorf tube. Carefully rinse the filter with ~ 50 uL BRB80 + 0.1% βME and transfer to same Eppendorf. Pipet total volume gently to homogenize solution.

3. Aliquot protein into sterile tubes and store at $-80\,$°C.

2.3.10.2   Option B: Concentration and buffer exchange with Zeba desalting columns

1. Concentrate protein as described above in section 2.3.10.1 steps 2a-2e to a volume between $700 - 4000\,$uL (for a 10 mL desalting column).

2. Use a 10 mL Zeba desalting column to exchange into BRB80 + 0.1% βME following manufacturer's protocol.

3. Aliquot protein into sterile tubes and store at $-80\,$°C.

Notes

- See product information for Amicon concentrators and Zeba desalting columns to determine appropriate centrifugation speed and time.

Materials and equipment

- 2 x Amicon Ultra 15 mL centrifugal filter unit, 10 kDa MWCO (UFC901024)

- BRB80 + 0.1% βME (added immediately prior to use)

- Zeba Spin Desalting Column, 7kDa MWCO, 10 mL (Thermo 89893/4)

- RC-5 centrifuge and SH-3000 swinging bucket rotor or similar, chilled

2.4   Isolation of His-tagged Tau Proteins

Our hexa-histidine (6x-His) tagged tau fusion proteins are engineered to contain an enzymatic cleavage site between the His-tag and tau to enable removal of the tag after tau isolation (Fig. 2.1). We use the sequence ENLYFQ(G/S), which is cleaved immediately after the Glutamine by the tobacco etch virus (TEV), leaving behind a single Glycine (or Serine; see manufacturer's information on ProTEV Plus for more details). This tag and subsequent purification methods are particularly useful in isolating tau fragments that are not easily isolated using ion-exchange chromatography, such as truncated and/or mutant tau constructs. The linker and tag can be positioned at either the N or C terminus; however, positioning the tag at the C terminus (Tau-linker-6xHis) leaves behind a slightly larger sequence after cleavage.

For preparation of His-tagged tau, the early protocol is identical to those outlined above in sections 2.3.1 - 2.3.4 and will not be repeated here. During harvest in section 2.3.5, the protocols remain identical with the exception of the re-suspension buffer. To this effect, we will highlight the differences in purification protocols below.

2.4.1   Modifications to early stages of the protocol

Harvest

Proceed as outlined in section 2.3.5, but re-suspend bacteria in Ni-Lysis buffer + 1 mM AEBSF. BRB80 can be substituted as long as it does not contain βME, which will reduce the free nickel in the column. We have encountered no difficulties in isolating tau without βME at this step.

High-Speed Centrifugation

Following centrifugation as in section 2.3.7, add AEBSF to 1 mM (do not add βME). We find that residual flocculent material in the lysate can interfere with subsequent column steps, so we therefore find it convenient to remove any remaining cell debris by filtering lysate through Whatman filter paper.

Additional Materials

- Ni-Lysis buffer: 5 mM Imidazole, 500 mM NaCl, 10 mM Tris, pH to 8.0, filter sterilized

2.4.2 Affinity chromatography with Ni-NTA agarose

1. Gently invert the 50% Ni-NTA agarose bead slurry to make sure that beads are fully suspended in solution. The binding capacity is 5-10 mg of protein per mL of resin (see manufacturer's information for more details).

2. Pipet 8 mL of Ni-NTA slurry into a capped 10 mL column and allow solution to come to room temperature as the beads settle (final column volume will be $\sim$ 4 mL).

3. After beads have settled, remove the cap and allow storage liquid to drain. Do not let the column run dry during this or any of the following steps.

4. Equilibrate resin with 100 mL of Ni-Lysis buffer, being careful not to disturb the resin surface. Reduce the liquid level above resin as much as possible without allowing the column to dry.

5. Load lysate onto column, collecting the flow-through. Allow to flow into the column until the level of the lysate is just above the resin. You may pause flow at this point

by capping the column or, if ready, immediately begin the wash.

6. Wash column with 50 mL of Ni-Lysis buffer, collecting the first and last mLs to run on a diagnostic SDS-PAGE gel.

7. Wash column with 50 mL of Ni-Wash buffer, collecting the first and last mLs in addition to 10 mL fractions throughout.

8. Elute protein with 50 mL of Ni-Elution buffer, collecting 5 mL fractions.

9. Wash column with 50 mL of 500 mM imidazole to remove any proteins still bound to the resin (save a sample from early in this wash for a diagnostic gel to visualize any protein that remained through elution steps).

10. Take a 20 uL sample of each fraction for diagnostic gels before storing them at $-20\,°$C.

11. Run an SDS-PAGE gel to identify tau-containing fractions.

12. Pool desired fractions and buffer exchange into BRB80 as described in section 2.3.10, but omit βME. βME and imidazole can both interfere with subsequent cleavage and tag removal.

13. Determine the protein concentration using methods outlined in section 2.5. Concentrated samples can be stored at $-80\,°$C and aliquots processed for applications as needed.

Notes

- Allowing the resin to come to room temperature prior to column packing prevents bubbles from forming during later steps.

- When adding lysate or performing wash steps, it is important that the column's resin is not disturbed and does not run dry. As such, use caution when adding liquid or modulating flow rate if using a peristaltic pump.

- Resin can be regenerated. See manufacturer's protocols.

- Alternatively, one can use a pre-packed Ni column (such as His-Trap HP, GE Healthcare # 17-5248-02) and an automated chromatography system.

Materials and equipment

All buffers must be filter sterilized

- 10-20 mL column with cap

- Peristaltic pump (optional)

- Ni-NTA agarose beads (Qiagen 30230) or similar

- Ni-Lysis buffer: 5 mM imidazole, 500 mM NaCl, 10 mM Tris, pH to 8.0

- Ni-Wash Buffer: 10 mM imidazole, 500 mM NaCl, 10 mM Tris, pH to 8.0

- Ni-Elution buffer: 100 mM imidazole, 500 mM NaCl, 10 mM Tris, pH to 8.0

- BRB80: 80 mM PIPES, pH 6.8, 1 mM EGTA, 1 mM $MgSO_4$, pH 6.8

- Amicon Ultra 15 mL centrifugal filter unit, 10 kDa MWCO

- Zeba Spin Desalting Column, 7kDa MWCO, 10 mL (optional)

2.4.3   Proteolytic cleavage to remove His-tag

1. Thaw ~ 1 mg of tau on ice and collect a 20 uL pre-cleavage sample for a diagnostic gel. Assemble the ProTEV reaction according to the manufacturer's protocol (1 mL total reaction volume).

2. Leave reaction on bench-top overnight. Collect a post-cleavage sample for a diagnostic gel. Optionally, monitor time course of cleavage by removing samples at several time points.

Notes

- Proteolytic cleavage reaction can be scaled according to volume and amount of protein. To do so, refer to product guidelines.

Materials and equipment

- ProTEV Plus enzyme, reaction buffer, and 100 mM DTT (Promega V6101)

2.4.4   Ni-NTA column for tag removal

1. Prepare column as in section 2.4.2 and equilibrate with 50 mL of BRB80.

2. Reduce liquid in column to just above the resin without drying.

3. Apply entire cleavage reaction to the column, allowing the sample to move all the way into the resin. Collect 1 mL fractions. Tau will flow through, while the cleaved tags and the ProTEV enzyme will remain bound to the column.

4. Apply 3 mL of BRB80 when the last of the sample has just entered the resin, taking care not to disturb the resin. Continue collecting 1 mL fractions.

5. Apply 10 mL of BRB80 as above, without disturbing resin. Continue collecting 1 mL fractions.

6. Wash column with 50 mL of Ni-Elution buffer, collecting first and last mLs as 1 mL fractions and the remaining volume in a 50 mL conical.

7. Remove 20 uL samples from all fractions for analytical SDS-PAGE gels to determine tau-containing fractions.

8. Pool desired fractions and add βME to 0.1%.

9. Buffer exchange into BRB80 + 0.1% βME or desired buffer, as in section 2.3.10.

10. Determine tau concentration as described below in section 2.5.

Materials and equipment as listed in section 2.4.2

2.5   Determination of Tau Concentration by SDS-PAGE and Comparison to a Tau Mass Standard

Quantification of tau concentration by Bradford analysis and comparison to a BSA standard curve can be off by a factor of up to 2.7 [Barghorn et al., 2005, Panda et al., 2003], likely due to the difference in amino acid composition between tau and BSA. Tau is also less amenable than many proteins to quantification using its extinction coefficient at 280 nm (reviewed in [Devred et al., 2010]), due to its low content of aromatic residues. Therefore, we have adopted a quantitative SDS-PAGE-based method of concentration determination that relies on comparison to a tau standard of known concentration, as determined by commercially available quantitative amino acid analysis. Once the concentration of the tau standard has been established, a dilution series is run against a

dilution series of the tau protein of unknown concentration. A standard curve of intensity as a function of protein concentration is then generated and used to interpolate the concentration of the unknown (Fig 2.3).

1. On ice, thaw an aliquot of a tau standard of known concentration, hereafter referred to as the "tau standard" and an aliquot of purified tau of unknown concentration, hereafter referred to as the "unknown."

2. Create a dilution series of both the tau standard and the unknown in Laemmli sample buffer. For best practice, we have found that loading $0.02 - 0.2$ ug protein/lane is a good working range for our tau standard ("0N4R" isoform, 383 amino acids).

3. Run an SDS-PAGE gel with both standard and unknown dilutions (Fig. 2.3A). For best practice, we have found that running 10 lanes of standard and 3 lanes of unknown generates a reliable standard curve.

4. Stain in Coomassie Brilliant Blue R stain for 1 hour, and then destain overnight.

5. For gel imaging and analysis we use a Li-COR Odyssey® infrared scanner and Odyssey® software, respectively (Coomassie Brilliant Blue R is visible in the 700 nm channel). We measure band intensity by drawing a rectangle around the largest band on the gel and then using this same rectangle to measure intensity of all bands on the gel. We measure the intensity of each band three times and then take the average.

6. Generate a standard curve for the tau standard by plotting ug protein/lane vs. band intensity (Fig. 2.3B). Interpolate values for unknowns from the standard curve.

7. Back-calculate the concentration of undiluted unknown sample, and average the values obtained from each of the different dilutions of the unknown.

8. Adjust assumed concentration of unknown to the interpolated average and run a confirmatory concentration gel. Three replicates are recommended.

Notes

- We store the tau standard in small aliquots at $-80\,°C$ in screw-top vials to guard against protein degradation and sublimation. For storage, the standard is diluted in Laemmli sample buffer at 40X the final working tau concentration. Upon thawing, sufficient 1X Laemmli sample buffer is added to bring the standard to the working tau concentration. This working solution of standard can be stored at $-20\,°C$ in the short term (approximately one month) but should be replaced if any breakdown products are noted.

- Coomassie Brilliant Blue R stain binds proportionally to a protein's basic residues [Tal et al., 1980]. This is why less protein per lane is required to visualize a protein like tau, which contains many basic residues, than is required to visualize many other proteins. As such, it is desirable to run the unknown tau isoform against an identical tau isoform standard if possible, or against one containing a comparable number of basic residues for the most accurate results. It may also be necessary to increase the amount of protein loaded per lane for different tau isoforms or tau fragments, depending on their amino acid composition.

- Linear regression of the tau standard generally produces a reliable standard curve with a high r^2 value, which indicates a good fit (ours are typically $r^2 \geq 0.98$). If a linear fit does not yield an adequate r^2 value, or if it appears to be a poor fit, data
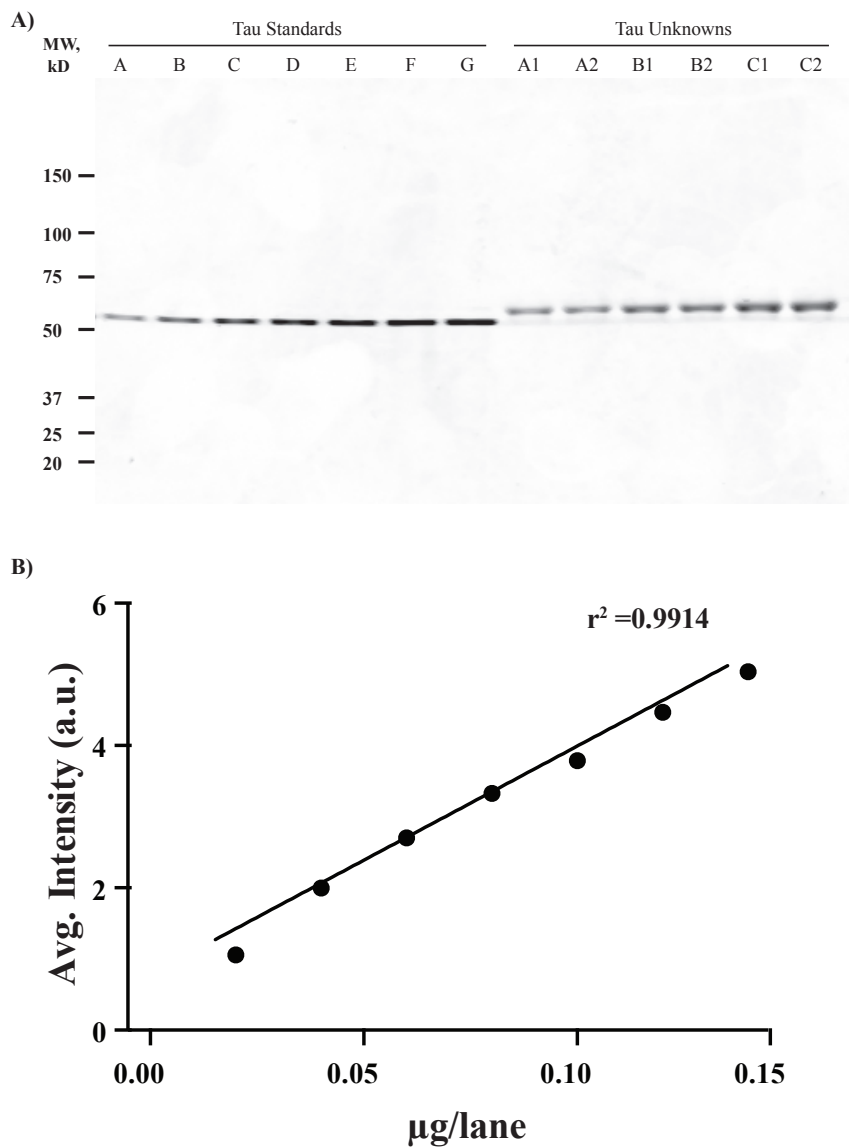
Figure 2.3: **Determination of tau concentration by SDS-PAGE gel and comparison to a tau mass standard.** (A) A dilution series of a tau mass standard ("0N4R" isoform, 383 amino acids) of known concentration, ranging from 0.02 - 0.14 ug tau/lane (lanes A-G), was run against a dilution series of purified tau of unknown concentration ("2N4R" isoform, 441 amino acids; lanes A1-C2, run in duplicate). (B) Band intensities were quantified. Standards were fit by linear regression and then used to interpolate the unknown concentration of the purified tau (see section 2.5).

can be fit instead with a nonlinear regression to a 2nd or 3rd order polynomial. The standard curve should not obviously plateau at higher concentrations; if it does, lower the standard concentration range.

- When doing regression analysis, do not force the line through (0,0). In our experience this results in poorer fits and less reproducibility.

- Discard any unknown intensity values that lie outside the range of the standard curve. The most accurate estimates are obtained within the range where the standards are approximately linear.

- For densitometric quantitation on the Li-COR Odyssey® imaging scanner and software (Li-COR Biosciences), we have found that the "Left-Right, Median" method of background subtraction produces the most reliable results. Practically, this means that the background value for each band is defined by the median intensity of pixels in a 1-pixel border to the left and right side of the selection; pixels above and below the band are ignored. This method is not suitable if the spaces between the bands are not well defined (i.e., if the bands touch each other).

- Some evidence suggests that quick-stain protocols such as those outlined in section 2.3.8 and 2.3.9 may provide less robustly quantitative data compared to a longer staining procedure such as we describe in section 2.5 [Luo et al., 2006, Weber et al., 1972, Wilson, 1983].

Materials

- Coomassie Brilliant Blue R stain (Thermo 20278, Sigma 27816) in 10% acetic acid, 10% isopropanol

- Destain solution (same as the staining solution, but omit the dye)

- Tau standard of known concentration (determined by amino acid analysis)

- LiCOR Odyssey Imaging System or similar

Chapter 3

Tau isoform-specific stabilization of intermediate states in microtubule assembly and disassembly

3.1 Permissions and Attributions

The content of chapter 3 is the result of a collaboration with Nichole E. LaPointe, Jiahao Liang, Kevin Ruan, Madeleine F. Shade, Leslie Wilson, and Stuart C. Feinstein. My contributions were in: experiment conceptualization and development of methodology, data curation, formal data analysis, experimental investigation, data visualization, writing the original manuscript draft, subsequent writing-review and editing.

This work has previously appeared in the *Journal of Biological Chemistry* [Best et al., 2019]. It is reproduced here with the permission of UCSB `https://doi.org/10.1074/jbc.RA119.009124`

3.2 Abstract

The microtubule (MT)-associated protein tau regulates the critical growing and shortening behaviors of MTs, and its normal activity is essential for neuronal development and

maintenance. Accordingly, aberrant tau action is tightly associated with Alzheimer's disease and is genetically linked to several additional neurodegenerative diseases known as tauopathies. Although tau is known to promote net MT growth and stability, the precise mechanistic details governing its regulation of MT dynamics remain unclear. Here, we have used the slowly-hydrolyzable GTP analog, guanylyl-(α,β)-methylene-diphosphonate (GMPCPP), to examine the structural effects of tau at MT ends that may otherwise be too transient to observe. The addition of both four-repeat (4R) and three-repeat (3R) tau isoforms to pre-formed GMPCPP MTs resulted in the formation of extended, multiprotofilament-wide projections at MT ends. Furthermore, at temperatures too low for assembly of bona fide MTs, both tau isoforms promoted the formation of long spiral ribbons from GMPCPP tubulin heterodimers. In addition, GMPCPP MTs undergoing cold-induced disassembly in the presence of 4R tau (and to a much lesser extent 3R tau) also formed spirals. Finally, three pathological tau mutations known to cause neurodegeneration and dementia were differentially compromised in their abilities to stabilize MT disassembly intermediates. Taken together, we propose that tau promotes the formation/stabilization of intermediate states in MT assembly and disassembly by promoting both longitudinal and lateral tubulin–tubulin contacts. We hypothesize that these activities represent fundamental aspects of tau action that normally occur at the GTP-rich ends of GTP/GDP MTs and that may be compromised in neurodegeneration-causing tau variants.

3.3   Introduction

Tau is a microtubule-associated protein (MAP) found primarily in neuronal axons and cell bodies. Under normal circumstances, tau is necessary for the establishment of neuronal cell polarity, the maintenance of neuronal cell morphology, and various microtubule-

dependent functions such as axonal transport [Bunker et al., 2004, Drubin et al., 1986, 1985, Caceres and Kosik, 1990, Esmaeli-Azad et al., 1994, Liu et al., 1999, Stamer et al., 2002]. Interestingly, although tau knockout mice exhibited a rather modest phenotype [Harada et al., 1994], tau/MAP1B double-knockout mice exhibited a much stronger phenotype than either individual knockout, demonstrating synergistic and necessary action by both MAPs [Takei et al., 2000]. Additionally, aberrant tau biochemistry has long been correlated with Alzheimer's disease and related dementias, known collectively as tauopathies. Specifically, biochemically altered tau is the primary component of neurofibrillary tangles, one of the two hallmark pathologies of Alzheimer's disease. Furthermore, human genetic analyses have demonstrated that both structural and regulatory errors in tau expression can cause neurodegeneration and dementia in frontotemporal dementia with parkinsonism-17 (FTDP-17), progressive supranuclear palsy, and a number of other tauopathies [Garcia and Cleveland, 2001, Wolfe, 2009, Wang et al., 2016]. Importantly, the molecular mechanism(s) by which aberrant tau structure–function or regulation results in disease pathogenesis remain unknown, although good evidence supporting both loss–of–function and gain–of–function mechanisms has been presented [Wang et al., 2016, Panda et al., 2003, Feinstein and Wilson, 2005, Goedert et al., 2000]. Among the proposed mechanisms underlying pathological tau action is altered tau–microtubule interactions, ultimately leading to microtubule destabilization and tau self-aggregation into neurofibrillary tangles [Wolfe, 2009, Wang et al., 2016]. Indeed, the vast majority of known pathological mutations in the tau gene leads to reduced tau affinity for MTs [DeTure et al., 2000, Bunker et al., 2006, LeBoeuf et al., 2008, Nagiec et al., 2001], reduced ability to regulate MT dynamics [Bunker et al., 2006, LeBoeuf et al., 2008, Hong et al., 1998], and increased propensity of tau aggregation [Lewis et al., 2000, Combs and Gamblin, 2012].

MTs are dynamic cytoskeletal polymers that are essential for many cellular processes,

including cell division, maintenance of cellular shape, intracellular transport, and cell signaling [Drechsel et al., 1992, Jordan and Wilson, 2004, Gustke et al., 1994, Panda et al., 1995]. The best understood aspect of tau action is to regulate MT dynamics, which are critical in order for MTs to perform their essential functions. The adult human central nervous system expresses six different isoforms of tau, generated by alternative splicing of exons 2, 3, and 10 of the mapt gene [Goedert et al., 1989]. The presence or absence of exon 10 in adults leads to the approximately equal expression of tau proteins possessing three or four adjacent, 31-amino acid–long, imperfect MT-binding repeats (designated as 3R or 4R tau, respectively, see Fig. 3.1). Notably, mutations in the mapt gene that disrupt the normal 3R/4R tau isoform ratio, leading to the overproduction of wild-type (WT) 4R tau, cause dementia [Spillantini et al., 2000, 1998]. Mechanistically, 3R and 4R tau regulate MT dynamics by

1. lowering the critical concentration of tubulin dimers required for MT assembly,

2. moderately increasing MT growth rates,

3. increasing the amount of time MTs spend in an attenuated or static state, and

4. suppressing the frequency of MT catastrophes (a switch from a growing or attenuated state to a shortening state) [Panda et al., 2003, Drechsel et al., 1992, Panda et al., 1995, Cleveland et al., 1977].

Importantly, 4R tau suppresses MT shortening rates and shortening lengths per event much more effectively than does 3R tau [Bunker et al., 2004, Panda et al., 2003, Trinczek et al., 1995, Levy et al., 2005]. Despite these insights, the underlying mechanism(s) by which tau binding to MTs and tubulin heterodimers mediates its regulation of MT dynamic instability remains poorly understood.

Multiple tau-binding sites upon MTs have been reported, including sites along the outer MT surface [Al-Bassam et al., 2002, Kellogg et al., 2018, Santarella et al., 2004, Kutter et al., 2016], at the longitudinal interface between heterodimers [Kadavath et al., 2015], and within the MT lumen (interior) [Kar et al., 2003, Martinho et al., 2018]. Importantly, kinetic analyses in vitro [Makrides et al., 2004] and in cells [Breuzard et al., 2013] indicate that tau has at least two modes of binding to MTs, one that is transient and readily exchangeable with tau in solution and another that is relatively nonexchangeable. The nonexchangeable binding site appears to be accessible only when tau is present during MT assembly and not when tau is added to pre-assembled MTs [Makrides et al., 2004]. The notion of a strong association between tau and MTs contrasts with recent studies indicating that tau's association with MTs is highly dynamic [Konzack et al., 2007, Samsonov et al., 2004, Janning et al., 2014, Hinrichs et al., 2012]. These data are all compatible with a model in which the dynamic tau population corresponds to the readily dissociable binding mode on the outside of the MT, while the second very stable binding mode corresponds to the tau-binding site within the lumen of the MT as described by Kar et al. [2003].

Tau binding to MTs reaches saturation at a molar ratio on the order of 1 tau per 5–10 tubulin dimers [Drechsel et al., 1992, Hirokawa et al., 1988, Kim et al., 1986], implying a high abundance of binding sites along the length of a MT. However, the abundance of these sites could obscure a much lower abundance of higher-affinity tau-binding sites at MT ends, where growing and shortening events occur. Indeed, this is the case for the MT-binding drug vinblastine [Wilson et al., 1982, Singer et al., 1989, Gigant et al., 2005, Jordan et al., 1986]. Tau also binds to free tubulin heterodimers and is capable of binding multiple heterodimers simultaneously via multiple motifs within the MT-binding repeats as well as sequences in the adjacent "pseudorepeat" R' [Kellogg et al., 2018, Li et al., 2015, Li and Rhoades, 2017]. These regions of tau can also interact with multiple sites
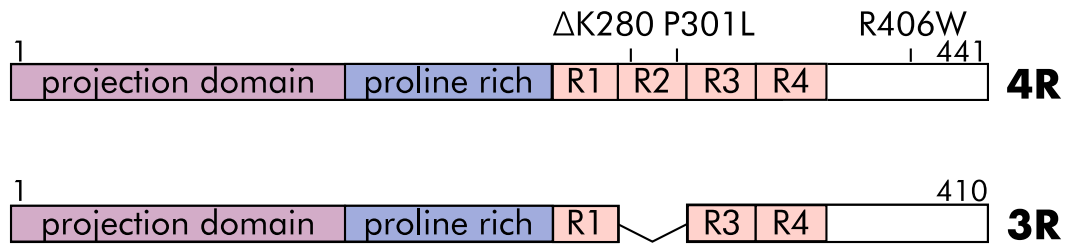
Figure 3.1: **Schematic of 4R (top) and 3R (bottom) tau** with major features labeled, including the MT-binding repeats (R1-R4).

on free tubulin heterodimers, including, but not limited to, the disordered, negatively charged C-terminal "tails" of $\alpha-$ and β-tubulin [Li et al., 2015, Li and Rhoades, 2017], which are also important for tau binding on the outer MT surface [Kellogg et al., 2018, Santarella et al., 2004, Sontag et al., 1999].

Nucleation, the rate-limiting step in MT assembly, is a complex process that culminates in the formation of the smallest energetically favorable tubulin oligomer necessary to promote assembly [Roostalu and Surrey, 2017]. Although the identity of this intermediate has remained elusive, a number of transient intermediate structures have been reported, including rings, twisted ribbons, and sheets [Kutter et al., 2016, Erickson and Voter, 1986, Sandoval and Weber, 1980a,b, Frigon and Timasheff, 1975, Erickson, 1974, Kirschner et al., 1975a, Voter and Erickson, 1984, Caudron et al., 2002, Chretien et al., 1995]. During nucleation, GTP-bound tubulin heterodimers first associate head–to–tail via longitudinal contacts to form protofilaments, which then associate via lateral contacts to form a MT [Roostalu and Surrey, 2017, Kirschner and Mitchison, 1986]. Protofilaments are curved in solution but are straight within the context of the MT lattice, constrained by lateral contacts with neighboring protofilaments [Chretien et al., 1995, Muller-Reichert et al., 1998, Hyman et al., 1995, Brouhard and Rice, 2014, Alushin et al., 2014]. Dynamic MT ends can switch stochastically between phases of assembly and disassembly.

At the heart of this "dynamic instability" is the hydrolysis of GTP by β-tubulin, which occurs at the longitudinal interface between two heterodimers following incorporation into the MT lattice and is thought to be accompanied by conformational changes that introduce additional lattice strain [Brouhard and Rice, 2014, Alushin et al., 2014]. MTs have been proposed to possess a stabilizing "GTP" or "GDP-Pi" cap at their plus-ends composed of tubulin heterodimers that have not yet undergone conversion to GDP. This cap serves to promote further MT elongation and prevent "catastrophe," a switch to a rapidly shortening state in which lateral contacts between protofilaments are lost and protofilaments peel outward from the body of the MT. While early models attributed the stabilizing effect of the GTP cap and assembly competency of GTP tubulin to an inherent difference in protofilament curvature between the GTP and GDP state (with GTP possessing a straight conformation), more recent work indicates that whereas GTP tubulin is straighter than GDP tubulin, it is also curved, arguing that straightening occurs as MT-specific lateral contacts are established [Alushin et al., 2014, Rice et al., 2008]. Thus, rather than protofilament curvature, the most recent picture of the conformational changes that accompany GTP hydrolysis includes compaction of the interface between longitudinally-associated heterodimers and rotation of α-tubulin into a more bent structure [Alushin et al., 2014, Zhang et al., 2015].

In an attempt to better understand how tau mechanistically regulates MT assembly and dynamic instability, we examined the action of tau at MT ends through experiments with the slowly-hydrolyzable GTP analog GMPCPP [Hyman et al., 1992]. MTs assembled with GMPCPP tubulin are widely believed to model the GTP-rich end of a normal (i.e. GTP/GDP)-growing MT [Muller-Reichert et al., 1998, Hyman et al., 1995, Alushin et al., 2014, Rice et al., 2008, Hyman et al., 1992]. This idea is supported by the fact that GTP and GMPCPP tubulin both maintain similar lateral contacts [Alushin et al., 2014]. Additionally, approximately equal MT elongation rates are observed in the

presence of GMPCPP and GTP [Hyman et al., 1992]. Furthermore, despite GMPCPP tubulin's enhanced nucleation abilities, early in vitro MT assembly experiments comparing the two nucleotides show that the same intermediate structures were produced in the early phases of MT nucleation, albeit in much larger quantities in GMPCPP-containing samples [Sandoval and Weber, 1980b]. We reasoned that the use of GMPCPP, with its enhanced nucleation ability and overall higher stability, might enable us to observe structural intermediates that would ordinarily be too transient to detect.

Here, we show that pre-assembled GMPCPP MTs develop extended projections composed of multiple aligned protofilaments upon the addition of tau. Furthermore, at temperatures too low for MT assembly, GMPCPP tubulin heterodimers co-incubated with tau form numerous long spirals reminiscent of the end projections observed at higher temperatures on pre-formed MTs. Next, GMPCPP MTs undergoing disassembly in the presence of 4R tau (and to a lesser extent 3R tau) also form spirals. Finally, we show that three tau mutations that cause neurodegeneration and dementia are compromised in their ability to stabilize MT disassembly intermediates. Taken together, we propose that tau acts to promote both longitudinal and lateral contacts to stabilize intermediate states that can be reached via both assembly and disassembly and that some of these abilities may be compromised in pathological tau. We hypothesize that these activities represent fundamental aspects of tau action that normally occur at the GTP-rich ends of GTP/GDP MTs.

3.4   Results

Given tau's potent regulation of MT dynamic instability, we focused our attention upon tau action at MT ends, where tau's regulatory effects upon dynamics must ultimately be put into action.

3.4.1 Tau promotes the stabilization of tubulin projections at the ends of pre-assembled GMPCPP microtubules

Pre-assembled GMPCPP MTs (at a final concentration of 0.5 uM tubulin) were incubated in buffer, plus or minus tau at a molar ratio of 1 : 5 tau:tubulin, for 10 min at 25 °C in a "decoration" assay (Fig. 3.1). We then examined MT end morphologies using transmission electron microscopy (TEM).

In the absence of tau, nearly all of the GMPCPP MTs possessed normal blunt or slightly splayed end morphologies (Fig. 3.1B), whereas the addition of 4R or 3R tau resulted in coiled projections at many ends (Fig. 3.1C, 3.1D, and 3.1E). The tau effect was rapid, specific, and observed across multiple independent tubulin and tau preparations (this is true for all experiments reported in this manuscript). Specifically, projections appeared within ~1 min of tau addition and were not observed when pre- assembled MTs were decorated with the MT-stabilizing drug taxol, the MT end-binding protein EB1, or non-MT interacting proteins with overall negative (BSA) or positive (histone) charges (Fig. A.1A).

In order to quantitatively assess these data, we developed a scoring system for the different MT end morphologies (Fig. 3.2E). "Blunt" and "splayed" describe normal MT end morphologies lacking "projections," with a "splayed" end having a slight gap between terminal protofilaments. "Projection" describes MT ends possessing either one projection $\geq$ 25 nm in length (one MT diameter) or at least three projections (with no length minimum). MT ends not fitting into any of the above three categories were extremely rare ($\sim$ 2 %) and were therefore excluded from the analysis.

As seen in Fig. 3.2F and Table A.1, projection frequencies significantly differed between the no tau control samples and tau decorated MTs (generalized linear model, GLM, p <0.0001). Control MTs exhibited almost exclusively blunt and splayed ends,

with only 6.3% of ends possessing projections. In contrast, MTs decorated with either 4R tau or 3R tau had greatly increased projection frequencies relative to the no tau control (57.7% and 57.8%, respectively; p <0.0001 for both comparisons), while the two tau isoforms were not different from one another. Interestingly, these end projections appeared to be derived primarily from "blunt" ended MTs as opposed to those with a "splayed" morphology (Fig. 3.2F).

Finally, MT length distributions measured before and after decoration with tau revealed no detectable change in MT length (excluding projection length) over the 10 min incubation at 25 °C (Fig. A.1B).

3.4.2 Are tubulin projections at MT ends the result of tau-mediated effects during MT assembly, disassembly, or both?

Projections at MT ends could result from tau- promoted growth via addition of soluble tubulin heterodimers onto existing MT ends, perhaps analogous to the curved protofilament sheets observed at fast-growing MT ends [Chretien et al., 1995]. However, since the final step in our GMPCPP MT preparation is centrifugation and resuspension in tubulin-free buffer (see Experimental Procedures), only minimal quantities of free tubulin heterodimers are expected to be present in these preparations. On the other hand, GMPCPP tubulin has an estimated critical concentration of only 20 nM for nucleated assembly onto pre-existing MTs [Hyman et al., 1992], and the critical concentration could be even lower in the presence of tau. Therefore, we hypothesized that small amounts of free tubulin subunits present in the GMPCPP MT preparation (carried over after centrifugation and/or arising during the storage process) might be sufficient to support some small amount of tau-mediated assembly at MT ends. Alternatively, if the projec-
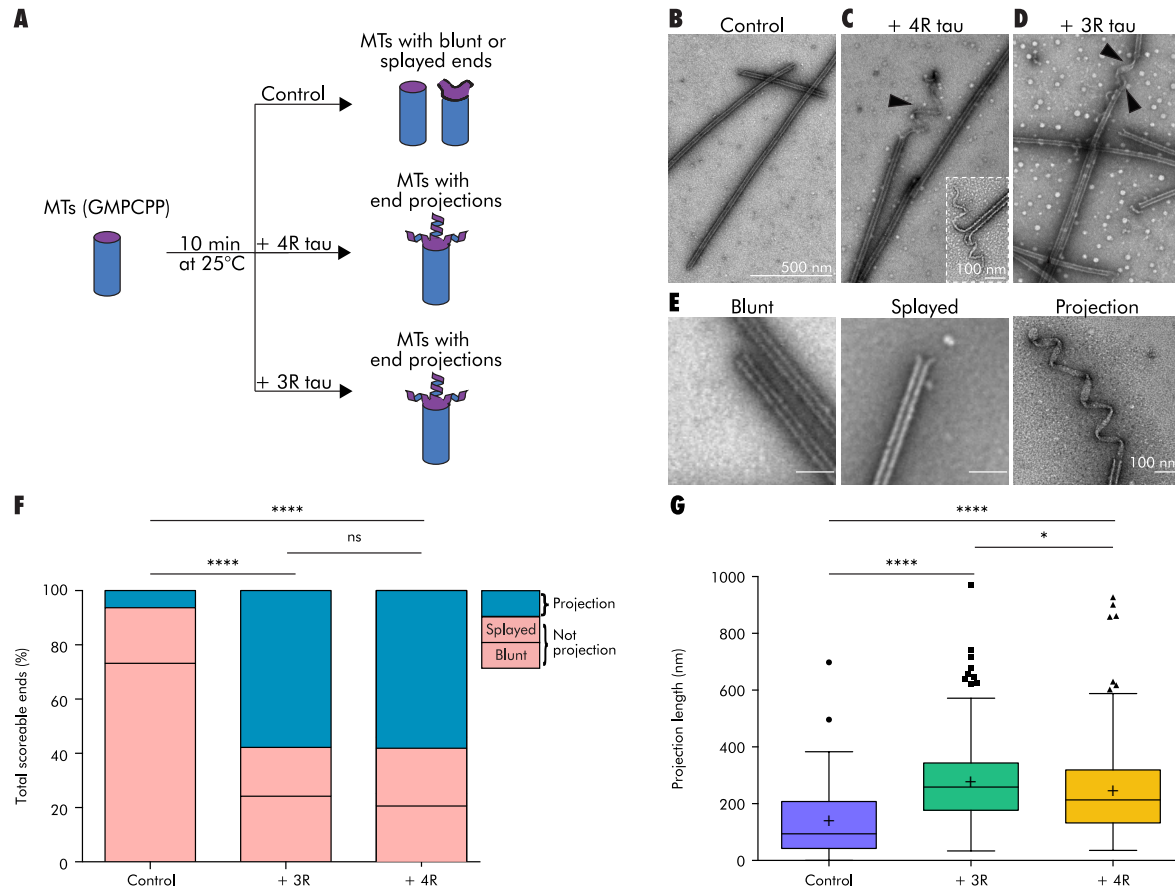
Figure 3.2: **Tau stabilizes projections at the ends of pre-assembled GMPCPP microtubules** (A) schematic of a GMPCPP MT decoration assay. (B) GMPCPP MTs in the absence of tau possess blunt or splayed ends. (C) and (D) GMPCPP MTs decorated with 4R tau or 3R tau, respectively, develop spiral, ribbon-like projections at microtubule ends (black arrowheads). Inset: high magnification image of an end projection. (E) scoring guide for MT ends. (F) and (G) projection frequency (F) and length (G) of GMPCPP MTs (0.5 uM) decorated with buffer or tau (4R or 3R, 1:5 tau:tubulin molar ratio). Bars show total counts summed across all experiments. Tukey's boxplot, horizontal line at the median, plus sign at the mean. Outliers shown as individual points. * p <0.05; **** p <0.0001; ns, not significant. See also Table A.1.

tions were generated during MT disassembly events, the simplest model would be that the projections represent a normally short-lived disassembly intermediate that is stabilized by tau, perhaps analogous to the protofilament peels observed at the ends of disassembling MTs [Muller-Reichert et al., 1998, Elie-Caille et al., 2007, Mandelkow et al., 1991, Sandoval et al., 1977, 1978].

Tau-induced projections form during MT assembly events

To begin assessing whether the projections in the decoration assays (Fig. 3.2) were the result of tau action during MT assembly, disassembly, or both, we exploited a differential activity of 4R and 3R tau that we and others have described in vitro and in cultured cells: although both 4R and 3R tau promote MT growth events to a similar extent, 4R tau suppresses MT shortening events much more effectively than does 3R tau [Bunker et al., 2004, Panda et al., 2003, Gustke et al., 1994, Trinczek et al., 1995, Levy et al., 2005, Goode et al., 2000]. Therefore, if the MT end projections were formed by tau action during MT assembly, 4R and 3R tau would be predicted to exhibit comparable projection formation abilities. Alternatively, if the projections were generated by tau action during MT disassembly, 4R tau would be predicted to exhibit increased projection frequency and/or longer projection lengths than those exhibited by 3R tau.

3R tau and 4R tau generate similar projections in MT decoration assays, supporting tau mediated formation of end projections during MT assembly events

The decoration assay presented in Fig. 3.2, in addition to revealing the existence of MT end projections in the presence of 4R and 3R tau, also addresses the question of whether or not projections can form during MT assembly events. For example, at a 1 : 5 tau:tubulin molar ratio (at which the MT lattice is saturated with tau and at which 3R tau promotes MT growth comparably to 4R tau [Panda et al., 2003, Levy et al., 2005], we found that the distribution of MT end morphologies was essentially identical with both tau isoforms (Fig. 3.2F and Table A.1). Further, projections were similar lengths

with both isoforms. 3R-decorated MTs had projections that were slightly longer, with a mean length of 275 ± 8.9 nm compared to 4R-decorated MTs with a mean length of 245 ± 9.3 nm. Both were significantly longer than the relatively rare projections observed in no tau controls (mean length 138 ± 13 nm, p <0.0001 for both comparisons; Fig. 3.2G and Table A.1). The small (30 nm) length difference between 3R- and 4R tau-promoted projections was statistically significant (p = 0.017). Nonetheless, the similar lengths and nearly identical abundance of 4R and 3R induced end projections support the notion that the projections are the result of tau-mediated stabilization of an assembly event. The simplest interpretation is that low levels of free tubulin subunits present in the assay mixtures were sufficient to support projection assembly.

We next reasoned that, while sufficient for some amount of projection assembly, the low level of free tubulin in the decoration assay could be a limiting factor. Therefore, as an additional assessment of the assembly origin model for projections, we performed decoration assays in which we supplemented the system with an additional 0.5 uM of free GMPCPP tubulin. In the presence of the additional tubulin, we observed increases in both projection frequency and projection length in tau-containing samples.. Specifically, projection frequency for 4R and 3R tau increased by 23% and 11%, respectively, while projection length increased by 43% and 30%, respectively.

Taken together, these data indicate that tau promoted tubulin assembly activity contributes to the generation of MT end projections.

In the absence of MT assembly, tau promotes formation of GMPCPP tubulin "spirals"

Interestingly, the decoration experiment presented in Fig. 3.2 did not result in a measurable change in MT length (Fig. A.1B). Therefore, we next asked if tau can promote the assembly of any alternative tubulin structures in the absence of pre- formed MTs, such as the rings, "twisted ribbons," and/or sheets observed at the earliest time points of MT assembly reactions under various conditions [Kutter et al., 2016, Frigon

and Timasheff, 1975, Voter and Erickson, 1984, Kirschner et al., 1975a, 1974, Wang et al., 2005]. It is especially notable that spirals observed with GMPCPP tubulin and high concentrations of Mg^{2+} can directly convert into MTs and have been proposed to correspond to sheet-like intermediates observed at growing MT ends [Wang et al., 2005].

In order to prevent assembly of complete MTs and therefore increase the likelihood of observing pre- MT structures, we performed our experiments at $4\,°C$. We incubated 0.9 uM GMPCPP tubulin heterodimers for 30 min at $4\,°C$ in the presence or absence of 4R or 3R tau (Fig. 3.3A). Under these conditions, both 4R tau and 3R tau promoted the assembly of long GMPCPP tubulin spirals (Fig. 3.3B), which we term "de novo" spirals to emphasize that the starting material was unpolymerized tubulin dimers rather than pre- assembled MTs. No tau containing control samples possessed far fewer and significantly shorter spirals (Fig. 3.3B, 3.3G, and 3.3H). The fact that spirals were observed even in the absence of tau suggests that these GMPCPP tubulin spirals, like those observed by Wang et al., using different conditions [Wang et al., 2005], represent a normal intermediate in GMPCPP tubulin assembly.

Width measurements from TEM images indicated that de novo spirals were 25.2 ± 0.9 nm, suggesting that our de novo spirals were composed of an average of $\sim$6 protofilaments. Both spiral number (Ordered heterogeneity, OH, p= 0.002) and spiral length (OH p = 0.002) were positively correlated with tubulin concentration (holding the tau:tubulin ratio constant; Fig. 3.3C, 3.3D, and Table A.2). In contrast, spiral length (OH p = 0.0004; Fig. 3.3F and Table A.3) but not spiral number (Fig. 3.3E and Table A.3) negatively correlated with increasing tau:tubulin molar ratios. One simple interpretation compatible with all of these data is that an increased number of tau molecules results in an increased number of spiral nucleation events, ultimately resulting in an increase in spiral abundance and a decrease in average spiral length as tubulin subunits become limiting. This would be consistent with tau lowering the critical concentration for spiral
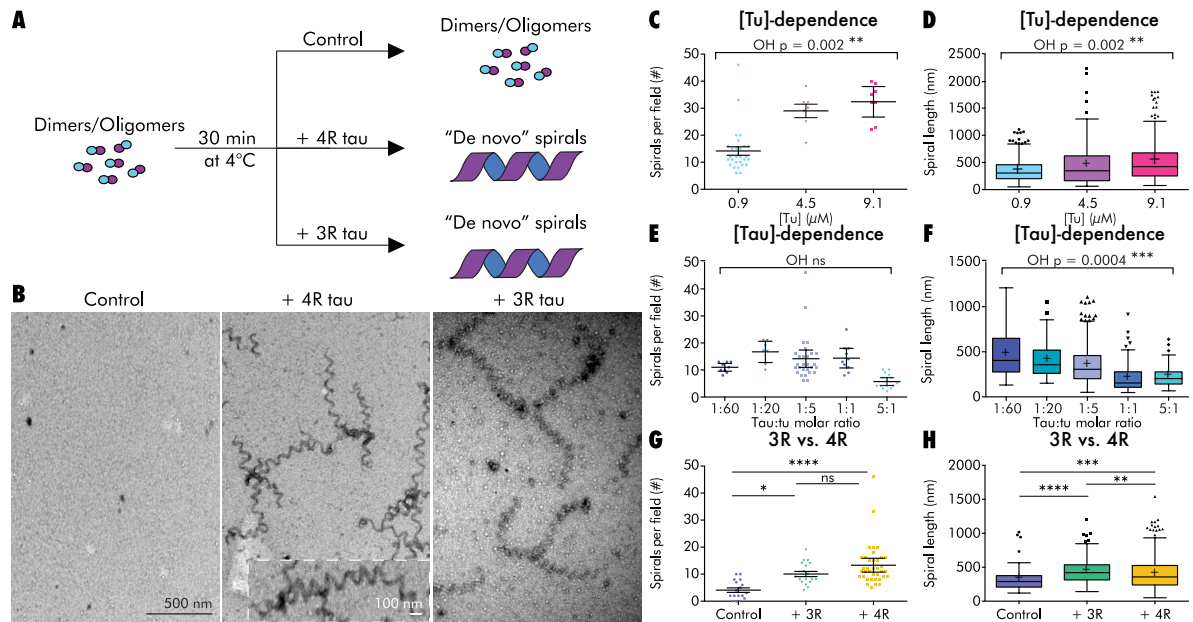
Figure 3.3: **Tau stabilizes a GMPCPP tubulin spiral structure under non assembly-promoting conditions.** (A) Schematic of a GMPCPP tubulin "de novo" spiral formation experiment (B) Left: GMPCPP tubulin dimers (0.9 uM) in the absence of tau only rarely form spirals. Center, right: In the presence of 4R tau and 3R tau, respectively (1 : 5 tau:tubulin molar ratio), GMPCPP tubulin dimers assemble into plentiful spirals. Inset shows a higher magnification image of a de novo spiral. (C, D) Effects of tubulin concentration on de novo spiral abundance (C) and length (D) with 4R tau at a constant 1 : 5 tau:tubulin molar ratio. (E, F) Effects of 4R tau concentration on de novo spiral abundance (E) and length (F) at a constant tubulin concentration of 0.9 uM. (G, H) De novo spiral abundance (G) and lengths (H) with 3R and 4R tau (1 : 5 tau:tubulin molar ratio). Graphs (D), (F), and (H) are Tukey's boxplots. Graphs (C), (E), and (G) show mean and 95% confidence interval (CI); each data point represents a randomly chosen field at 30,000X magnification. **** p <0.0001, *** p <0.001, ** p <0.01, * p <0.05. See also Tables A.2-A.4.

formation. On the other hand, the trend toward increased spiral abundance at higher tau:tubulin molar ratios did not reach statistical significance (Fig. 3.3E and Table A.3).

Next, we asked if both 3R and 4R tau isoforms promote de novo spiral assembly to the same extent. We incubated 0.9 uM GMPCPP tubulin alone or with 3R or 4R tau (1 : 5 tau:tubulin molar ratio) and then quantified spiral abundance and length. The three conditions differed significantly in both the numbers (ANOVA p < 0.0001) and lengths (Welch's ANOVA p < 0.0001) of de novo spirals. We found comparable numbers

of de novo spirals in the presence of 3R tau and 4R tau (Table A.4). Both tau isoforms assembled more spirals than controls (p = 0.011 versus 3R tau and p < 0.0001 versus 4R; Fig. 3.3G). Spirals were also longer in the presence of either tau isoform than in the no tau control (p < 0.0001 vs 3R tau and p = 0.0008 vs 4R tau). 3R tau produced the longest spirals, with a mean length of 450 ± 14 nm, compared to 402 ± 11 nm with 4R tau, and 319 ± 20 nm in controls (Fig. 3.3H and Table A.4). The length difference between 3R tau and 4R tau was statistically significant (p = 0.008). This observation is reminiscent of the longer projection lengths observed with 3R tau relative to 4R tau in the decoration assay (Fig. 3.2). Both of these observations would be predicted if 4R tau is a slightly stronger nucleator of spiral and MT formation (i.e., given limited free tubulin subunits, more nucleation events would result in shorter average lengths). Consistent with our earlier observations, a large increase in the tau concentration (to 5 : 1 tau:tubulin molar ratio) resulted in decreased mean spiral lengths for both 3R and 4R tau samples, giving spirals with mean lengths of 363 ± 14 nm and 364 ± 8.5 nm, respectively. These data are consistent with the comparable assembly- promoting activities of 3R and 4R tau reported in the literature and support the notion that spirals represent a tau-stabilized intermediate in MT assembly.

Under MT assembly conditions, incubation of tau with GMPCPP tubulin supports the model that tau prolongs an intermediate assembly state

Tau's ability to promote the assembly of *de novo* spirals under non-MT assembly conditions coupled with the assembly of a lesser number of spirals even in no tau controls led us to hypothesize that the spirals represent a normal intermediate in GMPCPP MT assembly and a fundamental component of tau action in MT assembly. Wang et al. (84), demonstrated that GMPCPP tubulin spirals formed at $4\,^{\circ}\text{C}$ and high Mg^{2+} concentrations could undergo a temperature- dependent conversion into MTs (without a depolymerization step), leading the authors to hypothesize a connection between their

spirals and the sheet-like intermediates sometimes observed at the ends of fast-growing GTP MTs [Wang et al., 2005]. The Wang et al. [2005] transition from spirals to MTs occurred around 25 °C, the critical temperature for GTP tubulin assembly [Wang et al., 2005]. In order to determine whether our tau induced *de novo* spirals could also transition to bona fide MTs, we prepared *de novo* spirals as above (0.9 uM GMPCPP tubulin, 1 : 5 4R tau:tubulin molar ratio, 30 min at 4 °C), then warmed the solution to 34 °C and examined the samples by TEM. Control reactions lacking tau contained abundant MTs with normal morphology. In contrast, we found few morphologically normal MTs in 4R tau-containing samples and instead observed tangled clumps of MTs, spirals, and ribbon-like sheets (data not shown).

We reasoned that our conditions might promote the formation of very long spirals that become highly tangled, thereby interfering with the temperature-induced conversion into MTs. To provide conditions in the tau samples that might be more conducive to complete MT assembly, we eliminated the incubation at 4 °C. Additionally, we increased the tubulin concentration to promote more nucleation events. Therefore, we repeated the tau plus tubulin co-assembly experiment at 6.6 uM tubulin (1 : 5 tau:tubulin). Reaction components were mixed together on ice and then immediately warmed to 34 °C. We took TEM samples as soon as possible ($\sim$ 5 min) after tau addition (in warm buffer, simultaneous with the temperature change) and then after 30 min and 24 h at 34 °C. Before the temperature increase, TEM revealed no visible structures (data not shown). In the absence of tau, MTs were observed at 5 min and greatly increased in number by 30 min (Fig. 3.4B). At these time points, no tau controls showed occasional spiral and ribbon-like structures, both free and at MT ends (Fig. 3.4B). By 24 h, most of these control MTs had normal end morphologies without projections. In contrast, non-MT structures were both much more common and longer at all time points in samples containing 4R tau. Spirals, but not MTs, were observed at 5 min (Fig. 3.4B). By 30 min,
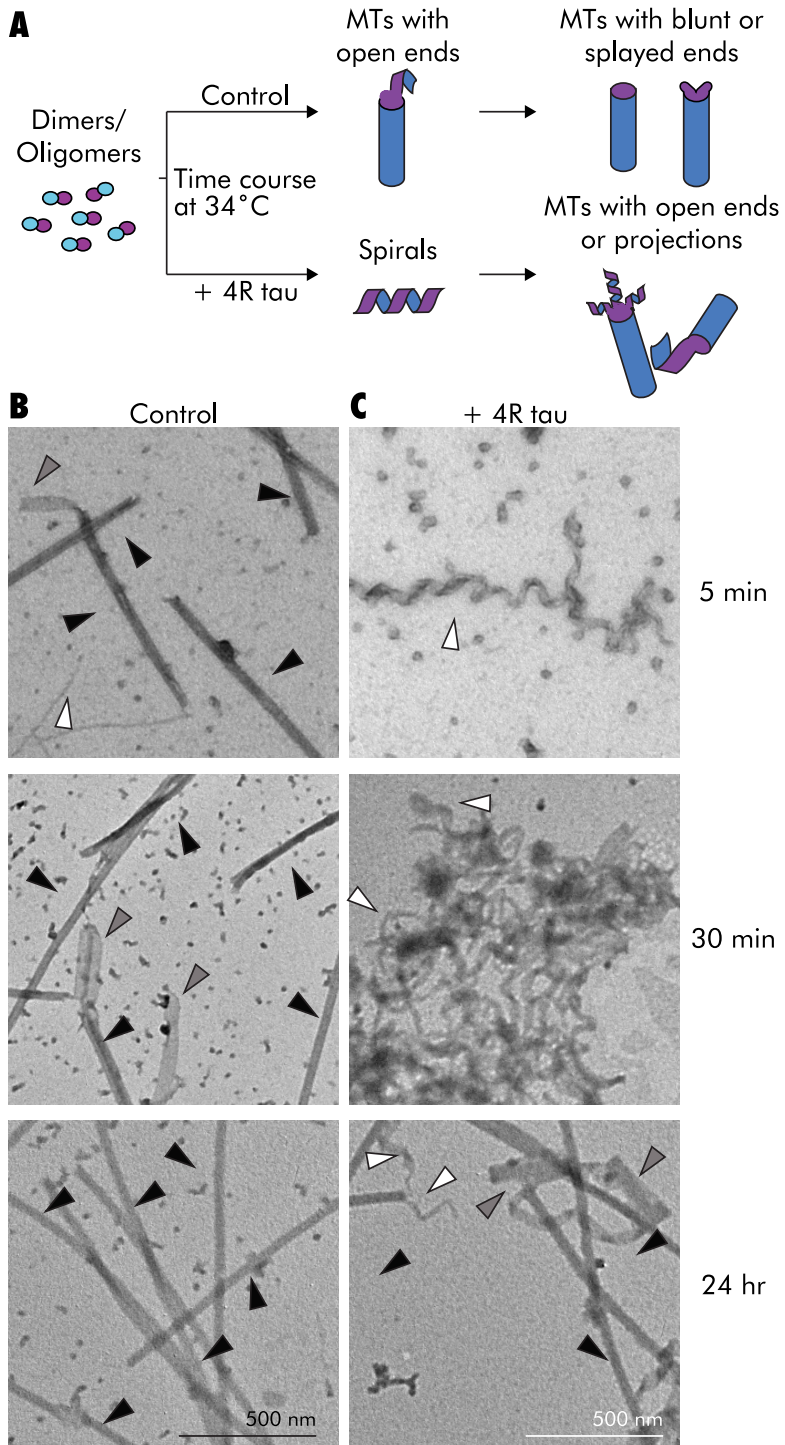
Figure 3.4: **TEM time course of GMPCPP tubulin assembly at** $34\,°C$ **suggests that tau prolongs an intermediate structural state.** (A), schematic of a warm co-assembly experiment. (B), assembly time course of 6.6 uM GMPCPP tubulin in the absence of tau. Note the presence of MTs (black arrowheads), spirals/projections (white arrowheads), and ribbon/sheet structures (gray arrow-heads) after only 5 min. By 30 min, more MTs and sheet structures that may be unfolded MTs have formed. By 24 h, there are many MTs with normal morphology. (C), assembly time course in the presence of 4R tau (1 : 5 tau/tubulin molar ratio). Note the lack of MTs at the earliest time point. By 30 min, MTs are still scarce and large, and tangled clumps of spirals are visible. After 24 h, some MTs are present, although tangled clumps and ribbons are still plentiful, especially in proximity to MT ends.

some rare MTs with long end projections were also present, although in tangled masses of spirals, MTs, and sheet- or ribbon-like structures (Fig. 3.4B). Width measurements suggested that some of these structures might represent unfolded, or not-yet-folded, MTs (average $\sim 75 \pm 9.6$ nm, which is the predicted circumference of a MT.) After 24 h, the 4R tau-containing sample showed more MTs than the 30 min sample, but many had long end projections and tangled masses were still present. Parallel experiments demonstrated that 3R tau also stabilized spirals and produced similar tangled masses as well as some normal MTs (data not shown). Importantly, parallel co-assembly experiments of GTP tubulin both with and without 4R tau yielded morphologically normal MTs (1 : 5 tau:tubulin molar ratio; Fig. A.2). Substitution of the MT stabilizing drug taxol for tau also led to MTs lacking projections. Taken together, the data support the notion that the spirals represent a prolonged view of a normally transient intermediate, assembled and stabilized as a result of normal tau activity.

3.4.3 Tau stabilizes tubulin spirals during GMPCPP micro-tubule disassembly

The results described above indicate that tau stabilizes an intermediate structure during the process of MT assembly. Next, we asked whether or not 4R tau, as a more potent stabilizer against MT shortening relative to 3R tau, more effectively stabilizes any MT disassembly intermediates compared to 3R tau. We returned to the use of pre-assembled GMPCPP MTs and pushed them toward cold temperature-induced disassembly in the presence or absence of 4R or 3R tau. If 4R is more effective than 3R tau, it should stabilize a MT disassembly intermediate that is more abundant and/or longer than similar non-MT structures observed in the presence of 3R tau or no tau controls.

We induced disassembly by diluting pre-assembled GMPCPP MTs into ice-cold buffer

alone or buffer containing tau (final tubulin ~0.5 uM, final molar ratio 1 : 5 tau:tubulin) and examined the structures present after 10 min by TEM (Fig. 3.5A). In the absence of tau, diluted MTs disassembled almost completely, containing only rare spirals (Fig. 3.5B). We refer to these as "disassembly" spirals to emphasize their origin from depolymerizing MTs. In contrast, MTs disassembled in the presence of 4R tau resulted in the presence of many more disassembly spirals than either 3R or control (Welch's ANOVA $p < 0.0001$; Fig. 3.5B and 3.5C). Specifically, 4R tau exhibited an average of 19 ± 1.4 spirals per field, compared to 3.7 ± 0.7 and 2.0 ± 0.3 for 3R tau ($p < 0.0001$) and no tau controls ($p < 0.0001$), respectively (Fig. 3.5C and Table A.5). We also observed significant differences in spiral lengths (Welch's ANOVA $p < 0.0001$). 4R tau-stabilized spirals were significantly longer on average (497 ± 14 nm) than the occasional 3R tau-stabilized (324 ± 16 nm, $p < 0.0001$) or control spirals (296 ± 23, $p < 0.0001$; Fig. 3.5D and Table A.5). It is also notable that 3R tau had a comparatively small, though statistically significant, effect in terms of both the spiral abundance and length versus the control samples ($p = 0.046$ and $p = 0.014$, respectively). Taken together, all of these data fit well with the well-established observation that 4R has a markedly more potent effect upon MT shortening events than does 3R tau [Bunker et al., 2004, Panda et al., 2003]. Increasing the tau:tubulin ratio from 1 : 5 to 10 : 1 (holding the tubulin concentration constant) had no effect on spiral abundance or length for both 4R and 3R tau (data not shown), indicating that tau isoform-specific differences in disassembly spiral stabilization are intrinsic properties of the proteins themselves.

In all cases measured, disassembly spirals were an average of 18.1 ± 0.4 nm wide, corresponding to ~4 protofilaments wide,. Together with the fact that the disassembly spirals were differentially stabilized by 4R tau versus 3R tau, this suggests that they may be distinct from *de novo* spirals.

MTs are known to be more resistant to cold-induced disassembly at higher con-
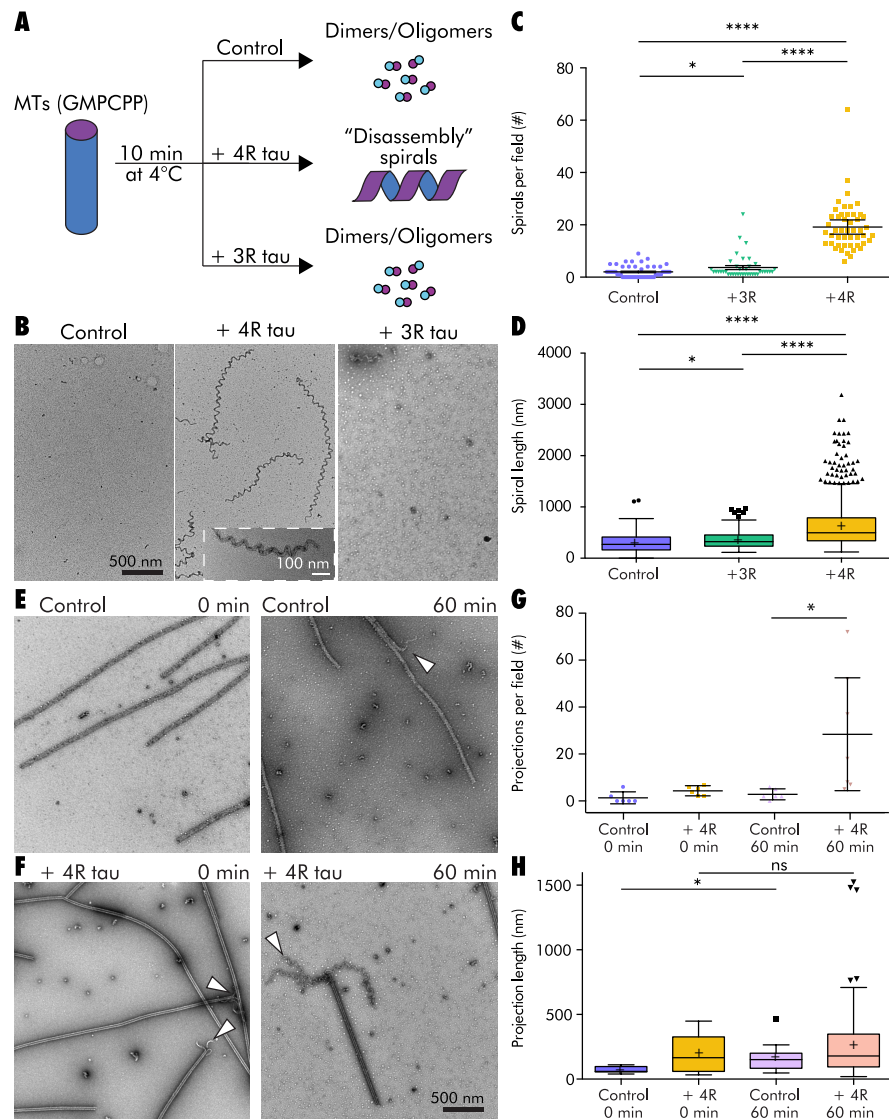
Figure 3.5: **Tau stabilizes a GMPCPP tubulin spiral structure that is reached through microtubule disassembly.** (A), schematic of a disassembly spiral experiment. (B), GMPCPP MTs (0.5 uM) diluted into ice-cold buffer in the absence of tau (left) or in the presence of 3R tau (right) disassemble into tubulin dimers and/or oligomers, with the occasional spiral observed. Cold dilution in the presence of 4R tau results in disassembly spirals (center). Inset shows a higher magnification image of a disassembly spiral. (C) and (D), disassembly spiral abundance (C) and length (D) from MTs disassembled in the presence of 3R or 4R tau. (E) and (F), time course of 6.1 uM GMPCPP MTs cooled to 4 °C in the absence (E) or presence (F) of 4R tau (1 : 4 tau:tubulin molar ratio). Note the presence of projections at MT ends in the presence of tau, even at the earliest time point (left), and persistence of MTs in both samples, even after 60 min (right). (G) and (H), projection abundance (G) and length (H) from (E) and (F), shown from one representative experiment. **** p < 0.0001; * p < 0.05; ns, not significant, p > 0.05. See also Table A.5.

centrations [Karr et al., 1980]. Therefore, we hypothesized that performing the same disassembly experiment at a higher MT concentration might slow depolymerization and allow us to better observe the transition from MTs to disassembly spirals. We cooled GMPCPP MTs (6.1 uM) to $4\,°C$ in the presence or absence of 4R tau (1 : 4 tau:tubulin; Fig. 3.5E and 3.5F). We took TEM samples immediately after tau addition (in ice cold buffer, simultaneous with the temperature change) and then again after 60 min. MT length measurements indicated that MTs disassembled over time to a nearly identical extent in the presence and absence of tau, from 3.1 ± 0.1 um to 2.1 ± 0.1 um in no tau controls (2-sample bootstrap p < 0.0001) and from 3.0 ± 0.1 um to 2.2 ± 0.1 um with 4R tau (2-sample bootstrap p ¡ 0.0001; Fig. A.3). Importantly, the ends of control MTs showed few projections during disassembly, with an average of 1.3 ± 1.0 projections per field (15% of total MT ends) at the initial time point and 2.8 ± 0.9 projections per field (20% of total MT ends) at the 60 min time point (Fig. 3.5G). In contrast, end projections for MTs incubated with 4R tau drastically increased in frequency over time, from 4.3 ± 0.8 projections per field (22% of total MT ends) initially to 28 ± 9.8 projections per field (94% of total MT ends) after 60 min (Fig. 3.5G). This is consistent with the results from Muller-Reichert et al. [1998] showing that $\sim$90% of both GDP and GMPCPP MT ends possessed "curved oligomers" upon inducing MT disassembly with high concentrations (24 mM) of Ca^{2+} [Muller-Reichert et al., 1998].

MTs disassembled in the presence of 4R tau had an average of 26 more projections per field at 60 min than no tau control samples (2-sample Alexander-Govern p = 0.040; Fig. 3.5G). The average projection length increased over time for both conditions, although the difference of 4R tau was not statistically significant. No tau control projection lengths increased from 69 ± 9.2 nm to 169 ± 33 nm (Difference in confidence intervals, DCI, p = 0.039), despite the low number of projections observed at each time point (n = 8 for 0 min and n = 12 for 60 min). Projection lengths in 4R tau-containing samples increased

from 194 ± 29 nm to 255 ± 18 nm, but this difference was not statistically significant (2-sample bootstrap p = 0.068; Fig. 3.5H). The lack of statistical significance for the 4R tau samples may due to the high variability in projection lengths exhibited by 0 min 4R tau samples (n = 25). Nonetheless, it is important to note that the presence of 4R tau resulted in longer and more numerous projections than no tau controls at each time point. These data suggest that 4R tau stabilizes an intermediate structure during MT disassembly, which may contribute to the ability of 4R tau but not 3R tau to stabilize MTs against catastrophe [Bunker et al., 2004, Panda et al., 2003, Trinczek et al., 1995, Levy et al., 2005].

Taken together, these analyses demonstrate the ability of 4R tau to stabilize an intermediate during MT disassembly.

3.4.4 Three FTDP-17 tau mutants are differentially compromised in their ability to stabilize disassembly spirals

We hypothesized that if the stabilization of intermediate structures in MT assembly and disassembly is a normal, physiological tau activity, then it may be compromised by disease-associated mutations in the tau gene. We therefore assessed the effects of three known human tau mutations that cause neurodegeneration, δK280, P301L, and R406W, for their abilities to stabilize i) assembly projections at MT ends and ii) disassembly spirals. At a structural level, the P301L and K280 mutations map within the MT binding repeat region, whereas R406W maps downstream of the MT binding repeat region in the C-terminal tail of the protein (Fig. 3.1). Functionally, P301L and δK280 exhibit loss-of-function effects on MT binding affinity and the ability to regulate MT dynamics [Goedert et al., 2000, DeTure et al., 2000, Bunker et al., 2006, LeBoeuf et al., 2008, Nagiec et al., 2001, Hong et al., 1998]. They also aggregate more readily than WT tau [Lewis et al.,

2000, Combs and Gamblin, 2012]. While R406W also causes disease, it has less marked effects on these parameters [Bunker et al., 2006, LeBoeuf et al., 2008, Barghorn et al., 2000].

We performed MT decoration experiments at 25 °C at a 10 : 1 tau:tubulin molar ratio with wild type 4R tau (WT) and the three tau mutant proteins. All four tau proteins increased the frequency of projections at MT ends relative to controls lacking tau. Specifically, WT 4R tau induced projections at 39% of microtubule ends, compared to 7.4% in the no tau control (Fig. 3.6A). The three mutants trended toward lower projection frequencies than WT (25%, 26%, and 29% of ends overall for P301L, δK280 and R406W, respectively; Fig. 3.6A and Table A.6). These differences came close to but did not reach statistical significance (GLM p = 0.058). Projection length analysis showed that WT 4R tau stabilized projections with a mean length of 252 $\pm$ 24 nm (Fig. 3.6B). While δK280 and R406W trended toward shorter mean projection lengths (171 $\pm$ 23 nm and 191 $\pm$ 21 nm, respectively), P301L projections (248 $\pm$ 38 nm) were similar to WT length, although there were no statistically significant differences between any mutant and WT (Welch's ANOVA, p = 0.06).

Next, we asked if the same tau mutants were able to stabilize disassembly spirals. GMPCPP MTs were diluted into cold buffer with or without each tau protein (final tubulin $\sim$ 0.5 uM, 1 : 5 tau:tubulin molar ratio) and incubated at 4 °C for 10 min. WT 4R tau stabilized an average of 7.9 $\pm$ 0.6 spirals per field with a mean spiral length of 570 $\pm$ 18 nm, compared to 2.8 $\pm$ 0.5 spirals per field and mean spiral length of 326 $\pm$ 30 nm in no tau controls (Fig. 3.6C, 3.6D, 3.6E, and Table A.7). All three tau mutants exhibited small but significant reductions in spirals per field relative to WT 4R tau (ANOVA p = 0.0002, Fig. 3.6C and 3.6E). The δK280 and P301L mutants were more markedly compromised, with an average of 4.4 $\pm$ 0.9 spirals per field in δK280 and 3.9 $\pm$ 0.9 in P301L (p = 0.0026 and p = 0.0007 vs WT, respectively). Spiral lengths also differed
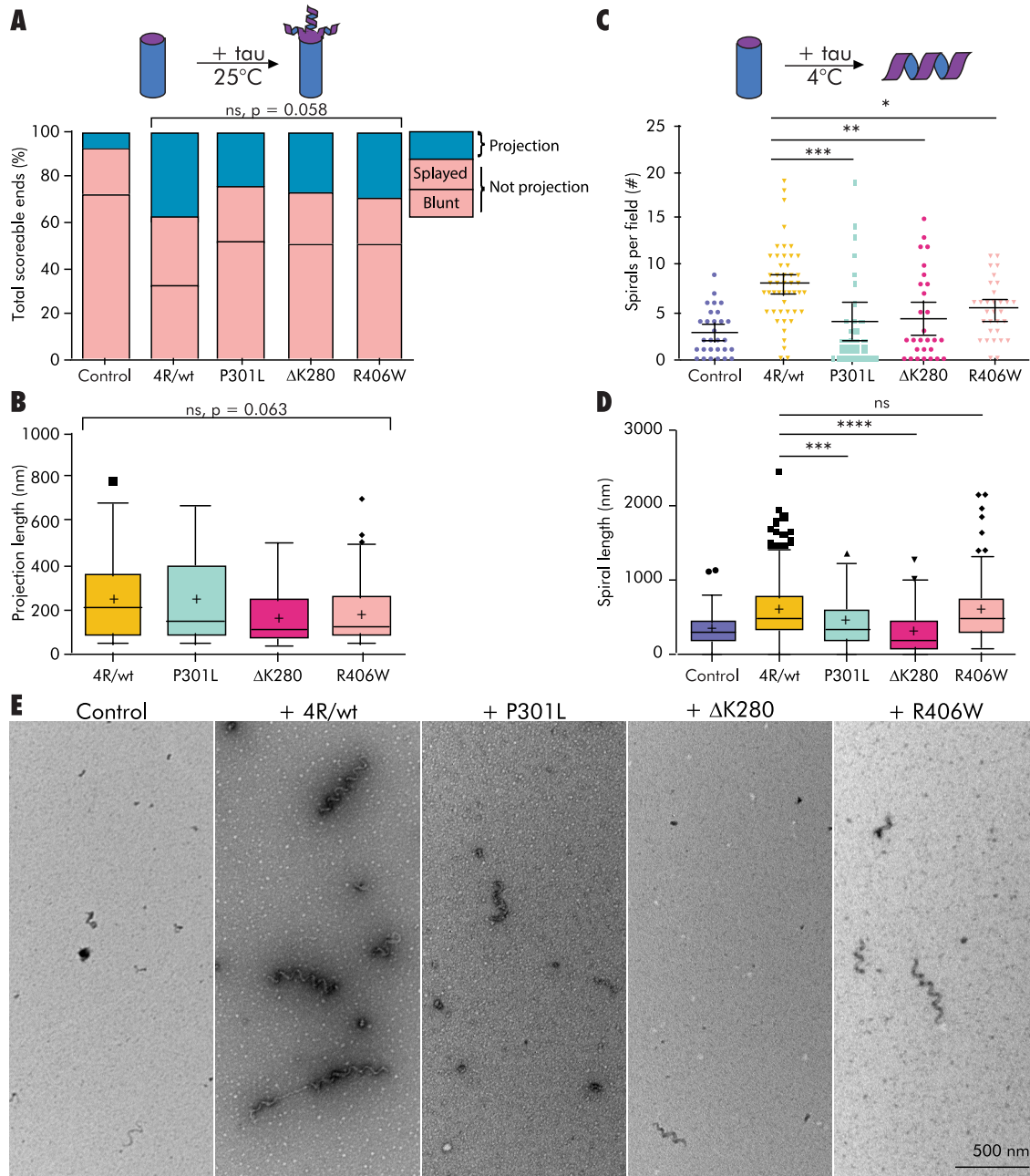
Figure 3.6: **FTDP-17 mutants show differential abilities to stabilize intermediate structures.** (A) and (B), projection frequency (A) and length (B) after decoration of GMPCPP MTs (0.5 uM) with WT 4R tau (4R/wt; 10 : 1 tau/tubulin molar ratio) or tau with the FTDP-17–associated tau mutations P301L, δK280, or R406W. (C)–(E), GMPCPP MTs (0.5 uM) disassembled in the presence of 4R/wt or FTDP-17 mutant tau (1 : 5 tau/tubulin molar ratio) differ in disassembly spiral abundance (C) and length (D). **** p < 0.0001; *** p < 0.001; ** p < 0.01; *, p < 0.05. ns, not significant, p > 0.05. See also Table A.6 and A.7.

amongst the tau mutants (Welch's ANOVA p < 0.0001). δK280 and P301L stabilized spirals with shorter mean lengths (297 $\pm$ 24 nm and 442 $\pm$ 27 nm, respectively) relative to WT 4R tau (p < 0.0001 and p = 0.0004). R406W, while still compromised compared to WT, appeared to be less affected than the other two mutants, stabilizing an average of 5.3 $\pm$ 0.5 spirals per field (p = 0.027 vs WT) that were no shorter than WT (579 $\pm$ 30 nm; Fig. 3.6D and Table A.7). In summary, mutations δK280 and P301L negatively affect tau's ability to stabilize disassembly spirals in terms of both quantity and length, whereas the R406W mutation only negatively impacts spiral quantity.

3.5   Discussion

The best understood role of tau in neuronal cell biology is to establish and maintain the proper regulation of MT dynamics, the growing and shortening events at MT ends. Proper regulation of these events is critical for many cellular functions, as evidenced by the deleterious effects of both MT stabilizing and destabilizing drugs [Jordan and Wilson, 2004]. Indeed, one often suggested model for pathological tau action in Alzheimer's and related tauopathies is the destabilization of axonal MTs, leading to aberrant axonal transport and neuronal cell death [Stokin and Goldstein, 2006, Brunden et al., 2017].

The simplest view of MT assembly involves the stepwise addition of individual tubulin dimer subunits onto the growing end of a MT [Schek et al., 2007]. Indeed, measurements of incremental length increases on very short time intervals (100 ms) during MT assembly using optical tweezers observed length increments of 8.1 nm (the length of a tubulin heterodimer) with only rare length increments greater than 16 nm (the length of two tubulin heterodimers)[Schek et al., 2007]. Alternatively, other assembly data suggested that MT length fluctuates "on sub second timescales, leading to apparent steps of 10–40 nm amplitude" [Kerssemakers et al., 2006], an observation that cannot be explained by

the stochastic addition and subtraction of 8 nm dimers alone. While the addition of tubulin oligomers rather than dimers at MT ends [Bähler et al., 2008] has been proposed to explain this discrepancy, others favor a "dynamic GTP cap" model where rapid growth and shortening at the MT plus end result in protofilaments containing unequal amounts of GTP-tubulin [Howard and Hyman, 2009]. This variation in cap size then adds to the overall variation in growth rate, as incoming dimers or oligomers which have a greater surface area to interact with (i.e. more neighbors) will have a higher probability of forming productive lateral interactions, eventually resulting in straightening and incorporation into the growing MT lattice. By virtue of their curved morphology, GTP tubulin oligomers or protofilaments that have not yet been bound laterally on both sides may also provide a target for end-specific MAPs. Indeed, MAPs including tau [Samsonov et al., 2004, Duan et al., 2017], CLIP-170 [Arnal et al., 2004], and EB1/3 [Guesdon et al., 2016], exhibit differential binding preferences based on the curvature of the tubulin.

We have used GMPCPP tubulin, which is widely used to mimic the pre-hydrolysis state of GTP tubulin, to explore effects of tau on MT assembly/disassembly structural intermediates that might otherwise be too transient to observe. We find that co-incubation of GMPCPP tubulin and tau resulted in the formation of tubulin spirals emanating i) from the ends of pre-assembled MTs at 25 °C, ii) from free tubulin heterodimers dimers at 4 °C, and iii) from free tubulin heterodimers dimers at 34 °C. Spirals were also formed when MTs were disassembled by cold temperature in the presence of 4R tau. Importantly, all of these spiral structures were also observed, albeit at much lower frequencies, in the absence of tau, and have also been observed in previous studies of both GTP and GMPCPP tubulin [Sandoval and Weber, 1980a, Muller-Reichert et al., 1998, Kirschner et al., 1975a], consistent with the notion that that they are bona fide intermediates in the MT assembly/disassembly processes.

Furthermore, we find that 3R and 4R tau isoforms were similarly able to promote MT

assembly intermediates but differ in their ability to stabilize disassembly intermediates, consistent with the well-established ability of 4R to suppress MT shortening events more effectively than does 3R tau [Bunker et al., 2004, Panda et al., 2003, Gustke et al., 1994, Trinczek et al., 1995, Levy et al., 2005, Goode et al., 2000]. Finally, we find that while three tau proteins harboring mutations that cause neurodegeneration and dementia were not compromised in their abilities to stabilize assembly intermediates (MT end projections), they were compromised in their abilities to stabilize disassembly intermediates (disassembly spirals). Collectively, our results indicate that stabilization of assembly/disassembly intermediates is a key feature of physiological tau action.

3.5.1 Intermediates in MT assembly, disassembly, and dynamics

It has been proposed that the primary force at play within the MT lattice is outward longitudinal bending due to the intrinsic curvature of tubulin protofilaments. In general, MT lateral bonds are estimated to be ∼5x weaker in strength than longitudinal bonds [Mandelkow et al., 1991, Vanburen et al., 2002]. As a result, the formation of these higher energy longitudinal bonds presents the larger barrier to MT nucleation, while the breakage of weaker lateral contacts between adjacent protofilaments at MT ends is believed to govern MT disassembly [Mandelkow et al., 1991, Bähler et al., 2008, Vanburen et al., 2002, Sept et al., 2003, Margolin et al., 2011]. Whereas a given region of tubulin heterodimers located within the main body of a MT is constrained in a straight conformation by lateral forces within the MT lattice on both sides, heterodimers/protofilaments near the MT end are less constrained structurally and may therefore realize some of their intrinsic curvature [Janosi et al., 2002], resulting in the gently curving sheets observed at growing MT ends [Chretien et al., 1995, Hyman et al., 1995, 1992]. Indeed, dynamic in-

stability is thought to derive from the GTP hydrolysis event (and the resulting increased lattice strain) that occurs post-incorporation into the MT lattice. At a critical point following GTP hydrolysis, lateral bonds can break and the liberated protofilament(s) can assume their intrinsic curvature and roll up, causing the straight and intact part of the tube to shorten. If the energy released by breaking lateral bonds at MT ends is insufficient to propagate down the length of the tube, or the liberated protofilament(s) engages with some other stabilizing component (such as tau or other MAPs), the result will be a "meta- stable" intermediate state in which the MT end is energetically relaxed but not actively depolymerizing [Janosi et al., 2002, Tran et al., 1997, Waterman-Storer and Salmon, 1997, Odde et al., 1999, Vorobjev et al., 1997]. This state defines a "rescue" event, when a depolymerizing MT switches to a paused or growth state. Thermal fluctuations may push MTs into or out of this meta-stable intermediate state, providing a possible explanation for the temperature- dependence of rescue and catastrophe frequencies [Janosi et al., 2002, Fygenson et al., 1994]. Janosi and colleagues have proposed that a meta-stable intermediate is a potential point for regulation by MAPs through GTP-tubulin association and/or dissociation rate, intrinsic curvature, and/or cooperative binding [Janosi et al., 2002].

The existence of intermediate states in MT assembly and disassembly was first described in early *in vitro* studies of MT nucleation and dynamics [Sandoval and Weber, 1980b, Erickson, 1974, Muller-Reichert et al., 1998, Kirschner et al., 1975a, Weingarten et al., 1974, Kirschner et al., 1974, Sandoval and Vandekerckhove, 1981]). Both rings and "twisted ribbon" (spiral) species form during MT nucleation in the presence of MAP-rich tubulin and GTP over the first ~ 4 minutes of assembly at $37\,°\text{C}$ [Erickson, 1974, Voter and Erickson, 1984, Kirschner et al., 1975a]. These authors noted that the "twisted ribbons"/spirals would provide a more favorable intermediate state than rings, which would have to undergo opening into a single linear oligomer prior to incorporation at

the growing MT end [Kutter et al., 2016]. Indeed, quantitative electron microscopy by Kirschner et al. [1975b], showed that ribbons were the predominant species in the first 30 s - 2 min after GTP addition, and their disappearance coincided with the appearance of increasing numbers of MTs [Kirschner et al., 1975b].

Spirals have also been observed in the earliest phases ($\sim$30 s) (i) when free GMPCPP tubulin dimers are incubated at $4\,^{\circ}$C in the presence of high concentrations of Mg^{2+} [Wang et al., 2005], and (ii) when GMPCPP MTs are disassembled in the presence of high concentrations of Ca^{2+} [Muller-Reichert et al., 1998, Sandoval et al., 1978]. The Mg-induced spirals, which Wang and colleagues proposed are analogous to the outwardly curved tubulin sheets observed at the ends of fast-growing GTP/GDP MTs *in vitro* using purified tubulin [Chretien et al., 1995], in cell extracts [Arnal et al., 2000], and in yeast [Hoog et al., 2011], may constitute an intermediate structure during MT assembly [Wang et al., 2005, Wang and Nogales, 2005]. Different conditions, such as temperature, tubulin concentration, salt concentration, or the presence of MAPs would be predicted to affect the equilibrium between sheet/MT elongation and sheet closure into MTs and could thereby affect global MT dynamics. For example, MAPs EB1 and EB3, which bind specifically to MT plus ends and promote MT growth as well as both rescue and catastrophe, have been shown to increase tubulin sheet formation as well as to promote sheet closure into MTs [Vitre et al., 2008, Maurer et al., 2014]. Interestingly, EBs exhibit preferential binding for the post-hydrolysis but pre- phosphate release GDP-Pi tubulin state (corresponding to the region immediately behind the GTP cap) but exhibit poor binding to GMPCPP MTs [Maurer et al., 2011, 2012].

Structural studies of the Mg-induced spirals described above revealed the existence of two types of lateral contacts, only one of which is present in the mature MT lattice [Wang et al., 2005, Wang and Nogales, 2005]. It seems reasonable to suggest that tube closure requires the conversion of the non-MT mode of lateral contacts to the MT mode

of contacts. We suspect that our tau-induced de novo spirals may possess similar types of lateral contacts as the Mg-induced spirals. The fact that our *de novo* spirals convert into intact MTs less effectively when warmed than do Mg- induced spirals [Wang et al., 2005] suggests that tau may preferentially stabilize the non-MT lateral contacts. Wang et al. [2005] note that the equilibrium between spiral and MT could be shifted based on the concentration of magnesium, with higher concentrations resulting in a longer time before conversion into MTs. In this regard, it is useful to recall that while Mg is normally necessary for MT assembly, it is not required for tau-mediated MT assembly [Devred et al., 2004]. Additionally, it appears that the tau-mediated spirals are more stable than the Mg- induced spirals, since formation of the Mg-induced spirals requires higher GMPCPP tubulin concentrations (18 – 27 uM tubulin compared to 0.9 uM with tau) and higher magnesium concentrations than the corresponding tau-induced spirals (6 – 20 mM Mg vs 0.015 – 4.5 uM tau).

3.5.2 Implications for tau's mechanism of action

The nature of the tau-MT interaction has been investigated for many years. Beginning with the acquisition of tau's amino acid sequence, Lee et al. [1988] proposed that the "repeat region" of tau might serve as a microtubule binding region, a hypothesis that was subsequently supported by direct experimental evidence [Trinczek et al., 1995, Goode and Feinstein, 1994, Butner and Kirschner, 1991, Lee et al., 1989]. Recent cryo-EM structural data [Kellogg et al., 2018], as well as several earlier studies, suggested that tau primarily stabilizes longitudinal tubulin-tubulin interactions [Al-Bassam et al., 2002, Kadavath et al., 2015, Devred et al., 2004]. In contrast, several other studies have argued that tau primarily stabilizes lateral contacts between protofilaments [Kar et al., 2003, Duan et al., 2017]. Our biochemical data suggest that tau promotes both longitudinal and lateral

interactions, as shown by longer spirals and projections (i.e. more longitudinal bonds) and more numerous spirals and projections (i.e. more protofilaments aligning together requires more lateral bonds) in tau- containing samples than in controls. Furthermore, as discussed above, our data suggest that tau may stabilize more than one type of lateral interaction.

How might these interactions mediate tau's effects on MT nucleation and the regulation of MT dynamics? Based on our observations and precedents in the literature, we suggest that tau promotes MT nucleation by first promoting the assembly and/or stabilization of longitudinal tubulin oligomers, which then associate laterally into small, slightly curved GTP-tubulin sheet- or spiral-like structures. It has been shown that tau can bind multiple tubulin dimers at once to form heterogeneous tau-tubulin "fuzzy" complexes that are positively correlated with the rate of MT assembly [Li and Rhoades, 2017]. These assembly intermediates might act as seeds and help to overcome the MT nucleation energy barrier. During MT growth, the sheet- or spiral-like structure may form on, or associate with, growing MT ends, forming new lateral interactions with other similar structures.

Our data suggest that promotion of tubulin sheet closure into a MT is not a tau-mediated event. The tau-stabilized spirals we observed, both at MT ends and free in solution, were inefficient at closing into MTs, especially under conditions promoting the formation of longer spirals (e.g. lower tau:tubulin molar ratios). Perhaps tubulin sheet closure is an intrinsic property of a MT end. In support of the latter perspective, control reactions containing only tubulin and no tau assemble efficiently into bona fide MTs. In contrast, the presence of tau in parallel reactions leads to abundant spirals and many fewer MTs. It is notable that at low concentrations, 4R tau exhibits a much stronger effect on the suppression of MT catastrophe ($\sim$30-fold) than it does on the promotion of MT growth ($\sim$1.5-fold). Perhaps tau primarily serves to promote assembly

and/or stabilization of spirals, an otherwise unstable intermediate that could either move toward tube closure by an intrinsic mechanism or rapid disassembly. This would also be consistent with the observations that addition of tau to MTs at steady state leads to a marked increase in the percentage of MTs that are neither growing nor shortening [Panda et al., 1995].

Finally, our disassembly experiments indicate that 4R tau more effectively stabilizes intermediates generated during MT disassembly than does 3R tau. The mechanisms underlying these differential activities remain unclear. We speculate that the differences may arise from the differential importance of lateral and/or longitudinal bonds in MT assembly and disassembly contexts. For example, 3R tau may be less efficient than 4R tau at stabilizing MT-specific lateral contacts, which would be predicted to primarily affect MT disassembly. On the other hand, the relatively equal abilities of both 3R and 4R tau to promote MT nucleation and assembly may derive from the promotion of longitudinal bonds and possibly also the non-MT type of lateral contacts.

The fact that the ability to stabilize disassembly intermediates appears to be compromised in three well-characterized mutant tau variants suggests that the loss of this ability may contribute to pathological tau action.

3.6   Experimental Procedures

Purification of tau and tubulin.

cDNA expression vectors (pRK) encoding human tau isoforms (2N3R, 0N4R, and 2N4R) were kind gifts from Dr. Kenneth Kosik (University of California, Santa Barbara) and Dr. Gloria Lee (Iowa State University). All tau constructs possessed both amino end, alternatively spliced insertions ("2N") except the pathological tau mutants, which

possessed zero inserts ("0N"). For experiments involving use of FTDP-17 mutants, 0N4R tau was used as the wild-type control since the mutations were in 0N4R background. Prior to experiments with mutants, experiments were performed to verify that 0N4R produced end projections and stabilized disassembly spirals to the same extent as 2N4R tau (data not shown). FTDP-17 tau mutation constructs (δK280, P301L, and R406W) were generated as described in [LeBoeuf et al., 2008] from the 0N4R wild type construct by QuikChange site-directed mutagenesis (Stratagene). All mutations were verified by DNA sequence analysis.

Tau was expressed and purified according to standard procedures described in [Best et al., 2017]. Briefly, tau was expressed in BL21(DE3) pLacI cells (Invitrogen). Bacteria were lysed by French press, boiled for 10 min, and then passed over a phosphocellulose column. Tau-containing fractions were subsequently pooled and then further purified using hydrophobic interaction column chromatography (HisTrap Phenyl HP, GE). Fractions containing pure tau were then pooled, concentrated, and buffer-exchanged into Na-BRB80 buffer (80 mM PIPES, 1 mM EGTA, 1 mM $MgSO_4$, pH 6.8 with NaOH) and stored at $-80\,°C$. Concentration was determined by SDS- PAGE comparison to a tau mass standard, the concentration of which had been established by mass spectrometry amino acid analysis [Panda et al., 2003].

Tubulin was purified as described in [Miller and Wilson, 2010] from bovine brain by three cycles of assembly and disassembly. Further separation of tubulin from microtubule associated proteins was achieved by elution through a phosphocellulose column equilibrated with 50 mM PIPES, 1 mM $MgSO_4$, 1 mM EGTA, 0.1 mM GTP, pH 6.8. Purified tubulin (¿99% pure) was drop-frozen in liquid nitrogen and stored at $-80\,°C$. All tubulin concentrations in this paper refer to the heterodimer (MW = 110,000 Da).

Preparation of GMPCPP microtubules.

GMPCPP microtubules were made as described in [Stumpff and Wordeman, 2007]. Briefly, purified tubulin (20 uM) was assembled in the presence of 1 mM GMPCPP (GpCpp; Jena Bioscience) for 30 min at 34 °C. The resulting microtubules were collected by centrifugation (52,000 x g, 25 °C, 12 min). In order to remove any residual GTP remaining in the microtubule lattice, microtubules were then depolymerized on ice, followed by a second warm assembly in buffer containing GMPCPP (0.5 mM). These GMPCPP microtubules were collected by centrifugation (12 min, 52,000 x g, 4 °C), gently resuspended in warm K-BRB80 buffer (80 mM PIPES, 1mM EGTA, 1mM $MgSO_4$, pH 6.8 with KOH), and then flash frozen in liquid nitrogen and stored at -80 °C in single-use aliquots.

GMPCPP microtubule decoration with tau.

Just prior to each experiment, a fresh tube of the GMPCPP microtubule stock was immediately transferred to a 34 °C water bath for 10 min in order to recover from the frozen state. Microtubules were then diluted into warm assay buffer (80mM PIPES, 1mM EGTA, 1mM $MgSO_4$, pH 6.8 with KOH) supplemented with 1mM DTT. Tau was thawed on ice and then warmed to 25 °C immediately prior to the experiment. Diluted microtubules were added to samples containing tau or buffer and incubated for 10 min at 25 °C.

Formation of GMPCPP tubulin "de novo" spirals.

GMPCPP microtubule stocks were removed from the -80 °C and immediately placed on ice for 30 minutes to depolymerize. This depolymerized tubulin was then diluted to an appropriate working concentration ($\sim$0.9 uM) with cold K-BRB80 supplemented with

1 mM DTT. This working dilution was then added to cold solutions of tau or tau buffer, mixed gently, and co-incubated on ice for an additional 30 minutes. For experiments using higher tubulin concentrations, MTs were prepared fresh as above immediately prior to the experiment and then were diluted to the appropriate concentration as needed.

Formation of GMPCPP tubulin "disassembly" spirals.

GMPCPP microtubules were removed from the freezer, incubated for 10 minutes at $34\,°C$, and then diluted into warm assay buffer as above. Microtubules were then added to cold tau or buffer and incubated at $4\,°C$ for 10 min. For experiments at higher tubulin concentrations, GMPCPP microtubules were prepared fresh as above, added to $25\,°C$ tau or buffer, and then chilled to $4\,°C$ for 60 min.

Transmission electron microscopy (TEM).

Samples were fixed with glutaraldehyde (0.2% final), applied to grids (200 mesh formvar/carbon/copper, Electron Microscopy Sciences), coated with cytochrome C, and then stained with uranyl acetate (1% final). Grids were randomly imaged at 2500X (for microtubule length measurements) and 30,000X (for end scoring, projection, and spiral measurements) magnifications using a JEOL 1230 transmission electron microscope (80 kV) and AMT image capture software. Images were then coded and analyzed blind in order to prevent investigator bias. At least 50 microtubule ends per sample were scored for all decoration experiments.

Statistical analysis.

Statistics were performed using RStudio (version 1.1.423; (RCore Team, 2018; RStudio Team, 2018)), JMP (JMP Pro 14), and Statistics101 (version 4.7, `http://www.`

`statistics101net`)). Note that exact p-values are only reported for p $\geq$ 0.0001.

For supplementary information, please see Appendix A.

Chapter 4

Microtubule and Tubulin Binding and Regulation of Microtubule Dynamics by the Antibody Drug Conjugate (ADC) Payload, Monomethyl Auristatin E (MMAE): Mechanistic Insights into MMAE-ADC Peripheral Neuropathy.

4.1 Permissions and Attributions

The content of chapter 4 is the result of a collaboration with Nichole E. LaPointe, Olga Azarenko, Herb Miller, Christine Genualdi, Stephen Chih, Ben-Quan Shen, Mary Ann Jordan, Leslie Wilson, Stuart C. Feinstein and Nicola J. Stagg, and it will be submitted as written to the journal *Toxicology and Applied Pharmacology*. My contributions to the work were in the experimental investigation, data visualization, and in writing, reviewing, and editing of the manuscript draft.

4.2   Abstract

Auristatins are an especially promising class of anti-cancer microtubule-targeting agents (MTAs), including the recently developed MMAE. Unfortunately, auristatins often exhibit toxic side effects including chemotherapy-induced peripheral neuropathy (CIPN). One approach to reduce CIPN is to more selectively target MTAs to cancer cells by coupling them to antibodies against a tumor cell antigen. However, the MMAE-ADC often still causes CIPN, likely from non-specific uptake of the MMAE-ADC by peripheral nerves. We employed both reconstituted *in vitro* systems and cultured human MCF7 cells to investigate molecular mechanisms underlying MMAE and MMAE-ADC action. *In vitro*, free MMAE bound to soluble tubulin heterodimers with a maximum stoichiometry of ~1:1, bound abundantly along the length of pre-assembled MTs and with high affinity at MT ends, introduced structural defects, suppressed MT dynamics, and reduced the kinetics and extent of MT assembly while promoting tubulin ring formation. In cells, MMAE suppressed proliferation, mitosis and MT dynamics, and disrupted the MT network. The effects of the MMAE-ADC on cells were qualitatively similar to free MMAE, although less potent, which is unsurprising since the antigen recognized by the antibody is not expressed by MCF7 cells (or peripheral neurons, which also lack the tumor antigen). Comparing MMAE action to other MTAs supports the model that differential induction of CIPN by different MTAs is driven by the precise mechanism(s) of each individual drug-MT interaction. Our data provide novel insights into molecular mechanisms underlying MMAE and MMAE-ADC action and their induction of CIPN.
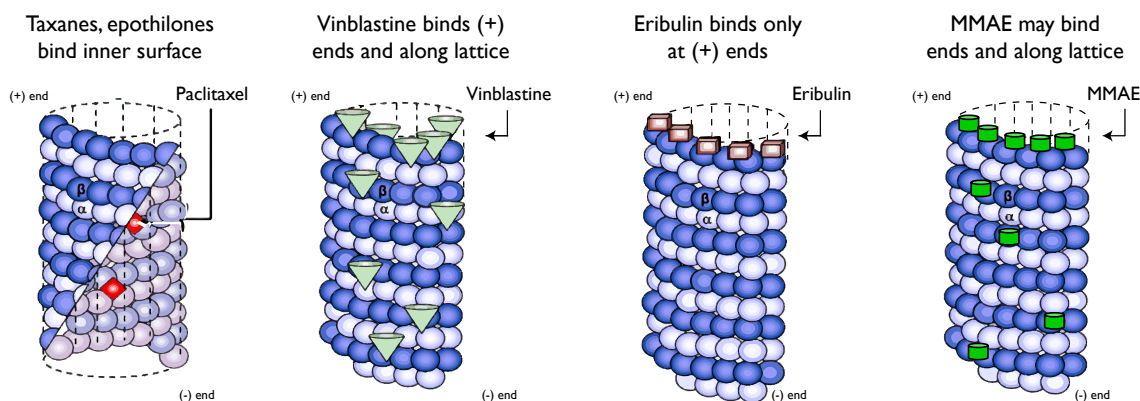
Figure 4.1: Graphical abstract showing proposed mechanism of MMAE-MT binding and comparison to other commonly used chemotherapy drugs, including taxanes and epothilones, vinblastine, and eribulin. Similar to vinblastine, MMAE may bind both at MT ends as well as along the lattice.

4.3   Introduction

Microtubule targeting agents (MTAs) are important chemotherapeutic drugs used to combat many types of cancer [Argyriou et al., 2012, 2011, Carlson and Ocean, 2011, Windebank and Grisold, 2008]. Mechanistically, MTA action derives from their ability to alter microtubule (MT) dynamics and/or regulatory mechanisms controlling MT dynamics and MT-based transport, which can, in turn, lead to tumor cell death [Argyriou et al., 2012, Field et al., 2014, Jordan and Wilson, 2004, Poruchynsky et al., 2015].

One especially promising class of MTAs are the auristatins, analogues of naturally occurring peptides called dolastatins that were first isolated from the sea hare Dolabella auricularia [Pettit et al., 1987]. Bai et al. [1990] demonstrated that the potent cytotoxicity and inhibition of proliferation exhibited by dolastatin 10 (in the picomolar range) correlated with its ability to inhibit MT assembly and tubulin-dependent GTPase activity. The net effect was G2/M cell cycle arrest and apoptosis. Initial clinical trials of dolastatin 10, however, were problematic because of toxic effects [Margolin et al., 2001, Mirsalis et al., 1999, Newman et al., 1994, Pitot et al., 1999]. Monomethyl auristatin E

(MMAE) is a more recently developed member of the auristatin class of MTAs that also shows very potent cytotoxicity.

While MTA chemotherapeutics exploit the critical importance of MTs in tumor cells, MTs are also essential for many functions in non-target tissues, including the peripheral nervous system. MTs are important for the maintenance of highly elongated neuronal morphologies and axonal transport, the rapid movement of cargo between neuronal cell bodies and distal nerve endings [Morfini et al., 2009]. As a result, the peripheral nervous system, which lacks the protection conferred upon the central nervous system by the blood-brain barrier, is highly susceptible to deleterious MTA-induced effects. Among the most frequent and serious side effects of MTA treatment is chemotherapy-induced peripheral neuropathy (CIPN), which manifests with symptoms ranging from numbness and tingling to hypersensitivity and severe neuropathic pain. CIPN symptoms generally exhibit a "stocking/glove" pattern, beginning at the most distal extremities, such as the fingertips and toes, and progressing proximally toward the trunk, suggesting that the longest axons are the most vulnerable [Argyriou et al., 2012, Carlson and Ocean, 2011, Windebank and Grisold, 2008]. The symptoms of CIPN can be sufficiently debilitating to limit treatment, and in some cases, can be life threatening. The only current strategies to address MTA-induced CIPN are dose delay, dose reduction, or discontinuation of treatment. Though MTAs may have a broad application in anti-cancer strategies, CIPN poses a major obstacle to successful clinical anti-cancer efforts.

One strategy to manage the systemic toxicity of these potent drugs is to covalently couple them to an antibody directed to an antigen expressed uniquely on the surface of the target tumor cells. These antibody-drug complexes are known as antibody-drug conjugates (ADCs) and include the MMAE ADCs Brentuximab vendotin and polatuzumab vendotin (Polivy), which are currently FDA-approved for treatment of some lymphomas. Upon internalization into the tumor target cells, the MMAE drug payload is released from

ADCs through proteolytic cleavage of the dipeptide linker (valine-citrulline) by cathepsin B. However, despite the promise of targeted design, many ADCs continue to exhibit a surprisingly high incidence of adverse effects. A recent meta-analysis found that these adverse effects are specific to the conjugated drug, i.e. the "payload" [Masters et al., 2017]. In the case of an ADC with MMAE as the payload, peripheral neuropathy is a major adverse effect that can be both severe and dose limiting, and further, it has been shown to be independent of the target of the antibody [Saber and Leighton, 2015]. Additionally, the significant clinical incidence of peripheral neuropathy with MMAE-conjugated ADCs was not predicted in earlier non-clinical toxicology studies [Stagg et al., 2016]. However, through investigative assessments, the peripheral neuropathy observed in patients has been attributed primarily to nonspecific uptake of the ADC by peripheral nerves and subsequent release of its MT targeted payload, (i.e., MMAE), leading to nerve degeneration [Stagg et al., 2016]. Release of free MMAE systemically has also been observed in patients and in nonclinical studies and could potentially be taken up by peripheral nerves, but the levels of free circulating drug are very low and unlikely to have much of an effect.

As there is still quite substantial exposure of the peripheral nerves to the MMAE payload as a result of the nonspecific uptake of the ADC, understanding how MMAE interacts with MTs leading to peripheral neuropathy is of great interest. One often-stated hypothesis for MTA-induced CIPN posits that the drugs interfere with normal MT-dependent axonal transport, which in turn initiates subsequent neurodegeneration. Interestingly, despite sharing the same molecular target (MTs), some of the newer MTAs exhibit reduced incidences and severities of CIPN. Investigations into this observation suggested that these differential frequencies of severe CIPN might derive from the different binding sites MTAs bind to on MTs and/or soluble tubulin and their resultant differential effects on MT dynamics [Benbow et al., 2017]. It has become increasingly

clear that gaining a more mechanistic understanding of MTA binding and regulation of MT dynamics is key to understanding both normal MT action and the resultant cellular and clinical consequences of misregulation by MTAs. Genualdi et al. [2020] analyzed published data on in vitro microtubule (MT) properties for different MTAs that cause varying levels of CIPN in patients and discussed possible mechanisms related to interaction with tubulin and MTs for the reduced CIPN with some MTAs. Eribulin, vinorelbine and vinfluinine, which all have less severe CIPN than the vinca alkaloids or taxanes, have unique MT properties consisting of reduced affinity and limited binding to MTs (i.e. bind only to the ends and not along the length). Binding more potently to tubulin in the absence of neuronal $\beta-$III tubulin was also observed with eribulin and may suggest specificity for tumor tubulin over neuronal tubulin.

The current study was designed to investigate the binding of MMAE as a free drug or as an ADC to MTs and free tubulin subunits, and its effects upon MT dynamics and MT morphology as well as cell proliferation, cell cycle regulation and the generation of mitotic spindle abnormalities in cultured human cells. In combination with comparisons made to other MTAs, our data provide further insights into the molecular mechanisms underlying normal MMAE action as well as those governing MMAE ADC-induced peripheral neuropathy.

4.4   Results

4.4.1   MMAE action on purified tubulin heterodimer subunits and microtubules

4.4.1.1   MMAE binds to soluble tubulin heterodimers with a maximum stoichiometry of ~1:1.

To determine the binding stoichiometry of MMAE to free tubulin subunits, soluble
MAP-free tubulin heterodimers were incubated with ^{3}H-MMAE for 12 min at 30 °C, and
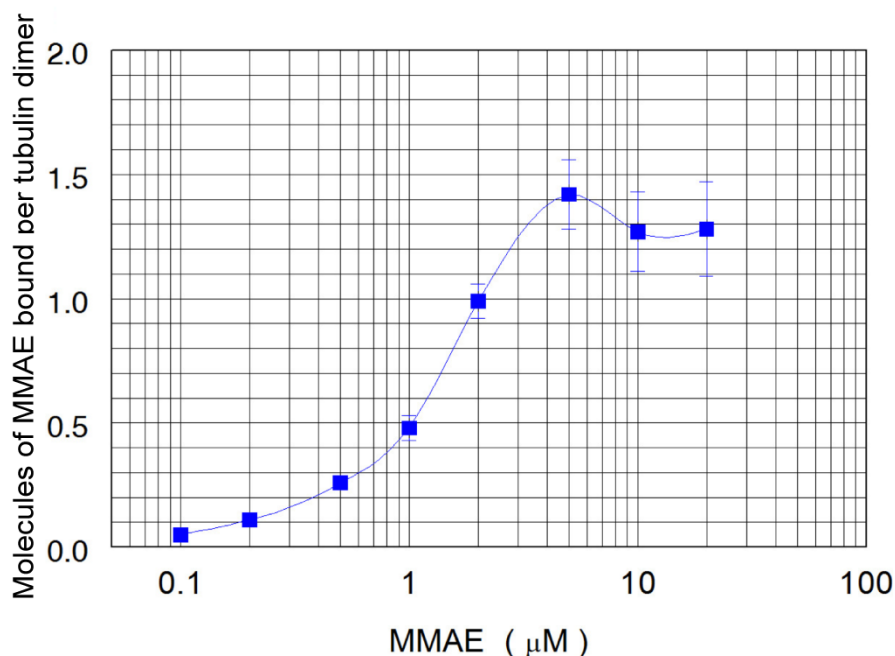then tubulin-bound drug was separated from free drug by size exclusion chromatography.

Figure 4.2: **MMAE binding to soluble tubulin heterodimers.** H^3-MMAE (0.1
– 20 uM) was incubated with soluble, MAP-free tubulin for 12 – 15 min at 30 °C,
and then tubulin and bound MMAE was separated from unbound MMAE by size
exclusion chromatography. MMAE bound with an apparent K$_d$ = 1.6 uM and a
maximum stoichiometry of ~1.3 drug molecules per tubulin heterodimer. Each data
point is the average from 3 – 4 experiments.

As shown in Figure 4.2, MMAE binding saturated at ~1.3 MMAE molecules/tubulin heterodimer and had an apparent K_d of ~ 1.6 uM, suggesting that MMAE binds to tubulin heterodimer subunits at a ratio of approximately 1:1.

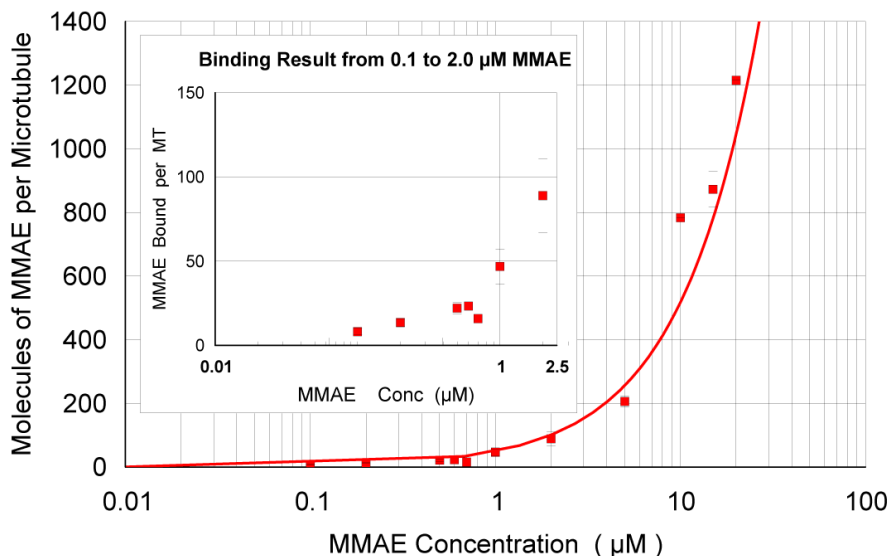### 4.4.1.2 MMAE binds with high affinity to MT ends and lower affinity along the MT length

Figure 4.3: **MMAE binding to microtubules.** H^3-MMAE (0.1 – 20 uM) was incubated with microtubules made from MAP-rich tubulin for 6 min at 30 °C, and microtubule-bound MMAE was separated from unbound MMAE by centrifugation. The ratio of H^3-MMAE to tubulin in the pellet was determined. Each point is the average of 2-4 experiments (inset) or 1-4 experiments (overall), and the line shows a best fit. See 4.7 for additional experimental details.

Next, the interaction between MMAE and pre-assembled MTs was investigated. MAP-rich tubulin was polymerized to steady-state at 30 °C and then incubated with ^{3}H-MMAE for 6 min, after which MT-bound drug was separated from free drug by centrifugation. Control experiments demonstrated that the brief 6 min incubation with MMAE did not affect the mass of MTs recovered after centrifugation although it did result in a modest drop in A$_{350}$ signal (Fig. B.1), indicating that this brief treatment of

MTs with MMAE causes a structural alteration that affects light scattering without affecting the ability to pellet. As shown in Figure 4.3, even at the highest concentration of MMAE tested (20 uM), MMAE binding did not even begin to saturate. In fact, even at this high concentration, the drug bound to only ∼20% of the total tubulin present in the MT polymers. These data indicate a low affinity, high stoichiometry binding of MMAE along the length of the MTs. Additionally, careful examination of the data from the low MMAE concentration part of the curve (inset) suggests a limited number of high-affinity (sub-micromolar) MMAE binding sites, most likely corresponding to the MT ends. This MMAE binding pattern is quite similar to that of vinblastine binding to MTs [Wilson et al., 1982].

4.4.1.3   MMAE introduces structural defects at both MT ends and along the MT length that may expose additional binding sites

The high abundance of MT binding sites for MMAE prompted us to examine the structural effects of MMAE upon pre-assembled MTs. MAP-rich MTs were prepared and incubated with MMAE as above and then examined by transmission (TEM). As shown in Figure 4.4, MMAE-treated MTs exhibited both peeling of protofilamentous structures at their ends and marked "bubble-like" defects along their lengths - the latter structures appear to be protofilaments that have loosened from the MT body in an unusual way and bulge or protrude out in a bubble or partial loop that is connected linearly (but not laterally) to the other seemingly normal protofilaments. This is especially clear in the 5 uM MMAE images (Fig. 4.4). These observations are consistent with recent work indicating that MMAE can interfere with lateral tubulin-tubulin contacts in MTs [Waight et al., 2016]. To the best of our knowledge, the observed bubble-like defects along the MT lengths are unique among all other MTAs. Additionally, many MTs appeared "wavy" as opposed to the usual rigid rod morphology. Finally, some MTs appeared severely
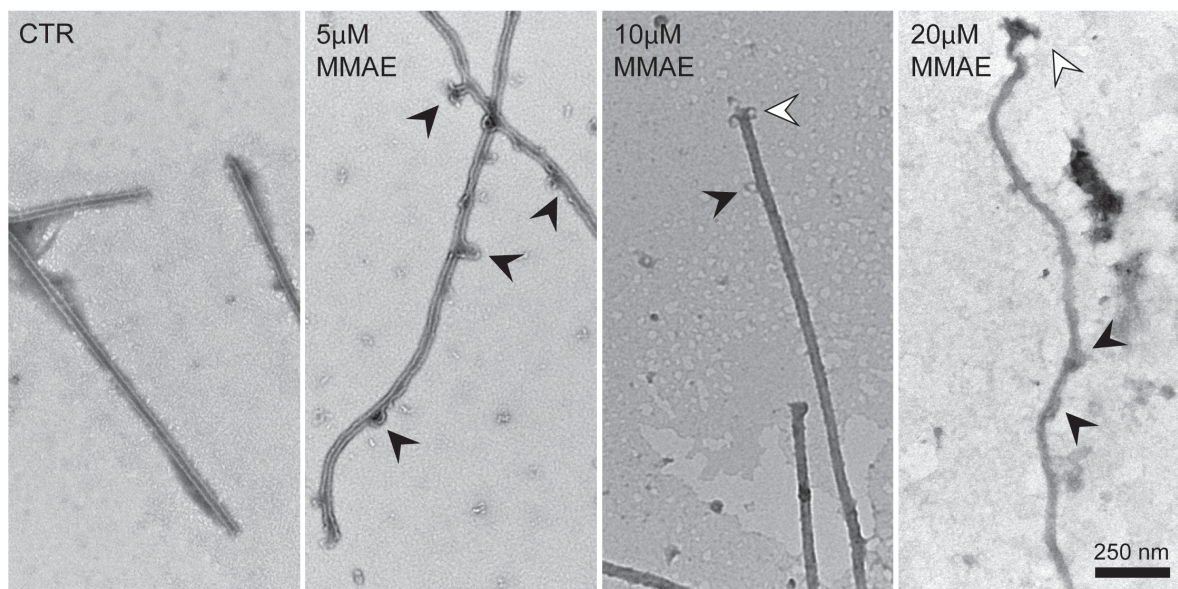
Figure 4.4: **Microtubules exposed to MMAE post-assembly show structural defects at their ends and along their lengths.** Microtubules exposed to MMAE for 6 minutes post-assembly have peeling ends (white arrows) and defects along their lengths (black arrows). The microtubule preparation and incubation time are identical to those used in in the microtubule binding experiments shown in Fig. 4.3. See Fig. B.1 for corresponding light scattering data.

affected while others in the same field appeared relatively normal, raising the possibility that MMAE action along the MT length may be cooperative, i.e., that MMAE binding may cause structural effects that expose additional MMAE binding sites. This would be consistent with the lack of binding saturation observed in Figure 4.3, even at the highest MMAE concentrations tested.

4.4.1.4   MMAE potently suppresses MT dynamics

The fundamental action of most MTAs is to modulate (usually to suppress) the dynamic behaviors of MTs, although different MTAs reportedly affect different individual parameters underlying this behavior (reviewed in [Jordan and Wilson, 2004]. Therefore, we evaluated the effects of MMAE upon the regulation of MT dynamics using MTs

composed of purified, MAP-free tubulin. MTs were assembled to equilibrium ($32\,°C$, 30 min) from seeds attached to glass coverslips, in the presence or absence of 100 nM MMAE. Under these conditions, tubulin was present in vast excess over drug. Key parameters of MT dynamics were quantified, including the (i) rate of growth and shortening, (ii) duration of growth and shortening events, (iii) fraction of time spent growing, shortening or attenuated, (iv) frequency of rescues (transitions from shortening to attenuation or growth) and catastrophes (transitions from growth or attenuation to shortening), and (v) overall "dynamicity", which is the total length grown and shortened by a MT divided by the total observation time of that MT.

As shown in Table 4.4.1.4 (right side of table), the most marked effects of MMAE on bovine MT dynamics were to reduce the growth and shortening lengths per event. MMAE also reduced the percentage of time MTs spent growing, increased the percentage of time that MTs spent in an attenuated state, increased the duration of attenuation events, and greatly reduced overall dynamicity. Box plot presentations of these data are presented in Fig. B. Finally, although MMAE trended towards decreasing shortening rate, growth rate and catastrophe frequency, the differences did not reach statistical significance.

4.4.1.5 MMAE potently reduces the kinetics and extent of MT assembly

In order to gain additional insights into the mechanisms of MMAE action, we next asked what effects MMAE might have upon the kinetics and steady-state products of MT assembly when it is present during MT assembly. MAP-rich tubulin was mixed on ice with varying concentrations of MMAE, and then transferred to $30\,°C$ to initiate MT assembly. As shown in Figure 4.5A, the presence of MMAE led to a concentration-dependent reduction in light scattering (A_{350}), with an IC_{50} of $\sim$3 uM. These same data are plotted in a normalized manner in Figure B.3, to better define the half time ($t_{1/2}$) for maximal assembly. A similar concentration-dependence was observed on the

Parameter	MCF7 Cells (MAP-rich)				MAP-free bovine brain tubulin			
	Control	MMAE, 0.5 nM (% change)	Difference in Means (95% CI)	p-value	Control	MMAE, 100 nM (% change)	Difference in Means (95% CI)	p-value
Growth rate (μm/min)	9.7 ± 0.20	7.5 ± 0.15 (-23%)	2.19 (1.71, 2.68)	<0.0001	1.1 ± 0.05	0.97 ± 0.07 (-12%)	0.13 (-0.05, 0.30)	NS
Growth length (μm)	1.8 ± 0.07	1.2 ± 0.05 (-30%)	0.52 (0.35, 0.79)	<0.0001	2.9 ± 0.31	1.6 ± 0.13 (-45%)	1.30 (0.68, 1.98)	0.0002
Growth duration (min)	0.19 ± 0.007	0.18 ± 0.007 (-6%)	0.01 (-0.01, 0.03)	NS	2.8 ± 0.30	1.9 ± 0.18 (-32%)	0.89 (0.24, 1.58)	0.009
Shortening rate (μm)	14.8 ± 0.5	11.0 ± 0.3 (-26%)	3.81 (2.65, 5.00)	0.0001	12.3 ± 1.9	9.1 ± 1.3 (-26%)	3.20 (-1.17, 7.96)	NS
Shortening length (μm)	1.8 ± 0.11	1.1 ± 0.06 (-38%)	0.69 (0.46, 0.93)	<0.0001	3.8 ± 0.56	2.2 ± 0.31 (-43%)	1.59 (0.40, 2.87)	0.012
Catastrophe frequency (#/min/MT)	3.0 ± 0.16	2.4 ± 0.15 (-20%)	0.61 (0.19, 1.03)	0.004	0.31 ± 0.06	0.24 ± 0.04 (-22%)	0.70 (-0.06, 0.21)	NS
Rescue frequency (#/min/MT)	9.5 ± 0.41	10.1 ± 0.37 (+6%)	-0.61 (-1.67, 0.48)	NS	2.5 ± 1.2	3.4 ± 1.4 (+35%)	-0.88 (-4.62, 2.66)	NS
Attenuation duration (min)	0.12 ± 0.004	0.16 ± 0.006 (+32%)	-0.04 (-0.05, -0.03)	<0.0001	0.79 ± 0.07	1.4 ± 0.15 (+79%)	-0.63 (-0.96, -0.31)	0.0002
Percent time growing (%)	49	40 (-18%)		-	79	49(-38%)		-
Percent time shortening (%)	24	19(-21%)		-	6	6		-
Percent time attenuated (%)	27	41(+52%)		-	15	45(+200%)		-
Dynamicity (μm/min/MT)	8.2 ± 0.27	5.0 ± 0.22 (-38%)	3.15 (2.47, 3.84)	<0.0001	1.7 ± 0.18	0.95 ± 0.13 (-44%)	0.77 (0.35, 1.22)	0.0008

Table 4.1: **Effects of MMAE on dynamic instability of microtubules in MCF7 cells or in vitro microtubules from MAP-free bovine brain tubulin.** Control (vehicle) and MMAE columns show mean ± s.e.m, and MMAE columns also indicate percent change from control and its direction. Statistical analysis of the difference between the means was determined, and the 95% CI for the difference and the p-value are indicated (see section 4.7).

110

mass of pelletable material harvested at the 60-min plateau time point (Fig. 4.5B). Importantly, since the tubulin concentration in these reactions was ∼16 µM while the IC_{50} for MMAE was ∼3 uM, these data indicate that the mechanism of MMAE action is sub-stoichiometric relative to tubulin, consistent with at least a subset of MMAE action being mediated at MT ends.

For comparison, we also measured the activity of an MMAE-Antibody Drug Conjugate (ADC; CNJ2985-gD-vc-MMAE, which recognizes an epitope expressed on the HSV-1 viral envelope) in this assay (Fig. B). The MMAE ADC contains ∼3.5 MMAE drugs per antibody. We assembled MTs as above in the presence of 1 uM or 5 uM MMAE-ADC (equivariant to 3.5 uM and 17.5 uM of free MMAE). The presence of the MMAE-ADC resulted in very high A_{350} light scattering signals, possibly indicative of nonspecific aggregation, and we were therefore unable to assess the effects of the ADC on MT assembly by this method. As an alternative approach, we centrifuged the samples at the 60-min time point and then used SDS-PAGE to determine what proportion of the pelleted material was tubulin. By this method, we found that 1 uM and 5 uM MMAE-ADC only reduced MT mass by 7% and 18%, respectively, compared to 28% and 77% with 1 uM and 5 uM free drug, respectively. Taking into account that there are ∼3.5 MMAE molecules per antibody, the simplest interpretation is that MMAE-ADC is approximately 14-fold less potent upon MT assembly compared to its free form. The difference in activities could result from greatly reduced accessibility of MMAE to its targets (tubulin and MTs) when it is conjugated to an antibody. The observed low activity of ADC on MT assembly might be due to a low level of MMAE released from ADC in the reaction mixture.
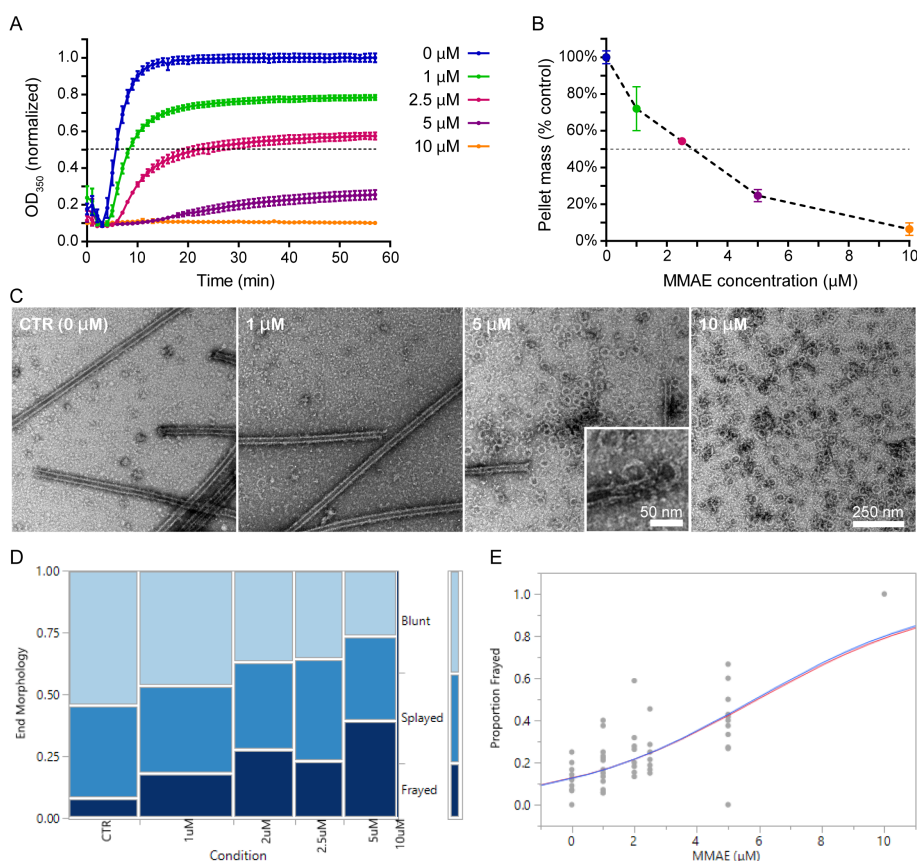
Figure 4.5: **MMAE inhibits the assembly of MAP-rich tubulin in vitro and
alters the morphology of MT ends.** Assembly mixes containing MAP-rich tubulin
($\sim$30 uM), 1 mM GTP, and various concentrations of MMAE were prepared on ice
and then transferred to a 30 °C spectrophotometer. A) Microtubule assembly was
monitored by light scattering at 350 nm. B) After 60 min, samples were centrifuged
to collect microtubules and the polymer mass was determined. Each data point in A
and B is the average of 2-4 experiments normalized to the pooled average of the control
(no MMAE) values. The dotted line indicates 50% of the control value. C) Samples
prepared for transmission electron microscopy in parallel with centrifugation show
an MMAE concentration-dependent transition from microtubules to tubulin rings.
Scale bar = 250 nm. Note that the 10 uM data show that the tubulin rings do not
scatter or sediment during centrifugation. D) MT end morphologies were categorized
as blunt, splayed, or frayed and scored in the absence (CTR) or presence of varying
concentrations of MMAE. The width of each set of bars is proportional to the total
number of ends scored in each condition (CTR n=184; 1 uM n=243; 2 uM n=160; 2.5
uM 126; 5 uM n=139; 10 uM n=2). The bar at the right indicates the proportions
across all experimental conditions. E) Logistic regression shows that the proportion
of frayed ends increases as a function of MMAE concentration (blue line; p <0.0001;
log-odds increase 0.33 per uM, 95%CL 0.24-0.43). Each point represents an individual
imaging field. Excluding the 10 uM data point had only minor effects (red line) and
did not change the interpretation. Data in D and E were pooled from 3 independent
experiments.

4.4.1.6 During MT assembly, MMAE reduces the length of assembled MTs, alters the morphology of MT ends, and promotes formation of tubulin rings.

To further characterize the concentration-dependent effects of MMAE on MAP-rich MT assembly in isolated MTs, we imaged MT assembly products at the 60-min time point in the above experiment by TEM (Fig. BC). Control samples had normal, linear MT structures with regular end morphologies (blunt or slightly splayed). In contrast, the presence of MMAE during MT assembly led to (i) a marked reduction in MT length (with a 50% reduction at $\sim$0.5 uM; Fig. B.5), (ii) an increase in the proportion of MT ends with an abnormal "frayed" appearance (Fig. BC-E), and (iii) a shift from MTs to tubulin ring structures (Fig. BC; Fig. B.6). Indeed, MTs were exceedingly rare at 10 uM drug. The formation of tubulin rings is consistent with earlier reports examining the parent compound, dolastatin 10 [Bai et al., 1995].

4.4.2 MMAE action in cultured MCF7 cells

Given the above-described insights into MMAE action in an isolated system, we next sought to mechanistically examine MMAE action in a cellular system. We chose MCF7 cells stably expressing EGFP-tubulin, as this is a well-characterized system in which we have an established methodology for assessing the cellular effects of MTAs. We evaluated the action and potency of MMAE as a free drug and as an ADC (CNJ2985-vc-MMAE). Cellular uptake of the ADC is followed by intracellular enzymatic cleavage of the vc peptide linker, releasing free drug. Importantly, since the epitope recognized by CNJ2985-vc-MMAE is not expressed on MCF7 cells, any effects on these cells are likely due to non-specific cellular uptake.

In order to ensure that experiments were performed when the intracellular drug con-
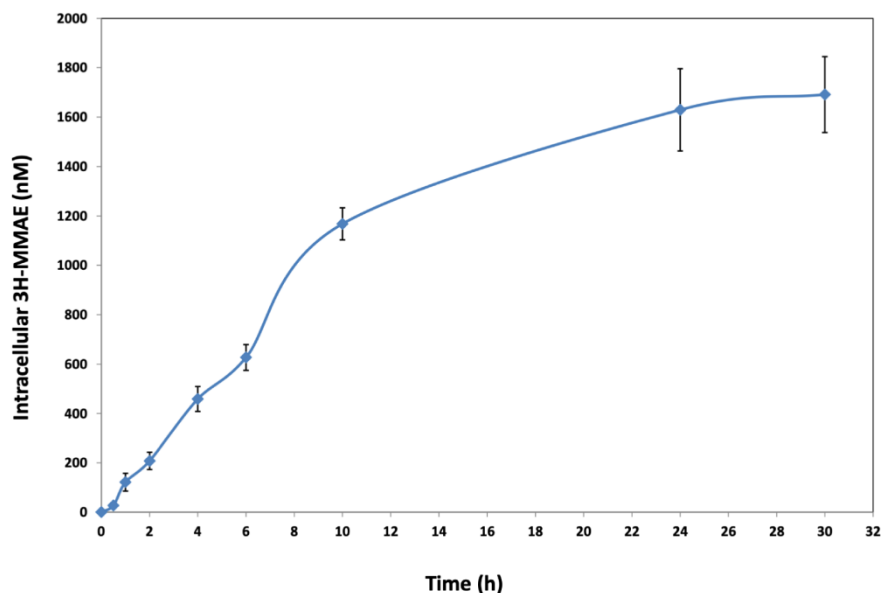
Figure 4.6: **Intracellular uptake of free MMAE.** MCF7 cells were incubated
with 10 nM tritiated MMAE ($[^3H]$-MMAE). At the indicated time points, samples
of cells were rinsed with fresh buffer, scintillation fluid added, and then radioactivity
measured in a scintillation counter. Data are from 4-5 experiments.

centration had reached steady state, we first determined the rate of MMAE uptake.
Cells were plated and treated with 10 nM ^3H-MMAE, and then the cellular drug content
was determined as a function of time. As shown in Figure 4.6, MMAE accumulation
proceeded relatively slowly, requiring 24 hr of exposure to reach a plateau.

4.4.2.1   MMAE, as a free drug but not as an ADC, potently inhibits cell proliferation, induces mitotic arrest, and alters spindle morphology in MCF7 cells

We first determined the effects of free MMAE upon cell proliferation using a sul-
forhodamine B (SRB) assay following a 96 hr drug incubation. The percent inhibition of
proliferation was determined over a range of MMAE concentrations. As shown in Figure
4.7, MMAE potently inhibited cell proliferation with an IC_{50} of 0.9 nM $\pm$ 0.24 nM.

Next, we examined the effects of MMAE upon the mitotic index, defined as the
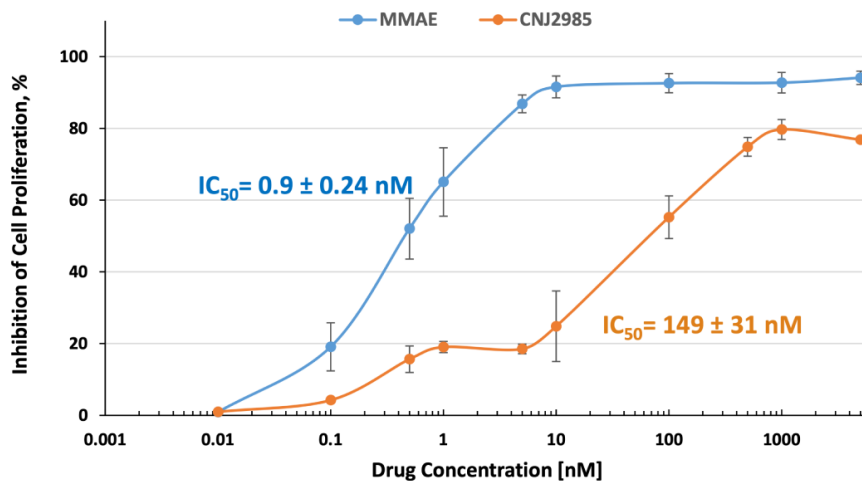
Figure 4.7: **Inhibition of MCF7 cell proliferation by MMAE as a free drug
(MMAE) and as an antibody- drug conjugate (CNJ2985).** The IC_{50} for cell
proliferation at 96 hours was 0.9 ± 0.2 nM for MMAE and 149 ± 31 nM for CNJ2985.

percentage of cells in mitosis at any given time. As shown in Figure 4.8A, MMAE
markedly and concentration-dependently increased the percentage of cells in mitosis,
with an IC_{50} of 0.5 nM. The maximum mitotic index observed was 55% at $\geq$ 10 nM
MMAE (Fig. 4.8B). Complementary cell cycle analyses demonstrated that free MMAE
strongly induced G2/M arrest in a concentration-dependent manner. Specifically, 50%
of the cells were blocked in G2/M after 24 hr of incubation at 1 nM MMAE (Fig. 4.8C).

Finally, we examined the effects of MMAE upon the morphology of the interphase
MT network and the mitotic spindle MTs. As shown in Figure 4.9, MMAE altered MT
structure in interphase cells and caused mitotic spindle abnormalities in a concentration-
dependent manner, beginning at very low concentrations (0.5 nM). Higher concentrations
of MMAE led to complete MT depolymerization and cell death (Fig. B.7).

The MMAE ADC also inhibited cell proliferation, increased the percentage of cells
in mitosis, altered the interphase MT network, and caused mitotic spindle abnormalities
similarly to free MMAE but with greatly reduced potency relative to the free drug. The
ADC inhibited cell proliferation with an IC_{50} of 149 ± 31 nM, 165-fold less potently than
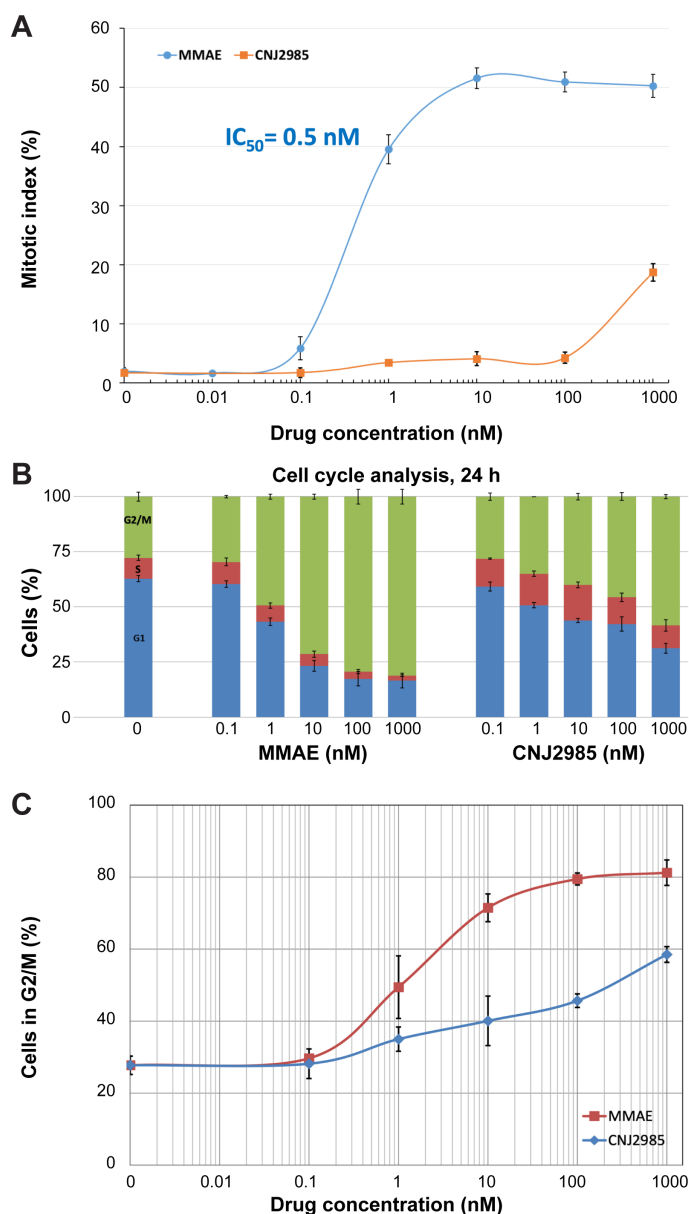
Figure 4.8: **Free MMAE affects mitotic index, cell cycle stage, and induces G2/M arrest at much lower concentrations than the MMAE-ADC.** A) Mitotic arrest at 24 hr in MCF7 cells incubated with MMAE as a free drug (MMAE) or an MMAE-ADC (CNJ2985). Free MMAE had an $IC_{50} = 0.5$ nM, and the maximum mitotic index (defined as the percentage of cells arrested in any stage of mitosis) was 55% at concentrations ≥ 10 nM. Mitotic arrest also occurred with the MMAE-ADC but did not reach a plateau at the concentrations tested, preventing an estimate of the IC_{50}. B) Cell cycle analysis after 24 h incubation with free MMAE or CNJ2985. C) Strong induction of G2/M arrest in MCF7 cells by MMAE in a concentration-dependent manner. After 24 hr, $\sim$50% of cells treated with 1 nM free MMAE are blocked in G2/M. CNJ2985 also induced G2/M arrest, but the effect did not reach a plateau at the concentrations tested.

free MMAE (Fig. 4.7). With respect to inhibition of mitosis, the ADC also increased the percentage of cells in mitosis, but 3-4 orders of magnitude less potently than the free drug (Fig. 4.8A). Because the effect of the ADC did not reach an upper plateau at the concentrations tested here, its IC_{50} could not be determined. Similarly, cell cycle analyses showed greatly reduced potency for the MMAE ADC compared with free MMAE (Fig. 4.8B), and induced G2/M arrest 2-3 orders of magnitude less potently than the free drug (Fig. 4.8C). The ADC had a moderate effect on interphase MTs, producing similar spindle abnormalities as free MMAE but only at much higher concentrations (200-1000 nM ADC was comparable to 0.5 nM free drug). Spindle abnormalities were not observed with ADC at 200 nM (but were obvious with free drug at 0.5 nM). At 1 uM, the MMAE ADC produced similar abnormalities to those of 0.5 nM MMAE (Fig. 4.9). Collectively, these results demonstrate that MMAE potently affects MCF7 cell proliferation, mitosis, and the integrity of the MT network both during interphase and mitosis. The effects of the MMAE ADC, although much less potent than the free drug, were qualitatively similar. As MCF7 cells lack the epitope that is recognized by the antibody, this suggests that some small subset of the MMAE ADC was non-specifically taken up into the cells and free MMAE released as a result of intracellular proteolysis. Since free MMAE acts on cells in the nM range and the MMAE ADC is 2-3 orders of magnitude less potent than the free drug in cells, we reason that the intracellular concentration of the MMAE resulting from non-specific uptake of the ADC is on the order of pM concentrations.

4.4.2.2 MMAE potently suppresses MT dynamics in cells, similar to its effects on purified tubulin in vitro.

We sought to quantitate the effects of MMAE upon the dynamics of cellular MTs. MCF7 cells were grown on coverslips and treated for 24 hr with 0.5 nM MMAE. We chose this drug concentration because it was the IC_{50} for mitotic block, and because af-
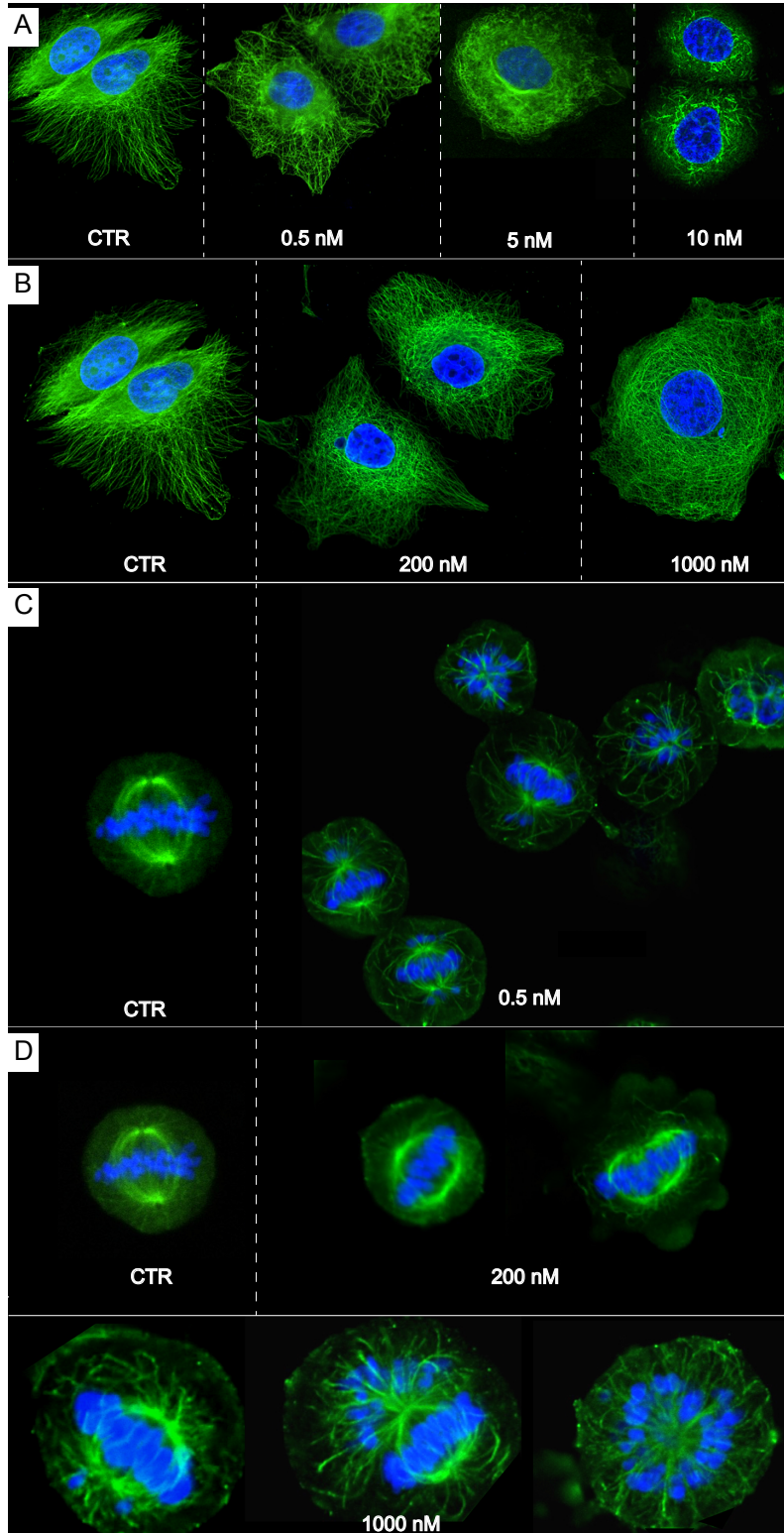
Figure 4.9: **Free MMAE alters the interphase MT network and mitotic spindle at much lower concentrations than the MMAE-ADC.** A) Free MMAE alters the interphase MT network (anti-α-tubulin, green) at concentrations > its mitotic IC_{50} (0.5 nM), similar to other MT-depolymerizing drugs (DNA stained with DAPI, blue). B) The MMAE-ADC (CNJ2985) has a moderate effect on interphase MTs at concentrations > 200 nM. C) Free MMAE induces spindle abnormalities at its mitotic IC_{50}, similar to other MT depolymerizing drugs. D) Top: 200 nM CNJ2985 does not induce significant spindle abnormalities. Bottom: Spindle abnormalities induced by 1000 nM CNJ2985 are similar to those produced by free MMAE at ~0.5 nM.

ter 24 hr at this concentration, cells maintained the flat morphology required for effective MT imaging. Following exposure to drug or vehicle, MTs were imaged by time-resolved confocal microscopy. As shown in Table 4.4.1.4, MMAE suppressed both the rate and length of growth and shortening events, greatly increased the duration of individual attenuation events, and increased the percentage of time MTs spent in an attenuated state. It also decreased catastrophe frequency without affecting rescue frequency. The strong suppressive effects of MMAE on MT dynamics were also apparent in overall dynamicity. Box plot presentations of these data are presented in Figure B.

4.5   Discussion

We have conducted a detailed investigation of MMAE action on MTs and free tubulin heterodimeric subunits, both as a free drug and as an ADC, employing both reconstituted in vitro systems consisting of heterodimeric tubulin subunits or MTs as well as cultured human MCF7 cells. In the reconstituted in vitro systems, free MMAE (i) binds to soluble tubulin heterodimers with a maximum stoichiometry of approximately 1 : 1, (ii) binds to pre-assembled MTs abundantly along the MT length and with high affinity at the ends, (iii) potently suppresses MT dynamics, (iv) introduces structural defects both at MT ends and along the MT length that may increase the number of drug binding sites, (v) reduces the kinetics and extent of MT assembly, and (vi) reduces the length of assembled MTs while promoting the formation of tubulin rings. In addition, our cellular studies demonstrate that MMAE potently suppresses (i) proliferation, (ii) mitosis, (iii) the integrity of the MT network (during both mitosis and interphase), and (iv) MT dynamics. The effects of the antibody-conjugated version of MMAE were qualitatively similar to those of free MMAE, although quantitatively much less potent. A reduction in potency is unsurprising given that these cells do not express the antigen recognized

by the conjugated antibody (much like would be expected for non-antigen presenting
peripheral neurons).

Previous mechanistic work has shown that MMAE-ADC action upon neuronal MTs
in peripheral nerves is mediated by nonspecific uptake of the entire MMAE-ADC into
the nerve cells followed by intracellular release of the anti-tubulin payload (i.e. MMAE),
leading to nerve degeneration [Stagg et al., 2016]. For this reason, the main focus of this
work was to understand how MMAE affects MT biochemistry and dynamics in purified
free tubulin/MTs as well as in cells. Taken together, the simplest interpretation of the
data is that MMAE binds extensively to both soluble tubulin and MTs and causes severe
dysregulation of the MT network. Specifically, MMAE binding to tubulin heterodimers
interferes with MT assembly. MMAE binding to pre-formed MTs along the MT length,
at MT ends, and perhaps also at new sites exposed by MMAE-induced structural defects
along the MT's length, results in substantial structural damage to the MTs. Since
MMAE-treated cells exhibit deficits in MT-mediated events such as proliferation, mitosis,
and the appearance of the MT network, we conclude that the structural effects observed
in purified tubulin/MTs likely underlie MT dysfunction in cells. While these effects are
ideal for attacking highly proliferative tumor cells, MT dysfunction will likely also have
negative consequences for peripheral nerves. Even though peripheral nerve cells are not
proliferating, they are susceptible to damage by MMAE and other MTAs because of the
essential role of the neuronal microtubule network for functions such as axonal transport
along the long axonal projections [Morfini et al., 2009, Almeida-Souza et al., 2011].

Although different MTAs interact with the same target (i.e., MTs) and alter MT
dynamics to promote tumor cell death, they vary in the frequency and severity of CIPN
observed in patients. Paclitaxel and vinblastine [Carlson and Ocean, 2011, Swain and
Arezzo, 2008, Younes et al., 2012] are the most commonly used MTAs and induce rela-
tively high levels of severe CIPN, while more recently developed MTAs such as eribulin

[Goel et al., 2009, Tan et al., 2009, Gradishar, 2011, Vahdat et al., 2009] and vinflu-nine[Swain and Arezzo, 2008] have markedly lower incidences. Since MTA-induced pe-ripheral neuropathy is likely due to the disruption of normal MT-dependent events such as axonal transport, understanding how different MTAs bind to different sites on MTs and/or soluble tubulin and differentially affect MT dynamics[Jordan and Kamath, 2007, Jordan and Wilson, 2004] compared to MMAE can provide mechanistic insights into MMAE-ADC peripheral neuropathy.

4.5.1 How might MMAE-ADCs induce severe peripheral neu-ropathy?

There are a number of non-mutually exclusive hypotheses that could account for the relatively high level of MMAE-ADC-induced severe peripheral neuropathy observed clinically. One possible hypothesis focuses upon the location and abundance of drug binding sites on MTs, leading to severe dysregulation of the MT network and disruption of MT-dependent events such as axonal transport. Once the MMAE ADC is taken up non-specifically in the peripheral nerve cells and MMAE is released, as demonstrated in this work, MMAE binds to abundant, lower affinity binding sites along the length of MTs as well as with a small number of higher affinity sites at MT ends. This pattern of binding to an abundant number of sites along the length of the MT has been observed with other MTAs that have a high incidence of severe CIPN including vinca alkaloids, paclitaxel and epothilones [Genualdi et al., 2020]. Many of the vinca alkaloids (i.e. vinblastine and vincristine) have a very similar binding pattern to MMAE, whereby they bind a large number of relatively low affinity binding sites along the MT length and to a small number of high affinity sites at MT ends [Gigant et al., 2005, Hans et al., 1978, Mirsalis et al., 1999, Wilson et al., 1975]. Paclitaxel and the epothilones also bind to

abundant sites along the length of the MT, although these binding sites are distinct from
MMAE and vinblastine binding sites since they are located on the inside of the MT
[Amos and Lowe, 1999, Bollag et al., 1995, Diaz et al., 1998, Nettles et al., 2004, Nogales
et al., 1998, 1995, Prota et al., 2013]. These various binding patterns are in contrast to
eribulin, which binds to only a small number of high affinity sites at MT ends but lacks
the abundant, low affinity sites along the length of the MT [Smith et al., 2010]. Eribulin
also exhibited markedly lower incidences of severe CIPN in patients. DM1, an approved
payload in ado-trastuzumab emtansine (T-DM1) was evaluated for its in vitro binding
as a free drug in the form of S-methyl-DM1 and was found to bind similarly to MMAE
(high affinity binding sites at the end and low affinity binding sites along the length
[Lopus et al., 2010]. Consistent with the above model, peripheral neuropathy has been
a frequent adverse event with almost all DM1 and DM4 containing conventional ADCs
[Bendell et al., 2013, Younes et al., 2012]. T-DM1, however, had a very low incidence
that was primarily grade 1 and sensory and did not result in dose delays, reductions
or discontinuations, which may be attributed to other properties of the ADC (e.g. less
uptake of the ADC and/or release of its payload in the peripheral nerves).

In addition, high affinity for MTs may contribute to the frequency of severe peripheral
neuropathy. Indeed, paclitaxel has a very high affinity for MTs, followed by vincristine
followed by vinblastine followed by eribulin [Lobert et al., 1996, Nogales et al., 1995, Smith
et al., 2010, Wilson et al., 1982]. This order of affinities correlates with the frequency of
severe peripheral neuropathy.

Yet another possible contributor to the frequency of severe peripheral neuropathy
derives from the fact that exposure of pre-formed MTs to either MMAE or vinblastine at
high concentrations induces structural defects in the MT lattice along the length of the
MT and protofilament peeling/fraying at MT ends (Fig. 4.4; [Jordan et al., 1986, Wilson
et al., 1982]). These lattice defects have been proposed to expose additional, otherwise

sequestered drug binding sites [Wilson et al., 1982]. Since these structural effects occur along the length of the MT lattice and require relatively high drug concentrations, these effects are likely mediated by drug binding at the abundant low affinity sites along the length of the MT. In contrast, exposure of pre-formed MTs to eribulin results in moderate "splaying" at plus MT ends but no defects along the length [Smith et al., 2010].

Mechanistically, drug-induced structural alterations along the length of MTs would be especially deleterious to neurons, which require especially stable MTs in their axonal compartments in order to conduct axonal transport [Baas et al., 2016]. Perhaps these defects in the MT lattice interfere with the ability of kinesin and/or dynein to translocate along MTs, thereby interfering with the essential transport of cargo between neuronal cell bodies and their distant synapses, such as has been observed in previous studies examining the effects of vincristine, paclitaxel, and ixabepilone on fast axonal transport [LaPointe et al., 2013, Smith et al., 2016]. In support of this hypothesis, eribulin, which binds exclusively at MT ends, exhibited weak effects upon the rates of axonal transport relative to vincristine, paclitaxel, and ixabepilone [LaPointe et al., 2013], all of which bind to high abundance sites along the MT length.

While differential MTA binding to MTs (both in terms of binding sites and affinities for those sites) may underlie their differential clinical incidences of CIPN, differences in MTA binding to free tubulin heterodimeric subunits may also play a role. MMAE, vinblastine, and eribulin all bind to free tubulin heterodimers. However, there are differences in the details of each binding event, leading to the formation of different MTA-tubulin structures. For example, at relatively high concentrations, MMAE binding to tubulin heterodimers leads to the formation of oligomeric rings, while vinblastine binding leads to formation of oligomeric spirals [Wilson et al., 1982]. This is consistent with both drugs binding along the length of a protofilament and promoting a curved structure by acting as a wedge between longitudinally stacked tubulin subunits [Gigant et al., 2005,

Wang et al., 2016]. However, the fact that MMAE generates rings while vinblastine generates spirals demonstrates that the exact binding events are distinct from one another. Indeed, even the closely related vinca alkaloid vinflunine demonstrates smaller spirals (and a lower rate of severe CIPN) than closely related vinblastine. In contrast, although eribulin also binds to tubulin heterodimers, no obvious oligomeric structures form [Alday and Correia, 2009, Dabydeen et al., 2006]. Mechanistically, different modes of binding to tubulin heterodimer subunits could easily lead to different structural effects and unique downstream impacts upon MT function. Consistent with this model, vinflunine has been shown to promote the formation of fewer, shorter oligomeric tubulin structures compared to vinblastine [Lobert et al., 1998].

A second hypothesis for the differential incidence of CIPN among MTAs posits different affinities for different tubulin isotypes. This seems plausible considering that each MTA has its own precise binding interactions with MTs/tubulin subunits, as demonstrated at the level of x-ray crystallography [Doodhi et al., 2016, Waight et al., 2016, Wang et al., 2016]. These subtle structural differences between the interactions of different MTAs with differentially expressed α or β tubulin isotypes would be predicted to affect the extent of MTA-mediated MT disruption and resulting cellular consequences. Consistent with this notion, eribulin is less active on MTs containing the neuronal-specific βIII tubulin isoform than on non-neuronal MTs found in other cell types that lack this isoform [Wilson et al., 2015]. An analysis of data generated with ixabepilone, paclitaxel or vincristine in similar experiments in bovine brain MTs or cultured cells (MCF7 or NSCLC H460) in the absence of neuronal βIII tubulin did not show increased activity [Genualdi et al., 2020]. It is possible that MMAE and other MTAs with relatively high frequencies of severe peripheral neuropathy may exhibit relatively strong interactions with the tubulin isotypes expressed in peripheral neurons, resulting in their accompanying deleterious consequences.

A third hypothesis for increased MMAE peripheral neuropathy is a more complete suppression of MT dynamics (i.e. both growth and shortening of MTs) than for some other MTAs, resulting in a more severe dysregulation of MT-dependent events such as axonal transport. At sub-stoichiometric concentrations in isolated MTs and in cells, both MMAE and vinblastine suppress MT growing and shortening parameters and greatly increase the time that MTs spend in an attenuated state ([Dhamodharan and Wadsworth, 1995, Jordan et al., 1985, Toso et al., 1993]; Table 4.4.1.4). Maytansine and its thio-containing derivative DM1 act similarly [Lopus et al., 2010]. More specifically, at these sub-stoichiometric concentrations, MMAE and vinblastine both increase the amount of time that MTs spend in an attenuated state by suppressing both the on rate (addition, growth) and the off rate (loss, shortening) of tubulin subunits. This mechanism of action has been proposed to represent "true kinetic suppression," as opposed to other MTAs that do not directly reduce both on and off rates [Castle et al., 2017]). For example, both eribulin [Jordan et al., 2005, Smith et al., 2010] and vinflunine [Ngan et al., 2000], which are both associated with relatively low incidences of CIPN clinically, affect MT growth but not shortening parameters, perhaps underlying their lower toxicities. Importantly, the potent action of all four of these drugs at sub-stoichiometric concentrations indicates that their suppressive effects on MT dynamics are most likely due to drug binding to, and action upon, high affinity binding sites located at MT ends.

4.5.2 Future Directions

Overall, this work suggests that MMAE causes severe MT dysregulation and provides possible hypotheses for MMAE-mediated inhibition of MT-dependent axonal transport leading to severe cases of peripheral neuropathy in patients. To further study these hypotheses, it will be valuable to study MMAE and other MTAs in neuronal cells. One es-

pecially attractive route might be to use models of nociceptor neurons such as human iPS cells differentiated into a nociceptor phenotype [Chambers et al., 2012]. These systems would allow an assessment of how MMAE and other MTAs affect critical neuron-specific features such as the maintenance of neurites and intracellular, MT-dependent transport. However, the highly elongated morphology of these neuronal systems and their very high axonal MT density make assays of individual MT dynamics challenging, although the use of super-resolution microscopy techniques have allowed for some advances [Dent, 2017]. Additionally, it would be very informative to test MMAE for its effects upon cells harboring or lacking the neural-specific βIII isoform of tubulin. As mentioned earlier, eribulin was found to be less active on βIII-containing MTs than on non βIII-containing MTs, perhaps contributing to eribulin's lower incidence of severe CIPN [Wilson et al., 2015]. One might hypothesize similar activity with MMAE on βIII-containing MTs as non βIII-containing MTs given the high incidences of severe peripheral neuropathy, but this would need to be assessed directly to establish if this is a good indicator of severe peripheral neuropathy risk. In addition, our data, when taken together with previous work showing nonspecific MMAE ADC uptake and the subsequent release of free MMAE into non-target cells [Stagg et al., 2016], support this mechanism as the likely main pathway for cytotoxic agent delivery to the peripheral nerves and the resulting peripheral neuropathy. Finally, efforts to develop new and improved tubulin/MT targeted drugs (MTAs and/or MTA conjugates) with reduced incidence of severe CIPN may be promoted by careful consideration of mechanisms and locations of binding events as well as the regulation of MT dynamics, as discussed here and more extensively in Genualdi et al. [2020].

4.6 Acknowledgments

4.7 Materials and Methods

Tubulin preparation. MAP (MT-associated protein)-rich tubulin ($\sim$70% tubulin, 30% MAPs) was obtained from crude bovine brain extract by three polymerization/depolymerization cycles [Miller and Wilson, 2010]. MAP-free tubulin was further purified with a phosphocellulose ion exchange column [Miller and Wilson, 2010]. Tubulin was stored in PEM50 (50 mM PIPES pH 6.8, 1 mM $MgSO_4$, 1 mM EGTA) with 0.1-0.2 mM GTP at 7-12 mg/mL, as measured by Bradford versus a BSA standard. Tubulin was drop-frozen in liquid nitrogen and stored at $-80\,°C$. Rhodamine-labeled tubulin was prepared from MAP-free tubulin as described [Hyman et al., 1991]. Biotinylated tubulin was purchased from Cytoskeleton. GMPCPP was purchased from Jena Bioscience.

Drug stocks. Unlabeled MMAE, tritium-labeled MMAE ([^{3}H]-MMAE), and MMAE ADC (CNJ2985-vc-MMAE) were provided by Genentech. [^{3}H]-MMAE (specific activity 863 mCi per mmole) was stored as a 1 mM stock in DMSO. Unlabeled drug was stored as a 10 mM stock in DMSO. The MMAE ADC was stored in water with 5-10% sucrose,

and molarity calculations were based on the molecular weight of the antibody.

MMAE binding to soluble tubulin in vitro. MAP-free tubulin (0.25 mg/mL, 2.3 uM) was prepared in PEM100 buffer (100 mM PIPES pH 6.8, 1 mM $MgSO_4$, 1 mM EGTA) with 100 uM GTP and then incubated with different concentrations of [3H]-MMAE (0.1 uM to 20 uM). After 12-15 min at 30 °C, the mixture was subjected to size exclusion chromatography to separate free drug from drug/tubulin/GTP complexes using Zeba Spin (2 mL) desalting columns prepared according to the manufacturer's instructions (Thermo Scientific) and centrifuged at 1000 x g for 4 min. The eluate was analyzed for protein content by Bradford and [3H]-MMAE content by liquid scintillation counting. Data shown are mean and SEM from 3-4 independent experiments per MMAE concentration

MMAE binding to MAP-rich MTs in vitro. MAP-rich tubulin (33 uM) was polymerized to steady-state in PEM100 with 1-2 mM GTP at 30 °C. Resulting MTs were sheared 6 times to increase the MT number concentration and to tighten the MT length distribution, and then incubated an additional 15 min to re-establish steady-state. Transmission electron microscopy (TEM) samples were taken to determine MT length distributions (measured using a Zeiss MOP III morphometric digitizing pad), and then MTs were aliquoted and incubated with [3H]-MMAE (1 uM to 20 uM). After 6 min, free drug was separated from MT-bound drug by centrifugation through 30% glycerol/10% DMSO cushions at 40,000 X g, 30 °C for 1 hr. Pellets were washed extensively and solubilized in water at 4 °C for 18 hr, then analyzed for protein and [3H]-MMAE content as described above. Molecules of bound drug per MT was calculated using a value of 1690 tubulin dimers per µm of MT length and a median MT length of 3.63 uM. Data shown are mean and SEM of 2-4 independent experiments per concentration for 0.1 – 15 uM MMAE, and a single experiment for 20 uM MMAE.

MMAE-induced MT disassembly in vitro. MTs were assembled from MAP-rich

tubulin as for binding experiments. After recovery to steady state, MMAE or MMAE ADC was added and light scattering at 350 nm (A350) was monitored. Samples for TEM were removed after 6 min, paralleling the drug exposure time in the MT-binding experiments, and then the A350 signal was measured until it plateaued.

Transmission electron microscopy (TEM). MTs were fixed with glutaraldehyde (final concentration, 0.1 - 0.2%) and then placed on 200-mesh formvar-coated copper grids (Ted Pella). After 1.5 min, sample droplets were displaced with cytochrome c (1 mg/mL) to improve staining, and then the grid was rinsed with deionized water and stained for 30 sec with 1% uranyl acetate. MTs were imaged on a JEOL 1230 electron microscope at 80 kV with AMT image capture software.

In vitro MT assembly and MT end morphology assays. Solutions of MAP-rich tubulin (∼2.4 mg/mL total protein; 16 uM tubulin) and MMAE or MMAE ADC were prepared on ice in PEM100, and then MT assembly at 30 °C was monitored by A350. After 1 hr, samples were removed and the remaining volume was centrifuged at 40,000 X g, 30 °C for 1 hr. Pellets were solubilized, and protein concentration was determined as above. Data are the result of 2-4 independent experiments per drug concentration and are shown as mean ± SEM. TEM images shown are from a single representative experiment. MT lengths were measured using Fiji (ImageJ, NIH).

Morphology of MT ends was determined from ≥5 TEM images per condition. Images from 3 independent experiments were pooled and anonymized, and then each MT end was categorized as "blunt", "splayed" (slightly flared), or "frayed" (having a projection at least as long as the MT width). Rare ends that did not fall into any of these categories were excluded from analysis. The proportion of frayed ends in each image was plotted as a function of MMAE concentration and analyzed by logistic regression in JMP Pro 13 (SAS).

In vitro MT dynamics assays. MTs were grown on coverslips from two types of

seeds (no difference was observed between the types): (i) axonemes prepared from sea
urchin sperm [Yenjerla et al., 2010] and attached directly to the coverslip; (ii) GMPCPP
MT seeds prepared [Gell et al., 2010] from a mixture of MAP-free rhodamine-labeled
tubulin, unlabeled tubulin, and biotinylated tubulin and attached via PEG-poly-L-lysine-
biotin (Surface Solutions) and NeutrAvidin (Thermo Fisher). Coverslips were blocked
with casein (4 mg/mL). MAP-free tubulin (10-11 uM 14% rhodamine-labeled) was diluted
into PMEM buffer (87 mM Pipes, 36 mM MES, 1 mM EGTA, 1.4 mM $MgSO_4$, pH
6.8) with 1 mM GTP, 10 mM DTT, an oxygen scavenging mixture (119 nM catalase,
214 U/mL glucose oxidase, and 40 mM D-glucose; Sigma C9322, Sigma G2133, and EM
Sciences DX0145-3, respectively), and 100 nM of drug or vehicle (0.1% final concentration
DMSO in all mixtures). Samples were incubated at 32 - 34 °C for 30 min to reach steady
state and then imaged on a temperature-controlled Leica SP8 resonant scanning confocal
microscope (63X oil objective), 1 frame every 2 s (10 min max per field of view, 45 min
max per sample). Kymographs were generated and analyzed in Fiji (ImageJ, NIH) with
KymographBuilder and then every second frame was averaged on the "time" axis to
improve visibility, resulting in a final interval of 4 s (matching the frame rate used to
collect the cellular data described below). Data were extracted from kymographs using
the Velocity Measurement Tool (`http://dev.mri.cnrs.fr/projects/imagej-macros/`
`wiki/Velocity_Measurement_Tool`). Definitions and criteria for all parameters were
essentially identical to those described for cellular data, except that the criterion for
growth and shortening events were ≥ 0.32 um vs. ≥ 0.3 um in cells. Data were pooled
from 5 experiments.

Statistical analysis of MT dynamics data. Data were processed and formatted in
R (v.3.3.3; [Team, 2016a,b], and then bootstrap analysis (106 iterations) was performed
in Statistics101 (v.4.6; `statistics101.net`) to determine whether or not observed dif-
ferences between the means for control and MMAE were statistically significant. Graphs

were generated in R with ggplot2 [H.Wickham, 2009] and then detailed in Adobe Illustrator. Boxplots show median (horizontal line) and 25th - 75th percentile; a white square indicates the mean. Whiskers extend 1.5 times the interquartile range, and more extreme data points are shown individually. Sample sizes are indicated on the x-axis.

Cell culture. MCF7 human breast adenocarcinoma cells stably transfected with EGFP-α-tubulin cDNA [Azarenko et al., 2014] were cultured in DMEM with 10% fetal bovine serum (Atlanta Biologicals, Inc.), 1% final concentration of nonessential amino acids, 100 units/mL penicillin, and 100 ug/mL streptomycin at 37 °C, 5.5% CO2. These cells were indistinguishable from unmodified MCF7 cells except for their fluorescent MTs and their doubling time of 35 hr, which was 20% slower than unmodified MCF7 cells. They constitutively express EGFP-α-tubulin and are referred to in this manuscript as simply MCF7 cells.

MMAE cellular uptake. To determine intracellular drug concentrations [Okouneva et al., 2008], MCF7 cells were seeded into poly-l-lysine-treated scintillation vials (1×105 cells, 2 mL). After 24 hr, media was replaced with fresh media containing 10 nM [^{3}H] MMAE or unlabeled drug. Media was removed 30 min to 20 hr after drug addition, vials rinsed twice with 1 mL PBS, and Ready Protein+(Beckman Coulter, Inc.) added for scintillation counting (LS 6500 Multi-Purpose Scintillation Counter; Beckman Coulter, Inc.).

Intracellular drug concentration = (moles of intracellular drug bound/mean cell volume) $\times$ (the number of cells per vial)(4.1)

Mean cell volume was calculated based upon the mean diameter of cells rounded by trypsinization (4.5710^{12} L ; n = 30).

Cell proliferation. Proliferation was measured by a modified sulforhodamine B (SRB) assay [Oroudjev et al., 2010]. Cells were seeded (5,000 cells/200 uL) in 96-well plates and incubated 24 hr. Fresh medium with or without the MMAE was added, and incubation continued for 96 additional hr. Cells were fixed, stained with SRB reagent, and optical density determined (490 nm; Victor3V Wallac 1420 Spectrophotometer, Perkin-Elmer). Triplicates of each condition were tested in each experiment. Results are mean ± SEM of ≥ 4 experiments. The concentrations that inhibited cell proliferation by 50% were calculated using Prism 4.0 software (GraphPad Software, Inc).

Cell viability and cell cycle analysis. Cells were seeded (6×104 cells/2 mL) in 6-well plates (24 hr), and then incubated with drug for 24, 48, or 72 hr. For viability, all cells were harvested and stained with ViaCount DNA binding dyes (5 min; EMD Millipore) and analyzed by flow cytometry (EasyCyte flow cytometer; Guava Technologies, Inc.) to distinguish live from apoptotic/dead cells.

For cell-cycle analysis, floating and adherent cells were collected, permeabilized with ice-cold 70% ethanol, washed with PBS, and stained with cell-cycle reagent (EMD Millipore). The DNA content of ≥5,000 cells was measured by flow cytometry and analyzed with ModFit LT software (Verity Software House). Results are mean ± SEM of ≥3 independent experiments.

Mitotic arrest. MCF7 cells were seeded as for cell viability and incubated with drug for 24 h; both floating and attached cells were collected and fixed in 3.7% formaldehyde (30 min), followed by cold methanol (10 min; [Okouneva et al., 2008]). Fixed cells were mounted on glass slides with antifade agent Prolong Gold-DAPI (Life Technologies, Inc.) to visualize DNA and examined by fluorescence microscopy (Nikon Eclipse E800, 40x objective). Mitotic cells were rounded cells with condensed chromosomes and no nuclear envelope. The percentage of mitotic cells was determined by counting 500 cells for each condition. Results are mean ± SEM, 3 experiments.

Cell immunofluorescence. Cells were seeded as for cell viability, incubated with drug for 24 hr, fixed with 3.7% formaldehyde followed by cold methanol [Okouneva et al., 2008], and stained with mouse monoclonal α-tubulin antibody (1:1,000 DM1A, Sigma) and FITC-conjugated goat anti-mouse antibody (1:1,000, Cappel MP Biochemicals). Centrosomes were stained with rabbit polyclonal anti-pericentrin (1:500, AB4448; Abcam) and rhodamine-conjugated goat anti-rabbit (1:500, Cappel). Cells were mounted as above and imaged using a spectral confocal Olympus Fluoview1000 microscope (FLV1000S, $\times$60 oil, N.A. 1.4 objective; Olympus).

Cellular MT dynamics. Cells were seeded on coverslips in 6-well plates (3×104 cells/mL, 2 mL/well) for 24 hr, and then media was replaced with fresh media containing 0.5 nM MMAE. Time-lapse images (38 frames/4-s intervals/1 h at $37 \pm 1\,°C$) were taken with a $\times$100 objective on the same microscope used for in vitro MT dynamics. Changes in the length of individual MTs were graphed versus time as "life history" plots. MT dynamics parameters were analyzed with IGOR Pro 6.0 [Oroudjev et al., 2010]. Changes in length ≥ 0.3 um were defined as growth or shortening events, < 0.3 um were pause (or attenuation). The time-based catastrophe frequency is the number of catastrophes (transitions from growth or pause to shortening) divided by total time spent growing and paused. Rescue frequency is the number of transitions from shortening to growth or pause divided by total time spent shortening. Dynamicity is total length grown and shortened divided by total duration of imaging a MT. Data were pooled from $\geq$3 experiments and then imported into R for statistical analysis and graphing (described above).

For supplementary information, please see Appendix B.

Chapter 5

Conclusions and Future Directions

Alzheimer's disease (AD) afflicts $\sim$5.7 million Americans, nearly 1.7% of the American population [Alzheimer's Association, 2017]. In 2020, care for AD patients in the US will cost \$305 billion ($>$1/3 the entire budget of the US Department of Defense, [DoD, 2020]). The growing human and fiscal impact of AD provides a powerful motivation to further understand the molecular mechanisms underlying its onset and progression, with the goal of providing a foundational understanding for subsequent rational drug design. Although tau's interactions with MTs have been studied for decades, little progress has been made regarding the real mechanisms underlying normal and pathological tau action.

It is widely held in the Alzheimer's field that trans-synaptically transferred tau corrupts the endogenous tau in the recipient cell via a prion-type of pathological folding mechanism [Liu et al., 2012], resulting in neurodegeneration. The actual mechanism of tau-mediated neurotoxicity remains poorly understood. Both gain-of-function [Gotz et al., 2001, LaPointe et al., 2009, Morfini et al., 2009, Cox et al., 2016] and loss-of-function [Panda et al., 2003, Feinstein and Wilson, 2005, Levy et al., 2005, Brunden et al., 2010, Zhang et al., 2012] models have been proposed. The demonstration that MT stabilizing drugs such as taxol and epothilone D can reverse Aβ mediated deficits in cultured neurons and mouse models of Alzheimer's provide important support for the loss-of-function perspective [Brunden et al., 2010, Zhang et al., 2012]. However, these

models need not be mutually exclusive. One important key to these mechanistic issues is the identity of the toxic form(s) of tau.

For many decades, NFTs were assumed to be a direct cause of neurotoxicity. More recent work, however, has demonstrated that large tau aggregates such as those that comprise the NFTs are not necessary for toxicity, and that smaller, oligomeric forms of tau are more likely candidates [Kopeikina et al., 2012, Kuchibhotla et al., 2014]. Tau's transition from a highly soluble protein to an insoluble NFT represents the end point of a derailed phase transition, but the mechanisms underlying this transition from normal to pathological remain unclear [Aguzzi and Altmeyer, 2016]. Tau's intrinsic disorder and resulting ensemble of different conformations makes it, like other intrinsically disordered proteins (IDPs), particularly susceptible to liquid-liquid phase separation (LLPS), which is defined by the coexistence of two or more spatially separated liquid phases. It's currently unclear how this phenomenon relates to tau's pathological aggregation, although one possibility is that enhanced LLPS leads to increased tau segregation into phase-separated droplets. This may prevent MT binding and may facilitate tau's pathological aggregation [Wegmann et al., 2018]. Consistent with this notion, Kanaan et al. [2020] found that both dementia-causing mutation P301L, as well as phosphorylation at a disease-associated epitope (AT8 epitope, including S202, T205, and S208), both enhanced tau LLPS and resulted in less tau exchange between droplets and solution [Kanaan et al., 2020].

Ultimately, the identity of toxic tau species, as well as the events leading to pathological tau oligomerization and downstream neurodegeneration and dementia in AD have yet to be determined. Aberrant changes in tau post-translational modifications have also been observed in AD - pathological tau exhibits a marked increase in phosphorylation [Mi and Johnson, 2006], changes in the pattern of acetylation [Cohen et al., 2011, Cook et al., 2014], as well as tau fragmentation [Park and Ferreira, 2005, Ferreira and Bigio,

2011, Gamblin et al., 2003, Reifert et al., 2011].

Below is a brief description of two major areas of work that build upon my dissertation work and that I would pursue were I to continue to work in this field. In fact, I have conducted initial experiments on these projects and anticipate that others in the lab will continue to pursue them in the future.

5.1   Tau phosphorylation

It has been widely appreciated for decades that pathological tau is hyper-phosphorylated relative to normal tau (containing $\sim$8 phosphates per molecule compared to $\sim$2 normally, although estimates vary widely) [Wang et al., 2016]. Tau phosphorylation precedes its pathological aggregation in tauopathy patients, suggesting its involvement in early disease pathogenesis [Braak et al., 1994, Mondragón-Rodríguez et al., 2008]. Embryonic tau is also highly phosphorylated (containing $\sim$7 phosphates per molecule; [Kenessey and Yen, 1993]), but, unlike NFT tau, still retains modest MT assembly-promoting activities [Yoshida and Ihara, 1993], suggesting that both the location and number of phosphorylation sites play an important role in the resulting impact on tau activities. However, despite the critical role tau phosphorylation clearly plays in normal and pathological tau action, it has been extremely challenging to study it in a rigorous and site-specific manner. More specifically, due to tau's large number of phosphorylatable residues (87 in the longest isoform) and its intrinsically disordered nature, preparation of phosphorylated tau for study via purified kinases suffers from both uncertain efficiency and specificity. Moreover, tau's possession of many phosphorylatable residues presents an enormous number of possible combinatorial combinations, something that has been impossible to experimentally assess. These issues can be avoided by a pseudo-phosphorylation approach (e.g. replacing serine (Ser, S) or threonine (Thr, T) with a negatively charged amino

acid such as glutamic (E) or aspartic (D) acid via site-directed mutagenesis), but the bi-
ological relevance of this imperfect mimic is very debatable. As a result, rigorous insight
into the fundamentally important question of how tau's hyperphosphorylation relates
to its pathological dysfunction, aggregation, and downstream neurodegeneration in AD
remains elusive.

Many of tau's pathologically phosphorylated residues reside within its MTBR and
PRR (Fig. 1.2), where they may disrupt the electrostatic interaction between tau's
mostly positively charged MTBR and tubulin's mostly negatively charged residues (re-
viewed in [Wang et al., 2016]). In support of this model, Kellogg et al. [2018]'s cryo-EM
structure of tau bound to a MT suggested that phosphorylation of S262 within the
MTBR, a modification commonly associated with AD, is predicted to disrupt crucial
hydrogen bonding with Glu-434 of α-tubulin, perhaps providing a mechanism underly-
ing this site's importance in disease [Kellogg et al., 2018]. On the other hand, while
phosphorylation at S262 resulted in decreased MT binding and MT assembly-promoting
activity *in vitro* [Kiris et al., 2011], it also *protected* against pathological aggregation
[Schneider et al., 1999]. In addition, phosphorylation of tau at certain residues adjacent
to the MTBR, including S396 and S404, is observed early in AD [Mondragón-Rodríguez
et al., 2014], results in decreased MT binding affinity and ability to promote MT as-
sembly [Kiris et al., 2011], and *increases* tau's pathological self-aggregation [Jeganathan
et al., 2008]. Further complicating the matter, Kiris et al. [2011] showed that tau pro-
teins pseudophosphorylated at two sites per molecule did not exhibit the sum of activities
of the two constituent, singly pseudophosphorylated molecules [Kiris et al., 2011]. Re-
markably, while singly pseudophosphorylated tau molecules, such as S262D and S396D,
were compromised in their binding to MTs and promotion of MT assembly, many of the
doubly pseudophosphorylated tau proteins, including S262D/S396D, restored tau's MT
assembly-promoting activity and binding affinity to wild-type levels [Kiris et al., 2011].

The technical inability to produce recombinant tau proteins with specific, efficient, *bona fide* phosphorylation at sites of interest has precluded our study of the structural and functional effects of tau phosphorylation to date. However, the adaptation of a state-of-the-art orthogonal translation system (OTS) recently developed in Dr. Jesse Rinehart's lab (Yale Univ.) would allow us to circumvent these progress-limiting technical roadblocks and synthesize recombinant tau with either phospho-serine (pSer) or phospho-threonine (pThr) at defined sites of interest with unprecedented efficiency, site-specificity, and purities approaching 90% [Pirman et al., 2015]. This technology is based on the principles of genetic code expansion, whereby an unnatural amino acid, such as pSer, is directly incorporated into recombinant proteins during canonical protein synthesis via STOP codon suppression. The pSer-OTS uses a dedicated aminoacyl-tRNA synthetase (pSer-RS) to charge pSer onto a UAG-decoding tRNA and an engineered elongation factor Tu (EF-pSer) that then delivers the pSer-charged tRNA to the ribosome. This would be the first study to apply this cutting-edge technology to tau and, if successful, would represent a huge advance in the current and future study of both normal and pathological tau structure/function.

We have begun to collaborate with Dr. Rinehart and his lab to produce tau proteins with pSer at positions S262 and S396 and pThr at position T217. These sites were chosen due to their tight correlation with AD: phosphorylation at S262 [Augustinack et al., 2002] and S396 [Mondragón-Rodríguez et al., 2014] are some of the earliest events in AD; and phosphorylation at T217 has recently been implicated as a useful early biomarker for AD [Janelidze et al., 2020]. Using Dr. Rinehart's technology, non-phosphorylated tau control proteins can be synthesized in the same cells in parallel, using machinery that incorporates unmodified Ser/Thr residues at the sites of interest, providing rigorous internal controls [Pirman et al., 2015]. In addition, we hope to conduct the first direct comparison between *bona fide* site-specific tau phosphorylation and pseudo-phosphorylation

to assess the latter's validity. All tau variants and controls will be confirmed by mass spectrometry and then compared using our lab's routine assays of tau function, including for its: ability to promote MT assembly and to bind to MTs [Kiris et al., 2011] *in vitro*; ability to stabilize newly-identified structural intermediates in MT assembly and disassembly *in vitro* ([Best et al., 2019], see also chapter 3); and propensity to self-assemble into pathological aggregates *in vitro*. Based on pseudo-phosphorylation or non-specific kinases studies, we hypothesize that phosphorylation at S262 [Biernat et al., 1993, Kiris et al., 2011], S396 [Evans et al., 2000], or T217 [Yoshida and Goedert, 2006] will impair both tau's ability to assemble and bind to MTs. We also predict that pT217 and pS396 will self-aggregate more readily than their non-phosphorylated counterparts, while pS262 will prove more resistant to aggregation.

The adaptation of Dr. Rinehart's system for the recombinant production of tau containing site-specific phosphorylation would finally enable us to characterize the functional effects of tau site-specific phosphorylation. More importantly, this would lay the groundwork for the adaptation of our system for the analysis of combinatorial tau phosphorylation on tau structure and function in a rigorous and site-specific way, something with incredible *in vivo* relevance that has been impossible to assess experimentally until now. Further, this work would provide a fundamentally important contribution to a critically important aspect of normal and pathological tau action that has suffered from inadequate rigor, and therefore credible data, for decades. Finally, these studies will inform the design of subsequent experiments in cells, although we recognize the difficulty in achieving the same degree of rigor as is possible with Dr. Rinehart's system.

5.2   Tau dimer- and oligomerization

While tau's pathological aggregation into the hallmark NFTs of AD appears primarily mediated by the C-terminal portion of the protein, especially the MTBR [Friedhoff et al., 1998, Wang et al., 2016], the vast majority of tau found in the extracellular space between donor and recipient neurons is truncated and lacks the MTBR [Meredith et al., 2013, Ferreira and Bigio, 2011]. Moreover, the N-terminal 17 kDa tau fragment (Fig. 1.2), which appears in the cerebrospinal fluid of Alzheimer's and tauopathy patients but not healthy, age-matched controls [Ferreira and Bigio, 2011], is neurotoxic when expressed in primary cell cultures [Park and Ferreira, 2005, Ferreira and Bigio, 2011], as well as in transgenic mice [Lang et al., 2014]. The MTBR-focused model of tau toxicity does not explain the toxicity of N-terminal tau fragments which lack the MTBR, nor how the trans-synaptic transfer of such fragments might propagate tau pathology and neurodegeneration.

In contrast to tau's pathological aggregation, the Feinstein lab [Feinstein et al., 2016, Rosenberg et al., 2008] and others [Wegmann et al., 2016] have suggested that tau may operate normally as a dimer or higher-order oligomer. Feinstein et al. [2016] proposed a model in which tau dimer-/oligomerization (hereafter referred to as "oligomerization" for simplicity) is mediated by an electrostatic zippering of two antiparallel N-terminal regions (NTR) into a dumbbell-type of structure [Rosenberg et al., 2008]. Consistent with this model, full-length tau migrated as multiple, distinct bands species during native gel electrophoresis, while tau deletion constructs lacking the N-terminal region migrated as single bands under the same conditions [Feinstein et al., 2016]. Furthermore, the 17 kDa fragment was sufficient for oligomerization, forming up to heptamers or octamers under native conditions, and dimers that persisted even in the denaturing conditions of SDS gels [Feinstein et al., 2016]. If this multimeric model of normal tau action is accurate, it provides a number of very interesting mechanistic insights into how tau might

regulate microtubule assembly, regulate microtubule dynamics, and promote microtubule bundling. It also provides a possible mechanism by which trans-synaptic N-terminal tau fragments might exert toxicity by hetero-oligomerizing with full-length tau in the recipient neuron, thereby acting as a dominant interfering protein and compromising the activity of the oligomeric tau complex. This model is consistent with experiments showing the 17 kDa fragment's inhibitory effects on pathological tau aggregation [Ferreira and Bigio, 2011].

Since oligomerization via tau's N-terminus may play an important role in mediating normal and pathological tau action, it is important to know *where* specifically in the NTR this oligomerization occurs. We will use split luciferase assays combined with a "wreck and check" strategy to map tau's oligomerization region in the same way that we and others have used deletion analyses in the past to define the MTBR [Butner and Kirschner, 1991, Goode and Feinstein, 1994, Goode et al., 1997, Gustke et al., 1994]. In this assay, tau constructs of interest are synthesized as fusion proteins with either the N-terminal half or C-terminal half of *Gaussia princips* luciferase ("luci-," amino acids 1-92, and "-ferase," amino acids 92-163, respectively). Neither half of luciferase is active on its own [Wegmann et al., 2016]. In the event of tau dimerization, the luciferase halves are brought together, allowing complementation and restoration of luciferase luminescence activity. Dr. Wegmann has generously given us the mammalian expression plasmids containing full-length tau fused to either luciferase fragment, which will serve as a positive control for tau oligomerization. Negative controls will include each tau plasmid transfected alone and co-transfection of two plasmids harboring the luciferase fragments but lacking tau sequences [Wegmann et al., 2016]. We will start by creating tau deletion constructs comprising both the N- (amino acids 1-230) and C-terminal (amino acids 256-441) regions of the protein fused to either luci- or -ferase. cDNAs encoding tau variants will be co-transfected and expressed in HEK293 cells, and three days later, standard luciferase

luminescence assays will be performed, as described in Wegmann et al. [2016].

We will test the hypothesis that the N-terminal region, which contains the full 17 kDa fragment, will be both necessary and sufficient for oligomerization in cells [Feinstein et al., 2016]. Should that prove true, we plan to generate additional deletion constructs lacking subsets of the necessary region(s) to more specifically pinpoint the residues necessary for the oligomerization activity. Amino acids 106-144 of tau are of particular interest, as previous work has shown that a tau106-144 fragment is sufficient for oligomerization *in vitro* [Feinstein et al., 2016]. On the other hand, Donhauser et al. [2017] suggested that both tau's N- and C-terminal halves may mediate its oligomerization activity [Donhauser et al., 2017], as similar electrostatic interactions between two C-terminal tail regions were reported. This revised model is consistent with our preliminary luciferase assay results, which show that constructs lacking tau's N-terminal region exhibit comparable oligomerization to full-length tau. Interestingly, we also observe that constructs lacking the C-terminus exhibit far higher luminescence than full-length tau, perhaps indicative of the NTR's promotion of higher order oligomers such as were observed by Feinstein et al. [2016]. Taken together, these initial results support a model in which both the N-terminal region and C-terminal region (CTR) are each sufficient but not necessary for tau oligomerization.

The role of both N- and C-terminal tau regions in tau oligomerization is not entirely surprising given the proposed electrostatic nature of the interaction. Specifically, within tau's C-terminal half, the MTBR is overall positively charged, while its tail region is mostly negatively charged. In addition, tau's N-terminal portion also contains regions with opposite net charges - the first half of tau's NTR is largely negatively charged, while the second half is largely positively charged. If tau oligomerization is electrostatically-mediated, we hypothesize it may require the participation of both positively and negatively charged tau regions. As such, we predict that constructs composed

of each differentially charged half of the NTR or CTR alone will be compromised in their oligomerization activity. However, we recognize that this may or may not be the case, and more than simple nested deletions may be necessary to accurately define the region of interest.

One key question we hope to answer with the luciferase assays is if tubulin is necessary for the observed tau oligomerization activity. Tan et al. [2019] recently described how the MT surface regulated reversible tau-tau associations mediated by tau's pseudorepeat R' region, leading to tau "condensates," or regions of higher tau molecule density, on certain regions of the MT lattice [Tan et al., 2019]. In another set of experiments, Hernández-Vega et al. [2017] observed that promotion of tau droplets via molecular crowding agents resulted in tubulin concentration, MT polymerization, and MT bundling within those drops [Hernández-Vega et al., 2017]. It is currently unclear how this phenomenon relates to tau oligomerization, its liquid-liquid phase separation (LLPS), or its pathological aggregation.

While recent technological advances have greatly enabled our understanding of the MT life cycle, as well as its regulation by MAPs, there is much left to learn about the mechanistic details underlying the tau-tubulin interaction and its effects on MT dynamic instability.

Appendix A

Supplementary information for Chapter 3

A.1 Statistical analysis:

Microtubule end morphology data. Count data were grouped into the binary categories of either "projection" or "not projection" (which includes blunt and splayed ends) and were then summed by condition across all experiments. We used a generalized linear model (GLM) with β-binomial error term and "identity" link (JMP Pro 14) to test for a significant effect of experimental condition on projection frequencies. Regression with β-binomial error terms provided a way to negate the potential pitfalls (reduced accuracy) of using a t-test-based or traditional linear model on data that do not fulfill the basic assumptions of these approaches due to their non-normal distribution, unequal variances across conditions (and resulting overdispersion), and strictly bounded nature of the response variable (projection frequency) to values falling between 0 and 1.

The identity link was chosen over the more common logit because of the categorical nature of the predictor (experimental condition).

After the beta binomial regression, pairwise comparisons were made using the "contrast" function (JMP), which uses a joint F test to test for significant differences between

the projection frequencies of the desired conditions. P-values were corrected for multiple comparisons using the sequential Bonferroni correction. 95% confidence intervals on projection frequencies were generated using the Wilson score (JMP), which provides an "approximate conservative" estimate of confidence intervals, although it assumes the data are normally distributed (which is true of binomial data at high enough n). Wilson score predictions were adjusted for multiple comparisons by dividing the input alpha (0.05) by N, where N was the number of comparisons.

Length and abundance data. Unless noted otherwise, length data, as well as abundance data, were first analyzed by Levene's test to determine if variances were equal across conditions (homoscedasticity), an important assumption of normal ANOVA tests. If data fulfilled this assumption, a type II ANOVA with a sequential Bonferroni correction for multiple comparisons was used to compare group means. In cases when the variances were unequal, Welch's ANOVA, which does not assume equal variances, followed by the sequential Bonferroni, was used to compare group means (RStudio, car package).

For the dependence of *de novo* spiral length and abundance on tau and tubulin concentrations, the family-wide ANOVA test (see above), if significant, was followed by an ordered heterogeneity test (JMP) to test for correlation between protein concentration (tau tubulin molar ratio or tubulin concentration) and spiral length. This approach is particularly useful for data in which the predictor (in this case tau or tubulin concentration) is ordered and is predicted to result in a response (spiral length or abundance) with a unidirectional trend [Rice and Gaines, 1994a,b, Gaines and Rice, 1990].

Lastly, projection length and MT length data shown in Fig. 3.5H and Fig. A.3C were analyzed to compare mean lengths within each condition over the 60 min incubation period. Because neither dataset met the assumptions for an ANOVA or other parametric test, nonparametric approaches were used. In cases when n >20, where n represents the number of random, independent fields of view quantified (at either 2500X (MT length) or

30,000X (projection length)), a 2-sample bootstrapping approach was used to compare groups (n = 1,000,000 iterations, Statistics101). In cases when n <20, we used a low power nonparametric test, the difference in confidence intervals (DCI) test (JMP), to test for differences in projection length in controls. For projection abundance data in Fig. 3.5G, because n <10 and variances were unequal, we used a 2-sample Alexander Govern test to test for differences in group means between control and 4R tau samples at 60 min.

A.2 Supplemental Figures
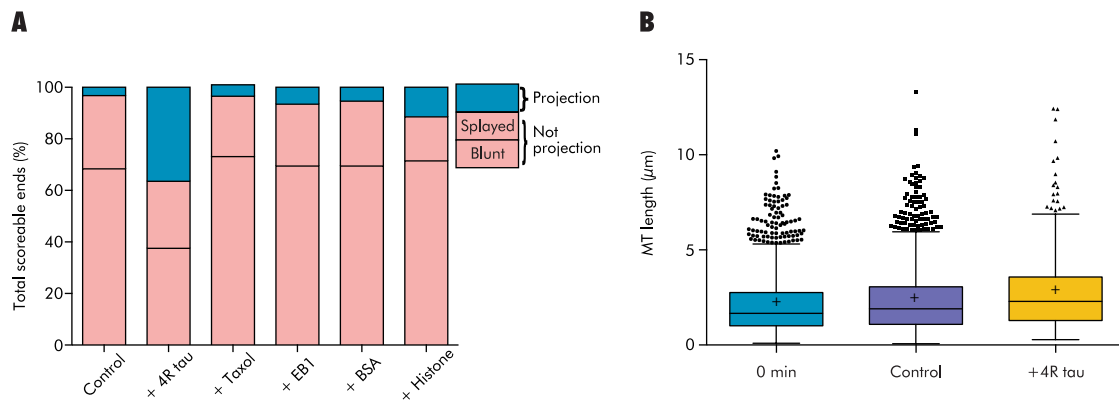
Figure A.1: **Decoration of pre-assembled GMPCPP microtubules with 4R tau.** (A) Specificity of end projections. GMPCPP MTs (0.5 uM) were incubated with 4R tau (10 : 1 tau:tubulin molar ratio), MT-stabilizing drug taxol (5 uM), MT-binding protein EB1 (5 uM), negatively charged BSA (5 uM), or positively charged histone (1.8 uM) in a decoration assay. (B) GMPCPP MT length over time (10 min) after decoration with buffer or 4R tau (1 : 5 tau:tubulin molar ratio).
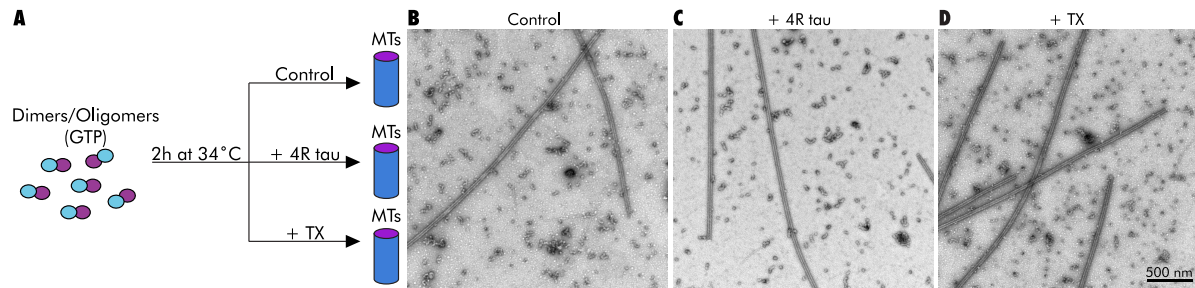
Figure A.2: **Microtubules co-assembled with 4R tau in the presence of GTP are morphologically normal.** (A) Schematic of a GTP co-assembly experiment. (B-D) Tubulin (26 uM) was assembled at $34\,°C$ for 2 h in the presence of 2 mM GTP either alone (B), with 4R tau (1 : 5 tau:tubulin molar ratio) (C), or with 10 uM taxol (TX) (D). All three assembly conditions resulted in morphologically normal MTs.
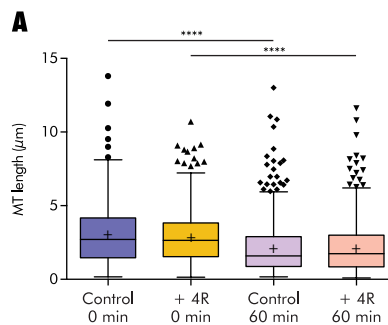
Figure A.3: **Microtubule length decreases as a result of cold-induced disassembly.** (A) Time course lengths of GMPCPP MTs (6.1 uM) cooled to $4\,°C$ in the presence or absence of 4R tau (1 : 4 tau:tubulin molar ratio). Note that while MT length decreases an identical amount over the 60 min incubation period in control and 4R tau-containing samples, the 4R tau-containing samples exhibit numerous projections. **** p <0.0001, *** p <0.001, ** p <0.01, * p <0.05.

Table 1. Effects of 3R and 4R tau on pre-assembled GMPCPP MT projection frequency and length

Condition	Total MT ends (#)	Ends with projections (#)	Projection frequency	CI(L)	CI(U)	Mean projection length (nm)	SEM	CI(L)	CI(U)	Total projections (#)	# expts
CTR	828	52	0.0628	0.045	0.086	138.0	13.0	112.6	164.0	92	19
3R tau	256	148	0.5781	0.503	0.650	275.0	8.9	257.8	293.0	254	2
4R tau	293	169	0.5768	0.507	0.644	245.0	9.3	226.6	263.4	298	3

*all at a constant [tubulin] of 0.5 μM and 1:5 tau:tubulin molar ratio

**values for 95% confidence intervals (CI(L) - CI(U)) of count data were generated by Wilson score

Table A.1: Effects of 3R and 4R tau on pre-assembled GMPCPP MT projection frequency and length.

Table 2. Tubulin concentration dependence of de novo spirals assembled with 4R tau

[Tubulin] (μM)	Spiral length					Spiral abundance					# expts
	Mean length (nm)	SEM	CI(L)	CI(U)	n	Mean per field (#)	SEM	CI(L)	CI(U)	n	
0.9	351.2	10.7	330.2	372.3	374	14.2	1.56	10.97	17.38	28	3
4.5	452.1	27.9	397.1	507.0	200	29.0	2.49	22.91	35.09	7	3
9.1	539.2	26.8	486.4	592.0	209	32.4	2.38	26.74	38.01	8	3

*all at 1:5 tau:tubulin molar ratio

**CI(L) and CI(U) show lower and upper bounds of 95% confidence interval

Table A.2: Tubulin concentration dependence of de novo spirals assembled with 4R tau

Table 3. 4R tau concentration dependence of de novo spirals

Tau:tu molar ratio	Spiral length					Spiral abundance					# expts
	Mean length (nm)	SEM	CI(L)	CI(U)	n	Mean per field (#)	SEM	CI(L)	CI(U)	n	
1:60	466.6	24.3	418.4	514.9	99	11	0.62	9.56	12.44	9	2
1:20	404.1	16.3	371.8	436.5	117	16.71	1.61	12.76	20.66	7	2
1:5	351.2	10.7	330.2	372.3	374	14.18	1.56	10.97	17.38	28	3
1:1	209.9	12.0	186.1	233.7	143	14.4	1.60	10.78	18.02	10	3
5:1	230.2	12.8	204.7	245.1	85	5.73	0.68	4.28	7.191	15	3

*all at a constant [tubulin] of 0.9 μM

**CI(L) and CI(U) show lower and upper bounds of 95% confidence interval

Table A.3: 4R tau concentration dependence of de novo spirals

Table 4. 3R and 4R tau-stabilized de novo spiral length and abundance

Condition	Spiral length					Spiral abundance					# expts
	Mean length (nm)	SEM	CI(L)	CI(U)	n	Mean per field (#)	SEM	CI(L)	CI(U)	n	
CTR	319.0	20.1	278.9	359.0	76	4.12	0.84	2.34	5.90	17	4
3R tau	449.8	14.2	421.8	477.8	181	10.06	0.97	8.02	12.09	18	2
4R tau	402.0	10.7	381.0	423.0	484	13.32	1.26	10.76	15.88	37	4

*all at a constant [tubulin] of 0.9 μM and 1:5 tau:tubulin molar ratio

**CI(L) and CI(U) show lower and upper bounds of 95% confidence interval

Table A.4: 3R and 4R tau-stabilized de novo spiral length and abundance

Table 5. 3R and 4R tau-stabilized disassembly spiral length and abundance

Condition	Spiral length					Spiral abundance					# expts
	Mean length (nm)	SEM	CI(L)	CI(U)	n	Mean per field (#)	SEM	CI(L)	CI(U)	n	
CTR	296.1	22.9	250.6	341.6	93	2.02	0.31	1.39	2.64	52	8
3R tau	324.0	15.7	334.0	396.3	129	3.67	0.74	2.12	5.17	39	6
4R tau	497.0	14.0	601.0	655.9	920	19.17	1.36	16.4	21.9	48	3

*all at a constant [tubulin] of 0.5 μM and 1:5 tau:tubulin molar ratio

**CI(L) and CI(U) show lower and upper bounds of 95% confidence interval

Table A.5:   3R and 4R tau-stabilized disassembly spiral length and abundance

Table 6. Projection frequency and length of pre-assembled GMPCPP MTs decorated with FTDP-17 mutant tau

Condition	Total MT ends (#)	Ends with projections (#)	Projection frequency	CI(L)	CI(U)	Mean projection length (nm)	SEM	CI(L)	CI(U)	# expts
4R/wt	212	78	0.3679	0.306	0.435	252.0	24.0	203.8	299.8	4
K280	136	36	0.2647	0.198	0.345	248.0	37.9	170.6	324.8	4
P301L	150	37	0.2467	0.185	0.321	171.0	23.0	124.3	217.7	4
R406W	104	30	0.2885	0.210	0.382	191.0	21.3	148.1	233.8	3

*all at a constant [tubulin] of 0.5 μM and 1:5 tau:tubulin molar ratio

**values for 95% confidence intervals (CI(L) - CI(U)) of count data were generated by Wilson score

Table A.6:   Projection frequency and length of pre-assembled GMPCPP MTs decorated with FTDP-17 mutant tau

Table 7. FTDP-17 mutant tau-stabilized disassembly spiral length and abundance

Condition	Spiral length					Spiral abundance					# expts
	Mean length (nm)	SEM	CI(L)	CI(U)	n	Mean per field (#)	SEM	CI(L)	CI(U)	n	
4R/wt	569.7	18.4	533.5	605.9	383	7.938	0.59	6.74	9.13	48	5
P301L	441.8	27.4	387.5	496.2	113	3.929	0.95	1.98	5.88	28	3
K280	297.4	24.3	249.4	345.4	128	4.357	0.89	2.54	6.18	28	3
R406W	578.8	29.8	520.0	637.7	163	5.258	0.54	4.15	6.36	31	3

*all at a constant [tubulin] of 0.5 μM and 1:5 tau:tubulin molar ratio

**CI(L) and CI(U) show lower and upper bounds of 95% confidence interval

Table A.7:   FTDP-17 mutant tau-stabilized disassembly spiral length and abundance

Appendix B

Supplementary information for Chapter 4
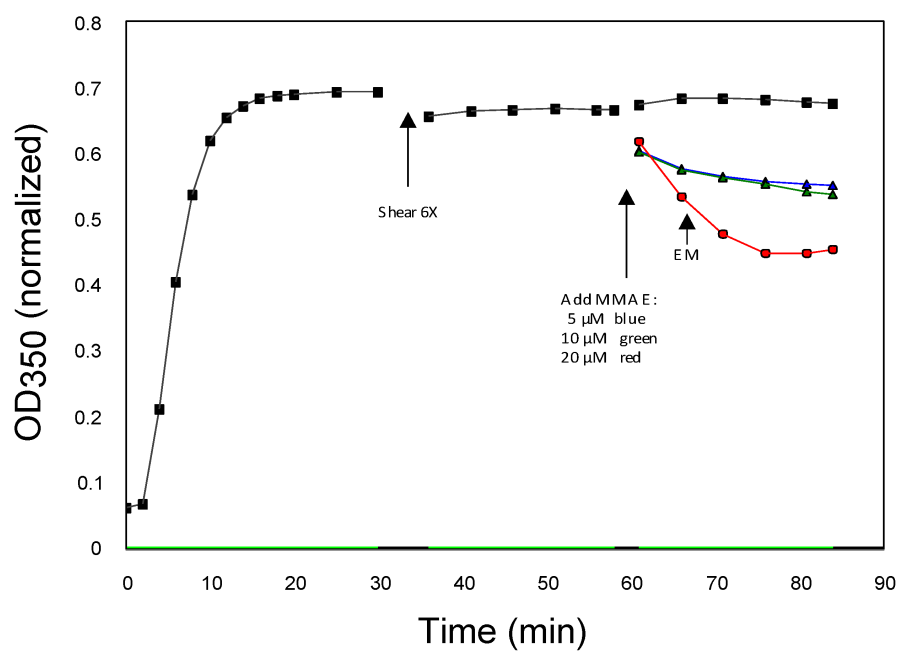
Figure B.1: **Light scattering analyses under conditions used for MMAE MT binding assays.** MAP-rich tubulin was mixed on ice with 1 mM GTP, and then assembly mixtures were transferred to a spectrophotometer at 30 °C. In order to increase the number of MTs in the reaction, the MTs were sheared with a syringe needle after 30 min during the initial phase and again after a total of 60 min. After allowing time for the mixture to re-establish steady state, varying concentrations of MMAE were added. Samples were prepared for EM 6 min post-MMAE addition (the incubation time used for MT binding experiments), while light scattering at 350 nm was monitored for an additional 25 min.
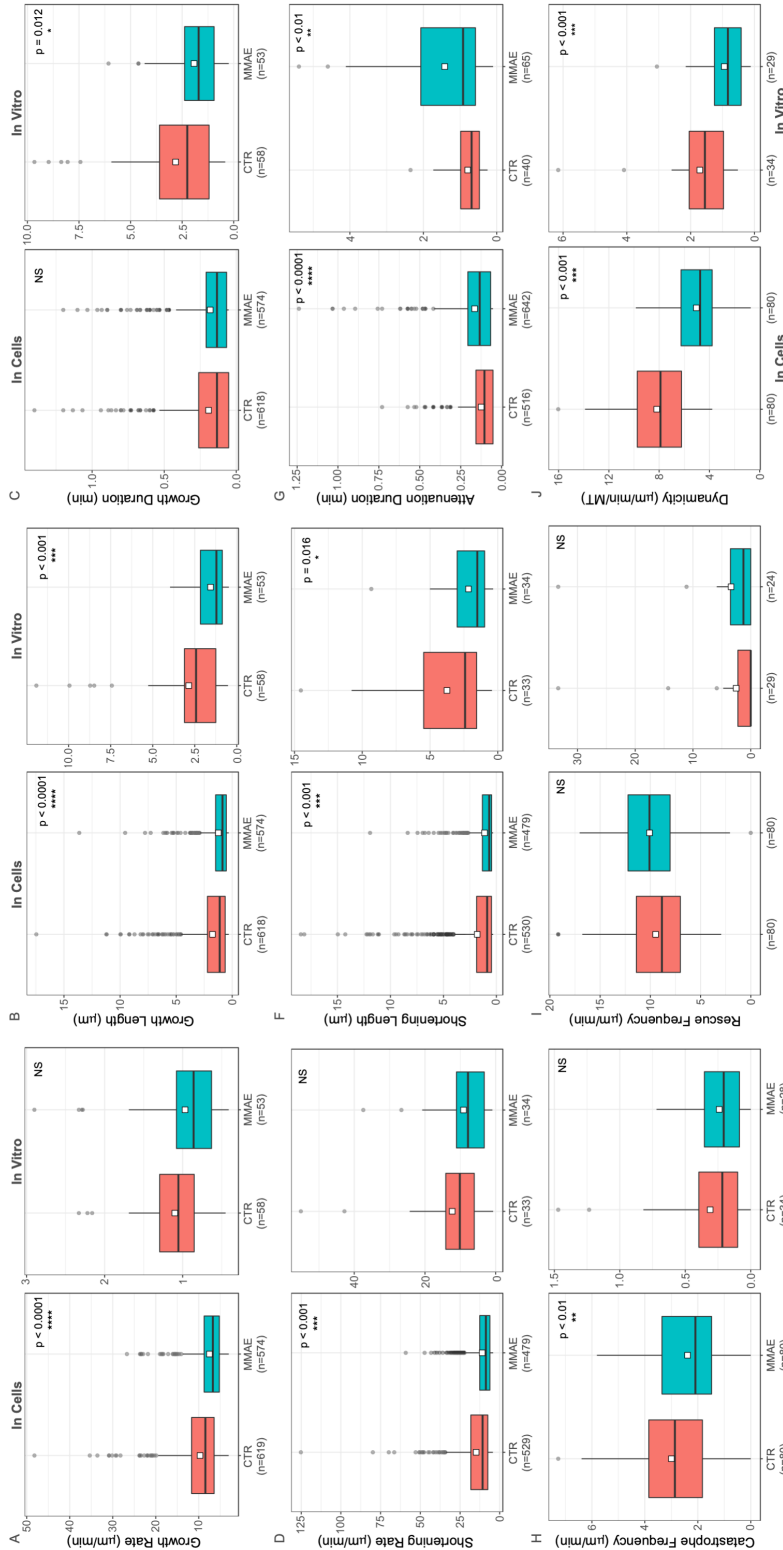
Figure B.2: **MMAE suppressed microtubule dynamic instability in cells and in vitro.** Panels show the effect of free MMAE in MCF7 cells (0.5 nM MMAE; left side of each panel) and in an in vitro system with MAP-free tubulin isolated from bovine brain (100 nM MMAE; right side of each panel). For definitions of each parameter, see 4.7. Graphs are box plots in which the horizontal line shows the median, the box shows the boundaries of the interquartile range (25th – 75th percentile), the whiskers show 1.5 times the interquartile range, and data points outside the whiskers are shown individually. A white diamond indicates the mean.

152
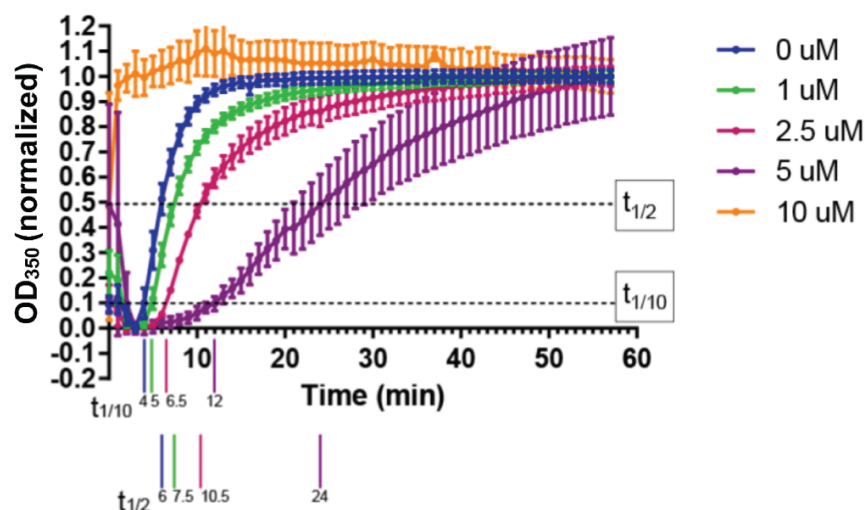
Figure B.3: **MMAE effects upon the kinetics of MAP-rich microtubule assembly, as indicated by an increase in the time required to achieve maximal assembly.** Data are the same as presented in Figure 4.5A, but here the data within each condition are scaled such that each assembly curve starts at 0 and ends at 1. This graph was used to visually estimate the time at which each condition reached one half its maximal assembly ($t_{1/2}$). The time required to reach one tenth of the maximal assembly ($t_{1/10}$) was also estimated, as it has been argued to be a better metric for microtubule assembly [Bonfils et al., 2007, Voter and Erickson, 1984]. MMAE increased both values in a concentration-dependent manner. Note that the data at 10 uM MMAE are an exception because there was almost no assembly at that concentration.
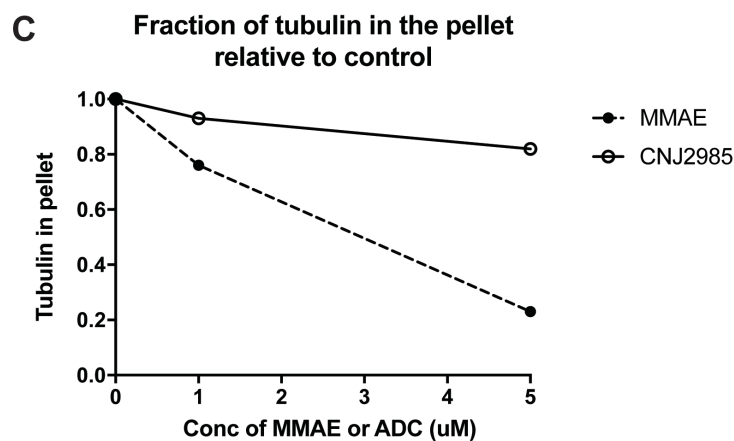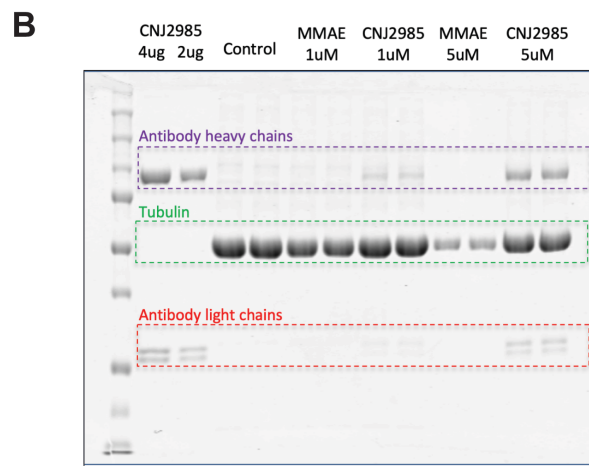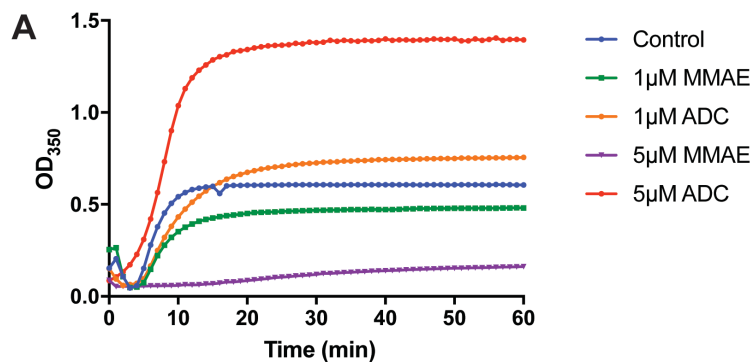
Figure B.4: **Free MMAE reduces MT assembly in vitro at lower concentrations than the MMAE-ADC.** A) Light scattering assay of MT assembly with MAP-rich tubulin (2.33 mg/mL) and 1 or 5 uM as a free drug or an ADC (same experimental conditions as in Fig. 4.5). The presence of the ADC increases light scattering in a concentration-dependent manner. B) After 1 hr of assembly samples were centrifuged and then the pellets were analyzed by SDS-PAGE and Coomassie stain in order to determine what fraction of the pellet was tubulin. C) The data in panel B were used to correct Bradford measurements of total protein in the pellet and to quantify the amount of tubulin in the pellet as a percent of total tubulin in each starting sample. Data are from one experiment.
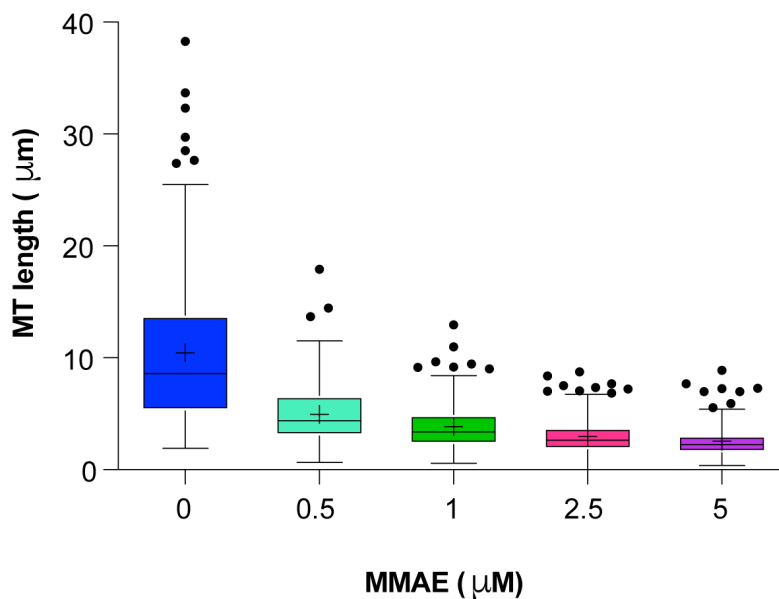
	0 μM	0.5 μM	1 μM	2.5 μM	5 μM
Median (μm)	4.38	3.40	2.64	2.24	7.76
Mean	10.44	4.94	3.86	2.97	2.55
SD	6.78	2.65	2.13	1.62	1.41
SEM	0.48	0.18	0.12	0.10	0.09
MTs measured (n)	196	220	307	268	251

Figure B.5: **Microtubules formed in the presence of MMAE are shorter than control microtubules.** Data are from one of the MT assembly experiments shown in Figure 4.5. MAP-rich tubulin (∼30 uM) was mixed on ice with varying concentrations of MMAE, and then transferred to 30 °C and allowed to assemble for 1 h, at which time samples were removed and prepared for transmission electron microscopy. Top panel: Boxplots of MT length in each condition, with a horizontal line at the median, Tukey-style whiskers showing 1.5 times the interquartile range, and more extreme data points shown individually. Means are indicated by "+" symbols. Bottom panel: Summary statistics.
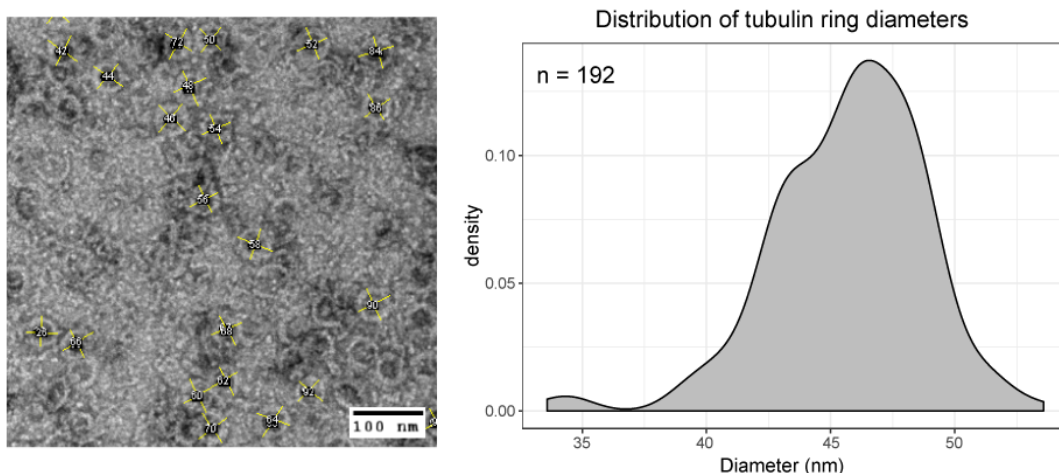
Figure B.6: **Morphology of tubulin rings formed in the presence of MMAE.**
Left: Transmission electron micrograph of MAP-rich tubulin (2.5 mg/mL) assembled
in the presence of 10 uM MMAE (from an experiment shown in Figure 4.5). The
overlay (yellow) shows measurements of ring diameter made in ImageJ. Each ring was
measured twice and the average was taken. Right: The distribution of average ring
diameter measurements from 192 rings, taken from four micrographs and 2 different
experiments. Mean = 45.7 nm, SD = 3.05 nm, SEM = 0.22 nm.
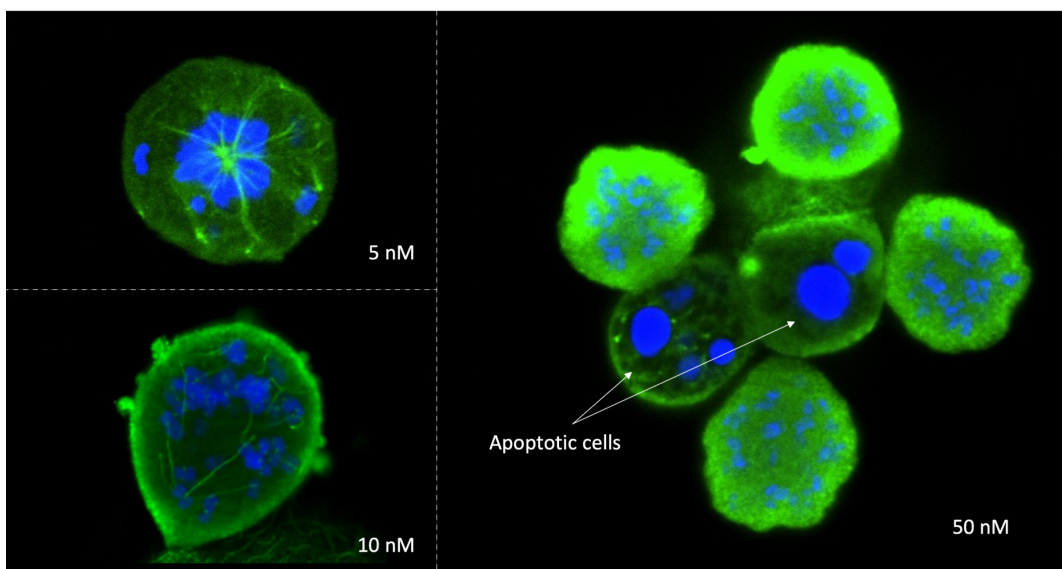
Figure B.7: **High concentrations of free MMAE lead to complete depoly-
merization of the microtubule network and cell death.** Panels show the effect
of free MMAE at concentrations of 5 nM, 10 nM, and 50 nM on MCF7 cells, includ-
ing the complete loss of the microtubule network (anti-α-tubulin, green) and nuclear
fragmentation (DAPI, blue).

Bibliography

A. Aguzzi and M. Altmeyer. Phase separation: Linking cellular compartmentalization to disease. *Trends Cell Biol*, 26(7):547–558, 2016. ISSN 1879-3088 (Electronic) 0962-8924 (Linking). doi: 10.1016/j.tcb.2016.03.004. URL `https://www.ncbi.nlm.nih.gov/pubmed/27051975`.

A. Akhmanova. Strengthening microtubules by cuts that heal. *Dev Cell*, 47(4):400–401, 2018. ISSN 1534-5807. doi: 10.1016/j.devcel.2018.11.002.

A. Akhmanova and M. O. Steinmetz. Control of microtubule organization and dynamics: two ends in the limelight. *Nat Rev Mol Cell Biol*, 16(12):711–26, 2015. ISSN 1471-0072. doi: 10.1038/nrm4084.

Jawdat Al-Bassam, Rachel S. Ozer, Daniel Safer, Shelley Halpain, and Ronald A. Milligan. Map2 and tau bind longitudinally along the outer ridges of microtubule protofilaments. *The Journal of Cell Biology*, 157(7):1187–1196, 2002. ISSN 0021-9525 1540-8140. doi: 10.1083/jcb.200201048.

P. H. Alday and J. J. Correia. Macromolecular interaction of halichondrin b analogues eribulin (e7389) and er-076349 with tubulin by analytical ultracentrifugation. *Biochemistry*, 48(33):7927–38, 2009. ISSN 1520-4995 (Electronic) 0006-2960 (Linking). doi: 10.1021/bi900776u. URL `https://www.ncbi.nlm.nih.gov/pubmed/19586046`.

L. Almeida-Souza, V. Timmerman, and S. Janssens. Microtubule dynamics in the peripheral nervous system: A matter of balance. *Bioarchitecture*, 1(6):267–270, 2011. ISSN 1949-0992 (Print) 1949-0992. doi: 10.4161/bioa.1.6.19198.

G. M. Alushin, G. C. Lander, E. H. Kellogg, R. Zhang, D. Baker, and E. Nogales. High-resolution microtubule structures reveal the structural transitions in alphabeta-tubulin upon gtp hydrolysis. *Cell*, 157(5):1117–29, 2014. ISSN 1097-4172 (Electronic) 0092-8674 (Linking). doi: 10.1016/j.cell.2014.03.053. URL `https://www.ncbi.nlm.nih.gov/pubmed/24855948`.

US. Alzheimer's Association. 2017 alzheimer's disease facts and figures. *Alzheimer's Dementia: The Journal of the Alzheimer's Association*, 13(4):325–373, 2017. ISSN 1552-5279(Electronic),1552-5260(Print). doi: 10.1016/j.jalz.2017.02.001.

G. Amadoro, M. T. Ciotti, M. Costanzi, V. Cestari, P. Calissano, and N. Canu. Nmda receptor mediates tau-induced neurotoxicity by calpain and erk/mapk activation. *Proc Natl Acad Sci U S A*, 103(8):2892–7, 2006. ISSN 0027-8424 (Print). doi: 0511065103[pii]10.1073/pnas.0511065103. URL `http://www.ncbi.nlm.nih.gov/entrez/query.fcgi?cmd=Retrieve&db=PubMed&dopt=Citation&list_uids=16477009`.

L. A. Amos and J. Lowe. How taxol stabilises microtubule structure. *Chem Biol*, 6(3): R65–9, 1999. ISSN 1074-5521 (Print) 1074-5521 (Linking). URL `https://www.ncbi.nlm.nih.gov/pubmed/10074470`.

A. A. Argyriou, P. Marmiroli, G. Cavaletti, and H. P. Kalofonos. Epothilone-induced peripheral neuropathy: a review of current knowledge. *J Pain Symptom Manage*, 42(6):931–40, 2011. ISSN 1873-6513 (Electronic) 0885-3924 (Linking). doi: S0885-3924(11)00208-9[pii]10.1016/j.jpainsymman.2011.02.022. URL `http://www.ncbi.nlm.nih.gov/entrez/query.fcgi?cmd=Retrieve&db=PubMed&dopt=Citation&list_uids=21621965`.

A. A. Argyriou, J. Bruna, P. Marmiroli, and G. Cavaletti. Chemotherapy-induced peripheral neurotoxicity (cipn): An update. *Crit Rev Oncol Hematol*, 82(1):51–77, 2012. ISSN 1879-0461 (Electronic) 1040-8428 (Linking). doi: S1040-8428(11)00131-4[pii]10.1016/j.critrevonc.2011.04.012. URL `http://www.ncbi.nlm.nih.gov/entrez/query.fcgi?cmd=Retrieve&db=PubMed&dopt=Citation&list_uids=21908200`.

I. Arnal, E. Karsenti, and A. A. Hyman. Structural transitions at microtubule ends correlate with their dynamic properties in xenopus egg extracts. *J Cell Biol*, 149(4): 767–74, 2000. ISSN 0021-9525 (Print) 0021-9525 (Linking). URL `https://www.ncbi.nlm.nih.gov/pubmed/10811818`.

Isabelle Arnal, Claire Heichette, Georgios S. Diamantopoulos, and Denis Chrétien. Clip-170/tubulin-curved oligomers coassemble at microtubule ends and promote rescues. *Current Biology*, 14(23):2086–2095, 2004. ISSN 0960-9822. doi: 10.1016/j.cub.2004.11.055. URL `https://dx.doi.org/10.1016/j.cub.2004.11.055`.

Joseph Atherton, Kai Jiang, Marcel M. Stangier, Yanzhang Luo, Shasha Hua, Klaartje Houben, Jolien J. E. van Hooff, Agnel-Praveen Joseph, Guido Scarabelli, Barry J. Grant, Anthony J. Roberts, Maya Topf, Michel O. Steinmetz, Marc Baldus, Carolyn A. Moores, and Anna Akhmanova. A structural model for microtubule minus-end recognition and protection by camsap proteins. *Nature Structural Molecular Biology*, 24(11):931–943, 2017. ISSN 1545-9985. doi: 10.1038/nsmb.3483. URL `https://doi.org/10.1038/nsmb.3483`.

J. C. Augustinack, J. L. Sanders, L. H. Tsai, and B. T. Hyman. Colocalization and fluorescence resonance energy transfer between cdk5 and at8 suggests a close association in pre-neurofibrillary tangles and neurofibrillary tangles. *J Neuropathol Exp Neurol*,

61(6):557–64, 2002. URL `http://www.ncbi.nlm.nih.gov/entrez/query.fcgi?cmd=Retrieve&db=PubMed&dopt=Citation&list_uids=12071639`.

Charlotte Aumeier, Laura Schaedel, Jérémie Gaillard, Karin John, Laurent Blanchoin, and Manuel Théry. Self-repair promotes microtubule rescue. *Nature cell biology*, 18(10):1054–1064, 2016. ISSN 1476-4679 1465-7392. doi: 10.1038/ncb3406. URL `https://pubmed.ncbi.nlm.nih.gov/27617929https://www.ncbi.nlm.nih.gov/pmc/articles/PMC5045721/`.

O. Azarenko, G. Smiyun, J. Mah, L. Wilson, and M. A. Jordan. Antiproliferative mechanism of action of the novel taxane cabazitaxel as compared with the parent compound docetaxel in mcf7 breast cancer cells. *Mol Cancer Ther*, 13(8):2092–103, 2014. ISSN 1538-8514 (Electronic) 1535-7163 (Linking). doi: 10.1158/1535-7163.MCT-14-0265. URL `https://www.ncbi.nlm.nih.gov/pubmed/24980947`.

P. W. Baas, A. N. Rao, A. J. Matamoros, and L. Leo. Stability properties of neuronal microtubules. *Cytoskeleton (Hoboken)*, 73(9):442–60, 2016. ISSN 1949-3592 (Electronic) 1949-3592 (Linking). doi: 10.1002/cm.21286. URL `https://www.ncbi.nlm.nih.gov/pubmed/26887570`.

Jürg Bähler, Julien Mozziconacci, Linda Sandblad, Malte Wachsmuth, Damian Brunner, and Eric Karsenti. Tubulin dimers oligomerize before their incorporation into microtubules. *PLoS ONE*, 3(11):e3821, 2008. ISSN 1932-6203. doi: 10.1371/journal.pone.0003821.

R. Bai, G. F. Taylor, J. M. Schmidt, M. D. Williams, J. A. Kepler, G. R. Pettit, and E. Hamel. Interaction of dolastatin 10 with tubulin: induction of aggregation and binding and dissociation reactions. *Mol Pharmacol*, 47(5):965–76, 1995. ISSN 0026-895X (Print) 0026-895X (Linking). URL `https://www.ncbi.nlm.nih.gov/pubmed/7746283`.

R. L. Bai, G. R. Pettit, and E. Hamel. Binding of dolastatin 10 to tubulin at a distinct site for peptide antimitotic agents near the exchangeable nucleotide and vinca alkaloid sites. *J Biol Chem*, 265(28):17141–9, 1990. ISSN 0021-9258 (Print) 0021-9258 (Linking). URL `https://www.ncbi.nlm.nih.gov/pubmed/2211617`.

L. Balabanian, C. L. Berger, and A. G. Hendricks. Acetylated microtubules are preferentially bundled leading to enhanced kinesin-1 motility. *Biophys J*, 113(7):1551–1560, 2017. ISSN 0006-3495. doi: 10.1016/j.bpj.2017.08.009.

P. Barbier, O. Zejneli, M. Martinho, A. Lasorsa, V. Belle, C. Smet-Nocca, P. O. Tsvetkov, F. Devred, and I. Landrieu. Role of tau as a microtubule-associated protein: Structural and functional aspects. *Front Aging Neurosci*, 11:204, 2019. ISSN 1663-4365 (Print) 1663-4365. doi: 10.3389/fnagi.2019.00204.

S. Barghorn, Q. Zheng-Fischhofer, M. Ackmann, J. Biernat, M. von Bergen, and E. Mandelkow. Structure, microtubule interactions, and paired helical filament aggregation by tau mutants of frontotemporal dementias. *Biochemistry*, 39(38):11714–21, 2000.

S. Barghorn, J. Biernat, and E. Mandelkow. Purification of recombinant tau protein and preparation of alzheimer-paired helical filaments in vitro. *Methods Mol Biol*, 299: 35–51, 2005. ISSN 1064-3745 (Print) 1064-3745 (Linking). URL `https://www.ncbi.nlm.nih.gov/pubmed/15980594`.

S. J. Benbow, K. M. Wozniak, B. Kulesh, A. Savage, B. S. Slusher, B. A. Littlefield, M. A. Jordan, L. Wilson, and S. C. Feinstein. Microtubule-targeting agents eribulin and paclitaxel differentially affect neuronal cell bodies in chemotherapy-induced peripheral neuropathy. *Neurotox Res*, 32(1):151–162, 2017. ISSN 1476-3524 (Electronic) 1029-8428 (Linking). doi: 10.1007/s12640-017-9729-6. URL `https://www.ncbi.nlm.nih.gov/pubmed/28391556`.

Johanna Bendell, George Blumenschein, Ralph Zinner, David Hong, Suzanne Jones, Jeffrey Infante, Howard Burris, Prabhu Rajagopalan, Martin Kornacker, David Henderson, Andrea Kelly, and Raffit Hassan. Abstract lb-291: First-in-human phase i dose escalation study of a novel anti-mesothelin antibody drug conjugate (adc), bay 94-9343, in patients with advanced solid tumors. *Cancer Research*, 73(8 Supplement): LB–291–LB–291, 2013. doi: 10.1158/1538-7445.Am2013-lb-291.

R. L. Best, P. J. Chung, S. J. Benbow, A. Savage, N. E. LaPointe, C. R. Safinya, and S. C. Feinstein. Expression and isolation of recombinant tau. *Methods Cell Biol*, 141:3–26, 2017. ISSN 0091-679X (Print) 0091-679X (Linking). doi: 10.1016/bs.mcb.2017.06.001. URL `https://www.ncbi.nlm.nih.gov/pubmed/28882309`.

Rebecca L. Best, Nichole E. LaPointe, Jiahao Liang, Kevin Ruan, Madeleine F. Shade, Leslie Wilson, and Stuart C. Feinstein. Tau isoform-specific stabilization of intermediate states during microtubule assembly and disassembly. *J Biol Chem*, 294(33): 12265–12280, 2019. doi: 10.1074/jbc.RA119.009124. URL `http://www.jbc.org/content/early/2019/07/02/jbc.RA119.009124.abstract`.

P. Bieling, L. Laan, H. Schek, E. L. Munteanu, L. Sandblad, M. Dogterom, D. Brunner, and T. Surrey. Reconstitution of a microtubule plus-end tracking system in vitro. *Nature*, 450(7172):1100–5, 2007. ISSN 0028-0836. doi: 10.1038/nature06386.

J. Biernat, N. Gustke, G. Drewes, E. M. Mandelkow, and E. Mandelkow. Phosphorylation of ser262 strongly reduces binding of tau to microtubules: distinction between phf-like immunoreactivity and microtubule binding. *Neuron*, 11(1):153–63, 1993. ISSN 0896-6273 (Print) 0896-6273 (Linking). URL `https://www.ncbi.nlm.nih.gov/pubmed/8393323`.

D. M. Bollag, P. A. McQueney, J. Zhu, O. Hensens, L. Koupal, J. Liesch, M. Goetz, E. Lazarides, and C. M. Woods. Epothilones, a new class of microtubule-stabilizing agents with a taxol-like mechanism of action. *Cancer Res*, 55(11):2325–33, 1995. ISSN 0008-5472 (Print) 0008-5472 (Linking). URL `https://www.ncbi.nlm.nih.gov/pubmed/7757983`.

C. Bonfils, N. Bec, B. Lacroix, M. C. Harricane, and C. Larroque. Kinetic analysis of tubulin assembly in the presence of the microtubule-associated protein togp. *J Biol Chem*, 282(8):5570–81, 2007. ISSN 0021-9258 (Print) 0021-9258. doi: 10.1074/jbc. M605641200.

E. Braak, H. Braak, and E. M. Mandelkow. A sequence of cytoskeleton changes related to the formation of neurofibrillary tangles and neuropil threads. *Acta Neuropathol*, 87 (6):554–67, 1994.

R. Brandt and G. Lee. Functional organization of microtubule-associated protein tau. identification of regions which affect microtubule growth, nucleation, and bundle formation in vitro. *J Biol Chem*, 268(5):3414–9, 1993. URL `http://www.ncbi.nlm.nih.gov/entrez/query.fcgi?cmd=Retrieve&db=PubMed&dopt=Citation&list_uids=8429017`.

G. Breuzard, P. Hubert, R. Nouar, T. De Bessa, F. Devred, P. Barbier, J. N. Sturgis, and V. Peyrot. Molecular mechanisms of tau binding to microtubules and its role in microtubule dynamics in live cells. *J Cell Sci*, 126(Pt 13):2810–9, 2013. ISSN 1477-9137 (Electronic) 0021-9533 (Linking). doi: 10.1242/jcs.120832. URL `https://www.ncbi.nlm.nih.gov/pubmed/23659998`.

G. J. Brouhard and L. M. Rice. The contribution of alphabeta-tubulin curvature to microtubule dynamics. *J Cell Biol*, 207(3):323–34, 2014. ISSN 1540-8140 (Electronic) 0021-9525 (Linking). doi: 10.1083/jcb.201407095. URL `https://www.ncbi.nlm.nih.gov/pubmed/25385183`.

Gary J. Brouhard and Luke M. Rice. Microtubule dynamics: an interplay of biochemistry and mechanics. *Nature Reviews Molecular Cell Biology*, 19(7):451–463, 2018. ISSN 1471-0080. doi: 10.1038/s41580-018-0009-y. URL `https://doi.org/10.1038/s41580-018-0009-y`.

K. R. Brunden, J. Q. Trojanowski, and V. M. Lee. Advances in tau-focused drug discovery for alzheimer's disease and related tauopathies. *Nature Reviews Drug Discovery*, 8(10):783–93, 2009. ISSN 1474-1784 (Electronic) 1474-1776 (Linking). doi: nrd2959[pii]10.1038/nrd2959. URL `http://www.ncbi.nlm.nih.gov/entrez/query.fcgi?cmd=Retrieve&db=PubMed&dopt=Citation&list_uids=19794442`.

K. R. Brunden, B. Zhang, J. Carroll, Y. Yao, J. S. Potuzak, A. M. Hogan, M. Iba, M. J. James, S. X. Xie, C. Ballatore, 3rd Smith, A. B., V. M. Lee, and J. Q. Trojanowski. Epothilone d improves microtubule density, axonal integrity, and cognition

in a transgenic mouse model of tauopathy. *J Neurosci*, 30(41):13861–6, 2010. ISSN 1529-2401 (Electronic) 0270-6474 (Linking). doi: 10.1523/JNEUROSCI.3059-10.2010. URL `https://www.ncbi.nlm.nih.gov/pubmed/20943926`.

K. R. Brunden, V. M. Lee, 3rd Smith, A. B., J. Q. Trojanowski, and C. Ballatore. Altered microtubule dynamics in neurodegenerative disease: Therapeutic potential of microtubule-stabilizing drugs. *Neurobiol Dis*, 105:328–335, 2017. ISSN 1095-953X (Electronic) 0969-9961 (Linking). doi: 10.1016/j.nbd.2016.12.021. URL `https://www.ncbi.nlm.nih.gov/pubmed/28012891`.

J. M. Bunker, L. Wilson, M. A. Jordan, and S. C. Feinstein. Modulation of microtubule dynamics by tau in living cells: implications for development and neurodegeneration. *Mol Biol Cell*, 15(6):2720–8, 2004. URL `http://www.ncbi.nlm.nih.gov/entrez/query.fcgi?cmd=Retrieve&db=PubMed&dopt=Citation&list_uids=15020716`.

J. M. Bunker, K. Kamath, L. Wilson, M. A. Jordan, and S. C. Feinstein. Ftdp-17 mutations compromise the ability of tau to regulate microtubule dynamics in cells. *J Biol Chem*, 281(17):11856–63, 2006. ISSN 0021-9258 (Print) 0021-9258 (Linking). doi: 10.1074/jbc.M509420200. URL `https://www.ncbi.nlm.nih.gov/pubmed/16495230`.

K. A. Butner and M. W. Kirschner. Tau protein binds to microtubules through a flexible array of distributed weak sites. *Journal of Cell Biology*, 115(3):717–30, 1991. ISSN 0021-9525 (Print).

A. Caceres and K. S. Kosik. Inhibition of neurite polarity by tau antisense oligonucleotides in primary cerebellar neurons. *Nature*, 343(6257):461–3, 1990. URL `http://www.ncbi.nlm.nih.gov/entrez/query.fcgi?cmd=Retrieve&db=PubMed&dopt=Citation&list_uids=2105469`.

M. Caplow. Microtubule dynamics. *Curr Opin Cell Biol*, 4(1):58–65, 1992. ISSN 0955-0674 (Print) 0955-0674. doi: 10.1016/0955-0674(92)90059-l.

M. Caplow and J. Shanks. Evidence that a single monolayer tubulin-gtp cap is both necessary and sufficient to stabilize microtubules. *Mol Biol Cell*, 7(4):663–75, 1996. ISSN 1059-1524 (Print) 1059-1524. doi: 10.1091/mbc.7.4.663.

M. F. Carlier. Nucleotide hydrolysis regulates the dynamics of actin filaments and microtubules. *Philos Trans R Soc Lond B Biol Sci*, 336(1276):93–7, 1992. ISSN 0962-8436 (Print) 0962-8436. doi: 10.1098/rstb.1992.0048.

K. Carlson and A. J. Ocean. Peripheral neuropathy with microtubule-targeting agents: occurrence and management approach. *Clin Breast Cancer*, 11(2):73–81, 2011. ISSN 1938-0666 (Electronic) 1526-8209 (Linking). doi: S1526-8209(11)00007-3[pii]10.1016/j.clbc.2011.03.006. URL `http://www.ncbi.nlm.nih.gov/entrez/query.fcgi?cmd=Retrieve&db=PubMed&dopt=Citation&list_uids=21569993`.

B. T. Castle, S. McCubbin, L. S. Prahl, J. N. Bernens, D. Sept, and D. J. Odde. Mechanisms of kinetic stabilization by the drugs paclitaxel and vinblastine. *Mol Biol Cell*, 28 (9):1238–1257, 2017. ISSN 1939-4586 (Electronic) 1059-1524 (Linking). doi: 10.1091/ mbc.E16-08-0567. URL `https://www.ncbi.nlm.nih.gov/pubmed/28298489`.

Brian T. Castle, Kristen M. McKibben, Elizabeth Rhoades, and David J. Odde. Tau avoids the gtp cap at growing microtubule plus ends. *bioRxiv*, page 2019.12.31.891234, 2020. doi: 10.1101/2019.12.31.891234. URL `https://www.biorxiv.org/content/ biorxiv/early/2020/01/01/2019.12.31.891234.full.pdf`.

N. Caudron, I. Arnal, E. Buhler, D. Job, and O. Valiron. Microtubule nucleation from stable tubulin oligomers. *J Biol Chem*, 277(52):50973–9, 2002. URL `http://www.ncbi.nlm.nih.gov/entrez/query.fcgi?cmd=Retrieve& db=PubMed&dopt=Citation&list_uids=12393880`.

S. M. Chambers, Y. Qi, Y. Mica, G. Lee, X. J. Zhang, L. Niu, J. Bilsland, L. Cao, E. Stevens, P. Whiting, S. H. Shi, and L. Studer. Combined small-molecule inhibition accelerates developmental timing and converts human pluripotent stem cells into nociceptors. *Nat Biotechnol*, 30(7):715–20, 2012. ISSN 1546-1696 (Electronic) 1087-0156 (Linking). doi: 10.1038/nbt.2249. URL `https://www.ncbi.nlm.nih.gov/pubmed/ 22750882`.

J. Chen, Y. Kanai, N. J. Cowan, and N. Hirokawa. Projection domains of map2 and tau determine spacings between microtubules in dendrites and axons. *Nature*, 360(6405):674–7, 1992. ISSN 0028-0836 (Print) 0028-0836 (Linking). doi: 10.1038/360674a0. URL `http://www.ncbi.nlm.nih.gov/entrez/query.fcgi?cmd= Retrieve&db=PubMed&dopt=Citation&list_uids=1465130`.

M. C. Choi, U. Raviv, H. P. Miller, M. R. Gaylord, E. Kiris, D. Ventimiglia, D. J. Needleman, M. W. Kim, L. Wilson, S. C. Feinstein, and C. R. Safinya. Human microtubule-associated-protein tau regulates the number of protofilaments in microtubules: a synchrotron x-ray scattering study. *Biophys J*, 97(2):519–27, 2009. ISSN 1542-0086 (Electronic) 0006-3495 (Linking). doi: S0006-3495(09)00953-9[pii]10.1016/ j.bpj.2009.04.047. URL `http://www.ncbi.nlm.nih.gov/entrez/query.fcgi?cmd= Retrieve&db=PubMed&dopt=Citation&list_uids=19619466`.

D. Chretien, S. D. Fuller, and E. Karsenti. Structure of growing microtubule ends: two-dimensional sheets close into tubes at variable rates. *J Cell Biol*, 129(5):1311–28, 1995. ISSN 0021-9525 (Print) 0021-9525 (Linking). URL `https://www.ncbi.nlm.nih.gov/ pubmed/7775577`.

D. W. Cleveland, S. Y. Hwo, and M. W. Kirschner. Physical and chemical properties of purified tau factor and the role of tau in microtubule assembly. *J Mol Biol*, 116 (2):227–47, 1977. URL `http://www.ncbi.nlm.nih.gov/entrez/query.fcgi?cmd= Retrieve&db=PubMed&dopt=Citation&list_uids=146092`.

T. J. Cohen, J. L. Guo, D. E. Hurtado, L. K. Kwong, I. P. Mills, J. Q. Trojanowski, and V. M. Lee. The acetylation of tau inhibits its function and promotes pathological tau aggregation. *Nat Commun*, 2:252, 2011. ISSN 2041-1723 (Electronic) 2041-1723 (Linking). doi: 10.1038/ncomms1255. URL `https://www.ncbi.nlm.nih.gov/pubmed/21427723`.

B. Combs and T. C. Gamblin. Ftdp-17 tau mutations induce distinct effects on aggregation and microtubule interactions. *Biochemistry*, 51(43):8597–607, 2012. ISSN 1520-4995 (Electronic) 0006-2960 (Linking). doi: 10.1021/bi3010818. URL `http://www.ncbi.nlm.nih.gov/entrez/query.fcgi?cmd=Retrieve&db=PubMed&dopt=Citation&list_uids=23043292`.

C. Conde and A. Caceres. Microtubule assembly, organization and dynamics in axons and dendrites. *Nat Rev Neurosci*, 10(5):319–32, 2009. ISSN 1471-003x. doi: 10.1038/nrn2631.

C. Cook, Y. Carlomagno, T. F. Gendron, J. Dunmore, K. Scheffel, C. Stetler, M. Davis, D. Dickson, M. Jarpe, M. DeTure, and L. Petrucelli. Acetylation of the kxgs motifs in tau is a critical determinant in modulation of tau aggregation and clearance. *Hum Mol Genet*, 23(1):104–16, 2014. ISSN 1460-2083 (Electronic) 0964-6906 (Linking). doi: 10.1093/hmg/ddt402. URL `https://www.ncbi.nlm.nih.gov/pubmed/23962722`.

K. Cox, B. Combs, B. Abdelmesih, G. Morfini, S. T. Brady, and N. M. Kanaan. Analysis of isoform-specific tau aggregates suggests a common toxic mechanism involving similar pathological conformations and axonal transport inhibition. *Neurobiol Aging*, 47:113–126, 2016. ISSN 1558-1497 (Electronic) 0197-4580 (Linking). doi: 10.1016/j.neurobiolaging.2016.07.015. URL `https://www.ncbi.nlm.nih.gov/pubmed/27574109`.

D. A. Dabydeen, J. C. Burnett, R. Bai, P. Verdier-Pinard, S. J. Hickford, G. R. Pettit, J. W. Blunt, M. H. Munro, R. Gussio, and E. Hamel. Comparison of the activities of the truncated halichondrin b analog nsc 707389 (e7389) with those of the parent compound and a proposed binding site on tubulin. *Mol Pharmacol*, 70(6):1866–75, 2006. ISSN 0026-895X (Print) 0026-895X (Linking). doi: 10.1124/mol.106.026641. URL `https://www.ncbi.nlm.nih.gov/pubmed/16940412`.

H. de Forges, A. Pilon, I. Cantaloube, A. Pallandre, A. M. Haghiri-Gosnet, F. Perez, and C. Pous. Localized mechanical stress promotes microtubule rescue. *Curr Biol*, 26(24): 3399–3406, 2016. ISSN 0960-9822. doi: 10.1016/j.cub.2016.10.048.

Erik W. Dent. Of microtubules and memory: implications for microtubule dynamics in dendrites and spines. *Molecular Biology of the Cell*, 28(1):1–8, 2017. ISSN 1059-1524. doi: 10.1091/mbc.e15-11-0769. URL `https://doi.org/10.1091/mbc.e15-11-0769`.

A. Desai and T. J. Mitchison. Microtubule polymerization dynamics. *Annu Rev Cell Dev Biol*, 13:83–117, 1997. URL `http://www.ncbi.nlm.nih.gov/entrez/query.fcgi?cmd=Retrieve&db=PubMed&dopt=Citation&list_uids=9442869`.

M. DeTure, L. W. Ko, S. Yen, P. Nacharaju, C. Easson, J. Lewis, M. van Slegtenhorst, M. Hutton, and S. H. Yen. Missense tau mutations identified in ftdp-17 have a small effect on tau-microtubule interactions. *Brain Res*, 853(1):5–14, 2000. URL `http://www.ncbi.nlm.nih.gov/entrez/query.fcgi?cmd=Retrieve&db=PubMed&dopt=Citation&list_uids=10627302`.

F. Devred, P. Barbier, S. Douillard, O. Monasterio, J. M. Andreu, and V. Peyrot. Tau induces ring and microtubule formation from alphabeta-tubulin dimers under nonassembly conditions. *Biochemistry*, 43(32):10520–31, 2004. ISSN 0006-2960 (Print) 0006-2960 (Linking). doi: 10.1021/bi0493160. URL `http://www.ncbi.nlm.nih.gov/pubmed/15301550`.

F. Devred, P. Barbier, D. Lafitte, I. Landrieu, G. Lippens, and V. Peyrot. Microtubule and maps: thermodynamics of complex formation by auc, itc, fluorescence, and nmr. *Methods Cell Biol*, 95:449–80, 2010. ISSN 0091-679X (Print) 0091-679X (Linking). doi: 10.1016/S0091-679X(10)95023-1. URL `https://www.ncbi.nlm.nih.gov/pubmed/20466148`.

R. Dhamodharan and P. Wadsworth. Modulation of microtubule dynamic instability in vivo by brain microtubule associated proteins. *J Cell Sci*, 108 (Pt 4):1679–89, 1995. URL `http://www.ncbi.nlm.nih.gov/entrez/query.fcgi?cmd=Retrieve&db=PubMed&dopt=Citation&list_uids=7615685`.

J. F. Diaz, J. M. Valpuesta, P. Chacon, G. Diakun, and J. M. Andreu. Changes in microtubule protofilament number induced by taxol binding to an easily accessible site. internal microtubule dynamics. *J Biol Chem*, 273(50):33803–10, 1998. ISSN 0021-9258 (Print). URL `http://www.ncbi.nlm.nih.gov/entrez/query.fcgi?cmd=Retrieve&db=PubMed&dopt=Citation&list_uids=9837970`.

US DoD, 2020. URL `http://www.defense.gov/News/Special-Reports/FY16-Budget`.

Z. J. Donhauser, J. T. Saunders, D. S. D'Urso, and T. A. Garrett. Dimerization and long-range repulsion established by both termini of the microtubule-associated protein tau. *Biochemistry*, 56(44):5900–5909, 2017. ISSN 0006-2960 (Print) 0006-2960. doi: 10.1021/acs.biochem.7b00653.

H. Doodhi, A. E. Prota, R. Rodriguez-Garcia, H. Xiao, D. W. Custar, K. Bargsten, E. A. Katrukha, M. Hilbert, S. Hua, K. Jiang, I. Grigoriev, C. P. Yang, D. Cox, S. B. Horwitz, L. C. Kapitein, A. Akhmanova, and M. O. Steinmetz. Termination of protofilament elongation by eribulin induces lattice defects that promote microtubule

catastrophes. *Curr Biol*, 26(13):1713–21, 2016. ISSN 1879-0445 (Electronic) 0960-9822 (Linking). doi: 10.1016/j.cub.2016.04.053. URL `https://www.ncbi.nlm.nih.gov/pubmed/27321995`.

D. N. Drechsel, A. A. Hyman, M. H. Cobb, and M. W. Kirschner. Modulation of the dynamic instability of tubulin assembly by the microtubule-associated protein tau. *Mol Biol Cell*, 3(10):1141–54, 1992. ISSN 1059-1524 (Print) 1059-1524 (Linking). URL `https://www.ncbi.nlm.nih.gov/pubmed/1421571`.

D. Drubin, S. Kobayashi, and M. Kirschner. Association of tau protein with microtubules in living cells. *Ann N Y Acad Sci*, 466:257–68, 1986. URL `http://www.ncbi.nlm.nih.gov/entrez/query.fcgi?cmd=Retrieve&db=PubMed&dopt=Citation&list_uids=2873777`.

D. G. Drubin, S. C. Feinstein, E. M. Shooter, and M. W. Kirschner. Nerve growth factor-induced neurite outgrowth in pc12 cells involves the coordinate induction of microtubule assembly and assembly-promoting factors. *J Cell Biol*, 101(5 Pt 1): 1799–807, 1985. URL `http://www.ncbi.nlm.nih.gov/entrez/query.fcgi?cmd=Retrieve&db=PubMed&dopt=Citation&list_uids=2997236`.

A. R. Duan, E. M. Jonasson, E. O. Alberico, C. Li, J. P. Scripture, R. A. Miller, M. S. Alber, and H. V. Goodson. Interactions between tau and different conformations of tubulin: Implications for tau function and mechanism. *J Mol Biol*, 429(9):1424–1438, 2017. ISSN 1089-8638 (Electronic) 0022-2836 (Linking). doi: 10.1016/j.jmb.2017.03.018. URL `https://www.ncbi.nlm.nih.gov/pubmed/28322917`.

S. Elbaum-Garfinkle, G. Cobb, J. T. Compton, X. H. Li, and E. Rhoades. Tau mutants bind tubulin heterodimers with enhanced affinity. *Proc Natl Acad Sci U S A*, 111(17): 6311–6, 2014. ISSN 1091-6490 (Electronic) 0027-8424 (Linking). doi: 10.1073/pnas.1315983111. URL `http://www.ncbi.nlm.nih.gov/pubmed/24733915`.

Céline Elie-Caille, Fedor Severin, Jonne Helenius, Jonathon Howard, Daniel J. Muller, and A. A. Hyman. Straight gdp-tubulin protofilaments form in the presence of taxol. *Current Biology*, 17(20):1765–1770, 2007. ISSN 09609822. doi: 10.1016/j.cub.2007.08.063.

H. P. Erickson. Assembly of microtubules from preformed, ring-shaped protofilaments and 6-s tubulin. *J Supramol Struct*, 2(2-4):393–411, 1974. ISSN 0091-7419 (Print) 0091-7419 (Linking). doi: 10.1002/jss.400020228. URL `https://www.ncbi.nlm.nih.gov/pubmed/4474573`.

H. P. Erickson and E. T. O'Brien. Microtubule dynamic instability and gtp hydrolysis. *Annu Rev Biophys Biomol Struct*, 21:145–66, 1992. ISSN 1056-8700 (Print) 1056-8700. doi: 10.1146/annurev.bb.21.060192.001045.

H. P. Erickson and W. A. Voter. Nucleation of microtubule assembly. experimental kinetics, computer fitting of models, and observations on tubulin rings. *Ann N Y Acad Sci*, 466:552–65, 1986. URL `http://www.ncbi.nlm.nih.gov/entrez/query.fcgi?cmd=Retrieve&db=PubMed&dopt=Citation&list_uids=3460431`.

B. Esmaeli-Azad, J. H. McCarty, and S. C. Feinstein. Sense and antisense transfection analysis of tau function: tau influences net microtubule assembly, neurite outgrowth and neuritic stability. *J Cell Sci*, 107 (Pt 4):869–79, 1994. URL `http://www.ncbi.nlm.nih.gov/entrez/query.fcgi?cmd=Retrieve&db=PubMed&dopt=Citation&list_uids=8056843`.

A. Ettinger, J. van Haren, S. A. Ribeiro, and T. Wittmann. Doublecortin is excluded from growing microtubule ends and recognizes the gdp-microtubule lattice. *Curr Biol*, 26(12):1549–1555, 2016. ISSN 0960-9822. doi: 10.1016/j.cub.2016.04.020.

D. B. Evans, K. B. Rank, K. Bhattacharya, D. R. Thomsen, M. E. Gurney, and S. K. Sharma. Tau phosphorylation at serine 396 and serine 404 by human recombinant tau protein kinase ii inhibits tau's ability to promote microtubule assembly. *J Biol Chem*, 275(32):24977–83, 2000. URL `http://www.ncbi.nlm.nih.gov/entrez/query.fcgi?cmd=Retrieve&db=PubMed&dopt=Citation&list_uids=10818091`.

Colby P. Fees and Jeffrey K. Moore. A unified model for microtubule rescue. *Molecular biology of the cell*, 30(6):753–765, 2019. ISSN 1939-4586 1059-1524. doi: 10.1091/mbc.E18-08-0541. URL `https://pubmed.ncbi.nlm.nih.gov/30672721https://www.ncbi.nlm.nih.gov/pmc/articles/PMC6589779/`.

H. E. Feinstein, S. J. Benbow, N. E. LaPointe, N. Patel, S. Ramachandran, T. D. Do, M. R. Gaylord, N. E. Huskey, N. Dressler, M. Korff, B. Quon, K. L. Cantrell, M. T. Bowers, R. Lal, and S. C. Feinstein. Oligomerization of the microtubule-associated protein tau is mediated by its n-terminal sequences: implications for normal and pathological tau action. *J Neurochem*, 137(6):939–54, 2016. ISSN 1471-4159 (Electronic) 0022-3042 (Linking). doi: 10.1111/jnc.13604. URL `https://www.ncbi.nlm.nih.gov/pubmed/26953146`.

S. C. Feinstein and L. Wilson. Inability of tau to properly regulate neuronal microtubule dynamics: a loss-of-function mechanism by which tau might mediate neuronal cell death. *Biochim Biophys Acta*, 1739(2-3):268–79, 2005. ISSN 0006-3002 (Print) 0006-3002 (Linking). doi: 10.1016/j.bbadis.2004.07.002. URL `https://www.ncbi.nlm.nih.gov/pubmed/15615645`.

A. Fellous, J. Francon, A. M. Lennon, and J. Nunez. Microtubule assembly in vitro. purification of assembly-promoting factors. *Eur J Biochem*, 78(1):167–74, 1977. URL `http://www.ncbi.nlm.nih.gov/entrez/query.fcgi?cmd=Retrieve&db=PubMed&dopt=Citation&list_uids=913395`.

A. Ferreira and E. H. Bigio. Calpain-mediated tau cleavage: a mechanism leading to neurodegeneration shared by multiple tauopathies. *Mol Med*, 17(7-8):676–85, 2011. ISSN 1528-3658 (Electronic) 1076-1551 (Linking). doi: 10.2119/molmed.2010.00220. URL `https://www.ncbi.nlm.nih.gov/pubmed/21442128`.

J. J. Field, A. Kanakkanthara, and J. H. Miller. Microtubule-targeting agents are clinically successful due to both mitotic and interphase impairment of microtubule function. *Bioorg Med Chem*, 22(18):5050–9, 2014. ISSN 1464-3391 (Electronic) 0968-0896 (Linking). doi: 10.1016/j.bmc.2014.02.035. URL `https://www.ncbi.nlm.nih.gov/pubmed/24650703`.

A. W. P. Fitzpatrick, B. Falcon, S. He, A. G. Murzin, G. Murshudov, H. J. Garringer, R. A. Crowther, B. Ghetti, M. Goedert, and S. H. W. Scheres. Cryo-em structures of tau filaments from alzheimer's disease. *Nature*, 547(7662):185–190, 2017. ISSN 1476-4687 (Electronic) 0028-0836 (Linking). doi: 10.1038/nature23002. URL `https://www.ncbi.nlm.nih.gov/pubmed/28678775`.

P. Friedhoff, M. von Bergen, E. Mandelkow, and P. Davies. A nucleated assembly mechanism of alzheimer paired helical filaments. *Proc Natl Acad Sci U S A*, 95(26):15712–7, 1998. URL `http://www.ncbi.nlm.nih.gov/cgi-bin/Entrez/referer?http://www.pnas.org/cgi/content/full/95/26/15712`.

Ronald P. Frigon and Serge N. Timasheff. Magnesium-induced self-association of calf brain tubulin. i. stoichiometry. *Biochemistry*, 14(21):4559–4566, 1975. ISSN 0006-2960. doi: 10.1021/bi00692a001. URL `https://dx.doi.org/10.1021/bi00692a001`.

H. Y. J. Fung, K. M. McKibben, J. Ramirez, K. Gupta, and E. Rhoades. Structural characterization of tau in fuzzy tau:tubulin complexes. *Structure*, 28(3):378–384.e4, 2020. ISSN 0969-2126. doi: 10.1016/j.str.2020.01.004.

D. K. Fygenson, E. Braun, and A. Libchaber. Phase diagram of microtubules. *Phys Rev E Stat Phys Plasmas Fluids Relat Interdiscip Topics*, 50(2):1579–1588, 1994. ISSN 1063-651X (Print) 1063-651X (Linking). URL `https://www.ncbi.nlm.nih.gov/pubmed/9962129`.

Steven D. Gaines and William R. Rice. Analysis of biological data when there are ordered expectations. *The American Naturalist*, 135(2):310–317, 1990. doi: 10.1086/285047. URL `https://www.journals.uchicago.edu/doi/abs/10.1086/285047`.

T. Chris Gamblin, Feng Chen, Angara Zambrano, Aida Abraha, Sarita Lagalwar, Angela L. Guillozet, Meiling Lu, Yifan Fu, Francisco Garcia-Sierra, Nichole LaPointe, Richard Miller, Robert W. Berry, Lester I. Binder, and Vincent L. Cryns. Caspase cleavage of tau: Linking amyloid and neurofibrillary tangles in alzheimer's disease. *Proceedings of the National Academy of Sciences of the United States of America*, 100

(17):10032–10037, 2003. ISSN 0027-8424 1091-6490. doi: 10.1073/pnas.1630428100. URL http://www.ncbi.nlm.nih.gov/pmc/articles/PMC187753/.

M. L. Garcia and D. W. Cleveland. Going new places using an old map: tau, microtubules and human neurodegenerative disease. *Curr Opin Cell Biol*, 13(1):41–8, 2001. URL http://www.ncbi.nlm.nih.gov/entrez/query.fcgi?cmd=Retrieve&db=PubMed&dopt=Citation&list_uids=11163132.

M. K. Gardner, B. D. Charlebois, I. M. Janosi, J. Howard, A. J. Hunt, and D. J. Odde. Rapid microtubule self-assembly kinetics. *Cell*, 146(4):582–92, 2011. ISSN 0092-8674. doi: 10.1016/j.cell.2011.06.053.

C. Gell, V. Bormuth, G. J. Brouhard, D. N. Cohen, S. Diez, C. T. Friel, J. Helenius, B. Nitzsche, H. Petzold, J. Ribbe, E. Schaffer, J. H. Stear, A. Trushko, V. Varga, P. O. Widlund, M. Zanic, and J. Howard. Microtubule dynamics reconstituted in vitro and imaged by single-molecule fluorescence microscopy. *Methods Cell Biol*, 95:221–45, 2010. ISSN 0091-679X (Print) 0091-679X (Linking). doi: 10.1016/S0091-679X(10)95013-9. URL https://www.ncbi.nlm.nih.gov/pubmed/20466138.

C. Genualdi, S. C. Feinstein, L. Wilson, M. A. Jordan, and N. J. Stagg. Assessing the utility of in vitro microtubule assays for studying mechanisms of peripheral neuropathy with the microtubule inhibitor class of cancer chemotherapy. *Chem Biol Interact*, 315: 108906, 2020. ISSN 0009-2797. doi: 10.1016/j.cbi.2019.108906.

E. A. Geyer, A. Burns, B. A. Lalonde, X. Ye, F. A. Piedra, T. C. Huffaker, and L. M. Rice. A mutation uncouples the tubulin conformational and gtpase cycles, revealing allosteric control of microtubule dynamics. *Elife*, 4:e10113, 2015. ISSN 2050-084X (Electronic) 2050-084X (Linking). doi: 10.7554/eLife.10113. URL https://www.ncbi.nlm.nih.gov/pubmed/26439009.

B. Gigant, C. Wang, R. Ravelli, and M. Knossow. [the regulation of tubulin by vinblastine]. *Med Sci (Paris)*, 21(10):814–5, 2005. ISSN 0767-0974 (Print) 0767-0974 (Linking). doi: 00/00/07/E7/[pii]10.1051/medsci/20052110814. URL http://www.ncbi.nlm.nih.gov/entrez/query.fcgi?cmd=Retrieve&db=PubMed&dopt=Citation&list_uids=16197897.

M. Goedert, M. G. Spillantini, M. C. Potier, J. Ulrich, and R. A. Crowther. Cloning and sequencing of the cdna encoding an isoform of microtubule-associated protein tau containing four tandem repeats: differential expression of tau protein mrnas in human brain. *Embo J*, 8(2):393–9, 1989. URL http://www.ncbi.nlm.nih.gov/entrez/query.fcgi?cmd=Retrieve&db=PubMed&dopt=Citation&list_uids=2498079.

M. Goedert, S. Satumtira, R. Jakes, M. J. Smith, C. Kamibayashi, 3rd White, C. L., and E. Sontag. Reduced binding of protein phosphatase 2a to tau protein with frontotemporal dementia and parkinsonism linked to chromosome 17 mutations. *J Neurochem*, 75(5):2155–62, 2000.

S. Goel, A. C. Mita, M. Mita, E. K. Rowinsky, Q. S. Chu, N. Wong, C. Desjardins, F. Fang, M. Jansen, D. E. Shuster, S. Mani, and C. H. Takimoto. A phase i study of eribulin mesylate (e7389), a mechanistically novel inhibitor of microtubule dynamics, in patients with advanced solid malignancies. *Clin Cancer Res*, 15(12):4207–12, 2009. ISSN 1078-0432 (Print) 1078-0432 (Linking). doi: 10.1158/1078-0432.CCR-08-2429. URL `https://www.ncbi.nlm.nih.gov/pubmed/19509177`.

B. L. Goode and S. C. Feinstein. Identification of a novel microtubule binding and assembly domain in the developmentally regulated inter-repeat region of tau. *J Cell Biol*, 124(5):769–82, 1994. ISSN 0021-9525 (Print) 0021-9525 (Linking). URL `https://www.ncbi.nlm.nih.gov/pubmed/8120098`.

B. L. Goode, P. E. Denis, D. Panda, M. J. Radeke, H. P. Miller, L. Wilson, and S. C. Feinstein. Functional interactions between the proline-rich and repeat regions of tau enhance microtubule binding and assembly. *Molecular Biology of the Cell*, 8(2):353–365, 1997. ISSN 1059-1524. URL `<GotoISI>://WOS:A1997WK47200013`.

B. L. Goode, D. G. Drubin, and G. Barnes. Functional cooperation between the microtubule and actin cytoskeletons. *Curr Opin Cell Biol*, 12(1):63–71, 2000. URL `http://www.ncbi.nlm.nih.gov/entrez/query.fcgi?cmd=Retrieve&db=PubMed&dopt=Citation&list_uids=10679357`.

J. Gotz, F. Chen, J. van Dorpe, and R. M. Nitsch. Formation of neurofibrillary tangles in p301l tau transgenic mice induced by abeta 42 fibrils. *Science*, 293(5534):1491–5, 2001. URL `http://www.ncbi.nlm.nih.gov/entrez/query.fcgi?cmd=Retrieve&db=PubMed&dopt=Citation&list_uids=11520988`.

W. J. Gradishar. The place for eribulin in the treatment of metastatic breast cancer. *Curr Oncol Rep*, 13(1):11–6, 2011. ISSN 1534-6269 (Electronic) 1523-3790 (Linking). doi: 10.1007/s11912-010-0145-9. URL `https://www.ncbi.nlm.nih.gov/pubmed/21104168`.

A. Guesdon, F. Bazile, R. M. Buey, R. Mohan, S. Monier, R. R. Garcia, M. Angevin, C. Heichette, R. Wieneke, R. Tampe, L. Duchesne, A. Akhmanova, M. O. Steinmetz, and D. Chretien. Eb1 interacts with outwardly curved and straight regions of the microtubule lattice. *Nat Cell Biol*, 18(10):1102–8, 2016. ISSN 1476-4679 (Electronic) 1465-7392 (Linking). doi: 10.1038/ncb3412. URL `https://www.ncbi.nlm.nih.gov/pubmed/27617931`.

N. Gustke, B. Trinczek, J. Biernat, E. M. Mandelkow, and E. Mandelkow. Domains of tau-protein and interactions with microtubules. *Biochemistry*, 33(32):9511–9522, 1994.

F. O. Hans, R. M. Dickerson, L. Wilson, and R. J. Owellen. Differences in the binding properties of vinca alkaloids and colchicine to tubulin by varying protein sources and methodology. *Biochem Pharmacol*, 27(1):71–6, 1978. ISSN 0006-2952 (Print) 0006-2952 (Linking). URL `https://www.ncbi.nlm.nih.gov/pubmed/563724`.

A. Harada, K. Oguchi, S. Okabe, J. Kuno, S. Terada, T. Ohshima, R. Sato-Yoshitake, Y. Takei, T. Noda, and N. Hirokawa. Altered microtubule organization in small-calibre axons of mice lacking tau protein. *Nature*, 369(6480):488–91, 1994. URL http://www.ncbi.nlm.nih.gov/entrez/query.fcgi?cmd=Retrieve&db=PubMed&dopt=Citation&list_uids=8202139.

F. Hernandez and J. Avila. Tauopathies. *Cellular and Molecular Life Sciences*, 64 (17):2219–33, 2007. ISSN 1420-682X (Print) 1420-682X (Linking). doi: 10.1007/s00018-007-7220-x. URL http://www.ncbi.nlm.nih.gov/entrez/query.fcgi?cmd=Retrieve&db=PubMed&dopt=Citation&list_uids=17604998.

A. Hernández-Vega, M. Braun, L. Scharrel, M. Jahnel, S. Wegmann, B. T. Hyman, S. Alberti, S. Diez, and A. A. Hyman. Local nucleation of microtubule bundles through tubulin concentration into a condensed tau phase. *Cell Rep*, 20(10):2304–2312, 2017. doi: 10.1016/j.celrep.2017.08.042.

A. Himmler. Structure of the bovine tau gene: alternatively spliced transcripts generate a protein family. *Mol Cell Biol*, 9(4):1389–96, 1989. URL http://www.ncbi.nlm.nih.gov/entrez/query.fcgi?cmd=Retrieve&db=PubMed&dopt=Citation&list_uids=2498650.

M. H. Hinrichs, A. Jalal, B. Brenner, E. Mandelkow, S. Kumar, and T. Scholz. Tau protein diffuses along the microtubule lattice. *J Biol Chem*, 287(46):38559–68, 2012. ISSN 1083-351X (Electronic) 0021-9258 (Linking). doi: 10.1074/jbc.M112.369785. URL https://www.ncbi.nlm.nih.gov/pubmed/23019339.

N. Hirokawa, Y. Shiomura, and S. Okabe. Tau proteins: the molecular structure and mode of binding on microtubules. *J Cell Biol*, 107(4):1449–59, 1988. URL http://www.ncbi.nlm.nih.gov/entrez/query.fcgi?cmd=Retrieve&db=PubMed&dopt=Citation&list_uids=3139677.

M. Hong, V. Zhukareva, V. Vogelsberg-Ragaglia, Z. Wszolek, L. Reed, B. I. Miller, D. H. Geschwind, T. D. Bird, D. McKeel, A. Goate, J. C. Morris, K. C. Wilhelmsen, G. D. Schellenberg, J. Q. Trojanowski, and V. M. Lee. Mutation-specific functional impairments in distinct tau isoforms of hereditary ftdp-17. *Science*, 282(5395):1914–7, 1998. URL http://www.ncbi.nlm.nih.gov/entrez/query.fcgi?cmd=Retrieve&db=PubMed&dopt=Citation&list_uids=9836646.

J. L. Hoog, S. M. Huisman, Z. Sebo-Lemke, L. Sandblad, J. R. McIntosh, C. Antony, and D. Brunner. Electron tomography reveals a flared morphology on growing microtubule ends. *J Cell Sci*, 124(Pt 5):693–8, 2011. ISSN 1477-9137 (Electronic) 0021-9533 (Linking). doi: 10.1242/jcs.072967. URL https://www.ncbi.nlm.nih.gov/pubmed/21303925.

J. Howard and A. A. Hyman. Growth, fluctuation and switching at microtubule plus ends. *Nat Rev Mol Cell Biol*, 10(8):569–74, 2009. ISSN 1471-0080 (Electronic) 1471-0072 (Linking). doi: 10.1038/nrm2713. URL `https://www.ncbi.nlm.nih.gov/pubmed/19513082`.

M. Hutton, C. L. Lendon, P. Rizzu, M. Baker, S. Froelich, H. Houlden, S. Pickering-Brown, S. Chakraverty, A. Isaacs, A. Grover, J. Hackett, J. Adamson, S. Lincoln, D. Dickson, P. Davies, R. C. Petersen, M. Stevens, E. de Graaff, E. Wauters, J. van Baren, M. Hillebrand, M. Joosse, J. M. Kwon, P. Nowotny, L. K. Che, J. Norton, J. C. Morris, L. A. Reed, J. Trojanowski, H. Basun, L. Lannfelt, M. Neystat, S. Fahn, F. Dark, T. Tannenberg, P. R. Dodd, N. Hayward, J. B. Kwok, P. R. Schofield, A. Andreadis, J. Snowden, D. Craufurd, D. Neary, F. Owen, B. A. Oostra, J. Hardy, A. Goate, J. van Swieten, D. Mann, T. Lynch, and P. Heutink. Association of missense and 5'-splice-site mutations in tau with the inherited dementia ftdp-17. *Nature*, 393 (6686):702–5, 1998. ISSN 0028-0836 (Print) 0028-0836 (Linking). doi: 10.1038/31508. URL `https://www.ncbi.nlm.nih.gov/pubmed/9641683`.

H.Wickham. *ggplot2:Elegant Graphics for Data Analysis*. Springer-Verlag, New Your, NY, 2009.

A. Hyman, D. Drechsel, D. Kellogg, S. Salser, K. Sawin, P. Steffen, L. Wordeman, and T. Mitchison. Preparation of modified tubulins. *Methods Enzymol*, 196:478–85, 1991. ISSN 0076-6879 (Print) 0076-6879 (Linking). URL `http://www.ncbi.nlm.nih.gov/pubmed/2034137`.

A. A. Hyman, S. Salser, D. N. Drechsel, N. Unwin, and T. J. Mitchison. Role of gtp hydrolysis in microtubule dynamics: information from a slowly hydrolyzable analogue, gmpcpp. *Mol Biol Cell*, 3(10):1155–67, 1992. ISSN 1059-1524 (Print) 1059-1524 (Linking). URL `https://www.ncbi.nlm.nih.gov/pubmed/1421572`.

A. A. Hyman, D. Chretien, I. Arnal, and R. H. Wade. Structural changes accompanying gtp hydrolysis in microtubules: information from a slowly hydrolyzable analogue guanylyl-(alpha,beta)-methylene-diphosphonate. *J Cell Biol*, 128(1-2):117–25, 1995. ISSN 0021-9525 (Print) 0021-9525 (Linking). URL `https://www.ncbi.nlm.nih.gov/pubmed/7822409`.

S. Inoue and E. D. Salmon. Force generation by microtubule assembly/disassembly in mitosis and related movements. *Mol Biol Cell*, 6(12):1619–40, 1995. ISSN 1059-1524 (Print). URL `http://www.ncbi.nlm.nih.gov/entrez/query.fcgi?cmd=Retrieve&db=PubMed&dopt=Citation&list_uids=8590794`.

S. Janelidze, E. Stomrud, R. Smith, S. Palmqvist, N. Mattsson, D. C. Airey, N. K. Proctor, X. Chai, S. Shcherbinin, J. R. Sims, G. Triana-Baltzer, C. Theunis, R. Slemmon,

M. Mercken, H. Kolb, J. L. Dage, and O. Hansson. Cerebrospinal fluid p-tau217 performs better than p-tau181 as a biomarker of alzheimer's disease. *Nat Commun*, 11 (1):1683, 2020. ISSN 2041-1723. doi: 10.1038/s41467-020-15436-0.

D. Janning, M. Igaev, F. Sundermann, J. Bruhmann, O. Beutel, J. J. Heinisch, L. Bakota, J. Piehler, W. Junge, and R. Brandt. Single-molecule tracking of tau reveals fast kiss-and-hop interaction with microtubules in living neurons. *Mol Biol Cell*, 25(22): 3541–51, 2014. ISSN 1939-4586 (Electronic) 1059-1524 (Linking). doi: 10.1091/mbc. E14-06-1099. URL https://www.ncbi.nlm.nih.gov/pubmed/25165145.

I. M. Janosi, D. Chretien, and H. Flyvbjerg. Modeling elastic properties of microtubule tips and walls. *Eur Biophys J*, 27(5):501–13, 1998. ISSN 0175-7571 (Print) 0175-7571. doi: 10.1007/s002490050160.

I. M. Janosi, D. Chretien, and H. Flyvbjerg. Structural microtubule cap: stability, catastrophe, rescue, and third state. *Biophys J*, 83(3):1317–30, 2002. ISSN 0006-3495 (Print) 0006-3495 (Linking). doi: 10.1016/S0006-3495(02)73902-7. URL https://www.ncbi.nlm.nih.gov/pubmed/12202357.

S. Jeganathan, A. Hascher, S. Chinnathambi, J. Biernat, E. M. Mandelkow, and E. Mandelkow. Proline-directed pseudo-phosphorylation at at8 and phf1 epitopes induces a compaction of the paperclip folding of tau and generates a pathological (mc-1) conformation. *J Biol Chem*, 283(46):32066–76, 2008. ISSN 0021-9258 (Print) 0021-9258 (Linking). doi: M805300200[pii]10.1074/ jbc.M805300200. URL http://www.ncbi.nlm.nih.gov/entrez/query.fcgi?cmd= Retrieve&db=PubMed&dopt=Citation&list_uids=18725412.

M. A. Jordan and K. Kamath. How do microtubule-targeted drugs work? an overview. *Curr Cancer Drug Targets*, 7(8):730–42, 2007. ISSN 1873-5576 (Electronic) 1568-0096 (Linking). URL http://www.ncbi.nlm.nih.gov/entrez/query. fcgi?cmd=Retrieve&db=PubMed&dopt=Citation&list_uids=18220533.

M. A. Jordan and L. Wilson. Microtubules as a target for anticancer drugs. *Nat Rev Cancer*, 4(4):253–65, 2004. URL http://www.ncbi.nlm.nih.gov/entrez/query.fcgi? cmd=Retrieve&db=PubMed&dopt=Citation&list_uids=15057285.

M. A. Jordan, R. H. Himes, and L. Wilson. Comparison of the effects of vinblastine, vincristine, vindesine, and vinepidine on microtubule dynamics and cell proliferation in vitro. *Cancer Res*, 45(6):2741–7, 1985. ISSN 0008-5472 (Print) 0008-5472 (Linking). URL https://www.ncbi.nlm.nih.gov/pubmed/3986806.

M. A. Jordan, R. L. Margolis, R. H. Himes, and L. Wilson. Identification of a distinct class of vinblastine binding sites on microtubules. *J Mol Biol*, 187(1):61–73, 1986. ISSN 0022-2836 (Print) 0022-2836 (Linking). URL https://www.ncbi.nlm.nih.gov/ pubmed/3959083.

M. A. Jordan, K. Kamath, T. Manna, T. Okouneva, H. P. Miller, C. Davis, B. A. Littlefield, and L. Wilson. The primary antimitotic mechanism of action of the synthetic halichondrin e7389 is suppression of microtubule growth. *Mol Cancer Ther*, 4 (7):1086–95, 2005. ISSN 1535-7163 (Print) 1535-7163 (Linking). doi: 4/7/1086[pii] 10.1158/1535-7163.MCT-04-0345. URL `http://www.ncbi.nlm.nih.gov/entrez/query.fcgi?cmd=Retrieve&db=PubMed&dopt=Citation&list_uids=16020666`.

Harindranath Kadavath, Romina V. Hofele, Jacek Biernat, Satish Kumar, Katharina Tepper, Henning Urlaub, Eckhard Mandelkow, and Markus Zweckstetter. Tau stabilizes microtubules by binding at the interface between tubulin heterodimers. *Proceedings of the National Academy of Sciences*, 112(24):7501–7506, 2015. ISSN 0027-8424 1091-6490. doi: 10.1073/pnas.1504081112.

Nicholas M. Kanaan, Chelsey Hamel, Tessa Grabinski, and Benjamin Combs. Liquid-liquid phase separation induces pathogenic tau conformations in vitro. *Nature Communications*, 11(1):2809, 2020. ISSN 2041-1723. doi: 10.1038/s41467-020-16580-3. URL `https://doi.org/10.1038/s41467-020-16580-3`.

S. Kar, G. J. Florence, I. Paterson, and L. A. Amos. Discodermolide interferes with the binding of tau protein to microtubules. *FEBS Lett*, 539(1-3):34–6, 2003. ISSN 0014-5793 (Print) 0014-5793 (Linking). URL `https://www.ncbi.nlm.nih.gov/pubmed/12650922`.

T. L. Karr, D. Kristofferson, and D. L. Purich. Mechanism of microtubule depolymerization. correlation of rapid induced disassembly experiments with a kinetic model for endwise depolymerization. *J Biol Chem*, 255(18):8560–6, 1980.

E. H. Kellogg, N. M. A. Hejab, S. Howes, P. Northcote, J. H. Miller, J. F. Diaz, K. H. Downing, and E. Nogales. Insights into the distinct mechanisms of action of taxane and non-taxane microtubule stabilizers from cryo-em structures. *J Mol Biol*, 429(5): 633–646, 2017. ISSN 0022-2836. doi: 10.1016/j.jmb.2017.01.001.

E. H. Kellogg, N. M. A. Hejab, S. Poepsel, K. H. Downing, F. DiMaio, and E. Nogales. Near-atomic model of microtubule-tau interactions. *Science*, 360(6394):1242–1246, 2018. ISSN 1095-9203 (Electronic) 0036-8075 (Linking). doi: 10.1126/science.aat1780. URL `https://www.ncbi.nlm.nih.gov/pubmed/29748322`.

A. Kenessey and S. H. Yen. The extent of phosphorylation of fetal tau is comparable to that of phf-tau from alzheimer paired helical filaments. *Brain Res*, 629(1):40–6, 1993. URL `http://www.ncbi.nlm.nih.gov/entrez/query.fcgi?cmd=Retrieve&db=PubMed&dopt=Citation&list_uids=8287279`.

J. W. Kerssemakers, E. L. Munteanu, L. Laan, T. L. Noetzel, M. E. Janson, and M. Dogterom. Assembly dynamics of microtubules at molecular resolution. *Nature*, 442(7103):709–12, 2006. ISSN 1476-4687 (Electronic) 0028-0836 (Linking). doi: 10.1038/nature04928. URL `https://www.ncbi.nlm.nih.gov/pubmed/16799566`.

H. Kim, C. G. Jensen, and L. I. Rebhun. The binding of map-2 and tau on brain microtubules in vitro: implications for microtubule structure. *Ann N Y Acad Sci*, 466:218–39, 1986. URL `http://www.ncbi.nlm.nih.gov/entrez/query.fcgi?cmd=Retrieve&db=PubMed&dopt=Citation&list_uids=3089106`.

E. Kiris, D. Ventimiglia, M. E. Sargin, M. R. Gaylord, A. Altinok, K. Rose, B. S. Manjunath, M. A. Jordan, L. Wilson, and S. C. Feinstein. Combinatorial tau pseudophosphorylation: markedly different regulatory effects on microtubule assembly and dynamic instability than the sum of the individual parts. *J Biol Chem*, 286(16):14257–70, 2011. ISSN 1083-351X (Electronic) 0021-9258 (Linking). doi: M111.219311[pii]10.1074/jbc.M111.219311. URL `http://www.ncbi.nlm.nih.gov/entrez/query.fcgi?cmd=Retrieve&db=PubMed&dopt=Citation&list_uids=21288907`.

M. Kirschner and T. Mitchison. Beyond self-assembly: from microtubules to morphogenesis. *Cell*, 45(3):329–42, 1986. URL `http://www.ncbi.nlm.nih.gov/entrez/query.fcgi?cmd=Retrieve&db=PubMed&dopt=Citation&list_uids=3516413`.

M. W. Kirschner, R. C. Williams, M. Weingarten, and J. C. Gerhart. Microtubules from mammalian brain: some properties of their depolymerization products and a proposed mechanism of assembly and disassembly. *Proc Natl Acad Sci U S A*, 71(4):1159–63, 1974. ISSN 0027-8424 (Print) 0027-8424 (Linking). URL `https://www.ncbi.nlm.nih.gov/pubmed/4524627`.

M. W. Kirschner, L. S. Honig, and R. C. Williams. Quantitative electron microscopy of microtubule assembly in vitro. *J Mol Biol*, 99(2):263–76, 1975a.

M. W. Kirschner, M. Suter, M. Weingarten, and D. Littman. The role of rings in the assembly of microtubules in vitro. *Ann N Y Acad Sci*, 253:90–106, 1975b. ISSN 0077-8923 (Print) 0077-8923 (Linking). URL `https://www.ncbi.nlm.nih.gov/pubmed/1056761`.

S. Konzack, E. Thies, A. Marx, E. M. Mandelkow, and E. Mandelkow. Swimming against the tide: mobility of the microtubule-associated protein tau in neurons. *J Neurosci*, 27(37):9916–27, 2007. ISSN 1529-2401 (Electronic) 0270-6474 (Linking). doi: 10.1523/JNEUROSCI.0927-07.2007. URL `https://www.ncbi.nlm.nih.gov/pubmed/17855606`.

K. J. Kopeikina, B. T. Hyman, and T. L. Spires-Jones. Soluble forms of tau are toxic in alzheimer's disease. *Transl Neurosci*, 3(3):223–233, 2012. ISSN 2081-3856 (Print) 2081-6936. doi: 10.2478/s13380-012-0032-y.

Kishore V. Kuchibhotla, Susanne Wegmann, Katherine J. Kopeikina, Jonathan Hawkes, Nikita Rudinskiy, Mark L. Andermann, Tara L. Spires-Jones, Brian J. Bacskai, and Bradley T. Hyman. Neurofibrillary tangle-bearing neurons are functionally integrated in cortical circuits in vivo. *Proceedings of the National Academy of Sciences*, 111

(1):510–514, 2014. doi: 10.1073/pnas.1318807111. URL `https://www.pnas.org/content/pnas/111/1/510.full.pdf`.

S. Kutter, T. Eichner, A. M. Deaconescu, and D. Kern. Regulation of microtubule assembly by tau and not by pin1. *J Mol Biol*, 428(9 Pt A):1742–59, 2016. ISSN 1089-8638 (Electronic) 0022-2836 (Linking). doi: 10.1016/j.jmb.2016.03.010. URL `https://www.ncbi.nlm.nih.gov/pubmed/26996940`.

A. E. Lang, D. N. Riherd Methner, and A. Ferreira. Neuronal degeneration, synaptic defects, and behavioral abnormalities in tau45-230 transgenic mice. *Neuroscience*, 275: 322–339, 2014. ISSN 03064522. doi: 10.1016/j.neuroscience.2014.06.017.

N. E. LaPointe, G. Morfini, G. Pigino, I. N. Gaisina, A. P. Kozikowski, L. I. Binder, and S. T. Brady. The amino terminus of tau inhibits kinesin-dependent axonal transport: implications for filament toxicity. *J Neurosci Res*, 87(2):440–51, 2009. ISSN 1097-4547 (Electronic). doi: 10.1002/jnr.21850. URL `http://www.ncbi.nlm.nih.gov/entrez/query.fcgi?cmd=Retrieve&db=PubMed&dopt=Citation&list_uids=18798283`.

N. E. LaPointe, G. Morfini, S. T. Brady, S. C. Feinstein, L. Wilson, and M. A. Jordan. Effects of eribulin, vincristine, paclitaxel and ixabepilone on fast axonal transport and kinesin-1 driven microtubule gliding: implications for chemotherapy-induced peripheral neuropathy. *Neurotoxicology*, 37:231–9, 2013. ISSN 1872-9711 (Electronic) 0161-813X (Linking). doi: 10.1016/j.neuro.2013.05.008. URL `https://www.ncbi.nlm.nih.gov/pubmed/23711742`.

Adria C. LeBoeuf, Sasha F. Levy, Michelle Gaylord, Arnab Bhattacharya, Ambuj K. Singh, Mary Ann Jordan, Leslie Wilson, and Stuart C. Feinstein. Ftdp-17 mutations in tau alter the regulation of microtubule dynamics. *Journal of Biological Chemistry*, 283(52):36406–36415, 2008. ISSN 0021-9258 1083-351X. doi: 10.1074/jbc.M803519200.

G. Lee, N. Cowan, and M. Kirschner. The primary structure and heterogeneity of tau protein from mouse brain. *Science*, 239(4837):285–8, 1988. ISSN 0036-8075 (Print) 0036-8075 (Linking). URL `https://www.ncbi.nlm.nih.gov/pubmed/3122323`.

G. Lee, R. L. Neve, and K. S. Kosik. The microtubule binding domain of tau protein. *Neuron*, 2(6):1615–24, 1989. URL `http://www.ncbi.nlm.nih.gov/entrez/query.fcgi?cmd=Retrieve&db=PubMed&dopt=Citation&list_uids=2516729`.

V. M. Lee. Biomedicine. tauists and beta-aptists united–well almost! *Science*, 293 (5534):1446–7, 2001. URL `http://www.ncbi.nlm.nih.gov/entrez/query.fcgi?cmd=Retrieve&db=PubMed&dopt=Citation&list_uids=11520974`.

S. F. Levy, A. C. Leboeuf, M. R. Massie, M. A. Jordan, L. Wilson, and S. C. Feinstein. Three- and four-repeat tau regulate the dynamic instability of two distinct microtubule subpopulations in qualitatively different manners. implications for neurodegeneration.

J Biol Chem, 280(14):13520–8, 2005. ISSN 0021-9258 (Print) 0021-9258 (Linking). doi: 10.1074/jbc.M413490200. URL `https://www.ncbi.nlm.nih.gov/pubmed/15671021`.

J. Lewis, E. McGowan, J. Rockwood, H. Melrose, P. Nacharaju, M. Van Slegtenhorst, K. Gwinn-Hardy, M. Paul Murphy, M. Baker, X. Yu, K. Duff, J. Hardy, A. Corral, W. L. Lin, S. H. Yen, D. W. Dickson, P. Davies, and M. Hutton. Neurofibrillary tangles, amyotrophy and progressive motor disturbance in mice expressing mutant (p301l) tau protein. *Nat Genet*, 25(4):402–5, 2000. URL `http://www.ncbi.nlm.nih.gov/entrez/query.fcgi?cmd=Retrieve&db=PubMed&dopt=Citation&list_uids=10932182`.

S. A. Lewis, I. E. Ivanov, G. H. Lee, and N. J. Cowan. Organization of microtubules in dendrites and axons is determined by a short hydrophobic zipper in microtubule-associated proteins map2 and tau. *Nature*, 342(6249):498–505, 1989. URL `http://www.ncbi.nlm.nih.gov/entrez/query.fcgi?cmd=Retrieve&db=PubMed&dopt=Citation&list_uids=2511449`.

X. H. Li and E. Rhoades. Heterogeneous tau-tubulin complexes accelerate microtubule polymerization. *Biophys J*, 112(12):2567–2574, 2017. ISSN 1542-0086 (Electronic) 0006-3495 (Linking). doi: 10.1016/j.bpj.2017.05.006. URL `https://www.ncbi.nlm.nih.gov/pubmed/28636913`.

X. H. Li, J. A. Culver, and E. Rhoades. Tau binds to multiple tubulin dimers with helical structure. *J Am Chem Soc*, 137(29):9218–21, 2015. ISSN 1520-5126 (Electronic) 0002-7863 (Linking). doi: 10.1021/jacs.5b04561. URL `https://www.ncbi.nlm.nih.gov/pubmed/26165802`.

G. Lindwall and R. D. Cole. The purification of tau protein and the occurrence of two phosphorylation states of tau in brain. *J Biol Chem*, 259(19):12241–5, 1984. URL `http://www.ncbi.nlm.nih.gov/entrez/query.fcgi?cmd=Retrieve&db=PubMed&dopt=Citation&list_uids=6090460`.

C. W. Liu, G. Lee, and D. G. Jay. Tau is required for neurite outgrowth and growth cone motility of chick sensory neurons. *Cell Motil Cytoskeleton*, 43(3):232–42, 1999. URL `http://www.ncbi.nlm.nih.gov/entrez/query.fcgi?cmd=Retrieve&db=PubMed&dopt=Citation&list_uids=10401579`.

L. Liu, V. Drouet, J. W. Wu, M. P. Witter, S. A. Small, C. Clelland, and K. Duff. Trans-synaptic spread of tau pathology in vivo. *PLoS One*, 7(2):e31302, 2012. ISSN 1932-6203 (Electronic) 1932-6203 (Linking). doi: 10.1371/journal.pone.0031302. URL `https://www.ncbi.nlm.nih.gov/pubmed/22312444`.

S. Lobert, B. Vulevic, and J. J. Correia. Interaction of vinca alkaloids with tubulin: a comparison of vinblastine, vincristine, and vinorelbine. *Biochemistry*, 35(21):6806–14,

1996. ISSN 0006-2960 (Print) 0006-2960 (Linking). doi: 10.1021/bi953037i. URL `https://www.ncbi.nlm.nih.gov/pubmed/8639632`.

Sharon Lobert, Jeffrey W. Ingram, Bridget T. Hill, and John J. Correia. A comparison of thermodynamic parameters for vinorelbine- and vinflunine-induced tubulin self-association by sedimentation velocity. *Molecular Pharmacology*, 53(5):908, 1998. URL `http://molpharm.aspetjournals.org/content/53/5/908.abstract`.

M. Lopus, E. Oroudjev, L. Wilson, S. Wilhelm, W. Widdison, R. Chari, and M. A. Jordan. Maytansine and cellular metabolites of antibody-maytansinoid conjugates strongly suppress microtubule dynamics by binding to microtubules. *Mol Cancer Ther*, 9(10):2689–99, 2010. ISSN 1538-8514 (Electronic) 1535-7163 (Linking). doi: 9/10/2689[pii]10.1158/1535-7163. MCT-10-0644. URL `http://www.ncbi.nlm.nih.gov/entrez/query.fcgi?cmd=Retrieve&db=PubMed&dopt=Citation&list_uids=20937594`.

S. Luo, N. B. Wehr, and R. L. Levine. Quantitation of protein on gels and blots by infrared fluorescence of coomassie blue and fast green. *Anal Biochem*, 350(2):233–8, 2006. ISSN 0003-2697 (Print) 0003-2697 (Linking). doi: 10.1016/j.ab.2005.10.048. URL `https://www.ncbi.nlm.nih.gov/pubmed/16336940`.

V. Makrides, T. E. Shen, R. Bhatia, B. L. Smith, J. Thimm, R. Lal, and S. C. Feinstein. Microtubule-dependent oligomerization of tau. implications for physiological tau function and tauopathies. *J Biol Chem*, 278(35):33298–304, 2003. URL `http://www.ncbi.nlm.nih.gov/entrez/query.fcgi?cmd=Retrieve&db=PubMed&dopt=Citation&list_uids=12805366`.

V. Makrides, M. R. Massie, S. C. Feinstein, and J. Lew. Evidence for two distinct binding sites for tau on microtubules. *Proc Natl Acad Sci U S A*, 101(17):6746–51, 2004. ISSN 0027-8424 (Print) 0027-8424 (Linking). doi: 10.1073/pnas.0400992101. URL `https://www.ncbi.nlm.nih.gov/pubmed/15096589`.

E. M. Mandelkow, E. Mandelkow, and R. A. Milligan. Microtubule dynamics and microtubule caps: a time-resolved cryo-electron microscopy study. *J Cell Biol*, 114(5):977–91, 1991. ISSN 0021-9525 (Print) 0021-9525 (Linking). URL `https://www.ncbi.nlm.nih.gov/pubmed/1874792`.

S. W. Manka and C. A. Moores. The role of tubulin-tubulin lattice contacts in the mechanism of microtubule dynamic instability. *Nat Struct Mol Biol*, 25(7):607–615, 2018. ISSN 1545-9985. doi: 10.1038/s41594-018-0087-8.

Gennady Margolin, Ivan V. Gregoretti, Trevor M. Cickovski, Chunlei Li, Wei Shi, Mark S. Alber, and Holly V. Goodson. The mechanisms of microtubule catastrophe and rescue: implications from analysis of a dimer-scale computational model. *Molecular Biology of*

the Cell, 23(4):642–656, 2011. ISSN 1059-1524. doi: 10.1091/mbc.e11-08-0688. URL `https://doi.org/10.1091/mbc.e11-08-0688`.

K. Margolin, J. Longmate, T. W. Synold, D. R. Gandara, J. Weber, R. Gonzalez, M. J. Johansen, R. Newman, T. Baratta, and J. H. Doroshow. Dolastatin-10 in metastatic melanoma: a phase ii and pharmokinetic trial of the california cancer consortium. *Invest New Drugs*, 19(4):335–40, 2001. ISSN 0167-6997 (Print) 0167-6997 (Linking). URL `https://www.ncbi.nlm.nih.gov/pubmed/11561695`.

Marlène Martinho, Diane Allegro, Isabelle Huvent, Charlotte Chabaud, Emilien Etienne, Hervé Kovacic, Bruno Guigliarelli, Vincent Peyrot, Isabelle Landrieu, Valérie Belle, and Pascale Barbier. Two tau binding sites on tubulin revealed by thiol-disulfide exchanges. *Scientific Reports*, 8(1):13846, 2018. ISSN 2045-2322. doi: 10.1038/s41598-018-32096-9. URL `https://doi.org/10.1038/s41598-018-32096-9`.

J. C. Masters, D. J. Nickens, D. Xuan, R. L. Shazer, and M. Amantea. Clinical toxicity of antibody drug conjugates: a meta-analysis of payloads. *Invest New Drugs*, 2017. ISSN 1573-0646 (Electronic) 0167-6997 (Linking). doi: 10.1007/s10637-017-0520-6. URL `https://www.ncbi.nlm.nih.gov/pubmed/29027591`.

S. P. Maurer, P. Bieling, J. Cope, A. Hoenger, and T. Surrey. Gtp s microtubules mimic the growing microtubule end structure recognized by end-binding proteins (ebs). *Proc Natl Acad Sci U S A*, 108(10):3988–3993, 2011. ISSN 0027-8424. doi: 10.1073/pnas.1014758108. URL `https://dx.doi.org/10.1073/pnas.1014758108`.

Sebastian Maurer, Franck Fourniol, Gergő Bohner, Carolyn Moores, and Thomas Surrey. Ebs recognize a nucleotide-dependent structural cap at growing microtubule ends. *Cell*, 149(2):371–382, 2012. ISSN 0092-8674. doi: 10.1016/j.cell.2012.02.049. URL `https://dx.doi.org/10.1016/j.cell.2012.02.049`.

Sebastian Maurer, Nicholas Cade, Gergő Bohner, Nils Gustafsson, Emmanuel Boutant, and Thomas Surrey. Eb1 accelerates two conformational transitions important for microtubule maturation and dynamics. *Current Biology*, 24(4):372–384, 2014. ISSN 0960-9822. doi: 10.1016/j.cub.2013.12.042. URL `https://dx.doi.org/10.1016/j.cub.2013.12.042`.

J. R. McIntosh, E. L. Grishchuk, M. K. Morphew, A. K. Efremov, K. Zhudenkov, V. A. Volkov, I. M. Cheeseman, A. Desai, D. N. Mastronarde, and F. I. Ataullakhanov. Fibrils connect microtubule tips with kinetochores: a mechanism to couple tubulin dynamics to chromosome motion. *Cell*, 135(2):322–33, 2008. ISSN 0092-8674. doi: 10.1016/j.cell.2008.08.038.

J. R. McIntosh, E. O'Toole, K. Zhudenkov, M. Morphew, C. Schwartz, F. I. Ataullakhanov, and E. L. Grishchuk. Conserved and divergent features of kinetochores

and spindle microtubule ends from five species. *J Cell Biol*, 200(4):459–74, 2013. ISSN 0021-9525. doi: 10.1083/jcb.201209154.

J. Richard McIntosh, Eileen O'Toole, Garry Morgan, Jotham Austin, Evgeniy Ulyanov, Fazoil Ataullakhanov, and Nikita Gudimchuk. Microtubules grow by the addition of bent guanosine triphosphate tubulin to the tips of curved protofilaments. *Journal of Cell Biology*, 217(8):2691–2708, 2018. ISSN 0021-9525. doi: 10.1083/jcb.201802138. URL https://doi.org/10.1083/jcb.201802138.

K. M. McKibben and E. Rhoades. Independent tubulin binding and polymerization by the proline-rich region of tau is regulated by tau's n-terminal domain. *J Biol Chem*, 294(50):19381–19394, 2019. ISSN 0021-9258. doi: 10.1074/jbc.RA119.010172.

Jr. Meredith, J. E., S. Sankaranarayanan, V. Guss, A. J. Lanzetti, F. Berisha, R. J. Neely, J. R. Slemmon, E. Portelius, H. Zetterberg, K. Blennow, H. Soares, M. Ahlijanian, and C. F. Albright. Characterization of novel csf tau and ptau biomarkers for alzheimer's disease. *PLoS One*, 8(10):e76523, 2013. ISSN 1932-6203. doi: 10.1371/journal.pone.0076523.

K. Mi and G. V. Johnson. The role of tau phosphorylation in the pathogenesis of alzheimer's disease. *Curr Alzheimer Res*, 3(5):449–63, 2006. ISSN 1567-2050 (Print) 1567-2050 (Linking). URL http://www.ncbi.nlm.nih.gov/entrez/query.fcgi?cmd=Retrieve&db=PubMed&dopt=Citation&list_uids=17168644.

H. P. Miller and L. Wilson. *Preparation of Microtubule Protein and Purified Tubulin from Bovine Brain by Cycles of Assembly and Disassembly and Phosphocellulose Chromatography*, volume 95, pages 3–15. Elsevier Inc., 2010.

J. C. Mirsalis, J. Schindler-Horvat, J. R. Hill, J. E. Tomaszewski, S. J. Donohue, and C. A. Tyson. Toxicity of dolastatin 10 in mice, rats and dogs and its clinical relevance. *Cancer Chemother Pharmacol*, 44(5):395–402, 1999. ISSN 0344-5704 (Print) 0344-5704 (Linking). doi: 10.1007/s002800050995. URL https://www.ncbi.nlm.nih.gov/pubmed/10501913.

S. Mondragón-Rodríguez, G. Perry, J. Luna-Muñoz, M. C. Acevedo-Aquino, and S. Williams. Phosphorylation of tau protein at sites ser(396-404) is one of the earliest events in alzheimer's disease and down syndrome. *Neuropathol Appl Neurobiol*, 40(2):121–35, 2014. ISSN 0305-1846. doi: 10.1111/nan.12084.

Siddhartha Mondragón-Rodríguez, Gustavo Basurto-Islas, Ismael Santa-Maria, Raúl Mena, Lester I. Binder, Jesús Avila, Mark A. Smith, George Perry, and Francisco García-Sierra. Cleavage and conformational changes of tau protein follow phosphorylation during alzheimer's disease. *International journal of experimental pathology*, 89(2):81–90, 2008. ISSN 1365-2613 0959-9673. doi: 10.1111/j.1365-2613.2007.

00568.x. URL `https://pubmed.ncbi.nlm.nih.gov/18336525https://www.ncbi.nlm.nih.gov/pmc/articles/PMC2525766/`.

G. A. Morfini, M. Burns, L. I. Binder, N. M. Kanaan, N. LaPointe, D. A. Bosco, Jr. Brown, R. H., H. Brown, A. Tiwari, L. Hayward, J. Edgar, K. A. Nave, J. Garberrn, Y. Atagi, Y. Song, G. Pigino, and S. T. Brady. Axonal transport defects in neurodegenerative diseases. *J Neurosci*, 29(41):12776–86, 2009. ISSN 1529-2401 (Electronic) 0270-6474 (Linking). doi: 29/41/12776[pii]10.1523/JNEUROSCI.3463-09. 2009. URL `http://www.ncbi.nlm.nih.gov/entrez/query.fcgi?cmd=Retrieve&db=PubMed&dopt=Citation&list_uids=19828789`.

M. Morris, S. Maeda, K. Vossel, and L. Mucke. The many faces of tau. *Neuron*, 70(3):410–26, 2011. ISSN 1097-4199 (Electronic) 0896-6273 (Linking). doi: S0896-6273(11)00311-4[pii]10.1016/j.neuron.2011.04.009. URL `http://www.ncbi.nlm.nih.gov/entrez/query.fcgi?cmd=Retrieve&db=PubMed&dopt=Citation&list_uids=21555069`.

T. Muller-Reichert, D. Chretien, F. Severin, and A. A. Hyman. Structural changes at microtubule ends accompanying gtp hydrolysis: information from a slowly hydrolyzable analogue of gtp, guanylyl (alpha,beta)methylenediphosphonate. *Proc Natl Acad Sci U S A*, 95(7):3661–6, 1998. ISSN 0027-8424 (Print) 0027-8424 (Linking). URL `https://www.ncbi.nlm.nih.gov/pubmed/9520422`.

D. B. Murphy and G. G. Borisy. Association of high-molecular-weight proteins with microtubules and their role in microtubule assembly in vitro. *Proc Natl Acad Sci U S A*, 72(7):2696–700, 1975. ISSN 0027-8424 (Print) 0027-8424. doi: 10.1073/pnas.72.7.2696.

E. W. Nagiec, K. E. Sampson, and I. Abraham. Mutated tau binds less avidly to microtubules than wildtype tau in living cells. *J Neurosci Res*, 63(3):268–75, 2001. URL `http://www.ncbi.nlm.nih.gov/entrez/query.fcgi?cmd=Retrieve&db=PubMed&dopt=Citation&list_uids=11170176`.

J. H. Nettles, H. Li, B. Cornett, J. M. Krahn, J. P. Snyder, and K. H. Downing. The binding mode of epothilone a on alpha,beta-tubulin by electron crystallography. *Science*, 305(5685):866–9, 2004. ISSN 1095-9203 (Electronic) 0036-8075 (Linking). doi: 10.1126/science.1099190. URL `https://www.ncbi.nlm.nih.gov/pubmed/15297674`.

R. A. Newman, A. Fuentes, J. M. Covey, and J. A. Benvenuto. Preclinical pharmacology of the natural marine product dolastatin 10 (nsc 376128). *Drug Metab Dispos*, 22(3): 428–32, 1994. ISSN 0090-9556 (Print) 0090-9556 (Linking). URL `https://www.ncbi.nlm.nih.gov/pubmed/8070319`.

Vivian K. Ngan, Krista Bellman, Dulal Panda, Bridget T. Hill, Mary Ann Jordan, and Leslie Wilson. Novel actions of the antitumor drugs vinflunine and vinorelbine on

microtubules. *Cancer Research*, 60(18):5045–5051, 2000. URL `http://cancerres.aacrjournals.org/content/canres/60/18/5045.full.pdf`.

A. M. Nicholson and A. Ferreira. Increased membrane cholesterol might render mature hippocampal neurons more susceptible to beta-amyloid-induced calpain activation and tau toxicity. *J Neurosci*, 29(14):4640–51, 2009. ISSN 1529-2401 (Electronic) 0270-6474 (Linking). doi: 29/14/4640[pii]10.1523/JNEUROSCI.0862-09.2009. URL `http://www.ncbi.nlm.nih.gov/entrez/query.fcgi?cmd=Retrieve&db=PubMed&dopt=Citation&list_uids=19357288`.

E. Nogales, S. G. Wolf, I. A. Khan, R. F. Luduena, and K. H. Downing. Structure of tubulin at 6.5 a and location of the taxol-binding site. *Nature*, 375(6530):424–7, 1995. URL `http://www.ncbi.nlm.nih.gov/entrez/query.fcgi?cmd=Retrieve&db=PubMed&dopt=Citation&list_uids=7760939`.

E. Nogales, S. G. Wolf, and K. H. Downing. Structure of the alpha beta tubulin dimer by electron crystallography. *Nature*, 391(6663):199–203, 1998. URL `http://www.ncbi.nlm.nih.gov/entrez/query.fcgi?cmd=Retrieve&db=PubMed&dopt=Citation&list_uids=9428769`.

E. Nogales, H. W. Wang, and H. Niederstrasser. Tubulin rings: which way do they curve? *Curr Opin Struct Biol*, 13(2):256–61, 2003. ISSN 0959-440X (Print) 0959-440x. doi: 10.1016/s0959-440x(03)00029-0.

D. J. Odde, L. Ma, A. H. Briggs, A. DeMarco, and M. W. Kirschner. Microtubule bending and breaking in living fibroblast cells. *Journal of Cell Science*, 112(19):3283, 1999. URL `http://jcs.biologists.org/content/112/19/3283.abstract`.

T. Okouneva, O. Azarenko, L. Wilson, B. A. Littlefield, and M. A. Jordan. Inhibition of centromere dynamics by eribulin (e7389) during mitotic metaphase. *Mol Cancer Ther*, 7(7):2003–11, 2008. ISSN 1535-7163 (Print) 1535-7163 (Linking). doi: 10.1158/1535-7163.MCT-08-0095. URL `https://www.ncbi.nlm.nih.gov/pubmed/18645010`.

E. Oroudjev, M. Lopus, L. Wilson, C. Audette, C. Provenzano, H. Erickson, Y. Kovtun, R. Chari, and M. A. Jordan. Maytansinoid-antibody conjugates induce mitotic arrest by suppressing microtubule dynamic instability. *Mol Cancer Ther*, 9(10):2700–13, 2010. ISSN 1538-8514 (Electronic) 1535-7163 (Linking). doi: 9/10/2700[pii]10.1158/1535-7163.MCT-10-0645. URL `http://www.ncbi.nlm.nih.gov/entrez/query.fcgi?cmd=Retrieve&db=PubMed&dopt=Citation&list_uids=20937595`.

D. Panda, B. L. Goode, S. C. Feinstein, and L. Wilson. Kinetic stabilization of microtubule dynamics at steady state by tau and microtubule-binding domains of tau. *Biochemistry*, 34(35):11117–27, 1995. ISSN 0006-2960 (Print) 0006-2960 (Linking). URL `https://www.ncbi.nlm.nih.gov/pubmed/7669769`.

D. Panda, H. P. Miller, and L. Wilson.   Determination of the size and chemical nature of the stabilizing "cap" at microtubule ends using modulators of polymerization dynamics. *Biochemistry*, 41(5):1609–17, 2002.   URL `http://www.ncbi.nlm.nih.gov/entrez/query.fcgi?cmd=Retrieve&db=PubMed&dopt=Citation&list_uids=11814355`.

D. Panda, J. C. Samuel, M. Massie, S. C. Feinstein, and L. Wilson. Differential regulation of microtubule dynamics by three- and four-repeat tau: implications for the onset of neurodegenerative disease. *Proc Natl Acad Sci U S A*, 100(16):9548–53, 2003. ISSN 0027-8424 (Print) 0027-8424 (Linking). doi: 10.1073/pnas.1633508100. URL `https://www.ncbi.nlm.nih.gov/pubmed/12886013`.

S. Y. Park and A. Ferreira.   The generation of a 17 kda neurotoxic fragment: an alternative mechanism by which tau mediates beta-amyloid-induced neurodegeneration.   *J Neurosci*, 25(22):5365–75, 2005.   ISSN 1529-2401 (Electronic) 0270-6474 (Linking).   doi: 25/22/5365[pii]10.1523/JNEUROSCI.1125-05.2005.   URL `http://www.ncbi.nlm.nih.gov/entrez/query.fcgi?cmd=Retrieve&db=PubMed&dopt=Citation&list_uids=15930385`.

G.R. Pettit, Y. Kamano, C.L. Herald, A.A. Tuinman, F.E. Boettner, H. Kizu, J.M. Schmidt, L. Baczynskyj, K.B. Tomer, and R.J. Bontems. The isolation and structure of a remarkable marine animal antineoplastic constituent: dolastatin 10. *Journal of the American Chemical Society*, 109(22):6883–6885, 1987. doi: 10.1021/ja00256a070.

Natasha L. Pirman, Karl W. Barber, Hans R. Aerni, Natalie J. Ma, Adrian D. Haimovich, Svetlana Rogulina, Farren J. Isaacs, and Jesse Rinehart. A flexible codon in genomically recoded escherichia coli permits programmable protein phosphorylation. *Nature Communications*, 6(1):8130, 2015. ISSN 2041-1723. doi: 10.1038/ncomms9130. URL `https://doi.org/10.1038/ncomms9130`.

H. C. Pitot, Jr. McElroy, E. A., J. M. Reid, A. J. Windebank, J. A. Sloan, C. Erlichman, P. G. Bagniewski, D. L. Walker, J. Rubin, R. M. Goldberg, A. A. Adjei, and M. M. Ames. Phase i trial of dolastatin-10 (nsc 376128) in patients with advanced solid tumors. *Clin Cancer Res*, 5(3):525–31, 1999. ISSN 1078-0432 (Print) 1078-0432 (Linking). URL `https://www.ncbi.nlm.nih.gov/pubmed/10100703`.

M. S. Poruchynsky, E. Komlodi-Pasztor, S. Trostel, J. Wilkerson, M. Regairaz, Y. Pommier, X. Zhang, T. Kumar Maity, R. Robey, M. Burotto, D. Sackett, U. Guha, and A. T. Fojo. Microtubule-targeting agents augment the toxicity of dna-damaging agents by disrupting intracellular trafficking of dna repair proteins. *Proc Natl Acad Sci U S A*, 112(5):1571–6, 2015. ISSN 1091-6490 (Electronic) 0027-8424 (Linking). doi: 10.1073/pnas.1416418112. URL `https://www.ncbi.nlm.nih.gov/pubmed/25605897`.

A. E. Prota, K. Bargsten, D. Zurwerra, J. J. Field, J. F. Diaz, K. H. Altmann, and M. O. Steinmetz. Molecular mechanism of action of microtubule-stabilizing anticancer

agents. *Science*, 339(6119):587–90, 2013. ISSN 1095-9203 (Electronic) 0036-8075 (Linking). doi: 10.1126/science.1230582. URL `https://www.ncbi.nlm.nih.gov/pubmed/23287720`.

Liang Qiang, Xiaohuan Sun, Timothy O. Austin, Hemalatha Muralidharan, Daphney C. Jean, Mei Liu, Wenqian Yu, and Peter W. Baas. Tau does not stabilize axonal microtubules but rather enables them to have long labile domains. *Current Biology*, 28(13): 2181–2189.e4, 2018. ISSN 0960-9822. doi: https://doi.org/10.1016/j.cub.2018.05.045. URL `http://www.sciencedirect.com/science/article/pii/S096098221830681X`.

J. Reifert, D. Hartung-Cranston, and S. C. Feinstein. Amyloid beta-mediated cell death of cultured hippocampal neurons reveals extensive tau fragmentation without increased full-length tau phosphorylation. *J Biol Chem*, 286(23):20797–811, 2011. ISSN 1083-351X (Electronic) 0021-9258 (Linking). doi: M111.234674[pii]10.1074/jbc.M111.234674. URL `http://www.ncbi.nlm.nih.gov/entrez/query.fcgi?cmd=Retrieve&db=PubMed&dopt=Citation&list_uids=21482827`.

J. B. Reinecke, S. L. DeVos, J. P. McGrath, A. M. Shepard, D. K. Goncharoff, D. N. Tait, S. R. Fleming, M. P. Vincent, and M. L. Steinhilb. Implicating calpain in tau-mediated toxicity in vivo. *PLoS One*, 6(8):e23865, 2011. ISSN 1932-6203 (Electronic) 1932-6203 (Linking). doi: 10.1371/journal.pone.0023865. URL `https://www.ncbi.nlm.nih.gov/pubmed/21858230`.

L. M. Rice, E. A. Montabana, and D. A. Agard. The lattice as allosteric effector: structural studies of alphabeta- and gamma-tubulin clarify the role of gtp in microtubule assembly. *Proc Natl Acad Sci U S A*, 105(14): 5378–83, 2008. ISSN 1091-6490 (Electronic). doi: 0801155105[pii]10.1073/pnas.0801155105. URL `http://www.ncbi.nlm.nih.gov/entrez/query.fcgi?cmd=Retrieve&db=PubMed&dopt=Citation&list_uids=18388201`.

W. R. Rice and S. D. Gaines. Extending nondirectional heterogeneity tests to evaluate simply ordered alternative hypotheses. *Proc Natl Acad Sci U S A*, 91(1):225–6, 1994a. ISSN 0027-8424 (Print) 0027-8424 (Linking). URL `https://www.ncbi.nlm.nih.gov/pubmed/8278369`.

William R. Rice and Steven D. Gaines. The ordered-heterogeneity family of tests. *Biometrics*, 50(3):746, 1994b. ISSN 0006-341X. doi: 10.2307/2532788. URL `https://dx.doi.org/10.2307/2532788`.

J. Roostalu and T. Surrey. Microtubule nucleation: beyond the template. *Nat Rev Mol Cell Biol*, 2017. ISSN 1471-0080 (Electronic) 1471-0072 (Linking). doi: 10.1038/nrm.2017.75. URL `https://www.ncbi.nlm.nih.gov/pubmed/28831203`.

J. Roostalu, N. I. Cade, and T. Surrey. Complementary activities of tpx2 and chtog constitute an efficient importin-regulated microtubule nucleation module. *Nat Cell Biol*, 17(11):1422–34, 2015. ISSN 1465-7392. doi: 10.1038/ncb3241.

J. Roostalu, C. Thomas, N. I. Cade, S. Kunzelmann, I. A. Taylor, and T. Surrey. The speed of gtp hydrolysis determines gtp cap size and controls microtubule stability. *Elife*, 9, 2020. ISSN 2050-084x. doi: 10.7554/eLife.51992.

K. J. Rosenberg, J. L. Ross, H. E. Feinstein, S. C. Feinstein, and J. Israelachvili. Complementary dimerization of microtubule-associated tau protein: Implications for microtubule bundling and tau-mediated pathogenesis. *Proc Natl Acad Sci U S A*, 105(21):7445–50, 2008. ISSN 1091-6490 (Electronic) 0027-8424 (Linking). doi: 10.1073/pnas.0802036105. URL `https://www.ncbi.nlm.nih.gov/pubmed/18495933`.

H. Saber and J. K. Leighton. An fda oncology analysis of antibody-drug conjugates. *Regul Toxicol Pharmacol*, 71(3):444–52, 2015. ISSN 0273-2300. doi: 10.1016/j.yrtph.2015.01.014.

A. Samsonov, J. Z. Yu, M. Rasenick, and S. V. Popov. Tau interaction with microtubules in vivo. *J Cell Sci*, 117(Pt 25):6129–41, 2004. ISSN 0021-9533 (Print). doi: 117/25/6129[pii]10.1242/jcs.01531. URL `http://www.ncbi.nlm.nih.gov/entrez/query.fcgi?cmd=Retrieve&db=PubMed&dopt=Citation&list_uids=15564376`.

I. V. Sandoval and J. S. Vandekerckhove. A comparative study of the in vitro polymerization of tubulin in the presence of the microtubule-associated proteins map2 and tau. *J Biol Chem*, 256(16):8795–800, 1981. URL `http://www.ncbi.nlm.nih.gov/entrez/query.fcgi?cmd=Retrieve&db=PubMed&dopt=Citation&list_uids=7263687`.

I. V. Sandoval and K. Weber. Different tubulin polymers are produced by microtubule-associated proteins map2 and tau in the presence of guanosine 5'-(alpha, beta-methylene)triphosphate. *J Biol Chem*, 255(19):8952–4, 1980a. ISSN 0021-9258 (Print) 0021-9258 (Linking). URL `https://www.ncbi.nlm.nih.gov/pubmed/6773956`.

I. V. Sandoval and K. Weber. Guanasine 5'-(alpha,beta-methylene)triphosphate enhances specifically microtubule nucleation and stops the treadmill of tubulin protomers. *J Biol Chem*, 255(14):6966–74, 1980b. ISSN 0021-9258 (Print) 0021-9258 (Linking). URL `https://www.ncbi.nlm.nih.gov/pubmed/7391061`.

I. V. Sandoval, E. MacDonald, J. L. Jameson, and P. Cuatrecasas. Role of nucleotides in tubulin polymerization: effect of guanylyl 5'-methylenediphosphonate. *Proc Natl Acad Sci U S A*, 74(11):4881–5, 1977. ISSN 0027-8424 (Print) 0027-8424 (Linking). URL `https://www.ncbi.nlm.nih.gov/pubmed/200938`.

I. V. Sandoval, J. L. Jameson, J. Niedel, E. MacDonald, and P. Cuatrecasas. Role of nucleotides in tubulin polymerization: effect of guanosine 5'-methylene diphosphonate. *Proc Natl Acad Sci U S A*, 75(7):3178–82, 1978. ISSN 0027-8424 (Print) 0027-8424 (Linking). URL `https://www.ncbi.nlm.nih.gov/pubmed/277919`.

R. A. Santarella, G. Skiniotis, K. N. Goldie, P. Tittmann, H. Gross, E. M. Mandelkow, E. Mandelkow, and A. Hoenger. Surface-decoration of microtubules by human tau. *J Mol Biol*, 339(3):539–53, 2004. ISSN 0022-2836 (Print). doi: 10.1016/j.jmb.2004. 04.008S0022283604004127[pii]. URL `http://www.ncbi.nlm.nih.gov/entrez/query. fcgi?cmd=Retrieve&db=PubMed&dopt=Citation&list_uids=15147841`.

R. B. Scheele and G. G. Borisy. Electron microscopy of metal-shadowed and negatively stained microtubule protein. structure of the 30 s oligomer. *J Biol Chem*, 253(8): 2846–51, 1978. ISSN 0021-9258 (Print) 0021-9258.

3rd Schek, H. T., M. K. Gardner, J. Cheng, D. J. Odde, and A. J. Hunt. Microtubule assembly dynamics at the nanoscale. *Curr Biol*, 17(17):1445–55, 2007. ISSN 0960-9822 (Print) 0960-9822 (Linking). doi: 10.1016/j.cub.2007.07.011. URL `https:// www.ncbi.nlm.nih.gov/pubmed/17683936`.

A. Schneider, J. Biernat, M. von Bergen, E. Mandelkow, and E. M. Mandelkow. Phosphorylation that detaches tau protein from microtubules (ser262, ser214) also protects it against aggregation into alzheimer paired helical filaments. *Biochemistry*, 38(12):3549–58, 1999. URL `http://www.ncbi.nlm.nih.gov/entrez/query.fcgi?cmd=Retrieve& db=PubMed&dopt=Citation&list_uids=10090741`.

C. W. Scott, A. B. Klika, M. M. Lo, T. E. Norris, and C. B. Caputo. Tau protein induces bundling of microtubules in vitro: comparison of different tau isoforms and a tau protein fragment. *J Neurosci Res*, 33(1):19–29, 1992. URL `http://www.ncbi.nlm.nih.gov/entrez/query.fcgi?cmd=Retrieve& db=PubMed&dopt=Citation&list_uids=1360542`.

Dominique Seetapun, Brian T Castle, Alistair J McIntyre, Phong T Tran, and David J Odde. Estimating the microtubule gtp cap size in vivo. *Current Biology*, 22(18):1681–1687, 2012. ISSN 0960-9822. doi: https://doi.org/10.1016/j.cub.2012.06.068. URL `http://www.sciencedirect.com/science/article/pii/S0960982212007440`.

D. Sept, N. A. Baker, and J. A. McCammon. The physical basis of microtubule structure and stability. *Protein Sci*, 12(10):2257–61, 2003. ISSN 0961-8368 (Print) 0961-8368 (Linking). doi: 10.1110/ps.03187503. URL `https://www.ncbi.nlm.nih.gov/pubmed/ 14500883`.

J.R. Simon and E.D. Salmon. The structure of microtubule ends during the elongation and shortening phases of dynamic instability examined by negative-stain electron microscopy. *Journal of Cell Science*, 96(4):571–582, 1990. URL `https://jcs. biologists.org/content/joces/96/4/571.full.pdf`.

W. D. Singer, M. A. Jordan, L. Wilson, and R. H. Himes. Binding of vinblastine to stabilized microtubules. *Mol Pharmacol*, 36(3):366–70, 1989. ISSN 0026-895X (Print) 0026-895X (Linking). URL `https://www.ncbi.nlm.nih.gov/pubmed/2571072`.

R. C. Sinjoanu, S. Kleinschmidt, R. S. Bitner, J. D. Brioni, A. Moeller, and A. Ferreira. The novel calpain inhibitor a-705253 potently inhibits oligomeric beta-amyloid-induced dynamin 1 and tau cleavage in hippocampal neurons. *Neurochem Int*, 53(3-4):79–88, 2008. ISSN 0197-0186 (Print) 0197-0186. doi: 10.1016/j.neuint.2008.06.003.

R. D. Sloboda and J. L. Rosenbaum. Purification and assay of microtubule-associated proteins (maps). *Methods Enzymol*, 85 Pt B:409–16, 1982. ISSN 0076-6879 (Print) 0076-6879 (Linking). URL `https://www.ncbi.nlm.nih.gov/pubmed/7121279`.

Roger D. Sloboda and Joel L. Rosenbaum. Decoration and stabilization of intact, smooth-walled microtubules with microtubule-associated proteins. *Biochemistry*, 18(1):48–55, 1979. ISSN 0006-2960. doi: 10.1021/bi00568a008. URL `https://doi.org/10.1021/bi00568a008`.

J. A. Smith, L. Wilson, O. Azarenko, X. Zhu, B. M. Lewis, B. A. Littlefield, and M. A. Jordan. Eribulin binds at microtubule ends to a single site on tubulin to suppress dynamic instability. *Biochemistry*, 49(6):1331–7, 2010. ISSN 1520-4995 (Electronic) 0006-2960 (Linking). doi: 10.1021/bi901810u. URL `https://www.ncbi.nlm.nih.gov/pubmed/20030375`.

J. A. Smith, B. S. Slusher, K. M. Wozniak, M. H. Farah, G. Smiyun, L. Wilson, S. Feinstein, and M. A. Jordan. Structural basis for induction of peripheral neuropathy by microtubule-targeting cancer drugs. *Cancer Res*, 76(17):5115–23, 2016. ISSN 1538-7445 (Electronic) 0008-5472 (Linking). doi: 10.1158/0008-5472.CAN-15-3116. URL `https://www.ncbi.nlm.nih.gov/pubmed/27488522`.

E. Sontag, V. Nunbhakdi-Craig, G. Lee, R. Brandt, C. Kamibayashi, J. Kuret, 3rd White, C. L., M. C. Mumby, and G. S. Bloom. Molecular interactions among protein phosphatase 2a, tau, and microtubules. implications for the regulation of tau phosphorylation and the development of tauopathies. *J Biol Chem*, 274(36):25490–8, 1999. URL `http://www.ncbi.nlm.nih.gov/entrez/query.fcgi?cmd=Retrieve&db=PubMed&dopt=Citation&list_uids=10464280`.

M. G. Spillantini, T. D. Bird, and B. Ghetti. Frontotemporal dementia and parkinsonism linked to chromosome 17: a new group of tauopathies. *Brain Pathol*, 8(2):387–402, 1998.

M. G. Spillantini, J. C. Van Swieten, and M. Goedert. Tau gene mutations in frontotemporal dementia and parkinsonism linked to chromosome 17 (ftdp-17). *Neurogenetics*, 2(4):193–205, 2000. URL `http://www.ncbi.nlm.nih.gov/entrez/query.fcgi?cmd=Retrieve&db=PubMed&dopt=Citation&list_uids=10983715`.

N. J. Stagg, B. Q. Shen, F. Brunstein, C. Li, A. V. Kamath, F. Zhong, M. Schutten, and B. M. Fine. Peripheral neuropathy with microtubule inhibitor containing

antibody drug conjugates: Challenges and perspectives in translatability from non-clinical toxicology studies to the clinic. *Regul Toxicol Pharmacol*, 82:1–13, 2016. ISSN 1096-0295 (Electronic) 0273-2300 (Linking). doi: 10.1016/j.yrtph.2016.10.012. URL `https://www.ncbi.nlm.nih.gov/pubmed/27773754`.

K. Stamer, R. Vogel, E. Thies, E. Mandelkow, and E. M. Mandelkow. Tau blocks traffic of organelles, neurofilaments, and app vesicles in neurons and enhances oxidative stress. *J Cell Biol*, 156(6):1051–63, 2002. URL `http://www.ncbi.nlm.nih.gov/entrez/query.fcgi?cmd=Retrieve&db=PubMed&dopt=Citation&list_uids=11901170`.

Michel O. Steinmetz and Andrea E. Prota. Microtubule-targeting agents: Strategies to hijack the cytoskeleton. *Trends in Cell Biology*, 28(10):776–792, 2018. ISSN 0962-8924. doi: https://doi.org/10.1016/j.tcb.2018.05.001. URL `http://www.sciencedirect.com/science/article/pii/S0962892418300965`.

G. B. Stokin and L. S. Goldstein. Axonal transport and alzheimer's disease. *Annu Rev Biochem*, 75:607–27, 2006. ISSN 0066-4154 (Print). URL `http://www.ncbi.nlm.nih.gov/entrez/query.fcgi?cmd=Retrieve&db=PubMed&dopt=Citation&list_uids=16756504`.

C. Strothman, V. Farmer, G. Arpag, N. Rodgers, M. Podolski, S. Norris, R. Ohi, and M. Zanic. Microtubule minus-end stability is dictated by the tubulin off-rate. *J Cell Biol*, 218(9):2841–2853, 2019. ISSN 0021-9525. doi: 10.1083/jcb.201905019.

F. W. Studier. Protein production by auto-induction in high density shaking cultures. *Protein Expr Purif*, 41(1):207–34, 2005. ISSN 1046-5928 (Print) 1046-5928 (Linking). URL `https://www.ncbi.nlm.nih.gov/pubmed/15915565`.

J. Stumpff and L. Wordeman. Chromosome congression: the kinesin-8-step path to alignment. *Curr Biol*, 17(9):R326–8, 2007. ISSN 0960-9822 (Print) 0960-9822 (Linking). doi: S0960-9822(07)01114-1[pii]10.1016/j.cub.2007.03.013. URL `http://www.ncbi.nlm.nih.gov/entrez/query.fcgi?cmd=Retrieve&db=PubMed&dopt=Citation&list_uids=17470346`.

S. M. Swain and J. C. Arezzo. Neuropathy associated with microtubule inhibitors: diagnosis, incidence, and management. *Clin Adv Hematol Oncol*, 6(6):455–67, 2008. ISSN 1543-0790 (Print) 1543-0790 (Linking). URL `http://www.ncbi.nlm.nih.gov/entrez/query.fcgi?cmd=Retrieve&db=PubMed&dopt=Citation&list_uids=18567992`.

Y. Takei, J. Teng, A. Harada, and N. Hirokawa. Defects in axonal elongation and neuronal migration in mice with disrupted tau and map1b genes. *J Cell Biol*, 150 (5):989–1000, 2000. URL `http://www.ncbi.nlm.nih.gov/entrez/query.fcgi?cmd=Retrieve&db=PubMed&dopt=Citation&list_uids=10973990`.

M. Tal, A. Silberstein, and E. Nusser. Why does coomassie brilliant blue r interact differently with different proteins? a partial answer. *J Biol Chem*, 260(18):9976–80, 1980.

A. R. Tan, E. H. Rubin, D. C. Walton, D. E. Shuster, Y. N. Wong, F. Fang, S. Ashworth, and L. S. Rosen. Phase i study of eribulin mesylate administered once every 21 days in patients with advanced solid tumors. *Clin Cancer Res*, 15(12):4213–9, 2009. ISSN 1078-0432 (Print) 1078-0432 (Linking). doi: 10.1158/1078-0432.CCR-09-0360. URL https://www.ncbi.nlm.nih.gov/pubmed/19509146.

R. Tan, A. J. Lam, T. Tan, J. Han, D. W. Nowakowski, M. Vershinin, S. Simo, K. M. Ori-McKenney, and R. J. McKenney. Microtubules gate tau condensation to spatially regulate microtubule functions. *Nat Cell Biol*, 21(9):1078–1085, 2019. ISSN 1465-7392. doi: 10.1038/s41556-019-0375-5.

R Studio Team, 2016a. URL https://www.R-project.org/.

R Studio Team, 2016b. URL http://www.rstudio.com/.

R. J. Toso, M. A. Jordan, K. W. Farrell, B. Matsumoto, and L. Wilson. Kinetic stabilization of microtubule dynamic instability in vitro by vinblastine. *Biochemistry*, 32(5):1285–93, 1993. ISSN 0006-2960 (Print) 0006-2960 (Linking). URL https://www.ncbi.nlm.nih.gov/pubmed/8448138.

P. T. Tran, R. A. Walker, and E. D. Salmon. A metastable intermediate state of microtubule dynamic instability that differs significantly between plus and minus ends. *J Cell Biol*, 138(1):105–17, 1997. ISSN 0021-9525 (Print) 0021-9525 (Linking). URL https://www.ncbi.nlm.nih.gov/pubmed/9214385.

B. Trinczek, J. Biernat, K. Baumann, E. M. Mandelkow, and E. Mandelkow. Domains of tau protein, differential phosphorylation, and dynamic instability of microtubules. *Mol Biol Cell*, 6(12):1887–902, 1995. ISSN 1059-1524 (Print) 1059-1524 (Linking). URL https://www.ncbi.nlm.nih.gov/pubmed/8590813.

L. T. Vahdat, B. Pruitt, C. J. Fabian, R. R. Rivera, D. A. Smith, E. Tan-Chiu, J. Wright, A. R. Tan, N. A. Dacosta, E. Chuang, J. Smith, J. O'Shaughnessy, D. E. Shuster, N. L. Meneses, K. Chandrawansa, F. Fang, P. E. Cole, S. Ashworth, and J. L. Blum. Phase ii study of eribulin mesylate, a halichondrin b analog, in patients with metastatic breast cancer previously treated with an anthracycline and a taxane. *J Clin Oncol*, 27(18): 2954–61, 2009. ISSN 1527-7755 (Electronic) 0732-183X (Linking). doi: 10.1200/JCO. 2008.17.7618. URL https://www.ncbi.nlm.nih.gov/pubmed/19349550.

V. Vanburen, D. J. Odde, and L. Cassimeris. Estimates of lateral and longitudinal bond energies within the microtubule lattice. *Proceedings of the National Academy of Sciences*, 99(9):6035–6040, 2002. ISSN 0027-8424. doi: 10.1073/pnas.092504999. URL https://dx.doi.org/10.1073/pnas.092504999.

V. VanBuren, L. Cassimeris, and D. J. Odde. Mechanochemical model of microtubule structure and self-assembly kinetics. *Biophys J*, 89(5):2911–26, 2005. ISSN 0006-3495 (Print) 0006-3495. doi: 10.1529/biophysj.105.060913.

Benjamin Vitre, Frédéric M. Coquelle, Claire Heichette, Cyrille Garnier, Denis Chrétien, and Isabelle Arnal. Eb1 regulates microtubule dynamics and tubulin sheet closure in vitro. *Nature Cell Biology*, 10(4):415–421, 2008. ISSN 1465-7392. doi: 10.1038/ncb1703. URL https://dx.doi.org/10.1038/ncb1703.

I. A. Vorobjev, T. M. Svitkina, and G. G. Borisy. Cytoplasmic assembly of microtubules in cultured cells. *Journal of Cell Science*, 110(21):2635, 1997. URL http://jcs.biologists.org/content/110/21/2635.abstract.

K. A. Vossel, K. Zhang, J. Brodbeck, A. C. Daub, P. Sharma, S. Finkbeiner, B. Cui, and L. Mucke. Tau reduction prevents abeta-induced defects in axonal transport. *Science*, 330(6001):198, 2010. ISSN 0036-8075. doi: 10.1126/science.1194653.

K. A. Vossel, J. C. Xu, V. Fomenko, T. Miyamoto, E. Suberbielle, J. A. Knox, K. Ho, D. H. Kim, G. Q. Yu, and L. Mucke. Tau reduction prevents abeta-induced axonal transport deficits by blocking activation of gsk3beta. *J Cell Biol*, 209(3):419–33, 2015. ISSN 0021-9525. doi: 10.1083/jcb.201407065.

W. A. Voter and H. P. Erickson. The kinetics of microtubule assembly. evidence for a two-stage nucleation mechanism. *J Biol Chem*, 259(16):10430–8, 1984. URL http://www.ncbi.nlm.nih.gov/entrez/query.fcgi?cmd=Retrieve&db=PubMed&dopt=Citation&list_uids=6469971.

A. B. Waight, K. Bargsten, S. Doronina, M. O. Steinmetz, D. Sussman, and A. E. Prota. Structural basis of microtubule destabilization by potent auristatin antimitotics. *PLoS One*, 11(8):e0160890, 2016. ISSN 1932-6203 (Electronic) 1932-6203 (Linking). doi: 10.1371/journal.pone.0160890. URL https://www.ncbi.nlm.nih.gov/pubmed/27518442.

R. A. Walker, E. T. O'Brien, N. K. Pryer, M. F. Soboeiro, W. A. Voter, H. P. Erickson, and E. D. Salmon. Dynamic instability of individual microtubules analyzed by video light microscopy: rate constants and transition frequencies. *J Cell Biol*, 107(4):1437–48, 1988. URL http://www.ncbi.nlm.nih.gov/entrez/query.fcgi?cmd=Retrieve&db=PubMed&dopt=Citation&list_uids=3170635.

R. A. Walker, S. Inoue, and E. D. Salmon. Asymmetric behavior of severed microtubule ends after ultraviolet-microbeam irradiation of individual microtubules in vitro. *J Cell Biol*, 108(3):931–7, 1989. ISSN 0021-9525 (Print) 0021-9525. doi: 10.1083/jcb.108.3.931.

H. W. Wang and E. Nogales. Nucleotide-dependent bending flexibility of tubulin regulates microtubule assembly. *Nature*, 435(7044):911–5, 2005. ISSN 1476-4687 (Electronic) 0028-0836 (Linking). doi: 10.1038/nature03606. URL `https://www.ncbi.nlm.nih.gov/pubmed/15959508`.

H. W. Wang, S. Long, K. R. Finley, and E. Nogales. Assembly of gmpcpp-bound tubulin into helical ribbons and tubes and effect of colchicine. *Cell Cycle*, 4(9):1157–60, 2005. ISSN 1551-4005 (Electronic) 1551-4005 (Linking). doi: 10.4161/cc.4.9.2042. URL `https://www.ncbi.nlm.nih.gov/pubmed/16123589`.

Y. Wang, F. W. Benz, Y. Wu, Q. Wang, Y. Chen, X. Chen, H. Li, Y. Zhang, R. Zhang, and J. Yang. Structural insights into the pharmacophore of vinca domain inhibitors of microtubules. *Mol Pharmacol*, 89(2):233–42, 2016. ISSN 1521-0111 (Electronic) 0026-895X (Linking). doi: 10.1124/mol.115.100149. URL `https://www.ncbi.nlm.nih.gov/pubmed/26660762`.

C. M. Waterman-Storer and E. D. Salmon. Microtubule dynamics: treadmilling comes around again. *Curr Biol*, 7(6):R369–72, 1997. URL `http://www.ncbi.nlm.nih.gov/entrez/query.fcgi?cmd=Retrieve&db=PubMed&dopt=Citation&list_uids=9197225`.

K. Weber, J. R. Pringle, and M. Osborn. Measurement of molecular weights by electrophoresis on sds-acrylamide gel. *Methods Enzymol*, 26:3–27, 1972. ISSN 0076-6879 (Print) 0076-6879 (Linking). URL `https://www.ncbi.nlm.nih.gov/pubmed/4680711`.

S. Wegmann, S. Nicholls, S. Takeda, Z. Fan, and B. T. Hyman. Formation, release, and internalization of stable tau oligomers in cells. *J Neurochem*, 139(6):1163–1174, 2016. ISSN 1471-4159 (Electronic) 0022-3042 (Linking). doi: 10.1111/jnc.13866. URL `https://www.ncbi.nlm.nih.gov/pubmed/27731899`.

Susanne Wegmann, Bahareh Eftekharzadeh, Katharina Tepper, Katarzyna M. Zoltowska, Rachel E. Bennett, Simon Dujardin, Pawel R. Laskowski, Danny MacKenzie, Tarun Kamath, Caitlin Commins, Charles Vanderburg, Allyson D. Roe, Zhanyun Fan, Amandine M. Molliex, Amayra Hernandez-Vega, Daniel Muller, Anthony A. Hyman, Eckhard Mandelkow, J. Paul Taylor, and Bradley T. Hyman. Tau protein liquid-liquid phase separation can initiate tau aggregation. *The EMBO journal*, 37(7):e98049, 2018. ISSN 1460-2075 0261-4189. doi: 10.15252/embj.201798049. URL `https://pubmed.ncbi.nlm.nih.gov/29472250https://www.ncbi.nlm.nih.gov/pmc/articles/PMC5881631/`.

M. D. Weingarten, M. M. Suter, D. R. Littman, and M. W. Kirschner. Properties of the depolymerization products of microtubules from mammalian brain. *Biochemistry*, 13(27):5529–37, 1974. ISSN 0006-2960 (Print) 0006-2960 (Linking). URL `https://www.ncbi.nlm.nih.gov/pubmed/4457112`.

M. D. Weingarten, A. H. Lockwood, S. Y. Hwo, and M. W. Kirschner. A protein factor essential for microtubule assembly. *Proc Natl Acad Sci U S A*, 72(5):1858–62, 1975. URL `http://www.ncbi.nlm.nih.gov/entrez/query.fcgi?cmd=Retrieve&db=PubMed&dopt=Citation&list_uids=1057175`.

Jr. Williams, R. C. and J. C. Lee. Preparation of tubulin from brain. *Methods Enzymol*, 85(Pt B):376–85., 1982.

C. M. Wilson. Staining of proteins on gels: comparisons of dyes and procedures. *Methods Enzymol*, 91:236–47, 1983. ISSN 0076-6879 (Print) 0076-6879 (Linking). URL `https://www.ncbi.nlm.nih.gov/pubmed/6190068`.

L. Wilson, K. M. Creswell, and D. Chin. The mechanism of action of vinblastine. binding of [acetyl-3h]vinblastine to embryonic chick brain tubulin and tubulin from sea urchin sperm tail outer doublet microtubules. *Biochemistry*, 14(26):5586–92, 1975. ISSN 0006-2960 (Print) 0006-2960 (Linking). URL `https://www.ncbi.nlm.nih.gov/pubmed/1203244`.

L. Wilson, M. A. Jordan, A. Morse, and R. L. Margolis. Interaction of vinblastine with steady-state microtubules in vitro. *J Mol Biol*, 159(1):125–49, 1982. ISSN 0022-2836 (Print) 0022-2836 (Linking). URL `https://www.ncbi.nlm.nih.gov/pubmed/7131559`.

L. Wilson, M. Lopus, H. P. Miller, O. Azarenko, S. Riffle, J. A. Smith, and M. A. Jordan. Effects of eribulin on microtubule binding and dynamic instability are strengthened in the absence of the betaiii tubulin isotype. *Biochemistry*, 54(42):6482–9, 2015. ISSN 1520-4995 (Electronic) 0006-2960 (Linking). doi: 10.1021/acs.biochem.5b00745. URL `https://www.ncbi.nlm.nih.gov/pubmed/26435331`.

A. J. Windebank and W. Grisold. Chemotherapy-induced neuropathy. *J Peripher Nerv Syst*, 13(1):27–46, 2008. ISSN 1529-8027 (Electronic) 1085-9489 (Linking). doi: JNS156[pii]10.1111/j.1529-8027.2008.00156.x. URL `http://www.ncbi.nlm.nih.gov/entrez/query.fcgi?cmd=Retrieve&db=PubMed&dopt=Citation&list_uids=18346229`.

M. S. Wolfe. Tau mutations in neurodegenerative diseases. *J Biol Chem*, 284(10):6021–5, 2009. ISSN 0021-9258 (Print) 0021-9258 (Linking). doi: 10.1074/jbc.R800013200. URL `https://www.ncbi.nlm.nih.gov/pubmed/18948254`.

C. Yang, J. Wu, C. de Heus, I. Grigoriev, N. Liv, Y. Yao, I. Smal, E. Meijering, J. Klumperman, R. Z. Qi, and A. Akhmanova. Eb1 and eb3 regulate microtubule minus end organization and golgi morphology. *J Cell Biol*, 216(10):3179–3198, 2017. ISSN 0021-9525. doi: 10.1083/jcb.201701024.

M. Yenjerla, M. Lopus, and L. Wilson. Analysis of dynamic instability of steady-state microtubules in vitro by video-enhanced differential interference contrast microscopy with an appendix by emin oroudjev. *Methods Cell Biol*, 95:189–206, 2010. ISSN 0091-679X (Print) 0091-679X (Linking). doi: S0091-679X(10)95011-5[pii]10.1016/ S0091-679X(10)95011-5. URL `http://www.ncbi.nlm.nih.gov/entrez/query.fcgi? cmd=Retrieve&db=PubMed&dopt=Citation&list_uids=20466136`.

H. Yoshida and Y. Ihara. Tau in paired helical filaments is functionally distinct from fetal tau: assembly incompetence of paired helical filament-tau. *J Neurochem*, 61(3):1183– 6, 1993. URL `http://www.ncbi.nlm.nih.gov/entrez/query.fcgi?cmd=Retrieve& db=PubMed&dopt=Citation&list_uids=8360683`.

Hirotaka Yoshida and Michel Goedert. Sequential phosphorylation of tau protein by camp-dependent protein kinase and sapk4/p38δ or jnk2 in the presence of heparin generates the at100 epitope. *Journal of Neurochemistry*, 99(1):154–164, 2006. ISSN 0022-3042. doi: 10.1111/j.1471-4159.2006.04052.x. URL `https://onlinelibrary. wiley.com/doi/abs/10.1111/j.1471-4159.2006.04052.x`.

A. Younes, A. K. Gopal, S. E. Smith, S. M. Ansell, J. D. Rosenblatt, K. J. Savage, R. Ramchandren, N. L. Bartlett, B. D. Cheson, S. de Vos, A. Forero-Torres, C. H. Moskowitz, J. M. Connors, A. Engert, E. K. Larsen, D. A. Kennedy, E. L. Sievers, and R. Chen. Results of a pivotal phase ii study of brentuximab vedotin for patients with relapsed or refractory hodgkin's lymphoma. *J Clin Oncol*, 30(18):2183–9, 2012. ISSN 1527-7755 (Electronic) 0732-183X (Linking). doi: 10.1200/JCO.2011.38.0410. URL `https://www.ncbi.nlm.nih.gov/pubmed/22454421`.

P. Zakharov, N. Gudimchuk, V. Voevodin, A. Tikhonravov, F. I. Ataullakhanov, and E. L. Grishchuk. Molecular and mechanical causes of microtubule catastrophe and aging. *Biophys J*, 109(12):2574–2591, 2015. ISSN 0006-3495. doi: 10.1016/j.bpj.2015.10.048.

B. Zhang, J. Carroll, J. Q. Trojanowski, Y. Yao, M. Iba, J. S. Potuzak, A. M. Hogan, S. X. Xie, C. Ballatore, 3rd Smith, A. B., V. M. Lee, and K. R. Brunden. The microtubule-stabilizing agent, epothilone d, reduces axonal dysfunction, neurotoxicity, cognitive deficits, and alzheimer-like pathology in an interventional study with aged tau transgenic mice. *J Neurosci*, 32(11):3601–11, 2012. ISSN 1529-2401 (Electronic) 0270-6474 (Linking). doi: 10.1523/JNEUROSCI.4922-11.2012. URL `https://www. ncbi.nlm.nih.gov/pubmed/22423084`.

R. Zhang, G. M. Alushin, A. Brown, and E. Nogales. Mechanistic origin of microtubule dynamic instability and its modulation by eb proteins. *Cell*, 162(4):849–59, 2015. ISSN 1097-4172 (Electronic) 0092-8674 (Linking). doi: 10.1016/j.cell.2015.07.012. URL `https://www.ncbi.nlm.nih.gov/pubmed/26234155`.

R. Zhang, B. LaFrance, and E. Nogales. Separating the effects of nucleotide and eb binding on microtubule structure. *Proc Natl Acad Sci U S A*, 115(27):E6191–e6200, 2018. ISSN 0027-8424. doi: 10.1073/pnas.1802637115.